

Dissertation

submitted to the

Combined Faculty of Natural Sciences and Mathematics

of Heidelberg University, Germany

for the degree of

Doctor of Natural Sciences

Put forward by

Florian Lach

born in: Lindenberg im Allgäu

Oral examination: May 12th 2022

**Chandrasekhar mass explosions of white dwarfs
as a model for type Ia supernovae and
their contribution to cosmic nucleosynthesis**

Referees: Prof. Dr. Friedrich K. Röpke
Prof. Dr. Simon C. O. Glover

Chandrasekhar mass explosions of white dwarfs as a model for type Ia supernovae and their contribution to cosmic nucleosynthesis

Abstract Although type Ia supernovae are widely applied as cosmological distance indicators and contribute significantly to the enrichment of the Universe with iron group elements, their physical nature is not clear yet. The heterogeneous class of type Ia supernovae is divided into several subtypes according to their observational properties, and a whole variety of possible explosion scenarios has been put forward in order to explain these extraordinarily bright events. The focus of this work lies on the numerical modeling of explosions in Chandrasekhar mass carbon-oxygen white dwarfs as well as on the investigation of the nucleosynthesis yields of several explosion channels. To this end, numerical simulations of the explosion, the propagation of radiation through the expanding debris, and the galactic chemical evolution of the Milky Way were conducted. It was found that, in line with earlier studies, deflagrations in Chandrasekhar mass white dwarfs are a viable model for type Iax supernovae, a subluminous subclass of type Ia supernovae. However, the parameter study employing different ignition conditions, central densities, metallicities, composition and rigid rotation revealed that the very faint end of the subclass can not be reproduced. Furthermore, a set of gravitationally confined detonation simulations has been carried out. In this scenario an initial deflagration is followed by a detonation initiated near the surface of the white dwarf core. It could be shown that the synthetic observables do not agree with either normal or subluminous type Ia supernovae but that objects similar to SN 1991T might be explained by this explosion mechanism. Finally, the nucleosynthesis yields of various different explosion models were analyzed. This study shows that explosions in sub-Chandrasekhar mass white dwarfs with an accreted helium shell can contribute significantly to the abundance of manganese, zinc, and copper in the Universe and should be included in future galactic chemical evolution studies.

Explosionen von weißen Zwergen nahe der Chandrasekhar-Masse als Modell für Typ Ia Supernovae und ihr Beitrag zur kosmischen Nukleosynthese

Zusammenfassung Obwohl die Verwendung von Typ Ia Supernovae zur Messung kosmologischer Entfernungen weit verbreitet ist und sie erheblich zur Anreicherung des Universums mit Eisengruppenelementen beitragen, ist ihr physikalischer Ursprung noch immer ungeklärt. Die heterogene Typ Ia Supernova Klasse ist basierend auf ihren optischen Eigenschaften in Unterklassen unterteilt und eine ganze Reihe an möglichen Szenarien wurden vorgeschlagen um diese außergewöhnlich hellen Ereignisse zu erklären. Der Fokus dieser Arbeit liegt auf der numerischen Modellierung von Explosionen in weißen Zwergen bestehend aus Kohlenstoff und Sauerstoff nahe der Chandrasekhar-Masse sowie auf der Untersuchung der Nukleosyntheseprodukte verschiedenster Explosionsszenarien. Zu diesem Zweck wurden numerische Simulationen der Explosion, des Strahlungstransportes durch das ausgestoßene Material sowie der chemischen Entwicklung der Milchstraße durchgeführt. In Übereinstimmung mit vorhergegangenen Studien wurde herausgefunden, dass Deflagrationen in weißen Zwergen nahe der Chandrasekhar-Masse ein gutes Modell für Supernovae vom Typ Iax, eine dunkle Unterklasse der Typ Ia Supernovae, darstellen. Die Parameterstudie mit verschiedenen Zündungskonfigurationen, Zentraldichten, Metallizitäten, Kompositionen und starr rotierenden Sternen macht jedoch deutlich, dass die dunkelsten Supernovae der Unterklasse nicht reproduziert werden können. Außerdem wurde eine Reihe an Simulationen des sogenannten “gravitationally confined detonation”-Szenarios durchgeführt. In diesem Modell folgt auf eine Deflagration eine Detonation, welche am Rand des gravitativ gebundenen Kerns zündet. Es wurde gezeigt, dass die berechneten Observablen nicht mit normalen oder dunklen Typ Ia Supernovae übereinstimmen. Objekte der überdurchschnittlich hellen Klasse benannt nach SN 1991T könnten allerdings durch diesen Mechanismus erklärt werden. Schließlich wurden die Produkte der Nukleosynthese von verschiedenen Explosionsmodellen analysiert. Diese Untersuchung zeigt, dass Explosionen in weißen Zwergen unterhalb der Chandrasekhar-Masse mit einer Schale aus akkretiertem Helium signifikant zur Häufigkeit der Elemente Mangan, Zink und Kupfer im Universum beitragen können und daher in zukünftigen Simulationen der chemischen Entwicklung des Universums berücksichtigt werden sollten.

Contents

1	Introduction - Development of the supernova theory in the historical context	11
2	This work	15
I	Type Ia supernovae	17
3	Observables	18
3.1	Photometry - Type Ia supernova light curves and their application to cosmology	19
3.2	Spectroscopy	24
3.3	Subclasses of type Ia supernovae	26
4	Physical foundations and explosion scenarios	30
4.1	White dwarf formation, structure, and accretion	31
4.2	Basic equations of fluid dynamics	35
4.3	Nuclear burning stages	36
4.4	Thermonuclear combustion	39
4.5	Explosion scenarios	43
4.6	Solving the progenitor problem	45
4.6.1	Supernova modeling pipeline	45
4.6.2	Galactic chemical evolution	46
4.6.3	Rates	46
4.6.4	Supernova remnants	47
5	Numerical modeling of type Ia supernovae	48
5.1	Hydrodynamic simulations - the LEAFS code	49
5.2	Nuclear network calculations - the YANN code	51
5.3	Radiative transfer modeling - the ARTIS code	52
II	Publications	53
6	Type Iax supernovae from deflagrations in Chandrasekhar mass white dwarfs	54

7	Models of pulsationally assisted gravitationally confined detonations with different ignition conditions	82
8	Nucleosynthesis imprints from different Type Ia supernova explosion scenarios and implications for galactic chemical evolution	98
III	Discussion	115
9	Summary of the scientific results	116
9.1	Publication 1: Type Iax supernovae from deflagrations in Chandrasekhar mass white dwarfs	116
9.2	Publication 2: Models of pulsationally assisted gravitationally confined detonations with different ignition conditions	118
9.3	Publication 3: Nucleosynthesis imprints from different Type Ia supernova explosion scenarios and implications for galactic chemical evolution	119
9.4	The broader picture	120
10	Summary and possible future work	122

Chapter 1

Introduction - Development of the supernova theory in the historical context

Until the beginning of the 20th century new stars suddenly appearing in the sky were simply termed *novae* (“nova” is the latin word for “new”). These rare events were puzzling to ancient observers since they challenged the Aristotelian system consisting of several heavenly spheres with fixed, immutable stars. Reports of new stars, or “guest stars” as Chinese astronomers called them, date back to AD 185 (Green 2017). Detailed historical records and their exact location, however, are only available for the five novae of AD 1006, 1054, 1181, 1572, and 1604 (Green 2002). Today it is well known that these historical events were supernovae (SNe), i.e., the explosion of stars at the end of their life time. The brightest among the historical SNe was the “guest star” of AD 1006 which was even visible at daylight during its early phase, and for roughly three years in total. A picture of a well-observed SN, SN 2011fe, is shown in the left panel of Fig. 1.1. It illustrates that the explosion of a single star can become as bright as a whole galaxy. Moreover, for all of the five historical events listed above a supernova remnant (SNR), i.e., a huge, expanding cloud of gas expelled by the explosion, could be identified whereas the crab nebula (categorized as M1, see right panel of Fig. 1.1) which is the remnant of SN 1054 is the most famous representative (Green 2017). In addition, the evolution of brightness over time, i.e., the light curve (LC), of the new star in AD 1572 was accurately recorded by Tycho Brahe. His notes were precise enough to make it possible for Walter Baade to classify the event as a Type I supernova (SN I, Marschall 1988, more details below and in Chapter 3).

The term supernova, however, was first used in a publication by Knut Lundmark in 1932 (Osterbrock 2001; Leibundgut 2017). SNe were then introduced as a separate class of transients by Baade and Zwicky (1934a,c,b) who claimed that SNe mark the end of the life of a star, are ~ 63 million times brighter than the Sun, are responsible for cosmic rays, and that gas is expelled at high velocities, leaving behind a neutron star. Their work was preceded by a prolonged argument about the structure, and, especially, the size of the Universe which culminated in the *great debate* between Harlow Shapley and Heber Curtis (Trimble 1995). Shapley advocated that spiral nebulae such as Andromeda are rather small objects and part of the Milky Way while Curtis had the opinion that they are independent galaxies, and, hence, very far away. Although novae were a pretty common phenomenon in the second half of the 19th century due to the availability of telescopes compared to the times of Tycho Brahe it was not clear how bright these transients actually were. The problem was that the distance could not be measured, and, therefore, one could not tell whether the transient was far away and very bright or nearby and comparatively



Figure 1.1: The left panel displays SN 2011fe in the Pinwheel galaxy, one of the best observed SNe to date. The right panel shows the crab nebula (SNR of SN 1054) observed in three colors. Green colored regions originate from hydrogen emission and blueish colors are due to synchrotron radiation of electrons emitted from a neutron star. Credit: B. J. Fulton, Las Cumbres Observatory Global Telescope Network (left), ESO (right).

faint. It was Edwin Hubble who used Cepheids¹ as distance indicators and showed that various spiral nebulae including Andromeda, also known as M31, are indeed located far outside of the Milky Way (Hubble 1929). This revolutionizing finding rendered the already bright nova of 1885 in the Andromeda nebula, also known as Hartwig’s nova (Copeland 1886), an unconceivably bright source. Lundmark (1925) then divided novae into two subclasses. These are the rare and luminous *upper class novae* and the common but faint *lower class novae*. Today, most of Lundmark’s lower class novae are associated with the so-called *classical novae* (CNe, see e.g., Starrfield et al. 2016 for an explanation of the mechanism behind CNe) while the upper class novae correspond to SNe.

After his bold predictions in 1934, Fritz Zwicky was eager to find new SNe and started the first systematic search in 1936. Together with Baade, who recorded the LCs, and Minkowski, who took spectra, he had already found three new SNe in 1937. Considering that only about two SNe are expected per galaxy and century (Tammann et al. 1994) this was a great success. Zwicky was also the main driver of SN searches during the following decades leading to 380 SN discoveries until his death in 1974 (Koenig 2005). Of course, as more and more observatories dedicated to the search for SNe were built and due to the fast advancement of technology including automated searches the number of known SNe increased fast with several hundreds of SNe being detected per year in recent times.

Although SN spectra were enigmatic, Minkowski found that they can be divided into two subgroups, i.e., SNe I exhibit no hydrogen (H) in their spectrum and supernovae of Type II

¹Cepheids are pulsating stars of variable brightness. Since their absolute luminosity is related to their pulsation period they are excellent standardizable candles used for distance measurements (see Feast and Walker 1987; Buchler 1997 or Feast 1999 for a review).

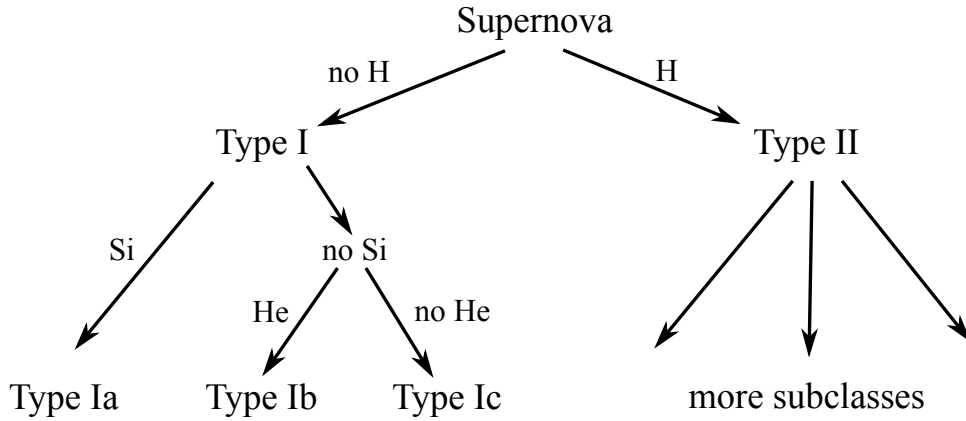


Figure 1.2: Supernova classification scheme based on spectral features.

(SNe II) show strong $H\alpha$ -lines (Minkowski 1941). Furthermore, SNe I appeared to form a homogeneous group of transients, which already prompted the idea that they could be used as distance indicators (see also Trimble 1982 for a review of the early SN research). This simple classification scheme was challenged when Bertola (1964) and Bertola et al. (1965) reported that SN 1962L and SN 1964L do not show the Si II absorption feature at 6355 \AA characteristic for SNe I near the maximum of the LC. It took around 20 years until, after the observation of the Si deficient SN 1983N and SN 1984L, a new subclass was introduced, namely SNe Ib (Elias et al. 1985). Consequently, the remaining objects of the SN I class were dubbed SN Ia. Only a few years later SNe Ic were separated from SN Ib because they do not show helium (He) lines in their spectrum (Wheeler and Harkness 1990) in contrast to SNe Ib. To date, due to the ever increasing number and quality of observations, many more subclasses of SNe II as well as SNe I exist (see Gal-Yam 2017; Taubenberger 2017). The classification scheme described above is visualized in Fig. 1.2. Of course, the subclasses mentioned can be subdivided even further based on more subtle characteristics of their LCs or spectra. However, the focus of this work lies solely on SNe Ia which will be discussed in more detail in Chapters 3 and 4. The classification of SNe is merely based on their spectra but does hint toward a common mechanism. In the case of SNe II, Ib, and Ic the ideas of Baade and Zwicky, i.e., that SNe gain their energy from gravitational collapse and leave behind a neutron star, stood the test of time. Since at least the detection of the neutrinos from SN 1987A the theory of gravitational collapse in SNe II is settled, and, therefore, they are referred to as core collapse supernovae (CCSNe). The leading paradigm is the delayed neutrino-heating mechanism (Janka 2017) first proposed by Colgate and White (1966) and further developed by Wilson (1985) and Bethe and Wilson (1985). When the final stage of nuclear burning, i.e., silicon (Si) burning (details follow in Section 4.3), has ceased, the dense iron core of a massive star contracts and deleptonizes until a proto-neutron star forms in the center. The infalling material then bounces off the stiff core and a shock is traveling outward. This shock, however, dies off due to photodissociation of iron. Subsequently, this shock is revived and accelerated again by neutrino-heating and material above the gravitationally bound core is expelled. SNe Ia, on the other hand, draw their energy from nuclear fusion reactions and are believed to originate from the thermonuclear explosion of a degenerate white dwarf (WD) star as suggested by Hoyle and Fowler (1960). The light emitted by a SN Ia primarily stems from the heating of the ejected material by the radioactive

decay² of ^{56}Ni to ^{56}Co which eventually decays to ^{56}Fe (Truran et al. 1967; Colgate and McKee 1969). Possible explanations of the exact explosion mechanism of SNe Ia will be elaborated in detail in Chapter. 4. In contrast to SNe II (e.g., SN 1987A, see for example Gilmozzi et al. 1987; Hillebrandt and Hoflich 1989) a progenitor star for SNe Ia has never been observed which still leaves room for a variety of possible explosion scenarios and a clear favorite has not emerged yet.

²The exponential decline of the LC hints toward a radioactive decay chain and it was Borst (1950) who suggested radioactivity as the energy source for the LC of SNe. The exact isotope, however, was not determined for the next 19 years.

Chapter 2

This work

This thesis is written in a cumulative format in accordance with the regulations of the Department of Physics and Astronomy of Heidelberg University. Three peer-reviewed articles in well acknowledged scientific journals build the main part of this thesis and include its contribution to the SNe Ia research. The author holds first authorship for all three publications.

Each publication contains an introduction containing theory and a scientific motivation relevant for the respective topic and aim. However, a broad coverage of the field of SNe Ia dedicated to non-experts is not a part of the published works. Therefore, the main part (Part II) is preceded by a more general introduction to the field (Part I). First, the observational properties, i.e., LCs and spectra, and the application of SNe Ia to cosmology will be reviewed in Chapter 3. The focus lies on the bulk of SNe Ia, the so-called normal SNe Ia. Subsequently, the distinct characteristics of various subtypes of SNe Ia will be explained. Second, in Chapter 4 the many variations and combinations of possible progenitor systems and explosion mechanisms will be summarized along with the theory needed to understand the main properties of each of these scenarios. This includes the physics of WD matter, fluid dynamics, thermonuclear combustion and nuclear burning. Moreover, a few common ways to infer the progenitor system and/or the explosion mechanism of SNe Ia are outlined. Third, Chapter 5 gives a more detailed overview of the numerical methods used in this thesis than is given in the publications. This includes the hydrodynamics code `LEAFS`, the nuclear network code `YANN` and the radiation transport code `ARTIS`. The main part (Part III) then comprises the publications:

Publication 1:

This work is dedicated to a certain subclass of SNe Ia, namely supernovae of type Iax (SNe Iax) which are characterized by a low luminosity, slowly expanding ejecta, and peculiar spectra compared to normal SNe Ia (see Section 3.3). The favored explosion mechanism for this class is a deflagration (see Section 4.4) inside a Chandrasekhar mass WD. The paper includes a large set of hydrodynamic explosion simulations which provide the dynamics and structure of the ejected material. Moreover, detailed isotopic abundances are calculated for each of the models and synthetic spectra and LCs are computed and compared to observations of SNe Iax. The result of this study is that pure deflagration models (see Section 4.5) remain a viable model for intermediately bright to very bright SNe Iax. The faintest events, however, are not reproduced naturally by this scenario.

Publication 2:

In this study, a particular explosion mechanism, the gravitationally confined detonation (GCD, see Chapter 4), is investigated. Within this scenario, a deflagration is followed by a detonation initiated in a later stage near the surface of the WD core. The methodology is similar to Publication 1. The aim is, however, not to look into a specific subclass such as SNe Iax but to judge whether a GCD can reproduce the observables of any class of SNe Ia. It is found that this explosion scenario can neither account for normal SNe Ia nor SNe Iax. However, the overluminous SN 1991T-like SNe (Section 3.3) might originate from this scenario.

Publication 3:

A very different approach compared to Publications 1 and 2 is followed in this work. Here, the elemental abundances ejected by a large variety of SN Ia model simulations are analyzed. The aim is to find specific characteristic elements for a certain explosion scenario to evaluate whether it is in agreement with the chemical evolution of the Universe. Indeed, it is found that thermonuclear explosions which include a detonation in a He shell (see Chapter 4 for more details on the double detonation mechanism) can contribute significantly to the cosmic abundances of manganese, copper, and zinc. These elements have not been taken into account as products of SNe Ia in previous galactic chemical evolution (GCE) studies aiming to unveil the origin of the elements.

The final part (Part III) of this thesis includes a brief summary of the work described in Publications 1, 2, and 3 and points out the most important findings relevant for current SN Ia research. Moreover, a clear connection between the three studies is worked out and their shortcomings and possible future projects are described and reviewed critically.

Part I

Type Ia supernovae

Chapter 3

Observables

Due to the extreme conditions prevailing inside a WD, i.e., temperatures T up to several 10^9 K during the explosion and densities of $\rho \gtrsim 10^8$ g cm $^{-3}$, experiments on Earth aiming to mimic a SN Ia explosion are not possible. Thus, the only available information of SNe Ia, and also other types of SNe, comes in the form of electromagnetic radiation originating from the hot expelled material.

SNe Ia emit most of their light from the ultraviolet (UV) regime to the near-infrared (NIR, [Leibundgut 2000](#)). In order to gain additional information light is observed through various filters, i.e., different colors. The most commonly employed passband filter system is the UBVRI system ([Johnson and Morgan 1953](#); [Cousins 1974](#); [Bessell 1990](#)) together with the JHK-system ([Persson et al. 1998](#)) to cover the range from the UV to the NIR. The wavelength ranges between $\sim 3\,000$ Å (U-Band) up to $\sim 24\,000$ Å (K-Band). Additionally, the Sloan Digital Sky Survey u'g'r'i'z'-System (from blue colors u' to red colors z') is employed in some studies. A prescription of how to transform between these two systems is given by [Jordi et al. \(2006\)](#). SNe Ia are not expected to be strong X-ray or radio emitters ([Leibundgut 2000](#)) and observations indeed show low evidence of radiation at these wavelengths ([Panagia et al. 2006](#); [Russell and Immler 2012](#); [Horesh et al. 2012](#)) in contrast to SNRs. In principle, SNe Ia are γ -ray emitters after the ejecta have become transparent. Detections of γ -rays, however, are rare and limited to very nearby objects ([Diehl and Timmes 1998](#); [Horiuchi and Beacom 2010](#)). Hence, radiation in UV, optical, and infrared bands (UVOIR) is a good approximation to the bolometric LC at early times which is defined as the cumulative radiation at all wavelengths.

Information is either gathered by photometric or spectroscopic measurements. Photometry collects the total flux emitted by a source of radiation and is useful to gain overall properties and to observe very faint transients. With a spectrometer, in contrast, the incoming light is split according to its wavelength and the flux can be displayed as a function of the latter. This enables observers to identify individual absorption or emission lines of an isotope, and, therefore, to infer the composition of the ejected material. Since more light is required to take a spectrum compared to the recording of a LC, this technique cannot be applied to the most subluminous or distant events. In the future, also neutrinos ([Kunugise and Iwamoto 2007](#); [Odrzywolek and Plewa 2011](#); [Seitenzahl et al. 2015](#)) and gravitational waves ([Falta et al. 2011](#); [Falta and Fisher 2011](#); [Seitenzahl et al. 2015](#)) from SNe Ia might be detected and offer new information on the explosion mechanism.

3.1 Photometry - Type Ia supernova light curves and their application to cosmology

It was already mentioned in Chapter 1 that the bolometric LC of a SN Ia is powered by the decay of ^{56}Ni to ^{56}Co (Colgate and McKee 1969). Due to its half-life of 6.075 d¹ γ -rays emitted in the β^+ -decay of ^{56}Ni heat the ejecta during the first ~ 2 weeks. Subsequently, positrons originating from the $^{56}\text{Co} \rightarrow ^{56}\text{Fe}$ decay become the main source of energy injection into the ejected material. Since the positron opacity is higher compared to γ -rays, they are trapped for longer times inside the expanding ejecta (Jerkstrand 2017). The slope of the postmaximum bolometric LC flattens as soon as the ^{56}Co -decay becomes dominant because the half-life of ^{56}Co is 77.236 d, and, thus, significantly longer than that of ^{56}Ni , slowing down the heating process. This notion was corroborated by Kuchner et al. (1994) who measured the flux ratio of certain Co III and Fe III emission features (for more details on spectroscopy see Section 3.2) in 13 SNe Ia between 38 and 310 d after peak brightness. They found that the Co-to-Fe ratio is in agreement with the radioactive decay of ^{56}Ni . The LC of SN 2011fe, a typical SN Ia, is shown in the left panel of Figure 3.1. The flattening of the decline due to the transition from ^{56}Ni to ^{56}Co is clearly visible at around 40 d after maximum light.

Arnett's rule

Arnett (1982) derived a simple analytic model for the early bolometric LCs of SNe Ia stating that the luminosity at maximum L_{max} equals the heating due to radioactive decay. This is a function of the rise time t_{R} from explosion to peak brightness and the initial mass of ^{56}Ni , $M(^{56}\text{Ni})$. The formula then simply follows from the nuclear decay chain of ^{56}Ni (Nadyozhin 1994):

$$L_{\text{max}} = E_{\text{Ni}} = \frac{1}{\tau_{\text{Co}} - \tau_{\text{Ni}}} \left[\left(Q_{\text{Ni}} \left(\frac{\tau_{\text{Co}}}{\tau_{\text{Ni}}} - 1 \right) - Q_{\text{Co}} \right) e^{-t_{\text{R}}/\tau_{\text{Ni}}} + Q_{\text{Co}} e^{-t_{\text{R}}/\tau_{\text{Co}}} \right] \frac{M(^{56}\text{Ni})}{56m_u}. \quad (3.1)$$

Here, E_{Ni} is the energy production rate, τ_i are the mean lifetimes, Q_i the energy released per decay of nucleus i and m_u is the atomic mass unit. This simplistic approach has some drawbacks such as its ignorance of the actual distribution of ^{56}Ni within the ejecta (Khatami and Kasen 2019) and the need for bolometric LCs (Contardo et al. 2000), i.e., observations in all bands. Nevertheless, it is commonly employed to estimate $M(^{56}\text{Ni})$ (see e.g., Stritzinger and Leibundgut 2005; Stritzinger et al. 2006) which is found to range between ~ 0.33 and $0.79 M_{\odot}$ (Stritzinger et al. 2006) for normal SNe Ia.

At later stages, roughly 1 000 d after explosion, also other radioactive decay chains such as $^{57}\text{Ni} \rightarrow ^{57}\text{Co} \rightarrow ^{57}\text{Fe}$, $^{55}\text{Co} \rightarrow ^{55}\text{Fe} \rightarrow ^{55}\text{Mn}$, and $^{44}\text{Ti} \rightarrow ^{44}\text{Sc} \rightarrow ^{44}\text{Ca}$ start to contribute to the bolometric LC (Seitenzahl et al. 2009b) and lead to a further flattening of the LC (see right panel of Figure 3.1). One complication making it hard to quantify the energy injection of a certain decay is the fact that the expelled material expands and cools. Matter then becomes more and more transparent to γ -rays as the density drops and later on also to leptons (Dimitriadis et al. 2017). This dynamical process makes it a complicated challenge to accurately predict observables of SNe Ia.

¹Nuclear properties are taken from <https://www.nndc.bnl.gov/nudat2/>.

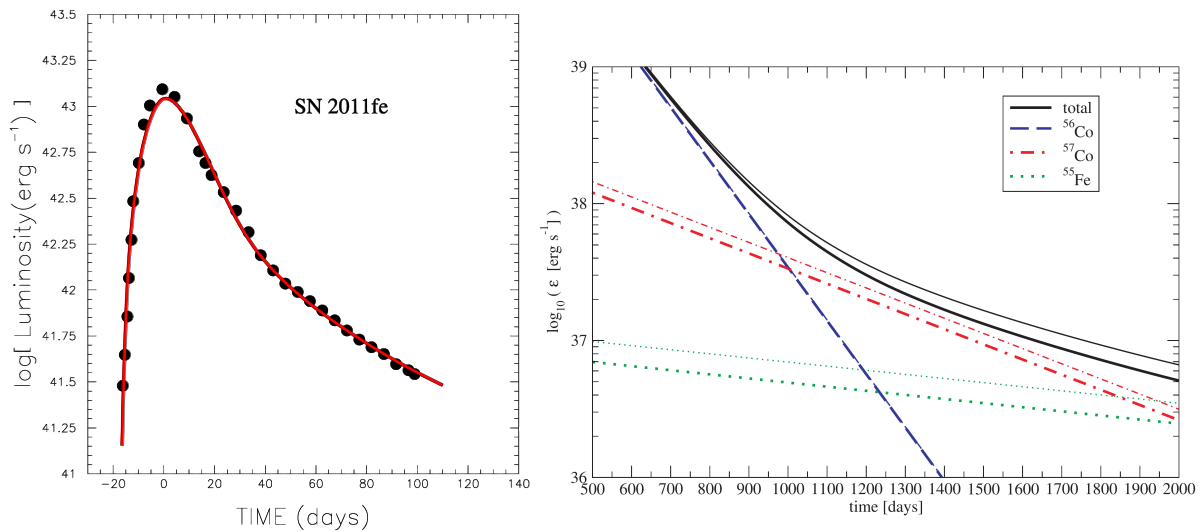


Figure 3.1: The left panel shows the bolometric LC of SN 2011fe (black dots) with an analytical LC based on the ^{56}Ni decay chain (red solid line, Credit: [Dado and Dar 2013](#)). A model late-time LC including long-lived isotopes with observations of SN 1998bw is shown in the right panel. Credit: [Seitenzahl et al. \(2009b\)](#).

Light curve colors

Not only the total flux but also the color-separated LCs (UBVRIJHK) contain useful information about the explosion process. Most of the thermal radiation of a SN Ia is emitted in the UV and blue optical bands, i.e., B and V-bands. The flux in infrared bands is largely due to absorption of UV-photons by iron group elements (IGEs) such as Fe or Co and their subsequent re-emission at larger wavelengths (fluorescence). Therefore, the UV flux is slightly lower than expected from a perfect black body ([Branch and Venkatakrisna 1986](#)). This effect is also called line blanketing because many overlapping absorption lines cover the shape of the actual thermal component.

In general, the LCs peak first in the NIR-bands (IJHK) and successively reach their maximum in bluer bands, i.e., BVR ([Contardo et al. 2000](#)), just a few days later, whereas the V-band is a good approximation for the bolometric LC ([Hamuy et al. 1996](#)). The U-band then breaks this trend and shows a faster rise time than the B-band. The time of B-band maximum is frequently taken as reference point and labeled as day 0. When going to the redder and NIR parts of the electromagnetic spectrum, the LCs exhibit a second peak approximately 20–30 d past maximum (compare Figure 3.2). This bump is found to occur later for brighter explosions ([Nobili et al. 2005](#)) and continuously vanishes for small ^{56}Ni masses ([Höflich et al. 1995](#); [Höflich et al. 2017](#)). The nature of this second bump, which can sometimes also be seen in the bolometric LC depending on its strength, is directly linked to the stratified ejecta structure of a SN Ia (more details follow in Chapter 4). [Kasen \(2006\)](#) explain this with an abruptly increasing emissivity of IGEs as soon as they recombine from doubly to singly ionized ions (see also [Pinto and Eastman 2000](#); [Jack et al. 2012](#); [Dessart et al. 2014b](#)). This occurs at a temperature of $T \sim 7000$ K. As the photosphere, i.e., the region from where radiation can escape², proceeds into the deeper layers

²Traditionally, the photosphere is defined as the surface where the optical depth reaches $\tau = 2/3$ ([Hubeny and Mihalas 2014](#)). In an idealized way, one can then assume the emission of black body radiation superimposed with spectral features. In reality, however, the photosphere is an extended region and also wavelength-dependent.

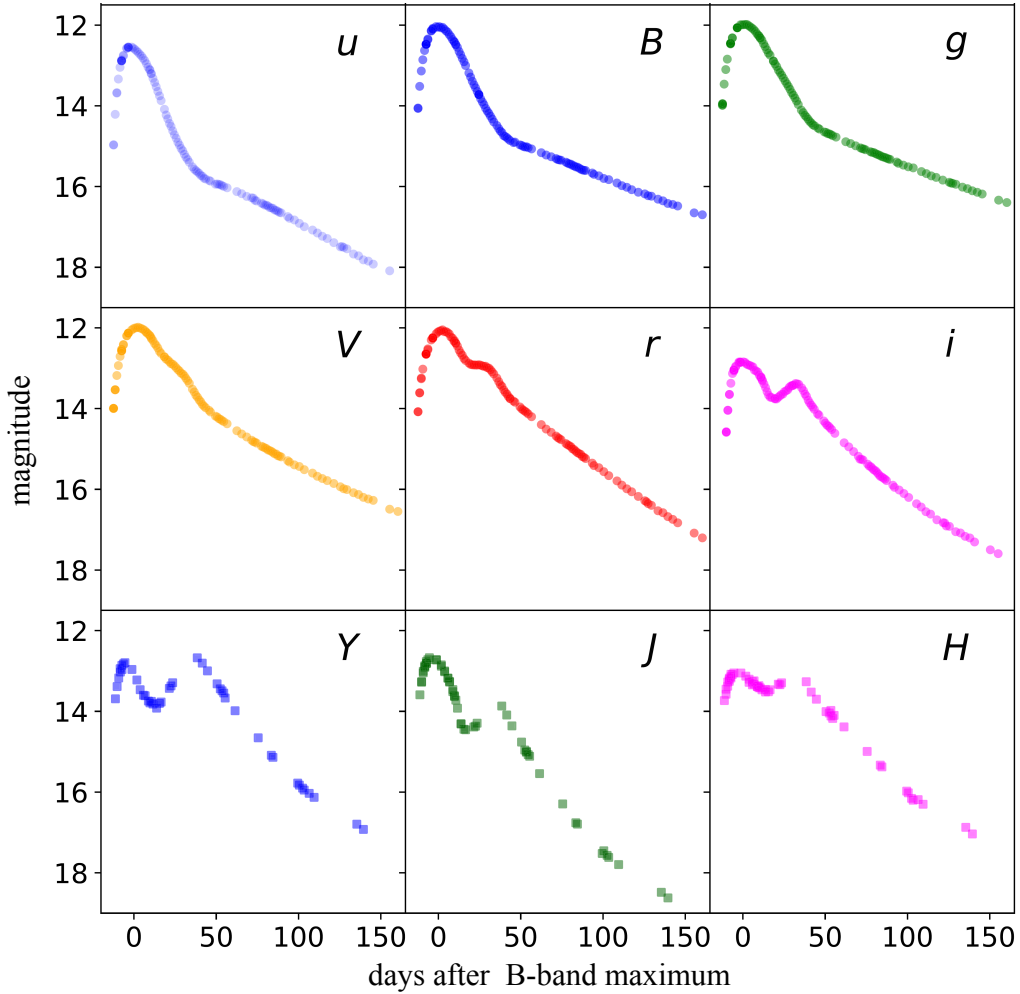


Figure 3.2: Multi-color LCs of SN 2012fr illustrating the varying LC shapes in different color bands. Credit: [Contreras et al. \(2018\)](#).

of the ejecta, matter expands, cools, and becomes more transparent. When the ionization front reaches the IGEs the flux in the NIR suddenly rises and forms the secondary peak observed in the IJHK-bands. Although the emissivity also rises in the B and V-band no secondary maximum occurs because matter is still opaque at these wavelengths. Thus, the magnitude and the time of the secondary maximum depend on the amount and the distribution of IGEs, in particular ^{56}Ni . [Dessart et al. \(2014b\)](#) also highlight the importance of forbidden Co II lines for the second maximum not included in the study of [Kasen \(2006\)](#). The decline rate at later times, after ~ 50 d, is almost constant and similar in all bands and for all SNe Ia ([Hamuy et al. 1996](#); [Lira et al. 1998](#)). This LC evolution in various bands is reflected in the color evolution of SNe Ia, which is pretty uniform. The (B-V) curve starts at ~ 0 around 0 d, and, subsequently, shows a rise, i.e., becomes redder, coinciding with the second NIR-maximum. After the maximum in (B-V) the color slowly turns blue again. The gradient between ~ 30 and 60 d is similar for all normal SNe Ia ([Phillips et al. 1999](#); [Burns et al. 2014](#)). The LC evolution described above is visualized in Figure 3.2 for the case of SN 2012fr.

Premaximum evolution

In addition to the postmaximum decline of the LCs also the premaximum evolution is worth an investigation. According to the “expanding fireball” model, the early LCs are broadly consistent with a t^2 dependency (Arnett 1982; Riess et al. 1999; Conley et al. 2006; Nugent et al. 2011; Piro 2012). The assumption of this model is that the effective temperature of the photosphere remains constant while the radius increases. Typical rise times are of the order of $t_R \sim 19d$ (Riess et al. 1999; Leibundgut 2000; Zheng et al. 2017; Dimitriadis et al. 2018). However, this simple model is insensitive to varying distributions of ^{56}Ni .

With the observation of very early LCs and high cadence studies deviations from the t^2 -shape have been observed. An early bump in the LC has been observed for SN iPTF14atg (Cao et al. 2015), SN 2015bq (Li et al. 2021), SN 2017cbv (Hosseinzadeh et al. 2017), or SN 2018oh (Li et al. 2019; Dimitriadis et al. 2018), for instance. This early emission is believed to either originate from the interaction of the ejecta with a companion star in a binary system (Kasen 2010) or circumstellar material (Piro and Morozova 2016), due to an enhanced abundance of ^{56}Ni in the outer layers (Magee et al. 2018; Magee and Maguire 2020; Shappee et al. 2018; Jiang et al. 2018) or because of short-lived radioactive isotopes produced in a surface detonation (Noebauer et al. 2017; Magee et al. 2021). While these studies can, in general, reproduce the shape of the early LC, other inconsistencies arise in the spectra (see Magee and Maguire 2020, for example). The origin of an excess of flux in the early LC still needs a deeper investigation since it probes the outermost layers of the ejecta and is expected to reveal information about the explosion mechanism.

Cosmology

As already mentioned in Chapter 1, the determination of distances was one of the greatest problems in the early 20th century. In addition, it was sensed at an early stage that SNe Ia might be helpful distance indicators due to their overall similarity. Furthermore, with their exceptional luminosity of $L_{\text{max}} \sim 10^{43} \text{ erg s}^{-1}$ they are observable out to high distances (Burns et al. 2010).

The astronomical magnitude system is a logarithmic scale where the apparent magnitude m at distance d and the absolute magnitude M , which corresponds to the brightness of the object at a distance of $d = 10 \text{ pc}$, is related to the measured flux $F(d)$ and $F(10 \text{ pc})$ by (Miles 2007)

$$m = -2.5 \log_{10}(F); \quad M = -2.5 \log_{10}(F(10 \text{ pc})). \quad (3.2)$$

It was Phillips (1993) (inspired by the work of Pskovskii 1977) who came up with a method to infer the absolute magnitude M (brightness) of SNe Ia from the shape of their B-, V-, or I-band LCs. In particular, they found that the decline in B-band 15 days after maximum light $\Delta m_{15}(B)$ is connected to the actual brightness of the event, i.e., the brighter the SN the lower $\Delta m_{15}(B)$. In other words: bright SNe Ia decline slower and show broader LCs than faint events. The width luminosity relation (WLR, sometimes also labeled “Phillips relation”) reads (Phillips 1993)

$$M_{\text{B,peak}} = -21.726 + 2.698 \Delta m_{15}(B). \quad (3.3)$$

Thus, for a SN Ia explosion with an apparent magnitude m and decline rate $\Delta m_{15}(B)$ the absolute magnitude M can be derived. The calibration of SNe Ia LCs has been refined over the past decades and also new methods have been developed. For instance, SNe Ia are found to be good standard candles in the NIR (Krisciunas et al. 2004; Krisciunas 2017; Freedman et al. 2009).

Moreover, standardizations also based on color curves and extinction by dust (MLCS, [Riess et al. 1996](#); [Jha et al. 2007](#)) and the spectral adaptive light curve template (SALT, [Guy et al. 2005](#)) method are widely applied.

The flux emitted by a point source is distributed onto a sphere, and, thus, the observed flux per area declines with $1/d^2$. The inverse square law $F(d_1)/d_2^2 = F(d_2)/d_1^2$ combined with Eq. 3.2 then gives the luminosity distance d_l

$$d_l = 10^{\frac{m-M}{5}+1}. \quad (3.4)$$

With the knowledge of m (measured directly) and M (from the WLR) it is straightforward to infer the distance to the object.

In addition to the apparent magnitude m also the redshift z of individual spectral lines of a SNe Ia can be measured. For nearby objects the redshift is connected to the velocity v via the Doppler formula $v = cz$ with the speed of light c . For cosmological distances, however, the expansion history of the Universe has to be taken into account. Note that the cosmological redshift is due to the expansion of space-time and not because of the relative movement between an emitting source and an observer like the Doppler shift. The cosmological luminosity distance reads ([Shchigolev 2017](#)):

$$d_l = c(1+z) \int_{z_1}^{z_2} \frac{dz'}{H(z')}. \quad (3.5)$$

$H(z)$ is the Hubble expansion parameter containing information about the cosmological model such as the energy density of baryonic and dark matter Ω_M , radiation Ω_r , dark energy Ω_Λ , and curvature Ω_k (Λ CDM-model, see [Perivolaropoulos and Skara 2021](#) for a review). The expansion parameter $H(z)$ is not necessarily constant with time, depending on the model parameters, and, therefore, has to be integrated over all redshifts z . For nearby objects, i.e., neglecting the expansion history, this reduces to the original Hubble law

$$v = H_0 d \quad (3.6)$$

which states that more distant objects move faster away from Earth ([Hubble 1929](#)). In this case, H_0 represents the local Hubble parameter at the current time. Due to the cosmological principle of isotropy this finding also indicates that space-time as a whole is expanding.

The Hubble constant H_0 for nearby SNe Ia found with the Calán/Tololo Survey has been determined by [Hamuy et al. \(1996\)](#) to $H_0 = 63.1 \text{ km s}^{-1} \text{ Mpc}^{-1}$. In the late 90s [Perlmutter et al. \(1999\)](#) and [Riess et al. \(1998\)](#) found that the expansion of the Universe is indeed accelerating by observing SNe Ia at high redshift. In detail, [Perlmutter et al. \(1999\)](#) observed and calibrated 42 SNe Ia (Supernova Cosmology Project) up to a redshift of $z = 0.83$ and found best agreement with a flat Universe dominated by dark energy, i.e., $\Omega_\Lambda = 0.72$ and $\Omega_M = 0.28$. Figure 3.3 shows that only for very distant SNe Ia ($z \gtrsim 0.3$) the deviation from a matter-dominated Universe ($\Omega_M = 1$) becomes apparent. For this result Saul Perlmutter, Brian P. Schmidt, and Adam G. Riess were awarded the Nobel prize in physics in 2011.

This application shows the importance to understand the mechanism behind SNe Ia since a precise modeling could help to calibrate their LCs with much more accuracy.

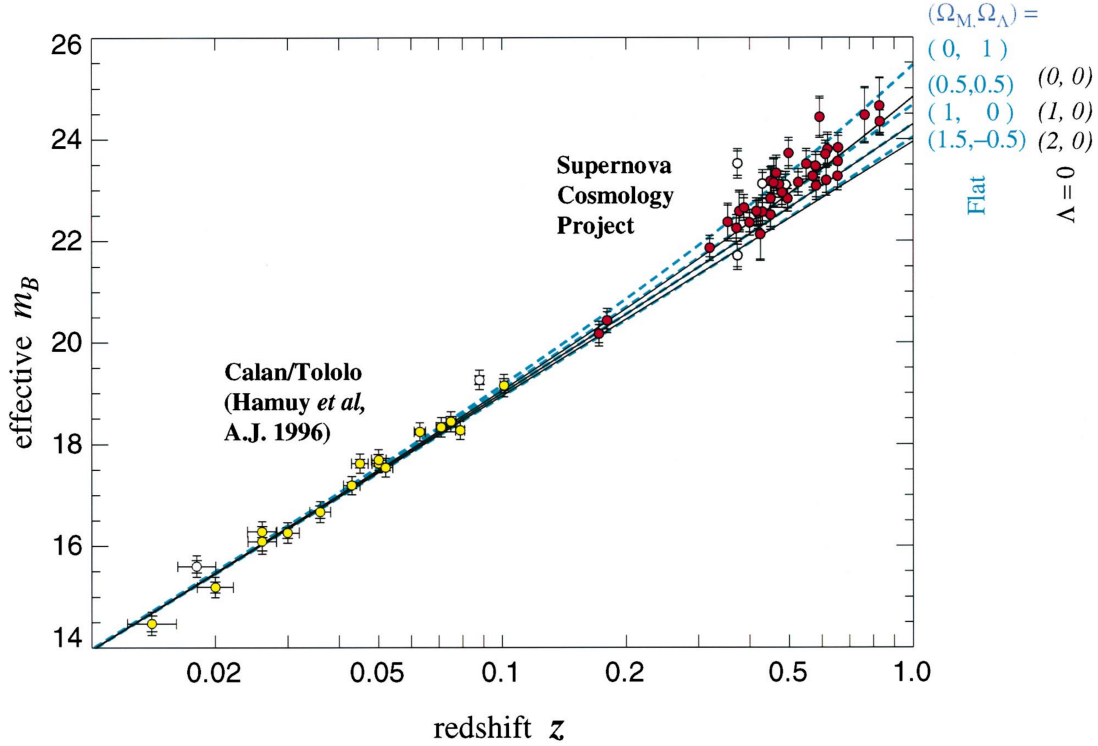


Figure 3.3: Hubble diagram showing SNe Ia of the Supernova Cosmology Project (red circles, [Perlmutter et al. 1999](#)) and those of the Calán/Tololo Survey (yellow circles, [Hamuy et al. 1996](#)). In addition, predictions of various cosmological models are displayed (solid and dashed lines). Credit: [Perlmutter et al. \(1999\)](#).

3.2 Spectroscopy

In addition to the overall emission of light manifested in the (bolometric) LCs, taking spectra of SNe Ia is of vital importance. These reveal, via specific absorption or emission lines, the presence of certain elements in the ejecta and their ionization states. By means of their relative strengths one can also estimate their relative abundances, and, thus, deduce the progenitor system and the explosion mechanism. Extensive reviews of SN Ia spectra were composed by [Filippenko \(1997\)](#) and [Parrent et al. \(2014\)](#), for instance.

Most importantly, SNe Ia do neither exhibit any signs of H nor He in their spectra at all times which separates them from SNe II and SNe Ib, respectively (see also Chapter 1). Before and around peak luminosity (photospheric phase) they are characterized by a strong absorption line of Si II at 6355 \AA , the “W” shaped absorption trough of Si II around 5468 and 5612 \AA , Ca II H&K lines at 3934 and 3968 \AA , and another Ca II feature at $\sim 8300 \text{ \AA}$. In addition, Si II features at 4000 and 5972 \AA , Mg II, Fe II, and the O I triplet are frequently observed in SNe Ia ([Silverman et al. 2012](#)). These broad lines exhibit a so-called P Cygni profile³ characteristic for fast expanding material. Typical velocities for the Si II feature lie between $10\,000$ and $12\,000 \text{ km s}^{-1}$ and are slightly higher for the Ca II features ([Filippenko 1997](#); [Silverman et al.](#)

³P Cygni profiles show a blue shifted absorption trough followed by a broad emission feature toward redder wavelengths. This is a geometrical effect of a spherically expanding atmosphere since photons traveling toward an observer (blue shifted) can be scattered away from the line of sight but photons traveling in all directions (also redshifted) can be scattered toward the observer.

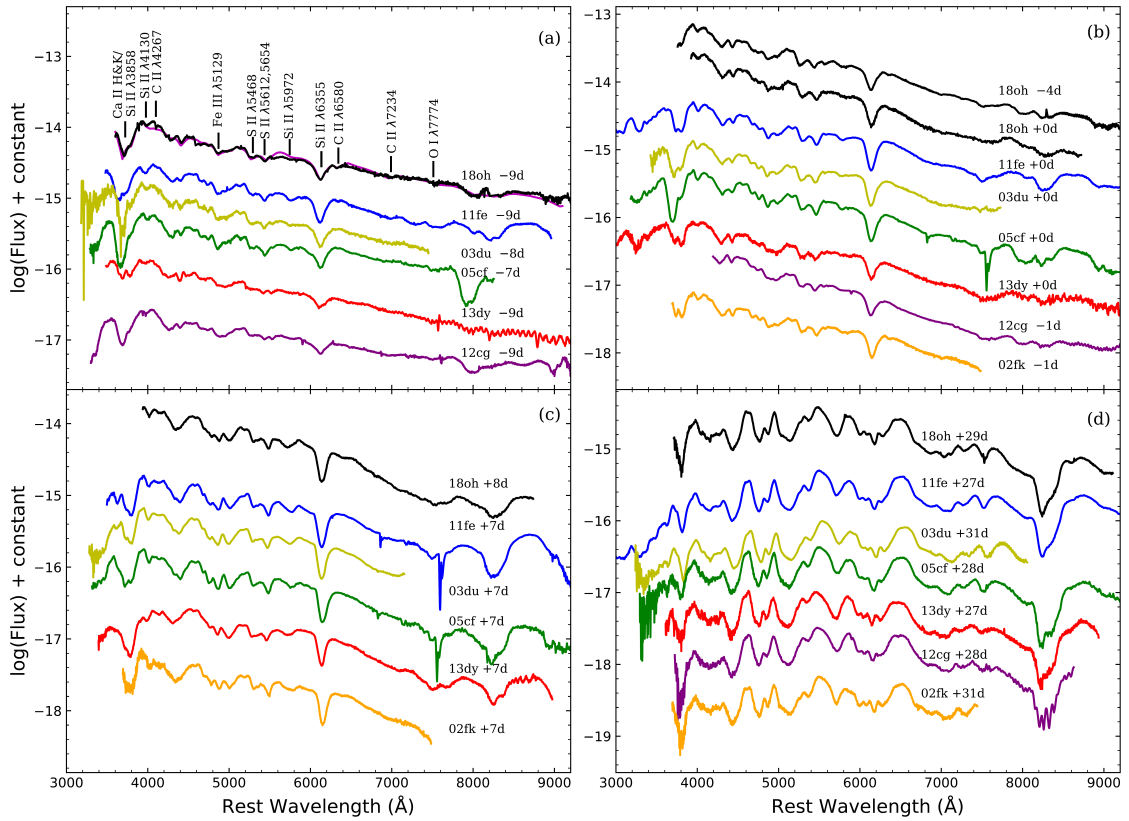


Figure 3.4: Spectra of various normal SNe Ia from approximately -9 d to about four weeks after B-band maximum. References for the individual observations can be found in [Li et al. \(2018\)](#). Credit: [Li et al. \(2018\)](#).

2012). These two features show a rather slow decline from -5 d but can also be observed at extremely high velocities $\gtrsim 20\,000$ km s $^{-1}$ ([Mazzali et al. 2005](#); [Foley et al. 2012](#); [Childress et al. 2013](#); [Siebert et al. 2019](#)). In general, velocity measurements of Si II, S II, Ca II, and O I indicate a layered ejecta structure and a continuous distribution without any clear sub-populations ([Silverman et al. 2012](#)). It was already mentioned in Section 3.1 that Fe and Co lines are blended strongly in the UV, and, hence, depress the overall flux at short wavelengths. Many SNe Ia ($\sim 20 - 40\%$) ([Parrent et al. 2011](#); [Folatelli et al. 2011](#); [Silverman and Filippenko 2012](#)) also exhibit C II lines at very early times $\lesssim -10$ d ([Li et al. 2019](#)) indicating unprocessed material in the outer layers of the ejecta.

After maximum light, lines of intermediate mass elements (IMEs), i.e., Si, S, Ca, O, or C, successively weaken and IGEs begin to play a dominant role after approximately two weeks. Nevertheless, features of IMEs are still visible. This transition to an IGE dominated spectrum also marks the time when the secondary maximum in the NIR LC starts to appear (see Section 3.1). Figure 3.4 visualizes the spectral evolution from premaximum to ~ 4 weeks after maximum light of a few normal SNe Ia. It is clearly visible that the prominent Si II and S II features vanish after 4 weeks and that more emission lines due to IGE start to appear between 3000 and 6000 Å. The Ca II line, however, is still prominent even at ~ 28 d.

The unambiguous identification of a particular element is a highly complicated task since there is hardly any feature which only shows contributions due to one element ([Parrent et al.](#)

2014). Also the continuum observed in SNe Ia spectra is not primarily due to electron scattering, photoionization (bound-free process) or inverse bremsstrahlung (free-free process), i.e., continuum processes. Instead, it is formed due to the blending of countless spectral lines, and, therefore, also called a pseudo-continuum (Sim 2017).

A few months after peak luminosity (~ 100 d) SNe Ia transition into the “nebular phase”. During this period the ejecta have become transparent, i.e., optically thin, and the innermost regions are revealed. Rather than a black body superimposed with absorption lines, the spectrum now turns into an emission line spectrum showing a plenitude of broad Fe III, II, Ni II, and Co III emission lines (Jerkstrand 2017; Botyánszki and Kasen 2017). Their velocities lie in the range of $3000 - 4000 \text{ km s}^{-1}$ at ~ 100 d and slowly decrease by a few km per day (Silverman et al. 2013). Furthermore, the evolution of the Co III feature can be employed to infer the ejected mass of ^{56}Ni (Childress et al. 2015) using the characteristics of radioactive decay (see also Section 3.1).

3.3 Subclasses of type Ia supernovae

In Chapter 1 it was already foreshadowed that SNe Ia can be subdivided into several classes. The observational characteristics of SNe Ia explained in Sections 3.1 and 3.2 describe the bulk of normal SNe Ia which make up $\sim 70\%$ (Li et al. 2001, 2011) of the whole class. A transient showing clear differences in its spectrum and/or LC evolution is considered a “peculiar” event. As more and more observations of SNe Ia were available during the past decades the introduction of new subclasses of peculiar SNe Ia with similar properties was necessary. However, all subtypes of SNe Ia are believed to be of thermonuclear origin although their observables might deviate strongly from normal SNe Ia. Extensive overviews of the division of SNe Ia were presented by Taubenberger (2017) and Gal-Yam (2017) and the following, rough characterization follows these works if not noted otherwise. Figure 3.5 depicts the most important classes in the $\Delta m_{15}(B) - M_{B,\text{max}}$ -plane. It can be seen that all but 91T-like objects (see below) deviate from the LC evolution of normal SNe Ia, i.e., they do not follow the WLR, making them not suitable as distance indicators. Although 91T-like SNe lie on the WLR they show clear discrepancies in their spectra distinguishing them from normal SNe Ia.

Super-Chandrasekhar SNe Ia

This type of SN Ia stands out from normal SNe Ia because of their extraordinarily high absolute magnitude of up to ~ -20.4 mag in the B band but moderate expansion velocities, and, thus, slow evolution of the LC in relation to their luminosity. They show rise times of $t_R \sim 23$ d and decline rates of $\Delta m_{15}(B) = 0.7 - 0.9$ mag. This property suggests a large mass of ^{56}Ni as well as a high total mass ejected from the system greatly exceeding the Chandrasekhar-mass limit of $\sim 1.4 M_\odot$ (see Section 4.1) for an electron degenerate WD. Therefore, they were dubbed “super-Chandrasekhar SNe Ia”. An alternative scenario was proposed by Hachinger et al. (2009) who find that the interaction of the ejecta with a companion star might be responsible for the high luminosity. Their overall LC evolution differs from normal SNe Ia in several ways. First, they show a significantly enhanced flux in the UV leading to a distinct color evolution. Second, they lack the secondary maximum in the IJHK-bands but show a prolonged plateau in these bands. Third, the brighter members such as SN 2009dc and SN 2007if lie significantly above the WLR. Finally, some members of the class show an unexpected drop in their late-time LCs

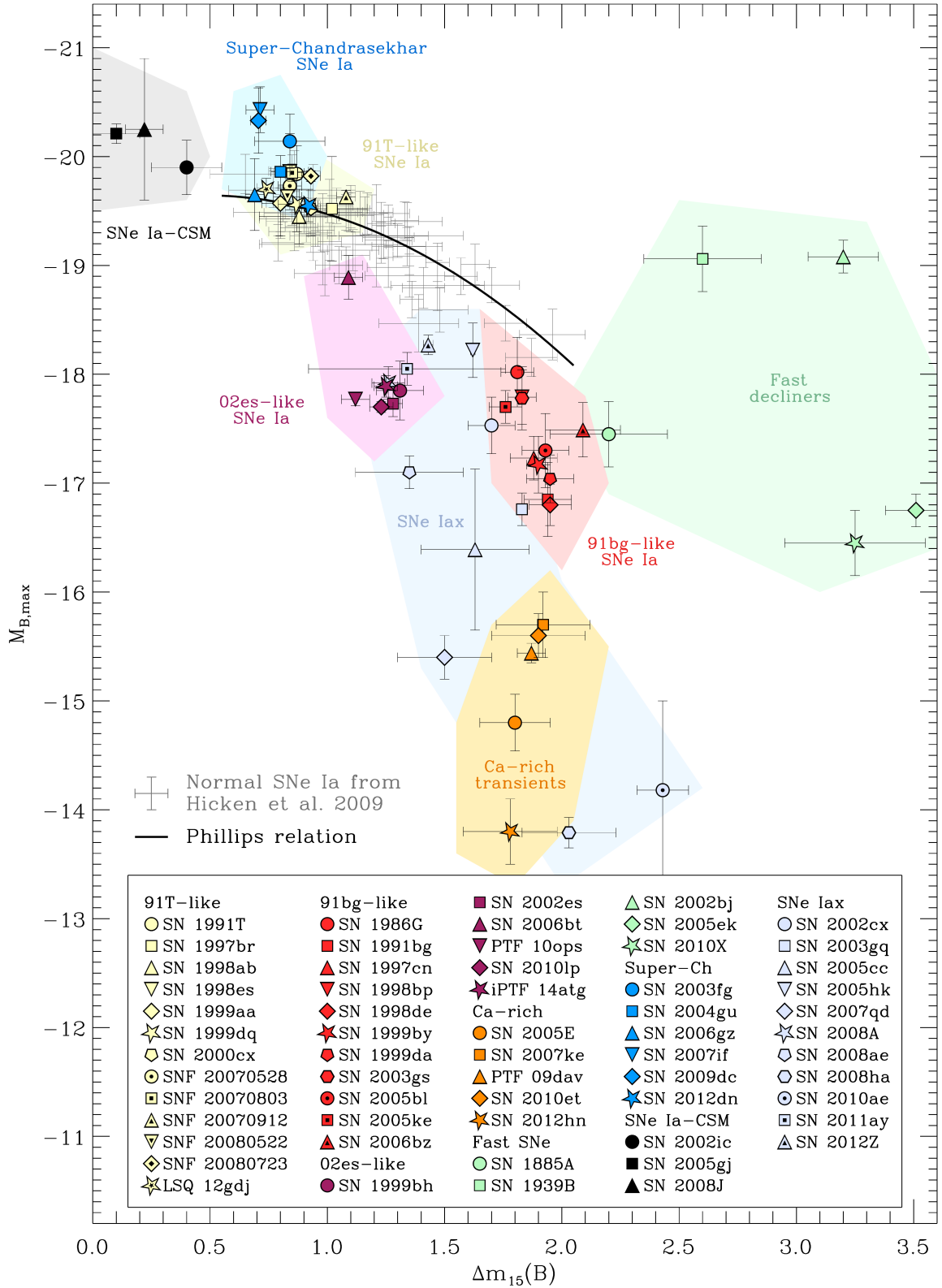


Figure 3.5: Subclasses of SNe Ia in the $\Delta m_{15}(B) - M_{B,\max}$ -plane. Normal SNe Ia gather around the WLR relation (solid black line). Credit: (Taubenberger 2017).

making them even fainter than normal SNe Ia. This late drop challenges the notion of ^{56}Co decay powering the late-time LC.

Spectroscopically, they differ in the fact that they show very prominent O I and even C II features until approximately two weeks after maximum. Also other features of IMEs are more prominent than IGEs during the early phase. The transition to an IGE dominated spectrum occurs slightly later than observed in normal events. In addition, their nebular spectra resemble those of normal SNe Ia. However, they exhibit lower velocities, and, hence, less blended emission features of IGEs.

91T-like SNe Ia

This group is named after the well observed SN 1991T (Filippenko et al. 1992b; Phillips et al. 1992) which shows a slightly higher overall luminosity than the average normal SN Ia. Their photometric properties are in line with the bulk of normal SNe Ia following the WLR which makes them also applicable for distance measurements.

In this case, the peculiarity stems from the observed spectra. The hallmark features of normal SNe Ia, namely those of Si II and the S II “W”, are completely absent before maximum light and only emerge weakly around peak luminosity. Instead, Fe III features are very strong during the early phase, indicating IGEs in the outermost layers of the ejecta. The evolution after maximum light then closely resembles normal SNe Ia.

91bg-like SNe Ia

In contrast to 91T-like and super-Chandrasekhar SNe the class of 91bg-like objects, named after SN 1991bg (Filippenko et al. 1992a), consists of subluminous events. Compared to normal SNe Ia they are about two to three times less luminous regarding their bolometric luminosity. Moreover, they are much fainter than normal events in the blue bands (1.5 – 2.5 mag) compared to NIR-bands (0.5 – 0.7 mag) leading to a very different color evolution around maximum light. Furthermore, they also lack a secondary maximum in the NIR-bands. In general, 91bg-like objects show a significantly faster LC evolution with rise times of 13 – 15 d and decline rates $\Delta m_{15}(B) > 1.8$.

The spectral evolution during the photospheric phase is again in rough agreement with normal SNe Ia, however, the spectra of 91bg-like transients evolve slightly faster. Some notable differences are prominent features of Ti II between ~ 4000 and 4400 \AA and the O I $\lambda 7774$ absorption trough. Moreover, the ejecta velocity, measured via the Si II $\lambda 6355$ feature, is in the range of slow normal SNe Ia. During the nebular phase 91bg-like events show only weak signs of the doubly ionized Fe III and Co III features but rather broad Fe II and Ca II lines.

02es-like SNe Ia

This subclass is rather new and only loosely defined to date. These explosions closely resemble 91bg-like objects regarding their LCs and spectra. Their key distinctive feature is their location in the $\Delta m_{15}(B) - M_{B,\text{max}}$ -diagram (see Figure 3.5). The overall evolution is much slower with $t_R \sim 19 - 20$ d, $\Delta m_{15}(B) \sim 1.1 - 1.3$ mag, and significantly lower ejection velocities.

Calcium-rich transients

Regarding their LC shapes Ca-rich SNe form a homogeneous group. Although they are significantly fainter with peak magnitudes between -14 and -16.5 mag, their photometric evolution is in good agreement with 91bg-like objects.

In contrast to other SNe, Ca-rich transients are characterized by the prominence of Ca in their nebular spectra and not by spectral features around maximum light. The nebular spectra are also devoid of Fe lines but show O I emission. In addition, their spectra around peak luminosity show He I lines untypical for SNe Ia but more characteristic for core-collapse SNe such as SNe Ib/c. However, although some observational properties hint toward a massive star as progenitor, Ca-rich transients are believed to be of thermonuclear origin (e.g., [Polin et al. 2021](#)). This is due to the fact that they are detected in rather old stellar environments and not in star forming regions and due to their low ejecta masses which seem to exclude a massive star as progenitor.

Type Iax supernovae

SNe Iax are reviewed in [Jha \(2017\)](#) and Chapter 6 covers this subclass in great detail. The characteristics of SNe Iax were defined by the prototypical object SN 2002cx ([Li et al. 2003](#)) which exhibits a relatively slow LC evolution compared to its luminosity and also shows no secondary maximum in the IJHK-bands.

The overall faint class of SNe Iax is characterized by maximum light spectra comparable to 91T-like objects, i.e., dominant signs of IGEs and only weak Si II and S II features, and very low ejecta velocities down to $\sim 2000 \text{ km s}^{-1}$ for the most subluminous members. Moreover, SNe Iax do not show a transition from the photospheric phase to the emission-dominated nebular phase.

Chapter 4

Physical foundations and explosion scenarios

Today it is widely accepted that SNe Ia originate from the explosion of an electron-degenerate carbon-oxygen (CO) WD which is based on the ideas of [Hoyle and Fowler \(1960\)](#). One of the first numerical simulations of explosive C burning has been presented by [Arnett \(1969\)](#) who showed that a centrally ignited detonation indeed leads to the total disruption of a $\sim 1.4 M_{\odot}$ star ejecting primarily ^{56}Ni at velocities up to $25\,000 \text{ km s}^{-1}$ (see also [Arnett et al. 1971](#)). These findings were in broad agreement with observations of SNe I and strengthened the notion of a thermonuclear explosion in degenerate matter. The assumption of WDs as the progenitor of SNe Ia is convenient since it naturally explains some of their characteristics. First, the relatively short rise times hint toward a rather compact object ([Hoyle and Fowler 1960](#)). Second, the absence of H and He in SNe Ia spectra is an indication toward a star which has already burned its H and He fuel ([Oke and Searle 1974](#)). Third, it was already found very early that SNe I preferentially occur in old stellar populations ([Finzi and Wolf 1967](#)) excluding a massive star origin. Moreover, as shown by [Arnett \(1969\)](#), the kinetic energies corresponding to $\sim 1 M_{\odot}$ of material converted to IGEs are in agreement with observations. Of course, also He or oxygen-neon (ONe) WDs could be considered as progenitors for SNe Ia. However, the explosion of a He WD does not compare well to SNe Ia ([Nomoto and Sugimoto 1977](#); [Woosley et al. 1986](#)) and ONe WDs were not expected to explode but to collapse [Nomoto and Kondo \(1991\)](#) and form a neutron star (but see [Jones et al. 2016](#)). In recent years, explosions of ONe WDs or hybrid carbon-oxygen-neon WDs were re-investigated as a model for SNe Ia ([Denissenkov et al. 2013, 2015](#); [Marquardt et al. 2015](#); [Kromer et al. 2015](#); [Bravo et al. 2016](#)).

Since a WD is a stable object it has to be disturbed somehow to ignite nuclear burning and trigger an explosion. Therefore, it is assumed that progenitors of SNe Ia are CO WDs in a close binary system and that the explosion occurs due to an interaction with a companion star. Traditionally, two scenarios are considered: (1) The *single-degenerate scenario* (SD), i.e., a WD accompanied by a main-sequence or red giant star ([Whelan and Iben 1973](#)), and (2) the *double-degenerate scenario* (DD) where the binary consists of two degenerate WDs ([Iben and Tutukov 1984](#); [Webbink 1984](#)). The explosion is then triggered either via accretion from the companion (possible in the SD and the DD channel) or due to the merger of two WDs (only in the DD channel).

From an explosion modeling point of view this separation is, however, not very useful since the actual outcome of the explosion is governed by two main factors: The first is the mass of

the exploding WD, i.e., is it near the Chandrasekhar mass limit of $\sim 1.4 M_\odot$ or is it significantly below at $\sim 1 M_\odot$? The second important parameter is the combustion mechanism: Is the WD material burned via a deflagration, a detonation or even a combination of both? These mechanisms and WD masses can, in principle, be combined in many ways and lead to very different results. In the next section, some basics of WD evolution, structure, and accretion will be covered followed by a brief review of the basic theory of fluid dynamics (Section 4.2), nuclear burning stages (Section 4.3), and the two combustion mechanisms (Section 4.4). Subsequently, the variety of relevant explosion scenarios including their advantages and shortcomings will be summarized in Section 4.5.

4.1 White dwarf formation, structure, and accretion

The concept of degeneracy is of vital importance for the formation of WDs and the triggering of an explosion inside a WD. At moderate temperatures and densities the electrons in a completely ionized plasma obey the classical Boltzmann distribution $f(p)$ with the momentum p . For decreasing T the peak of $f(p)$ increases and simultaneously shifts to lower values of p . More electrons can also be found at lower momentum states for higher densities since $f(p) \propto n_e$ with the total number of electrons n_e ¹ (see Figure 4.1). At some point, however, quantum mechanical effects have to be taken into account. The Pauli principle states that no more than two electrons of opposite spin can populate a quantum state of volume $dp^3 dV^3 = h^3$ (h is the Planck constant) setting an upper limit for the distribution of electrons in momentum space (Kippenhahn et al. 2012):

$$f(p) \leq \frac{8\pi}{h^3} p^2. \quad (4.1)$$

The situation is visualized in Figure 4.1 for different densities typical for WDs. As soon as the Boltzmann distribution exceeds the upper limit set by the Pauli principle, the electron gas is said to become degenerate and the electron pressure P_e becomes dominant over the classical ion pressure P_{ion} . Figure 4.1 also shows that even for extremely high temperatures of 10^{10} K matter above $\rho = 10^7 \text{ g cm}^{-3}$ is close to degeneracy. Thus, for characteristic conditions inside a WD of $\rho > 10^8 \text{ g cm}^{-3}$ and $T \sim 10^8$ K degenerate electron pressure clearly dominates.

For the limiting case of complete degeneracy, i.e., $T = 0$ K, the quantum states are filled up completely up to the Fermi energy E_F . The equation of state (EoS) of degenerate matter reads (a derivation can be found in Kippenhahn et al. 2012)

$$P_e = \frac{h^2}{20m_e m_u^{5/3}} \left(\frac{3}{\pi}\right)^{2/3} \left(\frac{\rho}{\mu_e}\right)^{5/3} \quad \text{non-relativistic,} \quad (4.2)$$

$$P_e = \frac{hc}{8m_u^{4/3}} \left(\frac{3}{\pi}\right)^{1/3} \left(\frac{\rho}{\mu_e}\right)^{4/3} \quad \text{extreme-relativistic.} \quad (4.3)$$

The crucial characteristic to note here is that the pressure is completely independent of temperature, and, thus, the mechanical structure is decoupled from the thermal structure. Of course,

¹The number of electrons is, of course, connected to the mass density ρ set by the ions by $\rho = (n_e m_B)/Y_e$ (Shapiro and Teukolsky 2004). m_B is the mean baryon mass (protons and neutrons) and Y_e the electron fraction, i.e., the number of electrons per baryon. For symmetric nuclei like ^{16}O with 8 protons, 8 neutrons and 8 electrons Y_e amounts to 0.5.

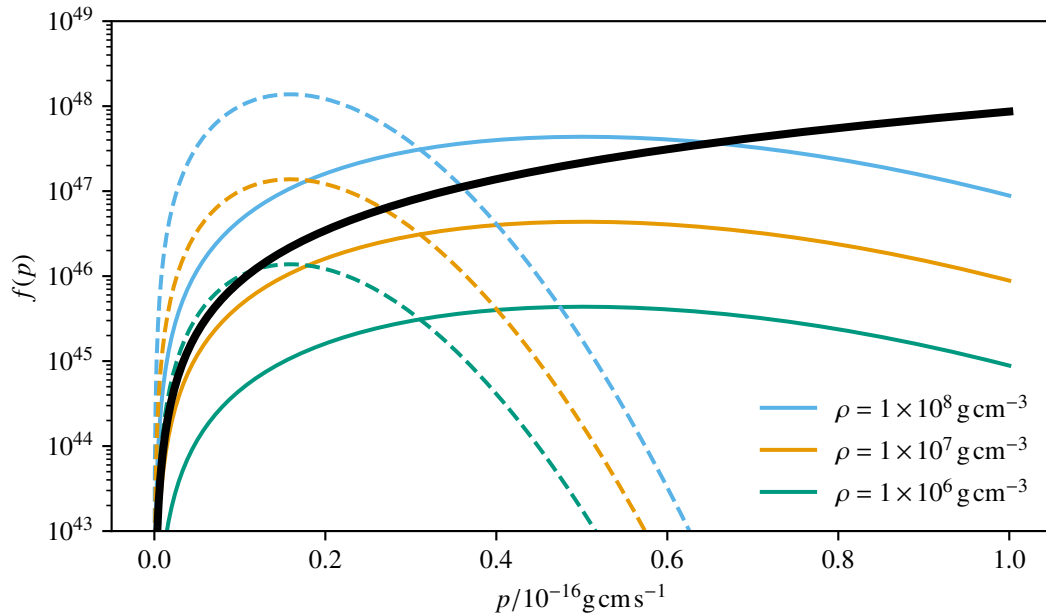


Figure 4.1: Classical Boltzmann distribution $f(p)$ for varying densities (see legend) and temperatures in pure CO matter. Solid lines are calculated at $T = 10^{10}$ K and dashed lines at $T = 10^9$ K. The thick black line represents the upper limit resulting from the Pauli principle.

there is a continuous transition between the relativistic and non-relativistic case and also between degenerate and non-degenerate matter often characterized by the degeneracy parameter $\eta = E_F/(n_e k_B T)$ comparing the Fermi energy to the thermal energy. The EoS for arbitrary degeneracy has to be solved numerically.

WD formation

According to [Althaus et al. \(2010\)](#) approximately 97% of all stars end their life as a WD. The pathway toward this final stage of stellar evolution can be described as follows: All stars, including our Sun, gain their energy from the fusion of H to He. This period of hydrostatic H burning is called the main sequence phase and can last, depending on the initial mass of the star, for several billion years. As soon as the fuel inside the stellar core is exhausted (earlier for more massive stars) the fusion process stops and the source of radiative energy stabilizing the core against gravity vanishes leading to a contraction of the core. If the heating due to the release of gravitational energy is sufficient to ignite the ashes of H burning, i.e., mostly He, a phase of hydrostatic core He burning ensues. This cycle of nuclear burning, fuel exhaustion, and contraction is repeated for C burning (main burning product of He burning), Ne burning, O burning, and Si burning up to Fe. Since the IGEs have the highest binding energy per nucleon, further exothermic fusion reactions are not possible and no additional burning stage ensues. Each of these burning stages leaves behind a shell of ash creating the typical onion skin structure of evolved stars ([Kippenhahn et al. 2012](#)). The final burning stage depends on the total mass of the star since it governs the gravitational energy available for heating. The more massive the star the further it climbs the ladder of burning stages.

If, for instance, the CO core left behind after He exhaustion does not become hot enough during contraction to ignite carbon burning it continues to collapse until it is stabilized by de-

generate electron pressure and becomes a WD. The heating of the core due to contraction also depends on the degree of degeneracy since the temperature slowly decouples from density and pressure (see Eq. 4.3). The same holds for a potential He core after H burning and the ONe core after C burning such that He, CO, and ONe WDs build the possible end stages of stellar evolution. CO WDs, i.e., the potential progenitors of SNe Ia covered in this work, form from stars with an initial mass of $2.3 M_{\odot} \lesssim M \lesssim 9 M_{\odot}$ (Siess 2007) and have final masses between ~ 0.2 and $1.2 M_{\odot}$ whereas most CO WDs have a mass of $\sim 0.6 M_{\odot}$ (Madej et al. 2004). Note, that only the evolution of the stellar core was discussed above and that the envelope (H and He in the case of a CO WD) is expelled due to stellar winds and thermal pulses on the asymptotic giant branch (Kippenhahn et al. 2012).

WD structure

The structure of a WD can be approximated by a polytropic relation (compare to Eq. 4.3)

$$P = K\rho^{\gamma} = K\rho^{1+1/n}; \quad n = \frac{1}{\gamma - 1}. \quad (4.4)$$

In the case of a non-relativistic, degenerate gas the polytropic index n equals $3/2$ and for the relativistic case $n = 3$. The structure of the star in hydrostatic equilibrium is then a solution of the *Lane-Emden equation* which yields a mass-radius and a radius-density relation for $n = 3/2$:

$$R \sim M^{-1/3}; \quad R \sim \rho_c^{-3/2} \quad (4.5)$$

with the central density ρ_c . Counterintuitively, the radius decreases with increasing mass (central density) making the WD more compact. As the material becomes more dense the polytropic index will shift toward $4/3$ since matter is expected to become fully relativistic above $\sim 10^7 \text{ g cm}^{-3}$ (Shapiro and Teukolsky 2004). In this case ($n = 3$) there is no connection between radius and mass but one fixed upper limit, the Chandrasekhar-mass limit (Chandrasekhar 1931):

$$M_{\text{Ch}} = \left(\frac{2}{\mu_e}\right)^2 \times 1.459 M_{\odot}. \quad (4.6)$$

The only parameter to influence M_{Ch} is the composition in the form of the mean molecular weight per electron μ_e which is roughly 2 because $\mu_e \sim 1/Y_e$ for H-poor material. This means that the total mass of a WD is independent of its central density. The radius still adjusts to ρ_c and goes to 0 for $\rho_c \rightarrow \infty$. Figure 4.2 illustrates the density profile of a M_{Ch} WD for densities between 10^9 and $6 \times 10^9 \text{ g cm}^{-3}$ (same progenitor models as used in Chapter 6). Although all models have the same mass (M_{Ch}), the density gradient steepens for higher ρ_c and the radius decreases. Moreover, it can be seen that most of the WD matter is above 10^7 g cm^{-3} , and, thus, fully relativistic which makes M_{Ch} a good estimate for their total mass. For masses above M_{Ch} the degenerate electron pressure cannot counteract gravity anymore, and, hence, the WD collapses. A detailed derivation of the structure of WDs can be found in Althaus et al. (2010) and Kippenhahn et al. (2012).

Typical masses of CO WDs interesting for the modeling of SNe Ia lie between $\sim 0.6 M_{\odot}$ and M_{Ch} with central densities of $\sim 10^8$ to $9 \times 10^9 \text{ g cm}^{-3}$. The radius of a M_{Ch} WD is close to $\sim 2000 \text{ km}$ comparable to the radius of the moon with a mass close to the solar mass M_{\odot} .

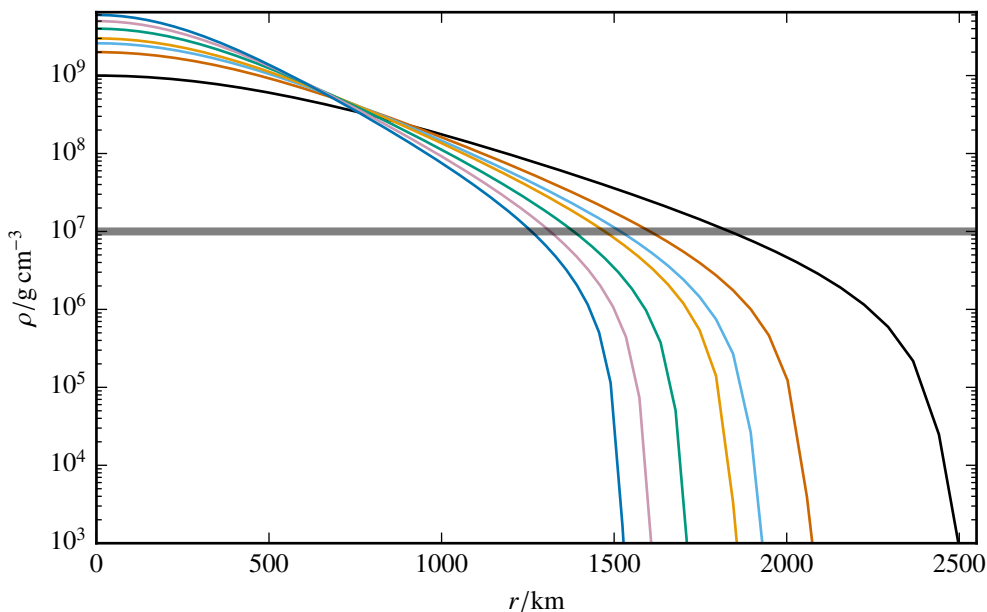


Figure 4.2: Density profiles of CO WDs with central densities between 10^9 and 6×10^9 g cm^{-3} . The broad horizontal line approximately separates non-relativistic from relativistic matter.

Accretion

To estimate the contribution of the SD scenario to the SN Ia rate, it is important to study the path of a newly formed WD toward M_{Ch} , i.e., the accretion phase in binary systems². At a mass slightly below M_{Ch} , convective carbon burning is ignited near the center of the WD, and, after a phase of steady burning, the so-called simmering phase, a thermonuclear runaway (TNR) might occur (see Zingale et al. 2009, 2011, 2013; Nonaka et al. 2012 for numerical simulations of this process). In the classical picture, the WD accumulates a H-rich envelope from its companion (Iben and Tutukov 1984), which successively heats up due to gravitational compression and eventually ignites H burning at the base of the shell. Under degenerate conditions the pressure is independent of temperature (see Eq. 4.3), and, therefore, the heat released by nuclear burning does not lead to an expansion. Because of the positive temperature dependence of the reaction rates a positive feedback loop is set up, i.e., more heating leads to higher reaction rates, and, hence, more heating. This process is called a thermonuclear runaway. These H shell flashes are associated with CNe (see Chapter 1) and a review can be found in Starrfield et al. (2016). This sequence of accretion and flash can then be repeated and leads to so-called recurrent novae with a period of ~ 10 years. Whether such a system could reach M_{Ch} and end up as a SNe Ia depends on its mass retention efficiency, i.e., the ratio of ejected to accumulated mass during one cycle.

The most important parameter affecting the accretion history is the accretion rate \dot{M}_{acc} . Nomoto et al. (2007) claim that there is a lower limit for steady H burning, i.e., the burning rate \dot{M}_{burn} equals \dot{M}_{acc} of $\sim 10^{-7} M_{\odot}/\text{yr}$, corroborating earlier results by Paczynski and Zytkov (1978); Yaron et al. (2005) and Sienkiewicz (1980). Shen and Bildsten (2007) also find a narrow range of \dot{M}_{acc} for stable H accretion around $\dot{M}_{\text{acc}} = 10^{-7} M_{\odot}/\text{yr}$. For lower \dot{M}_{acc} several flashes occur and a more detailed study of the mass retention is necessary. In contrast to that, Starrfield et al. (2012) explicate that steady H burning does not exist and that shell flashes occur at all

²Note that also accretion from a degenerate companion is possible (Tutukov and Yungelson 1996).

accretion rates. They, however, point out that a net accumulation of mass is possible if no mixing of core material into the envelope is assumed. In addition, there is also an upper limit of \dot{M}_{acc} for steady burning. According to Paczyński (1971) there is a core mass-luminosity relation limiting the burning rate in a spherical shell. Thus, at $\dot{M}_{\text{acc}} > \dot{M}_{\text{burn}}$ the excess material forms a dilute red giant-like envelope leading to a common envelope phase (Meng and Podsiadlowski 2017) and a possible inspiral and merger process not leading to a SN Ia (Nomoto et al. 1979). Meng and Podsiadlowski (2017) show, however, that SNe Ia can also be preceded by a common-envelope phase. Moreover, the accretion of He instead of H is also a possible scenario for a WD to reach M_{Ch} . The physics are similar to the accretion of H including the development of a degenerate envelope with the possibility of He shell flashes and a certain range of accretion rates allowing for steady burning (see e.g., Iben and Tutukov 1989, 1994; Kato and Hachisu 2004; Wang et al. 2009; Brooks et al. 2016; Wang et al. 2017; Wong and Schwab 2019; Wong et al. 2021).

The scenario of a WD approaching M_{Ch} has, for a long time, been the favored scenario for SNe Ia. Explosions ignited inside an accreted He shell before the core reached M_{Ch} are, however, also a promising explosion mechanism (see Section 4.5 for details on various explosion scenarios).

4.2 Basic equations of fluid dynamics

A compressible fluid can be described by a set of conservation laws known as the *Euler equations* (Toro 2009):

$$\frac{\partial}{\partial t} \rho + \vec{\nabla} \cdot (\rho \vec{v}) = 0, \quad (4.7)$$

$$\frac{\partial}{\partial t} (\rho \vec{v}) + \vec{\nabla} \cdot (\rho \vec{v} \otimes \vec{v}) = -\vec{\nabla} P, \quad (4.8)$$

$$\frac{\partial e_{\text{tot}}}{\partial t} + \vec{\nabla} \cdot (e_{\text{tot}} \vec{v}) = -\vec{\nabla} \cdot \left(\frac{P}{\rho} \vec{v} \right). \quad (4.9)$$

This system of nonlinear, hyperbolic, partial differential equations represents the conservation of mass (Eq. 4.7), conservation of momentum (Eq. 4.8) and the conservation of energy (Eq. 4.9). Here, e_{tot} denotes the total specific energy, i.e., specific kinetic and internal energy e_{int} , and \vec{v} the velocity. Since the system of five equations contains six unknowns a closure relation is needed. This is implemented via an EoS relating the thermodynamic variables, e.g., $e_{\text{int}} = e_{\text{int}}(\rho, P)$. The Euler equations neglect body forces such as gravity or electric fields, viscous effects, and heat conduction.

Viscosity of a fluid or material is governed by microphysical effects and the ratio of viscous forces versus inertial forces is given by the dimensionless *Reynolds number*

$$Re = \frac{\rho v(L)L}{\nu}. \quad (4.10)$$

L is a characteristic length scale of the problem, $v(L)$ the typical velocity on this length scale and ν the dynamical viscosity. For small Reynolds numbers $Re \lesssim 10$ velocity fluctuations are damped away by viscous forces, and the flow is laminar. In WD matter, however, Reynolds numbers of $\sim 10^{13}$ are reached indicating that viscosity plays a minor role, and that the flow

is fully turbulent (Woodsley et al. 2009). Moreover, Woodsley et al. (2007) state that convection is far more efficient than conduction processes which supports the disregard of heat flux in Eqs. 4.7, 4.8, and 4.9.

Since thermonuclear reactions alter the composition of the fluid they also affect the internal energy and need to be added to the energy equation (Eq. 4.9). Furthermore, the gravitational force acts as an external force and is introduced as a source term to Eqs. 4.8 and 4.9. The resulting system is called the *reactive Euler equations with gravity* and reads

$$\frac{\partial}{\partial t} \rho + \vec{\nabla} \cdot (\vec{v} \rho) = 0, \quad (4.11)$$

$$\frac{\partial}{\partial t} (\rho \vec{v}) + \vec{\nabla} \cdot (\rho \vec{v} \otimes \vec{v}) = -\vec{\nabla} P - \rho \vec{\nabla} \Phi, \quad (4.12)$$

$$\frac{\partial e_{\text{tot}}}{\partial t} + \vec{\nabla} \cdot (\vec{v} e_{\text{tot}}) = -\vec{\nabla} \cdot \left(\frac{P}{\rho} \vec{v} \right) - \vec{v} \cdot \vec{\nabla} \Phi + S, \quad (4.13)$$

where Φ represents the gravitational potential and S the energy input per unit time due to nuclear reactions. These equations build the basics for the numerical modeling of SNe Ia (see Chapter 5). It should be noted that the differential form of the Euler equations presented here is not suitable for discontinuities, i.e., shocks. They can, however, be written in an integral form covering shocks more appropriate for their numerical modeling (see e.g., LeVeque 2002; Toro 2009).

4.3 Nuclear burning stages

It was already mentioned several times that SNe Ia are the result of a thermonuclear explosion. It is a well known fact that the binding energy per nucleon rises from H up to a maximum around iron and nickel and subsequently drops toward heavier elements. Thus, the fusion of light nuclei with a mass number $A \lesssim 56$ releases energy while the fusion of heavy nuclei is an endothermic reaction. Since a fusion reaction relies on the frequency of interactions between nuclei and their respective kinetic energy to overcome the Coulomb repulsion, nuclear burning is a highly temperature and density dependent process. During hydrostatic burning, for instance main sequence H burning, the nuclear fuel is slowly consumed at roughly constant temperatures and densities while material is heated instantaneously by a combustion front (see Section 4.4) in explosive burning and subsequently cools and expands. The latter situation is found in SNe Ia and the characteristics of explosive burning as well as the nucleosynthesis yields are reviewed in detail in Chapter 8. Iliadis (2007) provides an extensive overview of nuclear reactions in stars and the following, brief discussion of the relevant burning stages closely follows his approach if not indicated otherwise.

Carbon burning

Since this work deals with CO WDs as the progenitor for SNe Ia the first burning stage to consider is C burning. At $T > 0.6 \times 10^9$ K (hydrostatic) or $T > 1.8 \times 10^9$ K (explosive) the average energy of a nucleus is high enough to overcome the Coulomb barrier of the $^{12}\text{C} + ^{12}\text{C} \rightarrow ^{24}\text{Mg}$ reaction. Due to the higher Coulomb repulsion the fusion of ^{12}C and ^{16}O or two ^{16}O nuclei is suppressed. Since the resulting ^{24}Mg nucleus is highly excited it decays very quickly leading

to the net primary reactions:



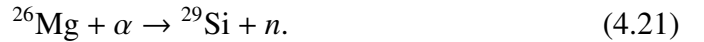
Subsequently, the produced light particles, i.e., protons p , neutrons n , and α -particles, react with either the CO fuel or the synthesized Na, Ne, and Mg isotopes. The primary products of C burning are then ^{16}O , ^{20}Ne , ^{24}Mg , and ^{23}Na with smaller traces of $^{25,26}\text{Mg}$ and ^{27}Al .

Neon burning

The isotope ^{20}Ne is photodisintegrated quickly at $T > 1.2 \times 10^9$ K (hydrostatic) or $T > 2.5 \times 10^9$ K (typical for explosive burning) even before the $^{16}\text{O} + ^{16}\text{O} \rightarrow ^{32}\text{S}$ reaction becomes relevant, and, thus, the next burning stage is called neon burning. After the primary photodissociation



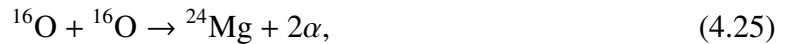
the liberated α -particles induce secondary reactions such as



Of course, a plenitude of other reactions involving n , p , and α -particles ensues, leading to a net increase of the ^{16}O abundance at the end of Ne burning with ^{24}Mg and ^{28}Si becoming most abundant. In addition, some trace nuclei like ^{27}Al , $^{29,30}\text{Si}$, ^{31}P , and ^{32}S are produced at lower fractions. This burning stage is not dominated by the fusion process of two heavy nuclei but can be seen as a rearrangement process via light particles such as α -particles, in particular.

Oxygen burning

As soon as the temperature rises above $\sim 1.5 \times 10^9$ K (hydrostatic) or $\sim 3.0 \times 10^9$ K (explosive), the fusion of two ^{16}O nuclei sets in with multiple possible outcomes:



Again, a variety of secondary reactions build up a small network and alter the composition involving the newly produced nuclei and liberated light particles. Moreover, due to the higher temperatures in O burning, photodissociation processes begin to play a significant role, especially in explosive O burning. The major products of O burning are ^{28}Si and ^{32}Si along with many rare isotopes between mass numbers A of 31 and 42.

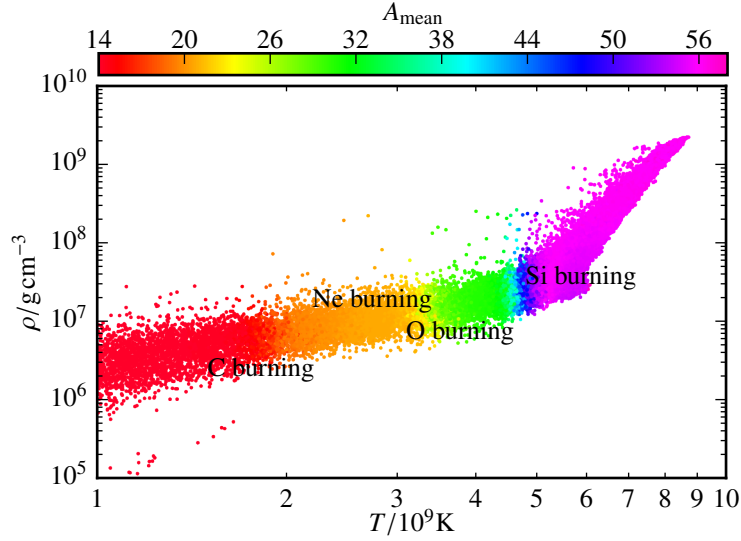


Figure 4.3: Tracer particles (fluid elements) of a SN Ia model (Model r_d2.6_Z in publication 1, Chapter 6) placed in the $T-\rho$ -plane (maximum T and ρ achieved during the explosion). The color represents the average mass number A_{mean} , and, hence, indicates the burning stage. Since there is a continuous transition between burning stages the label placing is only approximate.

Silicon burning

Similar to the case of neon burning, silicon burning can be viewed as a photodissociation and rearrangement process since the fusion of two ^{28}Si nuclei is not contributing significantly due to the huge Coulomb barrier. Instead, ^{28}Si (and also other IMEs) is destroyed and light particles, i.e., neutrons, protons, and α -particles, are produced which, in turn, accumulate on other nuclei to form heavier elements up to the iron peak. A special situation is encountered when all forward and backward reactions (strong and photodissociation processes) from α -particles to IGEs have come into equilibrium. In this state of nuclear statistical equilibrium (NSE) the abundances are uniquely determined by T , ρ , and Y_e only (see also Clifford and Tayler 1965; Woosley et al. 1973; Seitenzahl et al. 2009c). The composition shifts toward light nuclei for higher temperatures making the whole process temporarily endothermic. As matter cools in explosive burning, the abundances shift back toward IGEs and the energy stored in light particles is released. Furthermore, reactions start to fall out of equilibrium (freeze-out). This freeze-out process is of vital importance for the final abundances of silicon burning.

A more detailed discussion of silicon burning is omitted here since it is discussed in greater detail in Chapter 8. Hydrostatic core Si burning sets in at $T > 2.8 \times 10^9 \text{K}$ while explosive burning proceeds at $T > 4 \times 10^9 \text{K}$. Since the main products of Si burning are IGEs this represents the last stage of nuclear burning.

The various burning stages are visualized in Figure 4.3 using a numerical SN Ia model from Chapter 6. It shows the average mass number A_{mean} of the burning products as a function of the maximum temperature and density reached. As T and ρ rise A_{mean} also increases. Of course, there is not a sharp boundary between the burning stages such that the labels can only serve as a rough guidance. In addition to T and ρ , the nucleosynthesis products of nuclear burning also depend on the time scale of the expansion, i.e., the cooling, after the passage of the combustion front.

4.4 Thermonuclear combustion

Apart from the mass and structure of the exploding WD also the burning mechanism determines the outcome of the explosion. The two ways of thermonuclear combustion relevant for SNe Ia are detonations and deflagrations, respectively. In the simplest theory, the *Chapman-Jouguet theory*, the flame can be described as a discontinuity and nuclear (or chemical) reactions release their energy instantaneously behind the front (Fickett and Davis 1979). This is also a good approximation for the numerical modeling of SNe Ia since the flame width is many orders of magnitudes smaller than the exploding WD itself. From the Euler equations the *Hugoniot jump conditions* can be derived (see e.g., Fickett and Davis 1979; Sharpe 1999):

$$\rho v = \rho_0 D, \quad (4.28)$$

$$P + \rho v^2 = P_0 + \rho_0 D^2, \quad (4.29)$$

$$e_{\text{int}} + \frac{P}{\rho} + \frac{u^2}{2} = e_{\text{int},0} + \frac{P_0}{\rho_0} + \frac{D^2}{2}. \quad (4.30)$$

They account for conservation of mass, momentum and energy across the discontinuity in the shock frame. The subscript 0 denotes preshock states while variables without subscript represent postshock states. Moreover, $D = u_0$ is the shock velocity, i.e., the velocity of material streaming into the shock. Eliminating u and some rearrangements lead to

$$\mathcal{R} = (P - P_0) + \rho_0^2 D^2 \left(\frac{1}{\rho} - \frac{1}{\rho_0} \right) = 0, \quad (4.31)$$

$$\mathcal{H} = e_{\text{int},0} - e_{\text{int}} + Q + \frac{1}{2} \left(\frac{1}{\rho_0} - \frac{1}{\rho} \right) (P_0 - P) = 0. \quad (4.32)$$

The variable Q accounts for the energy released in nuclear reactions behind the shock. Note that the EoS also depends on the composition. Eq. 4.31 defines the Rayleigh-line \mathcal{R} connecting mechanically allowed pre- and postshock states while energetically allowed states lie on the Hugoniot curve \mathcal{H} (Eq. 4.32). Hence, the solution for the postshock states is defined by an intersection of the Rayleigh line with the Hugoniot curve. This is commonly illustrated in a $V - P$ -diagram with the specific volume $V = 1/\rho$ (see Figure 4.4). The left panel shows \mathcal{R} and \mathcal{H} for a shock wave in a non-reactive fluid, i.e., $Q = 0$. The detonation velocity D is represented by the gradient of \mathcal{R} , and, thus, the regions in the lower left and upper right part of the diagram are not accessible since they correspond to $D^2 < 0$ (compare Eq. 4.31). If D is known, the postshock state can be determined uniquely.

Detonations

A detonation is a shock wave, i.e., a discontinuity in pressure and density, traveling at supersonic velocities ($D > c_0$, where c_0 is the speed of sound in the unburned matter) with respect to the fuel ahead. This fuel is compressed, and, thus, heated instantaneously to temperatures high enough to ignite nuclear burning. In this simple theory reactions are expected to be exothermic. The situation is visualized in the right panel of Figure 4.4: Since e_{int} depends on the composition and the energy Q is released due to nuclear burning the postshock adiabat is shifted toward higher pressures (orange line) compared to the Hugoniot curve without reactions (black line). Therefore, there is a minimum velocity for the detonation, i.e., when the Rayleigh line is tangent to the Hugoniot curve (point c). This point is called the Chapman-Jouguet (CJ) point and

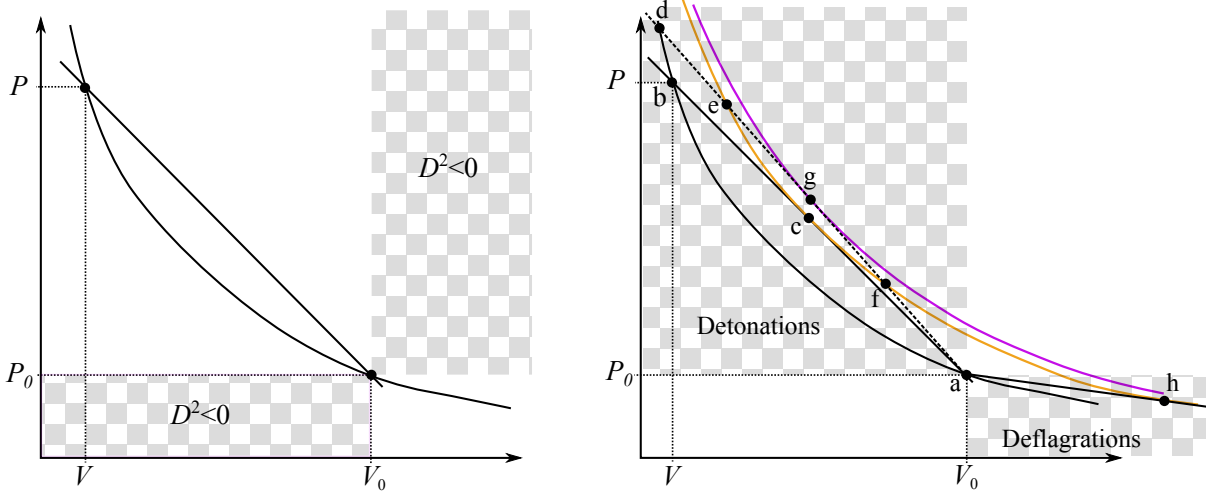


Figure 4.4: Schematic representation of the Hugoniot curve and the Rayleigh line in the $P - V$ -plane including possible pre- and postshock states labeled by letters from a to h. The left panel shows a shock adiabat without energy generation while the right panel includes nuclear burning behind the shock.

the corresponding velocity D_{CJ} equals the sound speed c in the burned material. It is commonly accepted that steady, self-supported detonations travel at D_{CJ} (Fickett and Davis 1979, also in CO WDs Buchler et al. 1971). Theoretically, the detonation velocity can exceed D_{CJ} , leading to two possible solutions for the final state (points e and f). The upper locus e corresponds to strong detonations and represents an unstable solution. Since here $D_{CJ} < c$ the detonation front is overtaken and weakened by a rarefaction wave following the shock front. Point f represents a weak detonation with $D_{CJ} > c$.

The reason why a weak detonation is not likely to be reached can be illustrated in terms of a slightly more advanced model, i.e., the ZND (Zel'dovich 1940; von Neumann 1942; Döring 1943) theory. Here, the assumption of instantaneously occurring nuclear reactions is abandoned. Instead, the shock discontinuity is followed by a reaction zone of finite thickness in steady flow. The state reached after all reactions have ceased is called the final state. Inside the hot reaction zone the burning stages described in Section 4.3 operate and convert the CO fuel to heavier elements. Fortunately, the CJ theory can still be applied since every state inside the reaction zone³ can be connected to the preshock states via the jump conditions (Eq. 4.30). The area between the initial Hugoniot curve (black line) and the final state (orange line) is continuously filled with adiabats corresponding to partially processed fuel ($0 < \lambda < 1$). Thus, the whole process can be viewed as follows: Material is compressed and heated and the state moves from point a to either b or d. Subsequently, reactions set in and the state moves down the Rayleigh line to the final state, either point c (CJ solution) or e (strong solution). The weak solution (point f) is not accessible since point e is reached before.

It turns out, however, that detonations in terrestrial experiments show a final point near the weak solution (Fickett and Davis 1979). Moreover, the incorporation of further complexities into the theory such as endothermic reactions or viscous effects indicates that a weak solution is achieved. For the case of endothermic reactions occurring inside the reaction zone this can again

³The reactions are frequently addressed by a reaction parameter λ with values between 0 for initial fuel and 1 at the final state. This makes $e_{\text{int}} = e_{\text{int}}(\rho, P, \lambda)$.

be visualized with the help of Figure 4.4. Imagine there is a state with higher energy release Q than the final state within the reaction zone. This state is depicted by the purple adiabat. From point d the state variables move downwards the dashed Rayleigh line crossing many virtual Hugoniot curves of partially burned material. The point g then corresponds to the CJ-state just before endothermic reactions set in. Thus, the state in sonic contact with the burning front lies within the reaction zone. The final state f is then reached as energy is consumed again by endothermic reactions. These *pathological detonations* then travel at a velocity higher than D_{CJ} . This situation is also encountered in silicon burning, in particular, in NSE (see Chapter 8 for details). Therefore, at high densities detonations are of the pathological type in SNe Ia (Gamezo et al. 1999; Sharpe 1999, but see Kushnir 2019).

Although detonations are not planar in reality but also show curvature effects and cellular instabilities (Fickett and Davis 1979; Gamezo et al. 1999; Timmes et al. 2000) these small scale patterns can be neglected for simulations of SNe Ia. For instance, Timmes et al. (2000) estimate that the cellular instability reduces the detonation speed to around 1 – 2% below the CJ-value.

Deflagrations

A close look at Figure 4.4 reveals that there are more intersections of \mathcal{R} and \mathcal{H} in the lower right part of the diagram. These solutions (only the CJ-solution is visualized via point h) depict deflagrations. The shallow gradient of \mathcal{R} indicates that there is only a very small difference in pressure between post- and preshock states and that the flame front travels slowly compared to detonations. More precisely, a deflagration propagates subsonically with respect to the fuel ahead and is not a compression wave but spreads due to heat conduction, which is a microphysical effect. Nuclear burning heats the fuel ahead until ignition. Also in this case, the burning stages described in Section 4.3 process the CO fuel depending on the temperatures and densities reached inside the reaction zone.

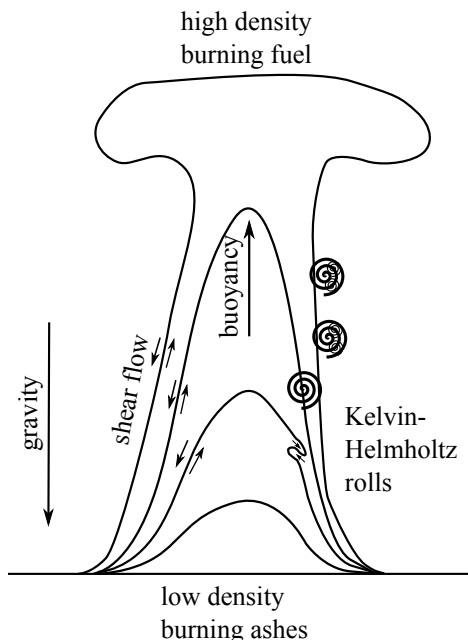


Figure 4.5: Schematic visualization of Rayleigh-Taylor plumes (buoyancy) and Kelvin-Helmholtz instabilities (shear). As the low density material rises against gravity shear flows develop at the interface of ash and fuel, leading to a turbulent cascade represented by spirals.

Moreover, a deflagration front is subject to hydrodynamic instabilities. First, the ashes exhibit lower densities than the fuel which leads to an inverse density stratification in a WD, and, thus, to buoyancy. The light, burned material rises and develops the typical mushroom shaped Rayleigh-Taylor plumes. This behavior is sketched schematically in Figure 4.5. In addition, a shear flow arises at the edge of the rising material, leading to Kelvin-Helmholtz instabilities. The flame wrinkles and forms the characteristic Kelvin-Helmholtz rolls. Within these forming spirals, called eddies, new shear flows arise, leading to a turbulent cascade transporting energy from large to small length scales until viscous effects become dominant and kinetic energy is dissipated to heat (Kolmogorov-scale, Kolmogorov 1941, 1962). The velocity of the flame front, the laminar velocity s_l governed by microphysical effects (mostly conduction, Timmes and Woosley 1992), is much smaller compared to the turbulent velocities introduced by Rayleigh-Taylor and Kelvin-Helmholtz instabilities. Therefore, a viable explosion produced by a deflagration crucially relies on a sound modeling of turbulence (Niemeyer and Hillebrandt 1995; Schmidt et al. 2006a,b). This also requires simulations in three dimensions since turbulence is inherently three-dimensional (3D, compare the results of Reinecke et al. 1999a to Reinecke et al. 2002b).

It is also important to note that Rayleigh-Taylor instabilities do not develop on arbitrary length scales, but that there is a minimum scale. This *fire polishing length* $\lambda_p = (gs_l^2)/(2\pi)(\rho_0 - \rho)/(\rho_0 + \rho)$ depends on the laminar flame speed, i.e., the propagation due to heat conduction only, on the density contrast between burned and unburned state, and on the gravitational acceleration g . Below this scale buoyancy instabilities are immediately smoothed out by the flame propagation. A similar length scale exists for Kelvin-Helmholtz instabilities. Since the typical eddy velocity decreases as energy is transported to smaller scales, the turbulent velocity at some point equals s_l at the so-called *Gibson scale* l_G . In this regime, shear instabilities are overrun by the flame front and no further turbulence is introduced. l_G in combination with the width of the reaction zone δ_{def} can also be used to separate two distinct deflagration burning regimes. For $l_G > \delta_{\text{def}}$ the structure of the reaction zone is not affected by turbulent motions and the deflagration resides in the *flamelet regime*. The *distributed burning regime* is characterized by $l_G < \delta_{\text{def}}$. Here the internal flame structure is significantly altered as turbulent motions drive into the reaction zone and partially destroy the flame front. Since l_G decreases and δ_{def} increases with density both regimes are encountered in SNe Ia explosions as the flame moves from the core to the outer layers of the WD (Röpke 2017).

Summary of the main differences

In summary, detonations are shock waves traveling at supersonic velocities. Thus, the WD structure is not able to adjust and matter is burned according to the initial density profile. Moreover, a one-dimensional (1D) plane wave is a good approximation for a detonation front. A deflagration instead propagates subsonically leading to an expansion of the whole star during the burning process. Although the laminar flame velocity is low compared to a detonation, hydrodynamic instabilities such as Rayleigh-Taylor and Kelvin-Helmholtz instabilities induce turbulence and significantly accelerate the burning. Due to the highly wrinkled flame surface a 3D modeling of deflagrations is indispensable.

4.5 Explosion scenarios

Pure carbon detonation

One of the earliest models for SNe Ia was calculated by [Arnett \(1969\)](#). They assumed that a CO WD close to M_{Ch} will detonate near the center (TNR, see Section 4.1) and find a strong explosion disrupting the whole star. Since most of the WD initially is at high densities ($\rho > 1 \times 10^7 \text{ g cm}^{-3}$) almost the whole star is burned via Si burning (compare Figure 4.3) and mostly IGEs are produced ([Arnett et al. 1971](#)). Hence, this model cannot reproduce the observational properties of SNe Ia, i.e., strong signs of Si, S, Ca etc. (see Section 3.2), and is not regarded as a candidate for SNe Ia.

If, however, the mass of the WD is significantly below M_{Ch} the production of IGEs is reduced in favor of IMEs. [Sim et al. \(2010\)](#) show that detonations in sub- M_{Ch} WDs ($M = 0.85 - 1.15 M_{\odot}$) yield results in broad agreement with observed SNe Ia. Since convective C burning inside the WD, the simmering phase, is only ignited at higher densities, i.e., near M_{Ch} , there remains the question of how explosive conditions (TNR) are reached in this scenario.

A possible way to ignite a detonation in sub- M_{Ch} WDs is the merger of two WDs in the DD scenario ([van Kerkwijk et al. 2010](#)). Simulations of this mechanism were carried out by [Lorén-Aguilar et al. \(2009\)](#); [Pakmor et al. \(2010, 2011, 2012\)](#). [Pakmor et al. \(2012\)](#), for example, calculated the merger of two almost equal mass WDs ($0.9 + 1.1 M_{\odot}$) and find good agreement with normal SNe Ia. Although the total mass of the system is above M_{Ch} the nucleosynthesis yields resemble those of sub- M_{Ch} detonations since the explosion is triggered during the violent merging process of the two WDs. In this case, matter is not concentrated at the center but rather smeared out at comparatively low densities. Finally, a detonation might also be triggered as a result of the head-on collision of two WDs ([Rosswog et al. 2009](#); [Raskin et al. 2009](#); [Kushnir et al. 2012](#)).

Double detonation

For reasons described above, a detonation in a M_{Ch} WD is excluded as an explosion mechanism for SNe Ia. Another solution to ignite a sub- M_{Ch} WD, in addition to the merger model, is to assume an initial detonation in an accreted He shell ([Taam 1980](#); [Nomoto 1982](#); [Woosley et al. 1986](#)) which then triggers a second detonation inside the CO core. Therefore, this scenario is called a *double detonation*. The CO detonation can either be ignited simultaneously with the He ignition at the edge of the WD (edge-lit detonation, [Livne and Glasner 1990](#); [Sim et al. 2012](#)), near the center of the CO core due to the convergence of two compression waves (converging shock mechanism, see [Livne 1990](#); [Livne and Arnett 1995](#); [Fink et al. 2007, 2010](#); [Townesley et al. 2019](#)), or at the opposite side of He ignition because the He detonation waves collide and ignite C near the surface (scissors mechanism, see [García-Senz et al. 1999](#); [Forcada et al. 2006](#); [Gronow et al. 2020](#)). In general, the overall observables are not highly sensitive to the actual C detonation ignition location. The He detonation products, however, are observed at high velocities and deteriorate the agreement of the sub- M_{Ch} detonation model with observed SNe Ia ([Kromer et al. 2010](#)). Therefore, the mass of the accreted He shell at the time of ignition has to be as low as possible. Recently, [Townesley et al. \(2019\)](#) and [Gronow et al. \(2021\)](#) tested different shell masses down to $0.02 M_{\odot}$ which reduces the observable signatures of He burning products. These promising results make the double detonation model one of the favorite scenarios to account for normal SNe Ia.

There is, however, also the possibility that no secondary C detonation is triggered. The result is a fast evolving and faint transient dubbed “.Ia SN” by Bildsten et al. (2007). Such models are candidates for Ca-rich transients (see also Section 3.3).

Pure deflagration

During the simmering phase in a M_{Ch} WD it is very likely that a deflagration instead of a detonation is ignited. This combustion mechanism brings the advantage that the star expands during the propagation of the flame and not all material is processed in complete Si burning (see Chapter 8). Therefore, a substantial amount of IMEs is produced in these explosions. Although the highly turbulent nature of a deflagration is a 3D phenomenon the earliest simulations have been carried out in 1D (Ivanova et al. 1974; Nomoto et al. 1976, 1984; Iwamoto et al. 1999). The effective flame speed was, however, an adjustable parameter in these studies. Nevertheless, 1D deflagrations in M_{Ch} lead to a good agreement between simulations and observations. In particular, the W7 model by Nomoto et al. (1984) is still frequently used as a benchmark model. Subsequently, with increasing computational resources two-dimensional (Livne 1993a,b; Arnett and Livne 1994a; Khokhlov 1995; Niemeyer and Hillebrandt 1995; Reinecke et al. 1999a; Livne et al. 2005; Leung and Nomoto 2020) and 3D (Reinecke et al. 2002b; Gamezo et al. 2004; Röpke 2005; Röpke et al. 2006, 2007b; Röpke and Niemeyer 2007; Röpke et al. 2007a; Pfannes et al. 2010; Jordan et al. 2012b; Ma et al. 2013; Malone et al. 2014; Long et al. 2014; Fink et al. 2014) deflagration studies were carried out. The overall picture emerging from these works is that a pure deflagration inside a M_{Ch} WD cannot account for normal SNe Ia since only moderately bright events can be reached in terms of ejected ^{56}Ni . Moreover, turbulent combustion leads to strongly mixed ejecta in contrast to the layered structure derived from observations for normal SNe Ia (see Section 3.2) which prevents the appearance of a secondary maximum in the NIR bands.

However, pure deflagrations may be a scenario for the subluminous class of SNe Iax. This connection is discussed in detail in Chapter 6.

Delayed detonation

As discussed above, a detonation in a M_{Ch} WD synthesizes almost exclusively IGEs. If the detonation is, however, preceded by a deflagration, the WD has expanded and the density has dropped such that also significant amounts of IMEs are produced in the detonation. The explosion starts off with a deflagration which burns the central parts of the star at high densities. Subsequently, as the turbulent deflagration enters the distributed burning regime a detonation might be triggered due to small scale velocity fluctuations interacting with the flame. Thus, the detonation is ignited at lower densities of $\rho \sim 10^7 \text{ g cm}^{-3}$. This explosion mechanism was proposed by Khokhlov (1991a,b,c) and investigated further by Arnett and Livne (1994b); Höflich et al. (1995); Gamezo et al. (2005); Röpke and Niemeyer (2007); Röpke (2007), and Seitzzahl et al. (2013b). The LCs and spectra of the delayed detonation model agree significantly better with normal SNe Ia than those of the pure deflagration scenario (Kasen et al. 2009; Sim et al. 2013; Blondin et al. 2012) since a certain degree of ejecta stratification is introduced. Although it is unclear whether a deflagration-to-detonation transition really occurs in nature this scenario is one of the potential explosion mechanisms accounting for normal SNe Ia besides the double detonation and the violent merger model.

Gravitationally confined detonation

The gravitationally confined detonation (GCD) scenario is a variant of the delayed detonation model. There is, however, no spontaneous ignition of a detonation required but the detonation is triggered dynamically. The classical GCD model was proposed by [Plewa et al. \(2004\)](#) and relies on a lop-sided deflagration ignition. Due to the buoyant rising of the deflagration only one side of the WD gets burned until the flame breaks through the surface of the star and escapes laterally to sweep across its surface. These ashes then collide at the antipode and material is compressed until a detonation is ignited. This detonation then burns the pre-expanded core and produces a healthy explosion. The relevance and the outcome of this kind of model as well as some alternative mechanisms are extensively reviewed in Chapter 7.

The list of possible SN scenarios above is by no means complete but involves the most frequently discussed models (see e.g., [Soker 2019](#) for more variants).

4.6 Solving the progenitor problem

No progenitor system of a SN Ia has been observed yet⁴, and the observation of a faint and distant WD before explosion is also a difficult task. Therefore, indirect methods have to be employed to infer the progenitor star of a SN Ia. A few of these theoretical approaches will be explained in the following sections.

4.6.1 Supernova modeling pipeline

A common way to investigate the explosion mechanism is to conduct a series of numerical simulations trying to mimic the various stages and physics of the thermonuclear explosion of a WD. This “modeling pipeline” is illustrated in Figure 4.6. Details on the numerical treatment are given in Chapter 5.

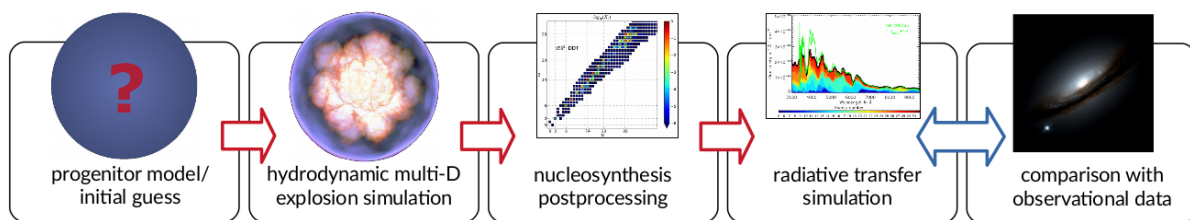


Figure 4.6: Supernova modeling pipeline. Credit: [Röpke and Sim \(2018\)](#).

The starting point is an initial model of a WD with a given mass, temperature profile, and composition. Furthermore, the ignition geometry is a free parameter. In the case of deflagrations, for instance, it is not clear whether the flame is ignited in a single spot or if the explosion starts off in several isolated points. Thus, the number of ignition points has also been used to determine the strength of the explosion (see Chapter 6 for a discussion on this point). A hydrodynamic simulation of the explosion stage is then carried out. This step yields the ejecta structure, kinetic energy, and the total mass ejected in the event (see Section 5.1 for details on

⁴But see [McCully et al. \(2014\)](#) for the possible detection of the companion star of SN 2021Z, a SN Iax.

the numerics). Subsequently, the nucleosynthesis yields are calculated with a nuclear network code in a postprocessing step. This step gives the abundances of all the isotopes produced during the explosion. The isotopic yields and the dynamical structure of the ejecta are then combined and used as input for radiative transfer calculations. These result in synthetic spectra and LCs which can then be compared to observations of SNe Ia. Since the whole pipeline is designed to form a sequence of self-consistent simulations the discrepancies between synthetic and real observables suggest variations in the initial model, and, thus, give hints toward the nature of the progenitor.

This method has widely been employed in 1D and 3D throughout the past decades (see e.g., [Höflich et al. 1993](#); [Höflich et al. 1995](#); [Höflich and Khokhlov 1996](#); [Kasen et al. 2006](#); [Röpke et al. 2007a](#); [Sim et al. 2012, 2013](#); [Kromer et al. 2013a,b](#); [Dessart et al. 2014a](#); [Townsend et al. 2019](#); [Gronow et al. 2020](#)) and is used in Chapters 6 and 7 to investigate the pure deflagration and the GCD scenario, respectively.

4.6.2 Galactic chemical evolution

Rather than using the nucleosynthesis yields as input for radiative transfer simulations, they can also be inserted into a GCE code. These simulations compute the evolution of the abundances of elements over cosmic time. Since the Universe consisted almost solely of H and He after the Big Bang and was continuously enriched with heavier elements ejected, for instance, by SNe, the metallicity, i.e., the fraction of elements heavier than He⁵, is used as a proxy for time in this framework. Thus, the composition of galaxies and stars is connected to their time of formation and the evolution of elements over time can be reconstructed from observations and compared to the outcome of GCE simulations. These calculations need many input parameters such as an initial mass function, star formation rates, star formation efficiencies, delay time distributions, and rates for astrophysical transients, yields of massive star winds, neutron star mergers, SNe II and SNe Ia (see [Matteucci 1996](#); [Côté et al. 2016](#) for a review). Works studying the chemical enrichment of the Universe were carried out by [Matteucci and Greggio \(1986\)](#); [Matteucci et al. \(2006\)](#); [Kobayashi et al. \(2006\)](#); [Kobayashi et al. \(2020\)](#); [Kobayashi and Nomoto \(2009\)](#) and [Prantzos et al. \(2018\)](#), for example.

Since the composition of SN Ia ejecta is not only different from SNe II but also differs among various SN Ia scenarios, the results of GCE simulations can be used to draw conclusions about the possible occurrence of a certain scenario. An extensive analysis of the nucleosynthesis yields of several SN Ia scenarios and their implication for GCE can be found in Chapter 8.

4.6.3 Rates

As already indicated above, the rates, i.e., the number of SNe per year, as well as delay times, i.e., the time it takes until explosion after the binary system has formed, influence the outcome of GCE simulations. Rates and delay times are theoretically predicted via binary population synthesis (see [Han et al. 2020](#) for a review) and put another constraint on the many possible scenarios for SNe Ia (see e.g., [Han et al. 1995](#); [Yungelson et al. 1995](#); [Wang et al. 2009](#); [Toonen et al. 2012](#)).

⁵In GCE models the metallicity is often represented by the ratio of Fe to H compared to their solar values: $[\text{Fe}/\text{H}] = \log [(\text{Fe}/\text{H})/(\text{Fe}_\odot/\text{H}_\odot)]$.

If, for instance, an explosion mechanism is in good agreement with observations according to the supernova modeling pipeline but predicted rates are too low to comply with the observed SN rate the scenario still needs a deeper investigation. Delay times in the SD scenario depend highly on the evolution of the secondary and the accretion process while a DD merger is characterized primarily by the initial separation of the two stars. Therefore, the SD scenario exhibits two delay time distributions describing H and He accretion, respectively. The rates calculated for the DD mergers are in better agreement with observations than the results for the SD model (Ruiter et al. 2009; Maoz et al. 2012; Ruiter 2019).

4.6.4 Supernova remnants

As time proceeds, the light of a SN fades and the ejecta interact with the surrounding circumstellar material (CSM) and interstellar matter (ISM). While the explosion of a SN Ia can only be observed as a point source, the structure of the expanding debris, i.e., the SNR, can be resolved, and, hence, can give hints toward the progenitor system or explosion mechanism (Milisavljevic and Fesen 2017). SNRs are observable at all wavelengths from radio to γ -rays.

X-ray observations are particularly useful to investigate the progenitor system since they reveal the composition of the ejecta. The SN ejecta drive a shock wave, the forward shock, into the surrounding medium heating it to X-ray emitting temperatures. Moreover, a reverse shock develops traveling backwards through the expanding ashes, leading to X-ray emission (see e.g., Reynolds 2017) for more details on the dynamical evolution of SNRs). The amount of neutron-rich IGEs such as Mn or stable Ni can then be used to discriminate between M_{Ch} and sub- M_{Ch} explosions (Yamaguchi et al. 2015). Furthermore, dominant contributions of IGEs and little signs of O separate SNe Ia from SNe II (Reynolds et al. 2007). Interaction with CSM is also a means of differentiating between the SD and the DD degenerate channel since the ambient medium should be devoid of material in the merger scenario in contrast to the environment of an accreting WD.

In addition, the morphology of SNRs contains information about the explosion itself. In order to compare observations to theoretical predictions the outcome of the hydrodynamic explosion simulation is evolved for several hundred years using an appropriate hydrodynamics code. The author of this thesis has also been involved in such a study carried out by Ferrand et al. (2021) providing the mapping of hydrodynamic explosion simulations combined with nucleosynthesis data. Ferrand et al. (2021) evolved pure deflagration as well as delayed detonation models of SNe Ia for 500 yr. They show that the morphology resulting from different combustion mechanisms as well as deflagration ignition conditions (100 versus 5 ignition spots) can still be distinguished after a few 100 years.

Chapter 5

Numerical modeling of type Ia supernovae

In order to shed light on the progenitor system and the explosion mechanism of SNe Ia, numerical simulations are inevitable (see Section 4.6). However, the multidimensional numerical modeling of the whole life of a star from its birth until the supernova event is virtually impossible with the currently available computational resources.

First, the length-scales involved span a range of a few orders of magnitude. While an ordinary main sequence star of $\sim M_{\odot}$ has a radius of $R_{\odot} \sim 696\,000$ km it can expand to a few $100 R_{\odot}$ during the giant phase and shrinks down to a radius of a few thousand km in the WD stage. Internal hydrodynamic processes such as convection and turbulence are relevant on length scales down to a few cm. Also the thermonuclear combustion fronts, i.e., deflagrations and detonations, can have a width on the order of a cm depending on the composition and density of matter. Second, the time-scales of the various stages of stellar evolution differ greatly. The main sequence phase lasts a few billion years, the simmering phase of the WD preceding the SNe Ia takes ~ 100 years and the explosion itself proceeds in less than 10 s. Subsequently, the radiative transfer processes in the expelled material have to be followed for a few 100 days. Moreover, the time-scale for nuclear reactions during explosive burning but also during hydrostatic burning is much shorter than the hydrodynamic time-scale. Finally, also the relevant physics change during the evolution of a star. While a rough treatment of convection and a nuclear network including ~ 10 isotopes is enough to capture the basic characteristics of the main sequence phase, a much more detailed prescription for turbulent motions and combustion fronts is necessary for a SN explosion simulation. In addition, the explosive nuclear burning proceeds until the iron peak nuclei, e.g., Fe, Co, Ni, Cu, and Zn, requiring a much larger nuclear network containing a few 100 isotopes. Later, during homologous expansion, i.e., a self similar, spherical expansion where the distance is direct proportional to velocity, hydrodynamic effects become irrelevant but radiation physics come into play.

Because of these complications, the various problems are tackled separately from each other with different numerical methods. Our work is restricted to the hydrodynamic simulation of the explosion of a WD, the determination of the explosive nucleosynthesis yields, and the subsequent radiation transport calculations. Therefore, the numerical codes appropriate for these purposes employed in this thesis will be described in the following.

5.1 Hydrodynamic simulations - the LEAFS code

The LEAFS code is a finite-volume fluid dynamics code based on PROMETHEUS by Fryxell et al. (1989) which was extended and adapted for simulations of SNe Ia by Reinecke et al. (1999b,a, 2002a). The separation of WD matter into small volumes (cuboids in LEAFS) is well justified as long as the mean free path of a particle is much smaller than the physical extent of the fluid cell. This ensures that microphysical effects due to the strong and electromagnetic force, i.e., collisions between nuclei, do not affect the fluid flow. The approach also assumes that the fluid components (electrons and nuclei) are in thermodynamic equilibrium, and, hence, average thermodynamic values can be assigned to a volume. The flux of mass, momentum, and energy over the cell boundaries is then described by three conservation laws: the reactive Euler equations (Eq. 4.11, 4.12, and 4.13) introduced in Section 4.2. To relate the thermodynamic quantities an EoS is required such that the temperature, for instance, can be uniquely determined by other state variables $T = T(\rho, e_i, \vec{X})$. Since the composition also influences the fluid properties the variable \vec{X} was introduced. The EoS implemented in the LEAFS code is the Helmholtz-EoS by Timmes and Swesty (2000) which is appropriate for arbitrarily degenerate conditions (see Section 4.1). The gravitational force in LEAFS is calculated using a fast Fourier-transform based method solving the full Poisson equation implemented by Schrauth (2015). This replaces the monopole solver used in previous studies employing LEAFS (see e.g., Röpke and Hillebrandt 2005; Fink et al. 2010; Seitenzahl et al. 2013b) and is much more accurate for asymmetric explosion scenarios. The author was responsible for the testing and bug-fixing of this new feature.

To calculate the fluxes over the cell boundaries, the averaged cell-centered values need to be reconstructed on the interfaces. The easiest way to do this is to assume a constant reconstruction, i.e., the cell centered value equals the value at the interface, and solve this so-called Riemann problem at each interface. This method was introduced by Godunov (1959). To better capture steep gradients, higher order methods are required. Therefore, LEAFS employs the piecewise parabolic method (Colella and Woodward 1984) and a Riemann solver appropriate to handle the influence of gravity on the cell states and large jumps in the EoS across flame fronts (Colella and Glaz 1985). Due to the high temperature behind the flame degeneracy is lifted (see Section 4.1) leading to very different characteristics of the EoS. Moreover, directional splitting is employed. The 3D problem is converted into a 1D one by successively calculating the advection in one direction. To assure higher order accuracy this step is reversed within every time step. Moreover, to ensure stability the time step is limited by the Courant-Friedrichs-Lewy (Courant et al. 1928) condition. This criterion makes sure that information cannot cross more than one cell interface per time step.

During the early development stages, LEAFS made use of a static Eulerian grid. It was realized early that the simulation needs to follow the evolution until homologous expansion of the ejecta is achieved. However, a simple expansion of the initial grid would lead to a very low resolution of the initial burning stages since the WD expands more than two orders of magnitude in the first ~ 100 s of the explosion and the resolution of the flame front, especially the turbulent motions of a deflagration, is of crucial importance. Therefore, Röpke (2005) implemented two nested, expanding grids. The inner grid is uniform and expands with the flame front while the outer, non-uniform grid tracks the expansion of the stellar surface. This approach ensures a reasonable resolution of the burning region but also allows to follow the expansion of the ejecta as a whole. Nevertheless, as the flame burns through the WD, the uniform grid covers the whole computational domain toward the end of the simulations and the overall resolution is reduced

compared to the initial one.

The nuclear energy generation in LEAFS is approximated via a small network of five pseudosppecies namely C, O, IMEs, IGEs, and α -particles including average values for the respective binding energy. C and O are converted to IMEs, IGEs, and α -particles according to precalculated tables in a calibration step (see [Fink 2010](#); [Ohlmann et al. 2014](#)). For detonations also the flame velocity is tabulated assuming CJ solutions.

To calculate detailed isotopic abundances, it is necessary to store thermodynamic quantities in tracer particles which are distributed randomly throughout the star. Each of these virtual particles is transported with the fluid flow and represents a certain mass fraction of the WD. In the simplest case all tracers have equal masses. This, however, leads to a decreasing number of tracer particles per volume for larger radii. In order to better capture the nucleosynthesis of a delayed detonation, i.e., a detonation occurring at moderate densities, [Seitenzahl et al. \(2010\)](#) introduced a hybrid approach allowing varying tracer masses. Furthermore, the tracers are used to map the abundances to the radiative transfer grid, and, therefore, a rather homogeneous distribution throughout the ejecta is desired.

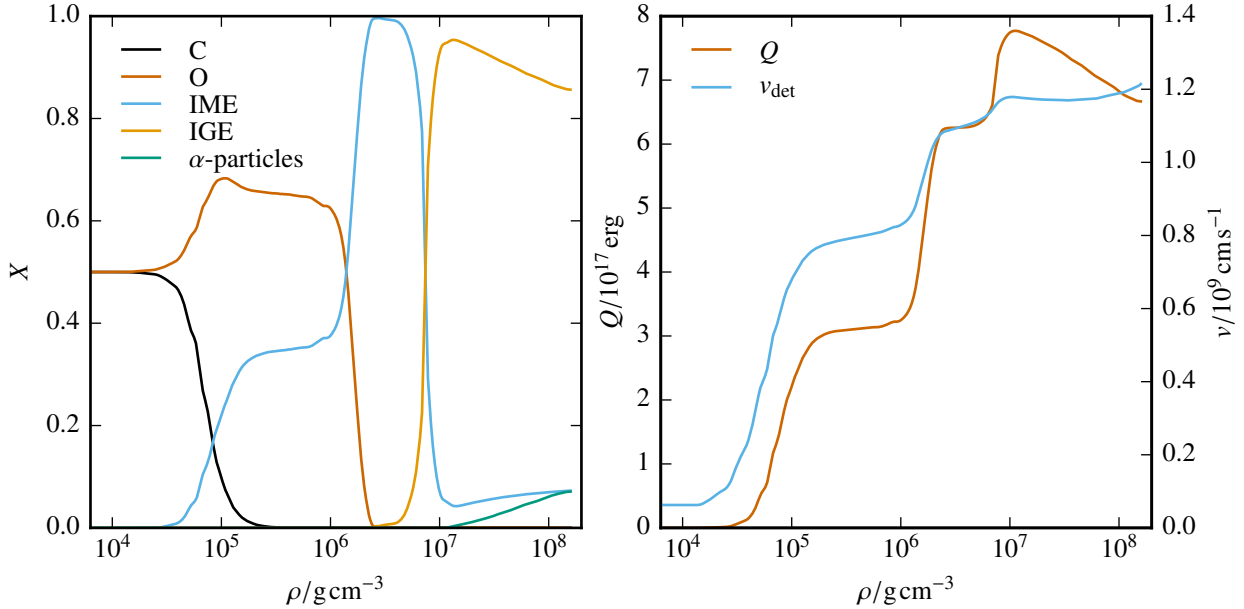


Figure 5.1: Abundance (left) and velocity (right) table for CO detonations at C/O=1 as calibrated by the author. The right panel also shows the energy Q released by nuclear reactions.

Since the EoS has been updated to the Helmholtz EoS ([Timmes and Swesty 2000](#)) the author had to redo the calibration. To this end, an explosion simulation using an abundance table converting all species to IGEs independent of density and temperature is carried out. Subsequently, a postprocessing step yields abundances and the respective energy release as a function of density. The new table then serves as input for another explosion simulation. This iteration cycle is stopped as soon as the energy release from the postprocessing and the hydrodynamic simulation have converged. A more detailed description of the calibration method can be found in [Fink \(2010\)](#). The resulting burning tables are displayed in Figure 5.1. The goal of this calibration step is to achieve the correct energy release behind the flame to correctly capture the dynamics of the explosion. Therefore, a one-to-one translation of the abundances to the final

yields of the postprocessing is not of interest. However, the various burning stages described in Section 4.3 and the endothermic behavior during NSE are visible. Directly after the shock front, i.e., before freeze-out, abundances are shifted toward α -particles. This stored energy is then released in later stages when NSE readjusts toward ^{56}Ni (see Section 4.3). This effect is also described in [Reinecke et al. \(2002c\)](#) and [Röpke and Hillebrandt \(2004\)](#).

The flame front itself is modeled via the levelset technique of [Osher and Sethian \(1988\)](#) and [Smiljanovski et al. \(1997\)](#) implemented by [Reinecke et al. \(1999b\)](#). In this approach the flame front is a discontinuity represented by the zero isosurface of a continuous signed distance function G . This isosurface separates fuel from ashes as material is only converted at flame crossing and energy is released according to the calibrated burning tables. In addition to the passive advection of the flame front with the fluid flow, the front advances either according to the detonation velocity table or the deflagration velocity (see below).

It was already mentioned in Section 4.4 that deflagrations introduce turbulence, and that these turbulent motions accelerate the fuel consumption, and, thus, the effective flame speed. However, since the turbulent cascade goes down to length scales orders of magnitudes smaller than the spatial resolution Δ in LEAFS, a subgrid model calculating the turbulent velocity fluctuation q_{sgs} on the subgrid scale (SGS) was implemented by [Schmidt et al. \(2006a\)](#). It is based on the filtering approach outlined by [Germano \(1992\)](#). Here, a low pass filter is applied to the dynamical equations governing the fluid flow separating resolved from unresolved motions below the grid scale. Imposing localized closures for second-order moments appearing in the filtered equations then yields the turbulent SGS energy, and, thus, the SGS velocity fluctuations. The effective deflagration speed can then be calculated as

$$s_{\text{def}} = \left(s_1^2 + C_t q_{\text{sgs}}^2 \right)^{1/2}. \quad (5.1)$$

The laminar flame speed s_1 is given by [Timmes and Woosley \(1992\)](#) and the burning coefficient C_t is set to 4/3 as found by [Schmidt et al. \(2006a\)](#).

5.2 Nuclear network calculations - the YANN code

For the radiation transport calculations and the insertion of SNe Ia yields into GCE models, detailed yields of all the isotopes produced during the explosion are needed. These nucleosynthesis yields are calculated detached from the hydrodynamic simulations using the values stored by the tracer particles such as the temporal evolution of ρ and T , and the initial composition X_{ini} . The change in the mass fraction of nucleus i can be written in a simplified way as

$$\begin{aligned} \frac{\partial X_i}{\partial t} = & \sum_{j,k} R_{jk} X_j X_k + \sum_k R_k(\beta) X_k + \sum_k R_k(\gamma) X_k \\ & - \sum_{i,k} R_{ik} X_i X_k - \sum_i R_i(\beta) X_i - \sum_i R_i(\gamma) X_i. \end{aligned} \quad (5.2)$$

The first term represents the creation of nucleus i via the reaction of two nuclei j and k , the second one the creation of i due to a β -decay of particle k and the third one the production of nucleus i via the photodisintegration of nucleus k . Terms 4 to 6 denote the respective destruction of nucleus i . For simplicity, reactions involving more than two particles, e.g., the triple- α reaction, are neglected here since they have a very low probability. The prefactor R , we refer to it

as the reaction rate here, contains the nuclear physics (e.g., density and temperature-dependent cross sections including resonances) as well as other parameters such as ρ and the Avogadro constant N_A omitted here for the sake of simplicity. The nuclear properties of many (exotic) isotopes have not been measured yet in the correct energy range. Thus, theoretical models have to be employed introducing significant uncertainties (Lippuner and Roberts 2017). Instead of the mass fraction X many studies employ the molar abundance $Y = X/A$ with the atomic mass number A . However, this choice only calls for an adjustment of the prefactors R .

Obviously, an equation like Eq. 5.2 can be written down for every nucleus in the network producing a large system of nonlinear, coupled ordinary differential equations describing the evolution of the specific abundances over time. In this work, the nuclear network code `YANN` (Pakmor et al. 2012) is employed to calculate the nucleosynthetic yields in the postprocessing step (see also Fig. 4.6). It includes reaction rates from the REACLIB library (Rauscher and Thielemann 2000), weak reaction rates from Langanke and Martínez-Pinedo (2001) and Coulomb corrections (see Wallace et al. 1982). The network used for the calculations in Publications 1, 2, and 3 contains 384 isotopes from p and n up to Ge. The matrix which has to be integrated to solve the system is of size $N \times N$ where N is the number of species in the network. Since many nuclei are not connected by reactions, this sparse matrix contains a lot of zero elements and includes a wide range of reaction rates producing a stiff system of equations which needs to be integrated implicitly (Timmes and Arnett 1999). Therefore, the method of Bader and Deuffhard (1983) is implemented.

5.3 Radiative transfer modeling - the ARTIS code

The RT calculations included in Publications 1 and 2 are not part of the contribution of the author to this thesis. They are, however, included in the publications, and, thus, the ARTIS code employed is described briefly here. The simulations were carried out by Fionntan Callan from Queen's University Belfast.

The ARTIS code is a 3D Monte Carlo radiative transfer code developed by Sim (2007) and Kromer and Sim (2009) based on methods presented in Lucy (2005). Data gained from the hydrodynamics and postprocessing, i.e., density, temperature, velocity, and abundances, is mapped to an expanding Cartesian grid using an SPH (smoothed particle hydrodynamics) approach. Since matter is in homologous expansion the hydrodynamics is now detached from radiative processes. Radioactive pellets are distributed across the grid according to the density profile and the distribution of radioactive isotopes such as ^{56}Ni , ^{56}Co , ^{52}Fe , or ^{48}Ti . Each decay then isotropically emits a γ -packet which is propagated through the ejecta via a Monte Carlo simulation. The same holds for UVOIR radiation (r-packets). Thermal kinetic energy is stored in k-packets while i-packets store atomic excitation or ionization energy. Interaction with matter is taken into account via Compton scattering and absorption of photons. Moreover, pair production of energetic quanta is included. These processes shift radiative energy between i-, r-, k-, and γ -packets according to the particular physical process involved. Line interactions are treated using the Sobolev approximation (Sobolev 1957), i.e., assuming that thermal velocities are negligible compared to the ejecta velocities. The assumption of homologous expansion as well as the Sobolev approximation hugely simplify the solution of the time dependent radiative transfer problem. Since the results of the RT calculations depend only on the input from the explosion simulation including the postprocessing and atomic data (describing line interactions), the outcome is parameter free and self-consistent.

Part II

Publications

Chapter 6

Type Ia_x supernovae from deflagrations in Chandrasekhar mass white dwarfs

Publication information:

Journal: Astronomy & Astrophysics (A&A), Volume 658, February 2022

Reference: F. Lach et al. 2022a, A&A, 658, A179

Digital Object Identifier: <https://doi.org/10.1051/0004-6361/202141453>

Status: Published on 21 February 2022

Credit: Florian Lach, A&A, 658, A179, 2022, reproduced with permission ©ESO

Authors:

Florian Lach (FL), Fionntan P. Callan (FPC), David Bubeck (DB), Friedrich K. Röpke (FKR), Stuart A. Sim (SAS), Manuel Schrauth (MS), Sebastian T. Ohlmann (STO), Markus Kromer (MK)

Author's contribution:

FL was responsible for writing the text of the manuscript (including abstract, introduction, and conclusions) except Section 6 which was provided by FPC. While FPC also carried out the radiative transfer simulations FL made the hydrodynamic and nuclear network simulations and the respective analysis and figures. The scientific content of the paper was mainly discussed in close collaboration with FPC, FKR and SAS. DB produced the rotating models in the course of a Master's Thesis which FL was mentoring. MS implemented the FFT gravity solver which is used in a peer-reviewed publication for the first time here. STO and MK were very helpful in the development of the presented models offering great assistance during the early phase of the PhD thesis.

Type Iax supernovae from deflagrations in Chandrasekhar mass white dwarfs

F. Lach^{1,2}, F. P. Callan³, D. Bubeck¹, F. K. Röpkke^{1,2}, S. A. Sim³, M. Schrauth⁴,
S. T. Ohlmann⁵, and M. Kromer¹

¹ Heidelberger Institut für Theoretische Studien, Schloss-Wolfsbrunnenweg 35, 69118 Heidelberg, Germany
e-mail: florian.lach@h-its.org

² Zentrum für Astronomie der Universität Heidelberg, Institut für Theoretische Astrophysik, Philosophenweg 12, 69120 Heidelberg, Germany

³ School of Mathematics and Physics, Queen's University Belfast, Belfast BT7 1NN, UK

⁴ Institute of Theoretical Physics and Astrophysics, University of Würzburg, 97074 Würzburg, Germany

⁵ Max Planck Computing and Data Facility, Gießenbachstr. 2, 85748 Garching, Germany

Received 2 June 2021 / Accepted 22 November 2021

ABSTRACT

Context. Due to the ever increasing number of observations during the past decades, Type Ia supernovae are nowadays regarded as a heterogeneous class of optical transients consisting of several subtypes. One of the largest of these subclasses is the class of Type Iax supernovae. They have been suggested to originate from pure deflagrations in carbon-oxygen Chandrasekhar mass white dwarfs because the outcome of this explosion scenario is in general agreement with their subluminous nature.

Aims. Although a few deflagration studies have already been carried out, the full diversity of the class has not been captured yet. This, in particular, holds for the faint end of the subclass. We therefore present a parameter study of single-spot ignited deflagrations in Chandrasekhar mass white dwarfs varying the location of the ignition spark, the central density, the metallicity, and the composition of the white dwarf. We also explore a rigidly rotating progenitor to investigate whether the effect of rotation can spawn additional trends.

Methods. We carried out three-dimensional hydrodynamic simulations employing the LEAFS code. Subsequently, detailed nucleosynthesis results were obtained with the nuclear network code YANN. In order to compare our results to observations, we calculated synthetic spectra and light curves with the ARTIS code.

Results. The new set of models extends the range in brightness covered by previous studies to the lower end. Our single-spot ignited explosions produce ⁵⁶Ni masses from 5.8×10^{-3} to $9.2 \times 10^{-2} M_{\odot}$. In spite of the wide exploration of the parameter space, the main characteristics of the models are primarily driven by the mass of ⁵⁶Ni and form a one-dimensional sequence. Secondary parameters seem to have too little impact to explain the observed trend in the faint part of the Type Iax supernova class. We report kick velocities of the gravitationally bound explosion remnants from 6.9 to 369.8 km s⁻¹. The magnitude as well as the direction of the natal kick is found to depend on the strength of the deflagration.

Conclusions. This work corroborates the results of previous studies of deflagrations in Chandrasekhar mass white dwarfs. The wide exploration of the parameter space in initial conditions and viewing angle effects in the radiative transfer lead to a significant spread in the synthetic observables. The trends in observational properties toward the faint end of the class are, however, not reproduced. This motivates a quantification of the systematic uncertainties in the modeling procedure and the influence of the ⁵⁶Ni-rich bound remnant to get to the bottom of these discrepancies. Moreover, while the pure deflagration scenario remains a favorable explanation for bright and intermediate luminosity Type Iax supernovae, our results suggest that other mechanisms also contribute to this class of events.

Key words. hydrodynamics – radiative transfer – instabilities – white dwarfs – supernovae: general – methods: numerical

1. Introduction

Type Ia supernovae (SNe Ia) have, for a long time, been thought to form a rather homogeneous class of cosmic explosions. In fact, the majority of events show similar photometric and spectroscopic behavior. Their light curves follow an empirical width-luminosity relation (WLR, Phillips relation, Phillips 1993), associating broad shapes with bright events. This property makes these so-called Branch-normal supernovae (Branch et al. 1993, 2006) standardizable candles, widely employed for distance measurements (Riess et al. 1996; Schmidt et al. 1998; Perlmutter et al. 1999; Jha et al. 2007). However, the increasing number of observations over the past decades led to the detection of outliers and eventually called for the introduction of several

subclasses of SNe Ia. These subtypes are believed to share the thermonuclear origin with normal SNe Ia, that is, the disruption of a carbon-oxygen (CO, in some cases also oxygen-neon (ONe), Marquardt et al. 2015; Kashyap et al. 2018) white dwarf (WD) due to explosive nuclear burning, but they exhibit clear differences in some characterizing properties (see Taubenberger 2017 for a review).

The largest of these subclasses of SNe Ia is the subluminous supernovae of Type Iax (SNe Iax), with more than ~50 members observed. According to Foley et al. (2013), SNe Iax might account for about 31% of all SNe Ia while Li et al. (2011) and White et al. (2015) estimated their rate to be ~5% (Jha 2017). The typical object for this class is SN 2002cx (Li et al. 2003), and, therefore, at least the brighter objects are also called

02cx-like events. [Foley et al. \(2013\)](#) named these transients SNe Iax and defined the key observational features of this class as follows: (i) no evidence of hydrogen in any spectrum, (ii) lower maximum-brightness photospheric velocity than any normal SN Ia, (iii) low absolute magnitude near maximum light in relation to the width of its light curve (i.e., they fall below the WLR), and (iv) spectra similar to SN 2002cx at comparable epochs.

While the first criterion represents the usual distinction between SNe Ia and supernovae of Type II, the second and third requirements suggest the production of only a small amount of energy. The optical emission from SNe Ia is powered by the radioactive decay of ^{56}Ni to ^{56}Co in the early phase, and, therefore, their brightness is directly linked to the ejected mass of ^{56}Ni . Peak absolute brightnesses derived from observations range between $-14 \geq M_V \geq -19$, inferred ^{56}Ni masses lie between 0.003 and $0.27 M_\odot$ ([Foley et al. 2013](#); [Jha 2017](#)), and ejected masses M_{ej} between $0.15 M_\odot$ for the faintest members of this class, such as SN 2008ha ([Foley et al. 2009](#)), and up to approximately M_{Ch} for the brightest events (e.g., SN 2012Z, [Stritzinger et al. 2015](#)). Normal SNe Ia, in contrast, eject between 0.3 and $0.9 M_\odot$ of ^{56}Ni ([Hillebrandt et al. 2013](#)). In addition, ejecta velocities are significantly lower than those of normal SNe Ia and usually fall below 8000 km s^{-1} down to $\lesssim 2000 \text{ km s}^{-1}$ for the faintest SNe Iax ([Foley et al. 2009](#)). However, *B*-band light curve decline rates span a similar range compared to normal events, but they cannot be connected to the corresponding brightness via the WLR, and, thus, SNe Iax are not employed as distance indicators. The shape of their light curves in the optical regime resembles normal SNe Ia while the prominent second peak in the near-infrared (NIR) bands (IJHK; [Hamuy et al. 1996](#); [Kasen 2006](#)) is absent in SNe Iax ([Foley & Kirshner 2013](#); [Magee et al. 2016](#); [Jha 2017](#)). Also the redder bands tend to decline slower compared to lower wavelengths ([Tomasella et al. 2016](#)) and show a larger variation in decline rates compared to normal SNe Ia. There is also a loose correlation between photospheric velocities and peak magnitudes ([McClelland et al. 2010](#); [Foley & Kirshner 2013](#)), that is, brighter events also show higher expansion velocities, challenged only by some outliers such as SN 2009ku ([Narayan et al. 2011](#)) and SN 2014ck ([Tomasella et al. 2016](#)). In addition, [Magee et al. \(2016\)](#) study the rise times of SNe Iax ($t_{\text{rise}} = 9\text{--}28$ d) and find an increasing trend with peak *r*-band magnitude, but again with a clear outlier, namely SN 2009eoi.

The near maximum spectrum of SN 2002cx, and, by definition those of other SNe Iax, is characterized by prominent Fe III lines and relatively weak signs of IMEs, for example, Si II and S II ([Branch et al. 2004](#)). Surprisingly, this is quite similar to the overluminous and rapidly expanding SN 1991T-like events. The photospheric velocity, however, is very low ($\sim 7000 \text{ km s}^{-1}$) making it easier to identify individual species since absorption and emission features are broadened less. About two weeks after maximum the Si II feature has disappeared and the spectrum is dominated by singly ionized iron group elements (IGEs). Until 56 d the spectrum resembles those of normal SNe Ia at slightly later times and has not turned nebular yet ([Branch et al. 2004](#)). The late-time spectra of SN 2002cx (227 and 277 d) were examined by [Jha et al. \(2006\)](#). They found that the spectra did not change significantly after 56 d post maximum and deviate significantly from those of normal SNe Ia. Instead of being dominated by forbidden lines of Fe and Co typical for nebular spectra they exhibit P Cygni features of Fe II but also IMEs and potentially signs of oxygen. [Foley et al. \(2016\)](#) also state that late-time spectra of SNe Iax only show minor changes over time and that

differences among the subclass originate primarily from different expansion velocities. Finally, they find clear signs of Ni II pointing toward a significant amount of stable Ni in the ejecta.

Several different progenitor systems and explosion mechanisms have been proposed for thermonuclear supernovae during the past decades. The explosion of the WD is triggered by the interaction with a hydrogen or helium-rich companion (single-degenerate scenario, [Whelan & Iben 1973](#)) or another WD (double-degenerate scenario, [Iben & Tutukov 1984](#)). Furthermore, the explosion is caused by a thermonuclear runaway in degenerate matter resulting in either a subsonic deflagration or a supersonic detonation. The propagation of a deflagration is mediated by heat conduction while a detonation proceeds as a shock wave. Moreover, a spontaneous transition from a deflagration to a detonation has been proposed by [Blinnikov & Khokhlov \(1986\)](#), [Khokhlov \(1989\)](#) and was studied by [Khokhlov \(1991\)](#), [Gamezo et al. \(2005\)](#), [Röpke \(2007\)](#), and [Seitenzahl et al. \(2013\)](#), for instance. Comprehensive summaries of the whole “zoo” of possible SN Ia explosion scenarios can be found in reviews, for example, [Wang & Han \(2012\)](#), [Hillebrandt et al. \(2013\)](#), [Livio & Mazzali \(2018\)](#), [Röpke & Sim \(2018\)](#), and [Soker \(2019\)](#).

One promising scenario for explaining SNe Iax is a M_{Ch} pure deflagration as proposed by [Branch et al. \(2004, 2006\)](#) for SN 2002cx and [Chornock et al. \(2006\)](#) and [Phillips et al. \(2007\)](#) for SN 2005hk. Recently, deflagrations in hybrid carbon-oxygen-neon (CONE) instead of pure CO WDs have also been considered as progenitors for SNe Iax ([Denissenkov et al. 2015](#); [Kromer et al. 2015](#); [Bravo et al. 2016](#)). This scenario naturally accounts for many characteristics of SNe Iax. Most notably, the simulations of these explosions do not eject enough ^{56}Ni to reach the absolute magnitudes of normal SNe Ia, and, depending on the ignition configuration, do not disrupt the whole WD, but leave behind a bound remnant ([Jordan et al. 2012](#); [Kromer et al. 2013](#); [Fink et al. 2014](#)). [Foley et al. \(2014\)](#) speculate about the existence of such a bound remnant in SN 2008ha and suggest that it emits a wind preventing the spectra from transitioning to the nebular phase which is one of the most characteristic properties of SN Iax spectra. Moreover, evidence for a bound remnant was also found in the slowly declining late-time light curve of SN 2014dt by [Kawabata et al. \(2018\)](#) and very recently in SN 2019muj ([Kawabata et al. 2021](#)). The latter also employ their analytical, phenomenological light curve model to other SNe Iax and conclude that their late-time light curves are well matched assuming radiating burning products at low velocities. The radiation of gravitationally bound or slowly expanding ^{56}Ni is also suspected to contribute to the light curves and spectra by [Foley et al. \(2016\)](#), [Magee et al. \(2016\)](#), and [Shen & Schwab \(2017\)](#).

These deflagrations lead to photospheric velocities in the observed range below those of normal SNe Ia. The detection of IGEs and IMEs in their spectra at all times and the lack of a second maximum in the NIR light curves (see [Kasen 2006](#)) suggests a rather mixed ejecta structure which is a natural outcome of a turbulent deflagration. However, the assumption of completely mixed ejecta in some bright SNe Iax has been challenged by [Stritzinger et al. \(2015\)](#), [Barna et al. \(2017, 2018\)](#). Therefore, a pulsational delayed detonation ([Höflich & Khokhlov 1996](#)) scenario was proposed for the most energetic SNe Iax ([Stritzinger et al. 2015](#)). However, the need for stratification in the moderately bright SN 2019muj was not found to be very strong for all elements except carbon in the outer layers ([Barna et al. 2021](#)). It should be noted that their approach is only sensitive to velocities between 3600 and $\sim 6500 \text{ km s}^{-1}$. In this

region, their stratified template model does not differ significantly from well mixed deflagration ejecta.

The single degenerate scenario suffers the problem of stripped hydrogen or helium from the companion star: It is expected that the explosion of the WD will remove material from its donor which should be seen in the late-time spectra (Pakmor et al. 2008; Lundqvist et al. 2013; Bauer et al. 2019). Since SNe Iax are less energetic than normal SNe Ia, Liu et al. (2013) and Zeng et al. (2020) argue that the stripped hydrogen or helium might stay below the detection limit. Magee et al. (2019) also look for helium features in SNe Iax and find that their NIR spectra are compatible with only very small amounts of helium and that it is easier to detect in fainter models. Another hint toward the M_{Ch} scenario for SNe Iax is the possible detection of a bright helium-star at the location of SN 2012Z (McCully et al. 2014a) because accretion of helium is a plausible way for a WD to reach M_{Ch} . McCully et al. (2022) present very late time observations of SN 2012Z up to 1425 d after maximum light. They find that the event is still about a factor of two brighter than pre-explosion and attribute this either to the shock-heated companion, a bound remnant (see above), or radioactive decay of long-lived isotopes other than $^{56,57}\text{Co}$. In addition, the recently detected hypervelocity WDs with an unusual composition (Raddi et al. 2019) have also been associated with the bound remnant WD cores found in simulations of M_{Ch} deflagrations. These characteristics make M_{Ch} deflagrations a promising scenario for SNe Iax and motivate a deeper investigation of this model. Moreover, their occurrence in star-forming regions of late type galaxies are in line with a WD accreting helium from its donor star (Lyman et al. 2018).

SNe Ia contribute substantially to cosmic nucleosynthesis (Nomoto et al. 2013; Thielemann et al. 2018) and it is widely accepted that they are required for the production of the neutron-rich element manganese alongside core-collapse supernovae (Seitenzahl et al. 2013; Kobayashi et al. 2006, 2020; Lach et al. 2020). Explosions of M_{Ch} WDs are able to produce super-solar amounts of Mn relative to Fe in their innermost, that is, densest, parts in normal freeze-out from nuclear statistical equilibrium (NSE, see Woosley et al. 1973; Hix & Thielemann 1999; Seitenzahl et al. 2009; Bravo 2019) since the rate of electron captures increases with density (Chamulak et al. 2008; Piro & Bildsten 2008; Brachwitz et al. 2000). Therefore, if SNe Iax originate from deflagrations in M_{Ch} WDs they are promising candidates for the enrichment of the Universe with Mn. Recently, double-detonation models for SNe Ia came into the focus as a production site of Mn, but they can probably not completely replace explosions of M_{Ch} WDs (Lach et al. 2020; Gronow et al. 2021).

Simulations of deflagrations in M_{Ch} CO WDs with a clear relation to SNe Iax have been carried out by Jordan et al. (2012), Long et al. (2014), Kromer et al. (2013, 2015), Fink et al. (2014), and Leung & Nomoto (2020). We summarize the findings and shortcomings of this previous work in more detail in Sect. 2.

As an alternative scenario, SN 2008ha has also been speculated to be a core-collapse SN (Valenti et al. 2009) or even a failed detonation of an ONe WD merging with a CO secondary (Kashyap et al. 2018). Fernández & Metzger (2013) also bring a detonation ignited in a WD-neutron star merger event into play for SNe Iax. While the historic SN Iax remnant SN 1181 is believed to originate from an ONe-CO WD merger (Oskinova et al. 2020; Ritter et al. 2021) the SN remnant Sgr A East has recently been associated with a failed deflagration producing a SN Iax (Zhou et al. 2021). Hence, the question whether

it is possible to explain the entire class of SNe Iax in the framework of the pure deflagration in a M_{Ch} WD model remains.

To address this question, we present an extensive set of three-dimensional (3D) full-star simulations of deflagrations in M_{Ch} CO WDs. Since the most realistic ignition configuration consists of only one spot (Kuhlen et al. 2006; Zingale et al. 2009; Nonaka et al. 2012) we restrict our suite of simulations to single-spot ignition. The location of this ignition spark and the central density are systematically varied to investigate the dependence on these parameters. With this study, we aim to extend the set of deflagration models toward the faintest events of the SNe Iax class and systematically determine expected properties of bound remnants. Furthermore, we aim to explore whether the restriction to a single ignition spark but variation of other parameters can change the general characteristics of pure deflagration models.

The paper is structured as follows: We give a summary of previous deflagration studies in Sect. 2 followed by a short overview of the numerical methods used to simulate the explosion in Sect. 3. Subsequently, we describe our initial models in Sect. 4 and discuss the results of the hydrodynamic simulations in Sect. 5. The outcome of the radiative transfer (RT) calculations is compared to observations in Sect. 6. Finally, we wrap up our findings and conclusions in Sect. 7.

2. Previous work

In the following we summarize the results of various works concerning the modeling of deflagrations in M_{Ch} WDs in connection to SNe Iax. These results help to understand the open questions and shortcomings of the currently available simulations and also guide the choice of parameters for the study carried out in our work.

2.1. Jordan et al. (2012)

Jordan et al. (2012, hereafter J12) present a set of models of pure deflagrations in CO M_{Ch} WDs. Since their models fail to ignite a delayed detonation and do not unbind the WD, they call these explosions failed-detonation SNe. They carry out two-dimensional (2D) as well as 3D hydrodynamic simulations, but do neither present detailed nucleosynthesis yields nor radiative transport calculations. Their M_{Ch} WD ($1.365 M_{\odot}$, $\rho_c = 2.2 \times 10^9 \text{ g cm}^{-3}$) is ignited in 63 spots of 16 km radius contained inside a sphere of 128 km radius. This sphere is located slightly off-center at distances of 48, 38, 28 and 18 km from the center of the WD. The 2D run, however, uses only four ignition sparks inside a circle with a radius of 64 km displaced by 70 km from the center of the WD.

As mentioned above, the explosion in the WD leaves behind a bound remnant in all of their simulations although 89 to 167% of the initial binding energy E_{bind} are released during the deflagration phase. This shows that the released energy is not necessarily distributed homogeneously and that multidimensional effects need to be taken into account. Their explosions eject between 0.23 and $1.09 M_{\odot}$ of material including 0.07 to $0.34 M_{\odot}$ of IGEs. Unfortunately, values for the production of ^{56}Ni are not given. The ejecta velocities lie below $10\,000 \text{ km s}^{-1}$ and they find an asymmetric ejecta structure characterized by a surplus of burning products at the ignition side and CO fuel in the opposite direction. These features lead them to the conclusion that their models might be candidates for SNe Iax, at least for the bright SN 2002cx-like members of this subclass. However, a

comparison of synthetic observables to observations is not part of this study.

Another interesting aspect investigated by J12 is the kick velocity v_{kick} of the bound remnant. Since the explosion proceeds asymmetrically the bound core receives a kickback between 119 and 549 km s⁻¹ which might be enough to unbind the remnant from the binary system. Together with its composition enriched by burning products such a puffed-up WD is a possible explanation for peculiar iron-rich WDs (see e.g., [Provencal et al. 1998](#); [Catalan et al. 2008](#) and for more recent works [Vennes et al. 2017](#); [Raddi et al. 2018a,b, 2019](#); [Neunteufel 2020](#)).

2.2. Long et al. (2014)

[Long et al. \(2014, hereafter L14\)](#) present a follow-up study of the work by J12. They utilize the same progenitor model, but also specify that they employ zero metallicity, a C/O ratio of 1 (i.e., 50% C and 50% O), and a constant temperature of $T = 3 \times 10^7$ K. The only free parameter is the ignition geometry. It consists again of bubbles of 16 km radius. These are confined to spheres of radius 128, 256 and 384 km located at the center of the WD. In addition, the total number of ignition sparks is varied between 63 and 3500. They carry out six 3D full-star simulations including a postprocessing step and one-dimensional (1D) RT calculations yielding synthetic light curves.

Although the total energy E_{tot} (sum of gravitational energy E_{grav} , kinetic energy E_{kin} and internal energy E_{I}) is positive in all their models we cannot judge whether the whole WD is unbound since it is not specified in the paper. They arrive at ⁵⁶Ni masses $M(^{56}\text{Ni})$ between 0.135 and 0.288 M_{\odot} , nuclear energies E_{nuc} between 6.78 and 9.60×10^{50} erg, and kinetic energies of the ejecta $E_{\text{kin,ej}}$ between 2.44 and 5.01×10^{50} erg. The main finding is that the initial spatial density of the ignition sparks as well as the outer radius of the confining sphere determine the outcome of the simulation. As a first effect, a dense distribution leads to a high burning rate in the early phase of the flame propagation. Subsequently, the bubbles merge very rapidly, and, thus, the flame surface decreases leading to a reduction in the burning rate. Second, the gravitational acceleration, and, therefore, the buoyant force increases with radius. This causes a rapid increase in the energy production for large ignition radii but also an earlier quenching of the flame as the deflagration reaches the outer part of the WD. There is most probably an optimal choice for the number of ignition sparks per volume and the maximum ignition radius in terms of $M(^{56}\text{Ni})$. The approximate number and spatial density of ignition kernels has already been estimated by [Röpke et al. \(2006a\)](#). In the study of L14 a modest number of bubbles (128) confined to a 128 km sphere yields the highest mass of ⁵⁶Ni while very many sparks (3500) inside a 384 km sphere set the lower limit.

Finally, an examination of the synthetic light curves shows that models ignited with ~ 100 kernels show more similarities to SNe Iax than vigorously ignited models with ~ 1000 sparks. However, also in this study only the luminosities of bright SNe Iax are reached.

2.3. Fink et al. (2014)

The work of [Fink et al. \(2014, hereafter F14\)](#) was developed simultaneously to the study of L14. They conduct 14 3D full-star simulations of pure deflagrations in M_{Ch} CO WDs studying mainly the impact of the ignition geometry. In detail, they vary the number N of ignition kernels from 1 to 1600, and,

for two models ($N = 300$ 1600), they also set up a denser distribution of the bubbles. Their initial WD has a central density of 2.9×10^9 g cm⁻³, a constant temperature of 5×10^5 K, and mass fractions of $X(^{12}\text{C}) = 0.475$, $X(^{16}\text{O}) = 0.50$ and $X(^{22}\text{Ne}) = 0.025$ to account for solar metallicity. Moreover, one model ($N = 100$) has also been calculated at central densities of 1.0×10^9 g cm⁻³ and 5.5×10^9 g cm⁻³.

Concerning the nuclear energy release and the production of ⁵⁶Ni F14 arrive at the same conclusion as L14 stating that models ignited in many, densely located sparks lead to less powerful explosions compared to moderately ignited WDs. The highest amount of ⁵⁶Ni is found in the model with 150 initial kernels. Moreover, the energy production in the high-density model does not differ significantly from their standard model while the low-density simulation leads to noticeable less released nuclear energy. However, the high-density model produces no more ⁵⁶Ni than the low-density run because of the more neutron-rich nucleosynthesis at high densities favoring the production of stable IGEs instead.

In contrast to L14, F14 also explicitly report the existence of bound remnants for models ignited in less than 100 spots. These remnants are enriched with burning products and reach masses up to 1.32 M_{\odot} . In addition, they also calculate their respective kick velocity, but arrive at values an order of magnitude below those presented by J12 ranging between 4.4 and 36 km s⁻¹. They speculate that their use of an approximate monopole solver for the gravitational force might account for the differences.

F14 also present synthetic light curves and spectra resulting from 3D RT simulations concluding that models with less than 20 ignition sparks are compatible with SNe Iax. However, even their faintest explosion ($N = 1$) does not reach the faintest members of the SN Iax class, SN 2008ha and SN 2019gsc. The predicted spectra look very similar without a significant viewing angle dependency. [Kromer et al. \(2013, hereafter K13\)](#) present an in-depth analysis of the explosion ignited in 5 bubbles (Model N5). They compare N5 to SN 2005hk and state that peak luminosity, the colors at maximum and the decline in UBV bands coincide very well. Also the presence of IGEs at all times and the lack of a secondary maximum matches the characteristics of SNe Iax. However, the decline in red bands (RIJH) is significantly too fast and also the B -band rise time is too short to conform with SN 2005hk. One way to achieve a slower decline and keeping the peak luminosity fixed is to increase the ejected mass at constant $M(^{56}\text{Ni})$. In addition, the influence of the bound remnant on the observables was not investigated yet.

2.4. Kromer et al. (2015)

In order to reach the faint end of the SN Iax subclass, [Kromer et al. \(2015, hereafter K15\)](#) carry out a deflagration simulation inside a M_{Ch} hybrid CONe WD. These progenitors had been proposed in the work of [Denissenkov et al. \(2013, 2015\)](#). The initial conditions, that is, density, temperature and ignition condition, were chosen to be similar to N5 of F14. The WD consists of a 0.2 M_{\odot} CO core and a 1.1 M_{\odot} ONe mantle. The burning is assumed to quench as soon as the flame reaches the ONe layer which leads to a very faint explosion ejecting only 0.014 M_{\odot} in total and $3.4 \times 10^{-3} M_{\odot}$ of ⁵⁶Ni. This provides a good fit to the peak luminosity of one of the faintest SN Iax, SN 2008ha. But still the decline (red bands) and rise of the light curve is too fast. Moreover, some line features around maximum cannot be reproduced. These deficiencies also hint toward too little ejected mass. K15 point out that the ⁵⁶Ni enriched bound remnant might also

have an influence on the light curve at late and possibly even early times depending on the structure of the remnant.

Bravo et al. (2016) also investigated the hybrid CONe WD scenario with 1D simulations and varying CO core masses. Their study includes pure detonations and delayed detonation models. They conclude that only delayed detonations resemble bright SNe Iax not reaching intermediate and low-luminosity events.

2.5. Leung & Nomoto (2020)

An extensive deflagration study with reference to SNe Iax was presented by Leung & Nomoto (2020, hereafter L20). They start with M_{Ch} CO and CONe WDs and vary the central density between $0.5 \times 10^9 \text{ g cm}^{-3}$ and $9.0 \times 10^9 \text{ g cm}^{-3}$. Furthermore, they use two different ignition conditions, that is, the c3-ignition by Reinecke et al. (1999a) and a single bubble. Unfortunately, they do not give details on the radius and the location of the ignition spark. Their simulations are conducted in 2D only and the emphasis in their work lies on the nucleosynthesis products and not on optical observables.

They report ^{56}Ni masses between 0.20 and $0.36 M_{\odot}$ and total ejected masses between 0.92 and $1.36 M_{\odot}$. This indicates that these models can only account for the brightest SNe Iax, such as SN 2012Z.

2.6. Summary

In summary, all the deflagration studies above claim to produce models which can account for SNe Iax although not all of them carry out RT simulations and compare to observations. In these cases, the claim originates from the low explosion energies, low ejecta velocities and low masses of ^{56}Ni compared to normal SNe Ia. It is also well known that pure deflagrations do not produce a secondary maximum in infrared bands. Studies including synthetic observables, L14, K13, F14, and K15, corroborate this claim. However, there are some discrepancies regarding the width of the model light curves (see above). Therefore, to explain the decline rate and rise times of SNe Iax and also the diversity among this subclass a much wider exploration of the parameter space is necessary.

Moreover, these modeled events cover a reasonable range in brightness, that is, ejected mass of ^{56}Ni , but they do not account for the full diversity of the class of SNe Iax and show a bias toward bright events while the fainter objects, for instance, SN 2008ha (Foley et al. 2009), SN 2010ae (Stritzinger et al. 2014), and SN 2019gsc (Srivastav et al. 2020; Tomasella et al. 2020) are not reached. One of the major shortcoming of the works mentioned above is their use of the ignition configuration, that is, the location, shape, size and number of the initial ignition kernels, as a free parameter to control the strength of the deflagration. This is in strong contrast to the works of Zingale et al. (2011) and Nonaka et al. (2012) which suggest the ignition in one spark off-center.

3. Numerical methods

For the hydrodynamic simulations we employ the LEAFS code which has already been successfully used for a large number of explosion simulations (e.g., Röpke & Hillebrandt 2005; Röpke et al. 2007; Seitenzahl et al. 2013; Fink et al. 2014, 2018; Ohlmann et al. 2014; Marquardt et al. 2015). It is based on the Prometheus code by Fryxell et al. (1989) that has been extended and adapted by Reinecke et al. (1999a) to simulate

SNe Ia. For solving the reactive Euler equations it takes a finite volume approach using the piecewise parabolic scheme by Colella & Woodward (1984). In order to treat flame fronts as discontinuities, the level-set technique (Osher & Sethian 1988) has been implemented by Reinecke et al. (1999b). Nuclear burning and, therefore, the production of energy at the flame front is taken care of by the appropriate conversion of 5 pseudospecies representing carbon, oxygen, IMEs, IGEs and α -particles (see Ohlmann et al. 2014). To follow the explosion until the expelled material expands homologously, Röpke (2005) implemented two nested expanding grids. The inner grid tracks the flame while the outer one follows the expansion of the star. The most recent developments are the implementation of the Helmholtz equation of state (EoS, Timmes & Arnett 1999) including Coulomb corrections and a fast Fourier transform based gravity solver which solves the full Poisson equation and replaces the monopole solver of previous simulations.

In order to capture the detailed nucleosynthesis, we employ the tracer particle method (Travaglio et al. 2004). Virtual particles are advected passively with the flow and record thermodynamic quantities such as temperature, density, pressure etc. In a postprocessing step the nucleosynthesis results are calculated with the nuclear network code YANN (Pakmor et al. 2012). We employ the 384 species network of Travaglio et al. (2004) based on work by Thielemann et al. (1996), Iwamoto et al. (1999), nuclear reaction rates (version 2009) from the REACLIB database (Rauscher & Thielemann 2000), and weak rates from Langanke & Martínez-Pinedo (2001).

To compare synthetic observables (i.e., light curves and spectra) with data, we carry out RT simulations using the 3D Monte Carlo RT code ARTIS (Sim 2007; Kromer & Sim 2009). ARTIS follows the propagation of γ -ray photons emitted by the radioactive decay of the nucleosynthesis products and deposits energy in the supernova ejecta. It then solves the RT problem self-consistently enforcing the constraint of energy conservation in the co-moving frame. Assuming a photoionization-dominated plasma, the equations of ionization equilibrium are solved together with the thermal balance equation adopting an approximate treatment of excitation. Since a fully general treatment of line formation is implemented, there are no free parameters to adjust. This allows direct comparisons to be made between the synthetic spectra and light curves and observational data. Line of sight dependent spectra are calculated employing the method detailed by Bulla et al. (2015) which utilizes “virtual packets”. This method significantly reduces the Monte-Carlo noise of the viewing angle dependent spectra.

4. Initial setup

We carried out full-star simulations of the explosion of a CO WD on a spatial grid with 528^3 cells in the nested expanding grid approach. This resulted in an initial resolution of 2.06 km per cell in the central part of the star for all initial models and guaranteed that the flame resolution is similar across all models during the early phase of the explosion. We distributed 4 096 000 tracer particles representing equal mass fractions of the material throughout the star. This rather large number was chosen to guarantee a sufficient representation of the ejecta since only a small part of the star is expected to become unbound. The metallicity in the hydrodynamic simulation was only represented by the electron fraction Y_e , which is set to the solar value $Y_e = 0.499334658$ according to the solar composition published by Asplund et al. (2009). In the nucleosynthesis postprocessing step we used the Asplund et al. (2009) values with C, O, and N

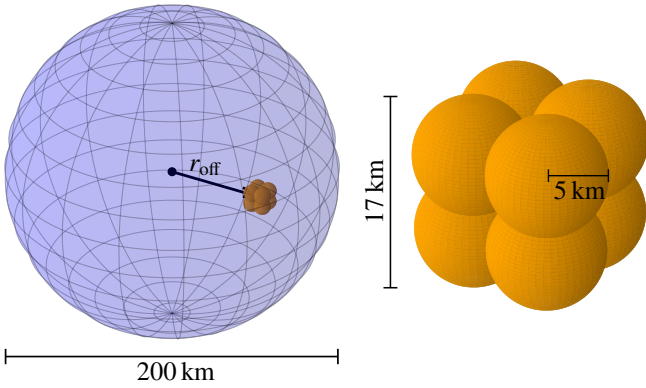


Fig. 1. Sketch of the ignition configuration. The blue sphere only serves to guide the eye. The enlarged figure shows the morphology of the ignition spark.

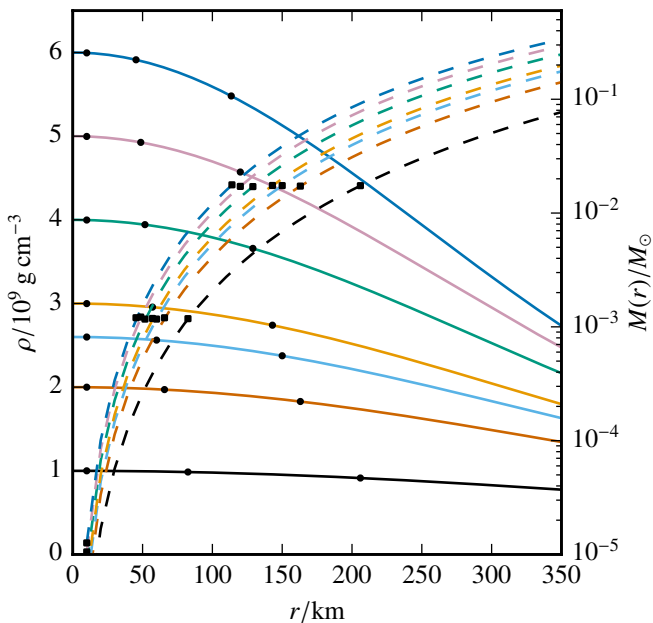


Fig. 2. Initial density profiles (solid lines), cumulative masses (dashed lines) and ignition radii indicated by scatter points. Solid squares depict that models with intermediate to high ignition radii are ignited at same mass coordinate.

isotopes converted to ^{22}Ne and ignoring hydrogen and helium. For subsolar metallicities, we did not simply scale all isotope mass fractions but fix the ratios of some α -elements to measurements in low-metallicity stars (i.e., $[\text{C}/\text{Fe}] = 0.18$, $[\text{O}/\text{Fe}] = 0.47$, $[\text{Mg}/\text{Fe}] = 0.27$, $[\text{Si}/\text{Fe}] = 0.37$, $[\text{S}/\text{Fe}] = 0.35$, $[\text{Ar}/\text{Fe}] = 0.35$, $[\text{Ca}/\text{Fe}] = 0.33$, $[\text{Ti}/\text{Fe}] = 0.23$, Prantzos et al. 2018). This choice reflects the fact that α -elements were overabundant at early times since they are primarily produced in core collapse supernovae. Moreover, all simulations assumed equal amounts of C and O in the WD material if not specified otherwise.

As pointed out in Sect. 1 the most probable ignition configuration is one single spot. Nonaka et al. (2012) find that the ignition is most probable between 40 and 75 km off-center with an upper limit of 100 km. Hence, we restricted this study to single-spot ignitions. To provide some initial perturbations for Rayleigh-Taylor instabilities to develop, the spark consists of 8 bubbles of 5 km radius slightly overlapping (see Fig. 1). This is the smallest reasonable size for the initial bubble considering the

resolution of ~ 2 km per cell. Since the actual ignition (the thermonuclear runaway) takes place on very small length scales (cm) the initial bubble should be chosen to be rather small to capture as much of the flame development as possible. Its actual shape at the beginning of our simulation is, however, an assumption.

Our standard initial model is inspired by the results of simulations of the simmering phase (Zingale et al. 2009). The central density ρ_c is set to $2.6 \times 10^9 \text{ g cm}^{-3}$, the central temperature to $6 \times 10^8 \text{ K}$ with an adiabatic decrease down to $1 \times 10^8 \text{ K}$, and constant afterwards. This temperature profile approximates the conditions during convective carbon burning prior to explosion and is thus better motivated from a physical point of view than the assumption of a cold isothermal WD. The actual effect, however, on the outcome of the simulation is small and should not be overestimated. The deflagration is ignited at an off-center radius of $r_{\text{off}} = 60 \text{ km}$, and, therefore, the model is named r60_d2.6_Z. The model name encodes the most important parameters, that is, the offset-radius in km (r), the central density in 10^9 g cm^{-3} (d), and the metallicity in units of the solar value Z_{\odot} (Z).

In this study, we varied r_{off} between 10 km and 206 km, ρ_c between 1 and $6 \times 10^9 \text{ g cm}^{-3}$ and the metallicity (only for the standard model) between $1 \times 10^{-4} Z_{\odot}$ and $2 Z_{\odot}$. Since the WD is spherically symmetric, the location of the ignition spot can be chosen arbitrarily. We always placed the spark on the positive x -axis with $x = r_{\text{off}}$ and $y, z = 0$. A summary of the suite of models and results for the ejecta, that is, unbound material with $E_{\text{kin}} > E_{\text{grav}}$, can be found in Table A.1. With respect to the r_{off} parameter we distinguish three groups in the set of models: (i) models that were ignited in the inner part of the star, that is, at 10 km. (ii) models in which the ignition is placed at around 60 km (standard model) always at the same mass coordinate, that is, $r_{\text{off}} = 45\text{--}82 \text{ km}$. (iii) models where the ignition kernel is located at around 150 km also always at the same mass coordinate, that is, $r_{\text{off}} = 114\text{--}206 \text{ km}$ (see also Fig. 2).

In addition, we have added two models of rigidly rotating WDs ignited at $r_{\text{off}} = 60 \text{ km}$ with a central density of $2 \times 10^9 \text{ g cm}^{-3}$. The ignition spark is located perpendicular to the rotation axis (z -axis) for the first model, r60_d2.0_Z_rot1 and directly on the rotation axis for the second, Model r60_d2.0_Z_rot2. Due to a more complex setup procedure of the initially rotating WD compared to the standard model the temperature in the rotating WDs is held constant at $5 \times 10^5 \text{ K}$. The rotation velocity is close to break-up velocity ($\Omega = 2.73 \text{ rad s}^{-1}$) increasing the mass of the WD by about $\sim 6\%$ to $1.438 M_{\odot}$. Moreover, we investigate a scenario with a carbon depleted core. In line with Lesaffre et al. (2006) and Ohlmann et al. (2014) the inner carbon mass fraction is reduced to 0.28 and joined smoothly with the outer regions ($X(\text{C}) = 0.5$) at a core mass of $\sim 1 M_{\odot}$. This model is labeled r60_d2.6_Z_c0.28.

5. Hydrodynamic simulations

The one-sided, single-spot ignition deflagration models of this work usually proceed as follows: The burnt fuel inside the hot bubble is lighter than its surroundings, and, thus, is subject to buoyancy. This is the reason why the flame cannot propagate against the density gradient and spreads to only one side of the WD. The deflagration itself is mediated by heat conduction, but the laminar burning speed of the flame is soon surpassed by the buoyant motion of the rising bubble. Subsequently, the burning becomes turbulent due to Rayleigh-Taylor and Kelvin-Helmholtz instabilities further increasing the fuel consumption. As soon as the turbulent flame reaches the outer parts of the WD, and, thus, lower densities, the burning quenches and the ashes

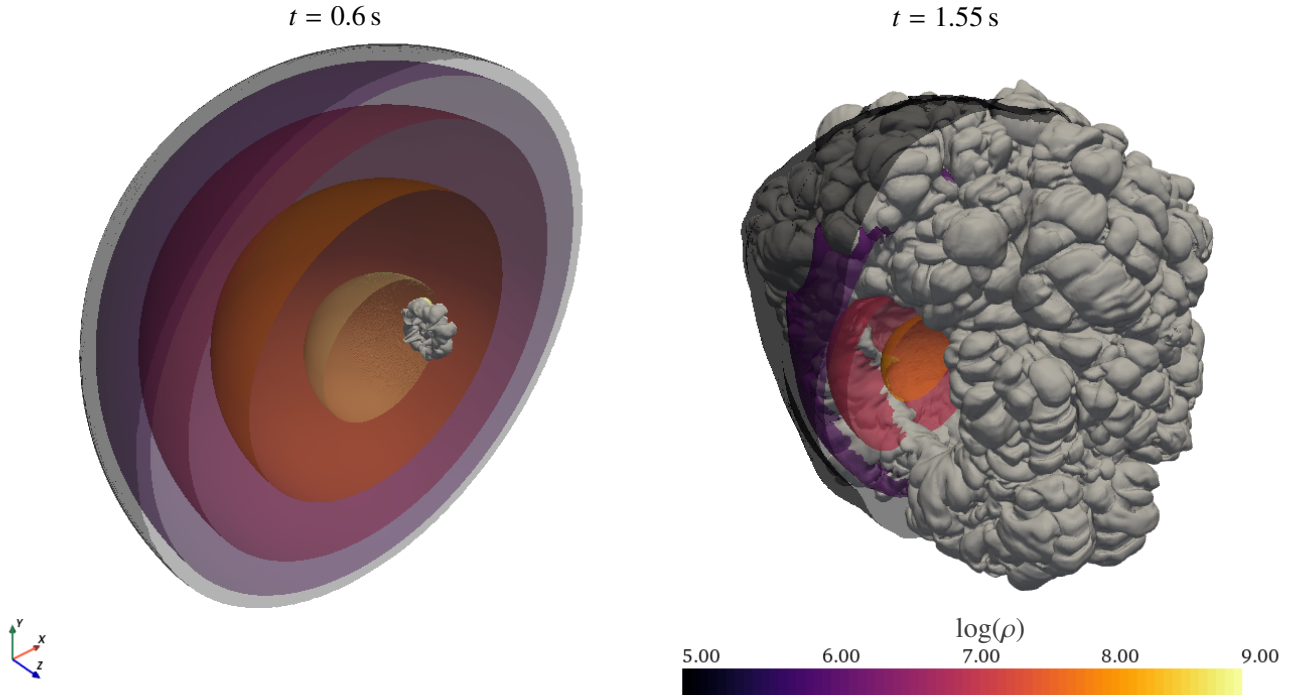


Fig. 3. Flame surface (gray) and isosurfaces of the density at $\rho = 10^5, 10^6, 10^7, 10^8, 10^9 \text{ g cm}^{-3}$ (see colorbar) for Model r60_d2.6_Z. *Left panel:* rising flame at $t = 0.6 \text{ s}$ while *right panel:* flame front when it has almost wrapped around the WD. We want to note, that the illustration is not to scale. In fact the WD has already expanded significantly in the *right panel*.

flow around the star to collide at the far side. This is illustrated in Fig. 3.

The key outcomes of our parameter study are summarized in Table A.1 for ejected material and in Table A.2 for the WD remnant. We find ^{56}Ni masses from 0.0058 to $0.092 M_{\odot}$ and ejected masses between 0.014 and $0.301 M_{\odot}$. It is interesting to note that the lowest as well as the highest ^{56}Ni mass (the mass of ^{56}Ni translates to the luminosity of the event and we therefore refer to bright and faint models when it comes to high or low ^{56}Ni masses, respectively) are found in high-density models. The brightest model is r10_d4.0_Z and the faintest one is Model r114_d6.0_Z. Overall, this suite of models neither reaches the bright members of the SNe Iax subclass (SN 2005hk, SN 2011ay, SN 2012Z, etc.) nor the very faint explosions (SN 2008ha, SN 2010ae, SN 2019gsc). However, the ^{56}Ni yield of our faintest model is only ~ 1.9 times higher than the estimated value of $3 \times 10^{-3} M_{\odot}$ for SN 2008ha (Foley et al. 2009). Furthermore, the brighter models of our sequence (r10_d4.0_Z, r10_d5.0_Z, r10_d6.0_Z) eject more ^{56}Ni than the N3 model of F14 although only one ignition spark has been used. The ^{56}Ni masses in this study and also in previous works are plotted against ejected mass in Fig. 4. Our models cover the low-energy end of the pure deflagration model distribution and show slight overlap with the F14 and J12 studies. Only the hybrid CONE WD model of K15 falls below the faintest model in the current study. Moreover, the new set of models extends the almost one-dimensional sequence in the $M(^{56}\text{Ni})$ – M_{ej} -plane. Despite varying initial conditions, that is, central densities and ignition configurations, and different codes employed, all models follow a linear relation between $M(^{56}\text{Ni})$ and M_{ej} to good approximation. However, it has been pointed out by K13 and K15 that an increase in M_{ej} at a constant value of $M(^{56}\text{Ni})$ is highly desirable to obtain broader light curves as observed in SNe Iax. The ratio of $M(^{56}\text{Ni})$ to M_{ej} is shown in Fig. 5. These values are

comparable to those presented by F14 and show only little scatter. Therefore, it seems unlikely that SNe Iax can be explained by only one scenario taking into account results of the currently available pure deflagration models.

Since the new set of single-spot ignited models only covers the fainter and moderately bright members of the SNe Iax class, we have relaxed the restriction of one ignition spark. We have recalculated Model N5 (5 ignition kernels) from F14 which has been compared to SN 2005hk by K13. The N5 ignition configuration has been combined with the initial condition of our standard model r60_d2.6_Z. We find that also with the updated version of the LEAFS code brighter SNe Iax can be reached. The new version of N5, Model N5_d2.6_Z, yields values of E_{nuc} , $M(^{56}\text{Ni})$, etc. (see Table A.1) slightly below those of the F14 version. This is due to the lower central density of $2.6 \times 10^9 \text{ g cm}^{-3}$ compared to $2.9 \times 10^9 \text{ g cm}^{-3}$ in the older run. The relations discussed above, however, do not change compared to the single-spot ignited models. Interestingly, Model N5_d2.6_Z is the brightest model in the current study with $M(^{56}\text{Ni}) = 0.136 M_{\odot}$ although Model r10_d6.0_Z releases more nuclear energy. The difference originates from the more neutron-rich nucleosynthesis at high densities reducing the amount of ^{56}Ni in relation to stable IGEs (see also Sect. 5.1).

5.1. Dependence on central density

The influence of the central density on the nuclear energy release is twofold: (i) Assuming an identical ignition geometry, more mass is burned initially in the high-density case, and, thus, the energy production is higher in the early phase of the deflagration. (ii) Due to the steeper density gradient the effective gravitational acceleration is larger at high densities, and, thus, the buoyancy force acting on the low-density bubble increases. This speeds up the growth of Rayleigh-Taylor instabilities and also

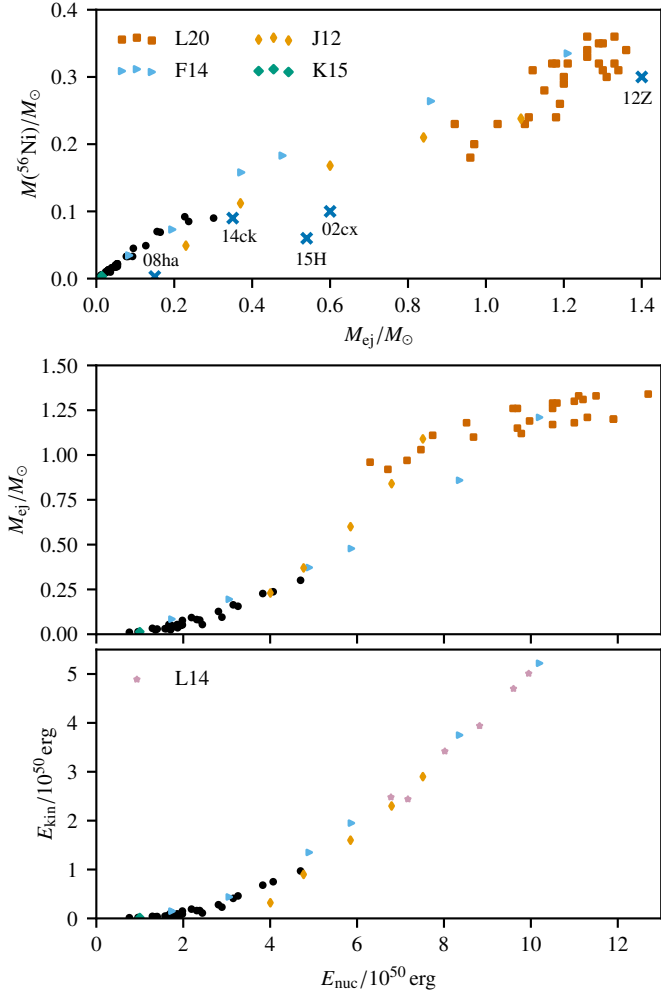


Fig. 4. Ejected ^{56}Ni mass vs. M_{ej} (upper panel), M_{ej} vs. E_{nuc} (middle panel) and $E_{\text{kin,ej}}$ vs. E_{nuc} (lower panel) for this work (black circles) and the works of J12, F14, K15 and L20. L12 only provide yields for IGEs, but not for ^{56}Ni . To provide an approximate value for ^{56}Ni , we multiplied the IGE masses with a factor of 0.7 in agreement with the M_{IGE} to $M(^{56}\text{Ni})$ ratios of L14 who use the same initial model. Measurements for $M(^{56}\text{Ni})$ and M_{ej} for SN 2002cx, 2008ha, 2012Z and were taken from McCully et al. (2014b), and references therein. Values for SN 2015H are from Magee et al. (2016) and for SN 2014ck from Tomasella et al. (2020).

the transition from the laminar burning regime to turbulent burning (see also Röpke & Hillebrandt 2006). Moreover, a rather small effect might stem from the fact that the laminar burning velocity itself is higher for higher densities (Timmes & Woosley 1992). This increase of the burning rate at early times is, however, counteracted by the expansion of the WD. Since the flame is faster at high densities, the WD expands in a shorter period of time and the flame reaches the surface significantly earlier than for low densities. Hence, the burning is quenched earlier and limits the amount of burnt material. This competition between flame propagation and expansion of the WD is of particular importance for the energy release of the models presented in this study.

An increase in the ejected mass of ^{56}Ni , that is, the brightness of the explosion, is also expected for higher densities. Since more material is burnt in total and especially at high densities more IGEs, and therefore also ^{56}Ni , will be produced. The synthesis of ^{56}Ni , however, does not increase linearly with the IGEs because of the neutron-rich environment due to an increasing

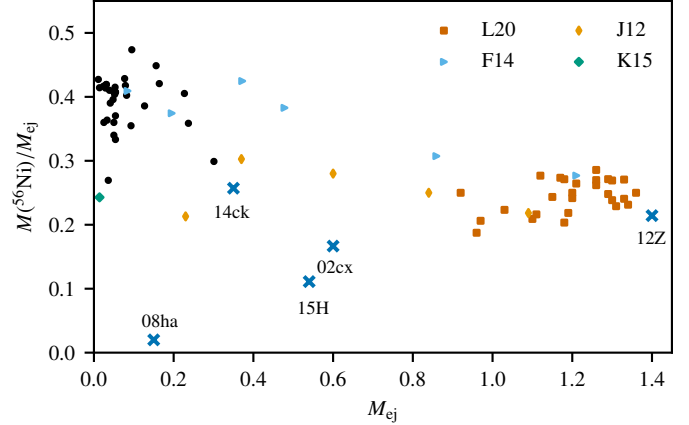


Fig. 5. Ejected mass vs. $M(^{56}\text{Ni})/M_{\text{ej}}$ for this work (black circles) and the works of J12, F14, K15, and L20.

rate of electron captures at high densities. If matter burns to NSE the neutron excess of the most abundant isotope is close to the neutron excess of the burning material, and, thus, the symmetric isotope ^{56}Ni is not favored under these conditions (see Woosley et al. 1973, for instance).

To isolate the influence of the initial central density, we compare models ignited at a fixed radius, that is, the models ignited at $r_{\text{off}} = 10$ km (r10_dXX_Z, see Table A.1). We observe a trend expected from theoretical considerations (see above): The nuclear energy release and the ejected masses increase from low (1×10^9 g cm $^{-3}$) to high (6×10^9 g cm $^{-3}$) central densities at ignition. Moreover, the value of $M(^{56}\text{Ni})$ in models r10_d5.0_Z and r10_d6.0_Z is lower than in Model r10_d4.0_Z although the IGE yields are higher. This is due to higher electron capture rates at high density, and, therefore, more neutron-rich environment. This indicates that Model r10_d4.0_Z is close to the brightest explosion we can produce with a single-bubble ignition (models at higher r_{off} are fainter, see Table A.1). The decreasing trend of $M(^{56}\text{Ni})/M_{\text{IGE}}$ is also present for all other ignition radii (see Table A.1). We find values of $M(^{56}\text{Ni})/M_{\text{IGE}}$ in the ejecta ranging from 0.88 at low central densities to 0.50 at high densities.

In summary, the flame evolves faster with increasing central density, and, thus, the energy released at early times rises. Therefore, the WD also starts to expand significantly earlier for higher central densities. However, the fast burning can always compensate for the expansion in models with fixed ignition radius (10 km) which leads to a monotonic increase of released nuclear energy with increasing central density.

5.2. Dependence on ignition radius

For a fixed central density, we observe the expected, decreasing trend in nuclear energy generation and ejected mass for increasing ignition radii (see Table A.1). This seems rather obvious because there is less mass available to burn for larger radii since the deflagration only propagates outward and not against the density gradient. However, the interplay between the flame velocity and the expansion of the WD (see Sect. 5.1) also is a significant factor here. We find that for all models except those with lowest density, that is, $\rho_c = 1 \times 10^9$ g cm $^{-3}$, the total amount of burnt mass decreases for larger ignition radii. The volume of the flame during the burning phase (until $t \sim 2$ s) is always largest for models ignited at large ignition radii reflecting the faster evolution of the flame due to the higher gravitational acceleration g (the maximum of g is only reached at $r > 400$ km). In contrast,

the total mass burned, and with it the nuclear energy release, is higher for small ignition radii. This reflects that the average density at which material is burned makes up for the smaller volume filled by the flame in the first ~ 2 s. Only in the case of Model r82_d1.0_Z, the increased flame velocity can overcompensate the expansion of the WD and leads to slightly higher nuclear energy release than for Model r10_d1.0_Z.

In the model sequences of intermediate and high ignition radii, that is, 45 to 82 km and 114 to 206 km, respectively, we have eliminated the difference in mass outside the ignition radius by igniting at the same mass coordinate (see also Fig. 2). For the reasons discussed above, the most energetic explosions in the intermediate sequence are those at low central density (r82_d1.0_Z and r65_d2.0_Z). E_{nuc} increases again for the highest central densities ($\rho = 5\text{--}6 \times 10^9 \text{ g cm}^{-3}$). This indicates that the flame speed starts to compensate for the expansion in these models. In the models with large ignition radii the differences almost vanish and the trend in E_{nuc} becomes monotonically decreasing. The lowest amount of ^{56}Ni ($M(^{56}\text{Ni}) = 0.0058 M_{\odot}$), and, therefore, also the faintest explosion results from the model at highest central density and largest ignition radius, that is, Model r114_d6.0_Z. This is still a factor of ~ 1.9 above the $M(^{56}\text{Ni})$ mass inferred from observations of SN 2008ha (Foley et al. 2009), but the trends in this study suggest that such a low value could easily be reached by increasing the ignition radius even further. Moreover, the $M(^{56}\text{Ni})$ to M_{IGE} ratio does not drop off very significantly for increasing densities since a larger part of the inner core is left unburned for a large ignition radius.

We note that for models ejecting very little mass, that is, $M_{\text{ej}} \lesssim 0.08 M_{\odot}$, the data show some scatter destroying monotonic trends. There is, in general, a decrease in $M(^{56}\text{Ni})$ in the model sequence with large ignition radius from Model r206_d1.0_Z to r114_d6.0_Z which is interrupted by an unexpected increase from Model r163_d2.0_Z to r150_d2.6_Z, for instance. We are not able to explain this deviation by any physical properties of the respective explosion model. Instead, we suspect that the real differences between these models are too subtle to be captured by our simulations.

5.3. Dependence on metallicity

The net effect of metallicity is that it introduces a neutron excess (reduction of Y_e) which has several effects on the explosion dynamics. First, the initial WD becomes more compact and lighter with increasing metallicity because the degenerate electron pressure decreases as Y_e decreases. Second, the laminar flame speed is enhanced by the presence of ^{22}Ne which is by far the most abundant species aside from C and O (Chamulak et al. 2007). This is, however, only important during the very early stages of the deflagration before turbulence introduced by Rayleigh-Taylor and Kelvin-Helmholtz instabilities governs the effective flame speed. Third, a neutron-rich environment leads to a decrease in the production of ^{56}Ni in NSE (Timmes et al. 2003) since it favors the synthesis of more tightly bound, neutron-rich nuclei such as $^{57,58}\text{Ni}$. Thus, the energy release is slightly higher for higher metallicity (Townsend et al. 2009). Finally, a reduction of Y_e has only negligible influence on the buoyancy force (Townsend et al. 2009). On average, the effect of metallicity on the explosion dynamics is rather small. This is supported by Models r60_d2.6_XZ ($X = 10^{-4}, 10^{-3}, 10^{-2}, 10^{-1}, 1, 2$). They can be seen as identical regarding their values for $E_{\text{nuc}}, M_{\text{ej}}, M(^{56}\text{Ni})$ since no real trend is visible in the data.

A decrease in $M(^{56}\text{Ni})$ is expected for low metallicities which might again help in reducing the $M(^{56}\text{Ni})$ to M_{ej} ratio. This trend, however, is too subtle to be observed in this study and the small scatter is more likely to originate from numerical inaccuracies. The value of Y_e in the high density regime of M_{Ch} explosions, in addition, is dominated by the effect of electron captures during the explosion whereas in sub- M_{Ch} models the initial metallicity is basically the only parameter determining the neutron excess. Nevertheless, the nucleosynthesis yields are expected to differ for varying metallicity. A detailed investigation of nucleosynthetic postprocessing data, however, is not the focus of this work. The nucleosynthesis yields of Model r60_d2.6_Z are included and analyzed in the work of Lach et al. (2020) labeled as Model R60. The model does produce a value of $[\text{Mn}/\text{Fe}] = 0.11$, and, thus, these explosions might play a role in the enrichment of the Universe with Mn in addition to helium shell detonations (Lach et al. 2020; Gronow et al. 2021) and various types of core collapse supernovae. The role of the latter is not a settled issue yet (compare the GCE studies of Prantzos et al. 2018; Kobayashi et al. 2020, for instance). The nucleosynthesis results of our parameter study will be published on HESMA (Kromer et al. 2017) for further use in GCE studies.

5.4. Rotating models

In the single degenerate scenario of SNe Ia the WD is not only expected to accrete mass from its donor star but also angular momentum (spin-up). This further stabilizes the WD against gravity and total masses highly exceeding M_{Ch} are possible (Yoon & Langer 2005). At some point, the material available for accretion might be exhausted and the accretion processes slows down or stops completely and a period of loss of angular momentum ensues (spin-down). During this spin-down the critical mass M_{crit} of the WD decreases and a deflagration might be ignited as soon as it is exceeded by the WD mass. A rigidly rotating WD serves as a lower limit for M_{crit} . This spin-up/spin-down scenario was proposed by Di Stefano et al. (2011).

Based on the work of Pfannes et al. (2010), we expect minor differences between the rigidly rotating models and the non-rotating model. On the one hand, more mass is available for burning ($\sim 6\%$) in the rotating case which can lead to a higher nuclear energy release. On the other hand, the rotating WD progenitor is more tightly bound making it harder to eject material. Moreover, due to the shallower density gradient the relative fraction of IGEs compared to the total mass of the burning products decreases with increasing rotation velocity. These effects are even more prominent for fast, differentially rotating WDs (see also Fink et al. 2018). In addition, the propagation of the deflagration front is influenced by rotation. Since buoyancy is stronger parallel to the rotation axis due to the steeper density gradient and the flow vertical to the latter is suppressed because the material needs to gain angular momentum, the flame preferentially rises toward the poles. Therefore, the ignition conditions in this study have a large influence on the explosion compared to centrally distributed, multiple ignition sparks.

We compare the rotating models (Model r60_d2.0_Z_rot1 and r60_d2.0_Z_rot2) to Model r65_d2.0_Z. The minor difference in r_{off} is not expected to obscure the differences originating from rotation. Table A.1 reveals that the outcome of the explosion indeed depends on the ignition location. The nonrotating model is bracketed by the rotating explosions in terms of $E_{\text{nuc}}, M_{\text{ej}}, M(^{56}\text{Ni}), M_{\text{IGE}}, M_{\text{IME}}$ and $E_{\text{kin,ej}}$. Model r60_d2.0_Z_rot1 yields higher values than Model r60_d2.0_Z_rot2 and is therefore expected to be brighter as well. The reason for this is that

Model r60_d2.0_Z_rot2 is ignited on the rotation axis, and, thus, the flame spreads along this axis very fast and leads to a fast expansion of the star (see the discussion on expansion v.s. flame speed in Sect. 5.2). In Model r60_d2.0_Z_rot1 the deflagration is ignited perpendicular to the rotation axis which prevents burning directly toward the surface by the rotation and propagates toward north and south pole instead. The consequence of this is that the expansion is delayed, more material is burned and the explosion is more vigorous. However, these rigidly rotating models do not introduce any new characteristics in terms of their global properties to the model sequence. This indicates that rigidly rotating WDs as progenitor cannot add any diversity to our models for SNe Iax.

5.5. Carbon-depleted model

Another way to modify the progenitor is to vary its C/O ratio. The C mass fraction in the center of the WD is determined by the initial mass and metallicity of its zero-age main sequence progenitor and is expected to lie below 0.5 (Umeda et al. 1999; Domínguez et al. 2001). The value of $X(\text{C})$ is further reduced during convective carbon burning (simmering phase) while the outer layers accumulated via accretion and subsequent shell burning exhibit $\text{C/O} \sim 1$ (Lesaffre et al. 2006). To investigate the effects of a reduced C mass fraction, we have calculated an explosion, Model r60_d2.6_Z_c0.28, set up with a C-depleted core (see Sect. 4) with a C mass fraction reduced to $X(\text{C}) = 0.28$. The total energy released during the explosion decreases with decreasing $X(\text{C})$ since the nuclear binding energy of O is higher than of C. This also decreases the buoyancy force and leads to a slower propagation of the flame. Therefore, Umeda et al. (1999) claim that higher $X(\text{C})$ leads to brighter SN events and Khokhlov (2000) and Gamezo et al. (2003) find that the burning in C depleted material is delayed. However, Röpke & Hillebrandt (2004) and Röpke et al. (2006b) examine the influence of the C/O ratio in 3D simulations and detect that its effect on the flame propagation is more subtle. In detail, the nuclear energy is buffered in α -particles when material is burned to NSE and only released in later stages of the explosion. This temporary storage of energy is enhanced for higher $X(\text{C})$ suppressing the buoyancy, and, thus, the propagation of the flame. Therefore, the C mass fraction does not affect the total production of IGEs significantly.

We corroborate this result with Model r60_d2.6_Z_c0.28 and find approximately the same total amount of IGEs and ^{56}Ni as in the standard model r60_d2.6_Z (see Tables A.1 and A.2) although the nuclear energy released is lower for the C-depleted model. This, however, leads to less ejected mass in Model r60_d2.6_Z_c0.28. In contrast to the vigorously ignited models of Röpke et al. (2006b), the C/O ratio has an influence on the ejecta mass in sparsely ignited models. Since the relations between M_{ej} , E_{nuc} , M_{IGE} and $M(^{56}\text{Ni})$ do not show any deviations from the other models of the sequence (see Fig. 4) the carbon mass fraction is just another way to vary the brightness of the explosion but does not seem to help explaining the trends observed among SNe Iax.

5.6. Bound remnant

All models presented in this work are not energetic enough to unbind the WD completely. They leave behind massive bound remnants. These objects consist of a rather dense CO core and a puffed-up envelope of ashes admixed with CO material. This shell material is settling onto the WD core. If these stars manage to escape the binary system, for instance via a natal kick due

to the asymmetric ignition, they can potentially be observed as chemically peculiar, high-velocity WDs. The first candidate for a SN Iax postgenitor, LP40–365, was observed by Vennes et al. (2017) and studied in more detail by Raddi et al. (2018a,b). Moreover, two more possible remnants of thermonuclear supernovae were discussed by Raddi et al. (2019). Although there are hints that these stars might be the product of a failed deflagration their origin is not completely established yet. Therefore, it is necessary to further investigate the long-term evolution of the bound remnant beyond 1D models (see Shen & Schwab 2017; Zhang et al. 2019) and also to obtain more detailed observations of such objects to shed light on their origin. Finally, a sound understanding of the structure and composition of the envelope is of vital importance since it may contribute to the light of the actual SN event (Kromer et al. 2013, 2015) and solve the problem of the fast decreasing light curve in current deflagration models. The 1D study of Shen & Schwab (2017) on this problem shows that a post-SN wind driven by the delayed decay of ^{56}Ni in the envelope of the remnant contributes to the late-time bolometric light curve of the postgenitor. This contribution is in rough agreement with observed late-time light curves of SNe Iax.

Since the LEAFS code uses an expanding grid to track the ejecta the dense core is not very well resolved at the end of the simulations. Therefore, we can only provide some basic properties of the bound core directly after the explosion at $t = 100$ s (see Table A.2). First, all our models leave behind massive remnants in the mass range of $1.09\text{--}1.38 M_{\odot}$. These consist of a dense CO core ($\rho \gtrsim 10^5 \text{ g cm}^{-3}$) with a diameter of $\sim 4 \times 10^9$ cm and a large envelope polluted with burning products, that is, IGEs and IMEs (see Fig. 6). Unfortunately, we do not have postprocessing data for the remnant, and, hence cannot provide detailed nucleosynthesis results. From the hydrodynamic simulation we infer a mass fraction of $0.78\text{--}3.0\%$ of IMEs and $4.2\text{--}10.1\%$ of IGEs including $3.0\text{--}8.7\%$ of ^{56}Ni in the bound remnant. The amount of IGEs left inside the remnant is always larger than the amount of ejected IGEs except for the five most energetic explosion models. Moreover, the settling material is not well mixed showing alternating plumes of ash and fuel (see Fig. 6). The most noticeable feature is the prominent, cone-shaped region of unburned fuel at the left-hand side, that is, negative x -direction. This is exactly the opposite side of the ignition spark location and thus was not reached by the deflagration.

If we expect these peculiar WDs to be observed as single hyper-velocity runaway stars they need to escape the binary system via a natal kick, for example. While F14 report a maximum kick velocity of only 36 km s^{-1} J12 find velocities of up to 549 km s^{-1} , which is sufficient to unbind the WD from its binary system. One possible explanation for this discrepancy was the monopole gravity solver employed by F14 which does not capture the full geometry of these asymmetric explosions. Here, we use an updated version of the LEAFS code accounting for self-gravity with an FFT gravity solver (see Sect. 3). We find kick velocities v_{kick} , that is, the center of mass velocity of bound material, from 6.4 to 370 km s^{-1} . Interestingly, v_{kick} does not simply scale with explosion strength but is highest for low energetic models, decreases to around zero for intermediate ones and increases again for the most vigorous explosions (see Table A.2). Table A.2 also shows the kick velocity in x -direction v_x . Since the flame is located off-center (positive x -direction in Fig. 6) and propagates outward, the WD is expected to receive a recoil momentum in the opposite direction, that is, the negative x -direction. This holds true for the most energetic explosions. The reason why the direction of the kick changes from negative to positive x -direction is hidden in the dynamical evolution

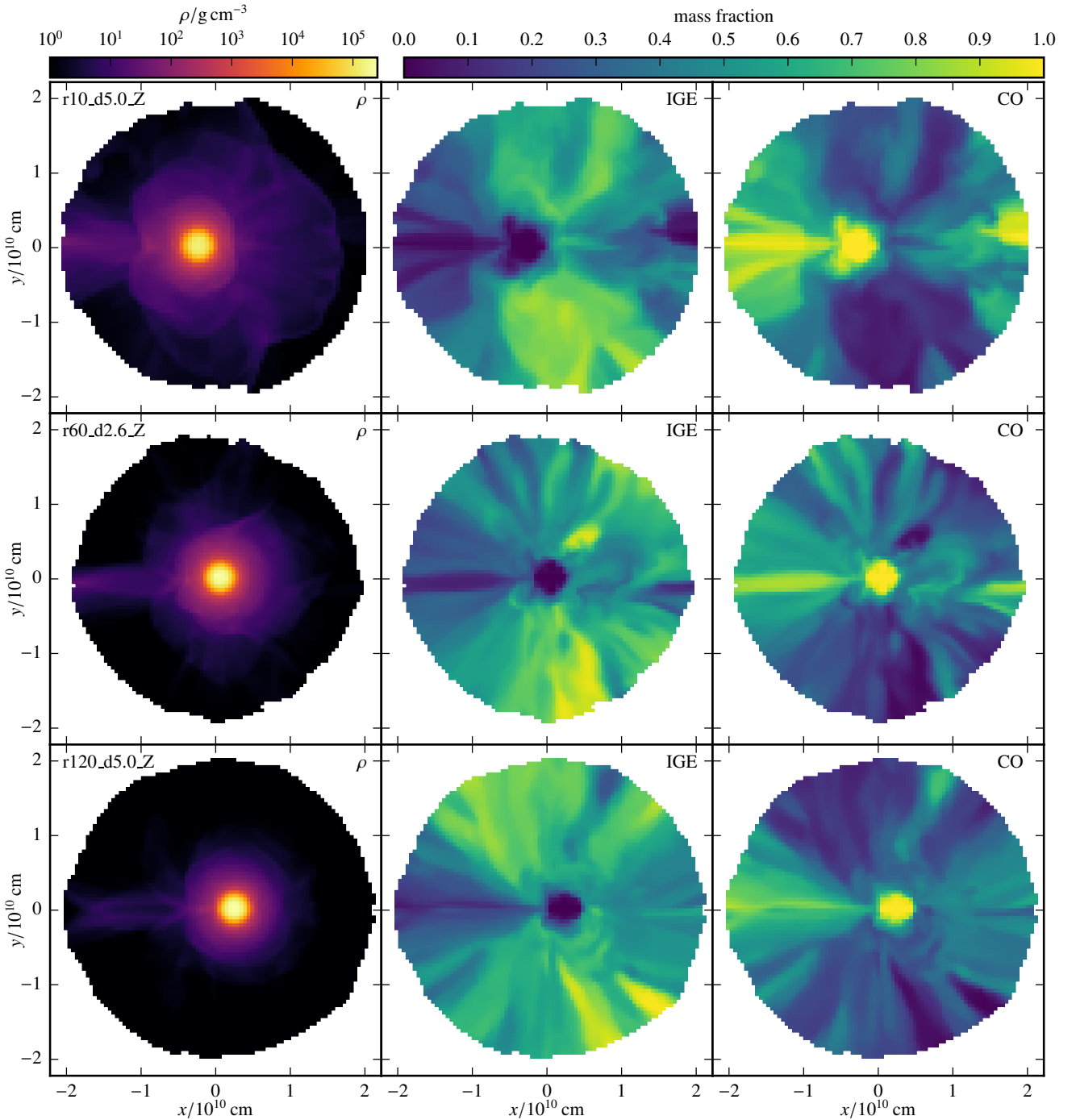


Fig. 6. Slices (x - y -plane) of density, IGE and CO mass fraction in the bound remnant for the bright model r10_5.0_Z (*upper row*) the moderately bright model r60_d2.6_Z (*middle row*) and the faint model r120_d5.0_Z (*lower row*).

of these kinds of explosions. In general, the one-sided ignition causes the flame to propagate to one direction only since a deflagration cannot proceed against the density gradient. In this case, the flame propagates to the right-hand side (positive x -direction, compare Figs. 6 and 7) until it reaches the surface of the WD and quenches. It then wraps around the star, the ashes eventually collide at the opposite side, and a strong flow is driven toward the inner regions. This flow then counteracts the initial momentum transferred by the flame propagation. The more vigorous the explosion the faster is the expansion of the WD and thus the ashes hardly collide at the far side of the star for our most energetic models. Therefore, the WD is pushed to the

left (negative x -direction). For decreasing deflagrations strengths the momentum injected by the initial flame propagation drops and the star expands more slowly. Thus, the clash of the ashes at the antipode, and, subsequently, the inward flow of material becomes stronger until both effects balance each other and lead to almost zero kick velocity (intermediate models). In the case of our weaker explosions, the kick caused by the collision of the ashes dominates and leads to a push to the right-hand side (positive x -direction). The very faintest model in our parameter study, Model r114_d6.0_Z, breaks this trend and shows again a low kick velocity in the negative x -direction. Here, the total amount of mass brought to the surface by the deflagration has

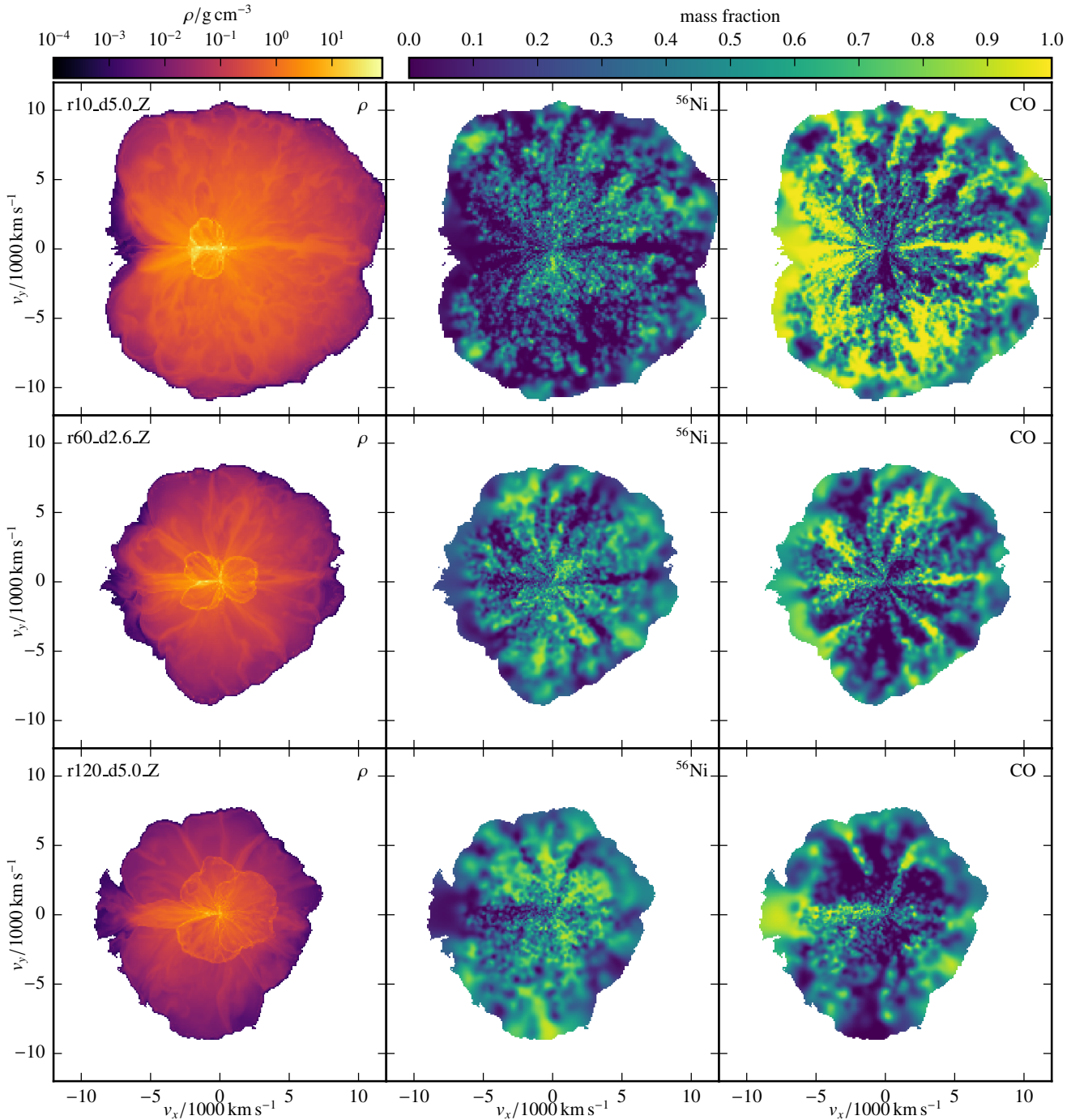


Fig. 7. Ejected material mapped to a velocity grid to serve as initial model for the RT. Shown are slices (x - y -plane) of density, ^{56}Ni and CO mass fraction for the bright model r10_d5.0_Z (*upper row*) the moderately bright model r60_d2.6_Z (*middle row*) and the faint model r120_d5.0_Z (*lower row*).

become too low to impact the momentum of the remnant. This shows that the final value of v_{kick} strongly depends on the ignition geometry and the explosion strength. Finally, the remnant in Model N5_d2.6_Z receives a kick of 264.6 km s^{-1} which is significantly higher than 5.4 km s^{-1} reported by F14 employing a monopole gravity solver. This shows that the new solver has a large impact on the dynamics of these asymmetric explosion simulations.

We emphasize that there is a large scatter in the values of v_{kick} . The very coarse treatment of the inner parts of the WD at late times is most probably the reason for this, and, espe-

cially the differences in v_{kick} for the models at different metallicity (r60_d2.6_Xz) lack an explanation since their energy release does not differ significantly. This suggests that the values can vary on the order of $\sim 100 \text{ km s}^{-1}$ and can only serve as a rough estimate. However, the trend in v_x explained above is not affected.

5.7. Ejecta

We have compiled slices through the ejecta of three representative models in Fig. 7 displaying the density, ^{56}Ni mass fraction,

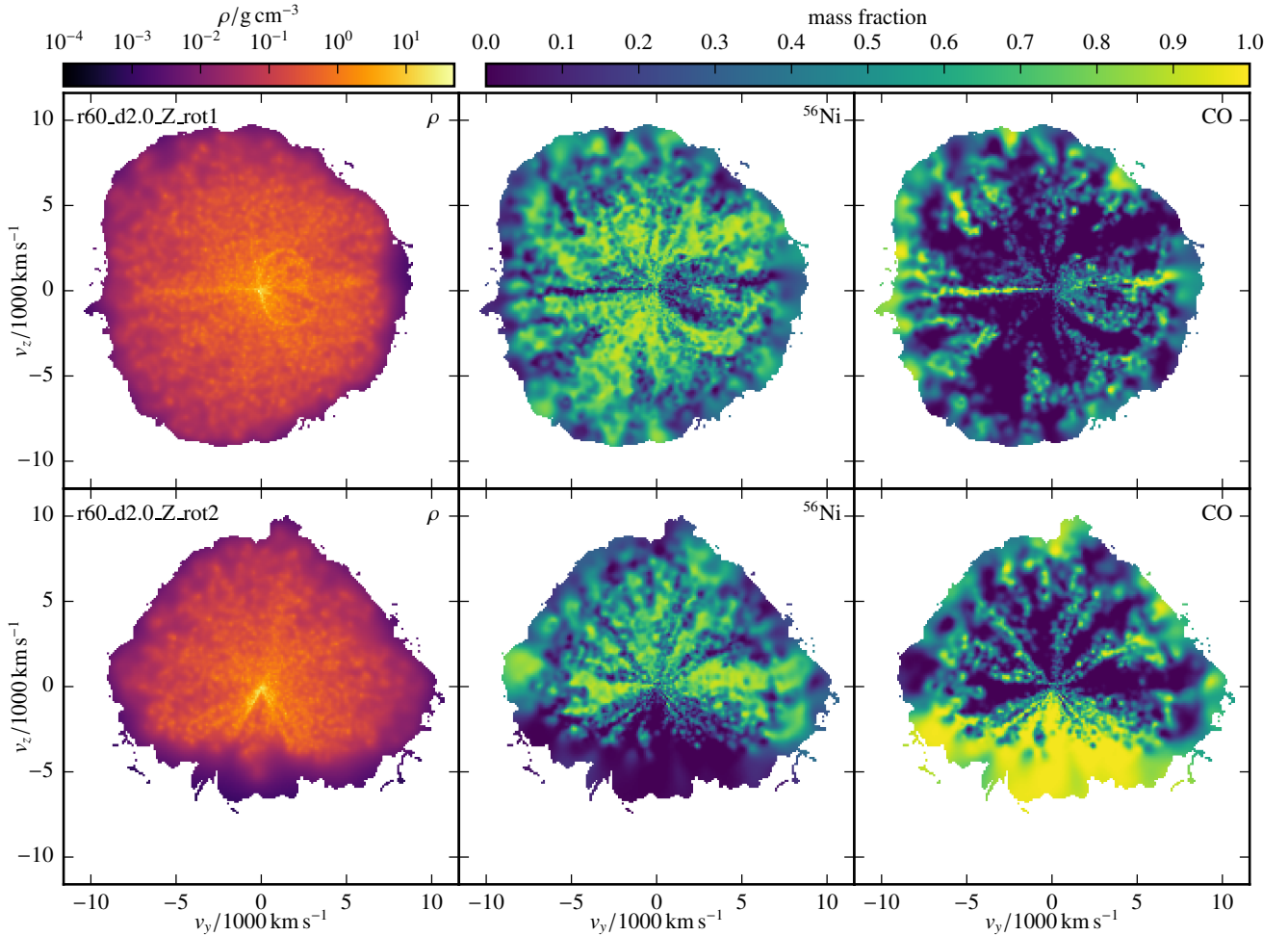


Fig. 8. Same as Fig. 7 (y - z -plane), but for the rotating Models r60_2.0_Z_rot1 (upper row) and r60_d2.0_Z_rot2 (lower row).

and CO mass fraction, respectively. These models include r10_d5.0_Z (bright event, upper row), r60_d2.6_Z (intermediate brightness, middle row) and r120_d5.0_Z (faint event, lower row). Despite the asymmetric ignition, the ejecta in general appear spherically symmetric. Only for the bright model r10_d5.0_Z the material is skewed slightly to the side of the initial ignition (right-hand side in Fig. 7). This is due to the fact that the fast expansion prevents the ashes from wrapping around the core completely (see also Sect. 5.6). Moreover, it is also most apparent in r10_d5.0_Z that the opposite side of the ignition kernel is deficient in ^{56}Ni (also burning products in general) which may introduce some viewing angle dependency in the synthetic spectra and light curves (see Sect. 6.3). This characteristic was also reported by J12. Apart from that, the ejecta are well-mixed (see also Fig. 9) showing a star-shaped pattern created by the Rayleigh-Taylor plumes. The rotating models, in contrast, show a more asymmetric structure (see Fig. 8). The ejecta in Model r60_d2.0_Z_rot1, for instance, are slightly shifted to the negative y -axis (left-hand side in Fig. 8). This is due to the angular momentum barrier (see Sect. 5.4) hindering the flame from sweeping around the WD as easily as in the nonrotating case. Model r60_d2.0_rot2, ignited on the rotation axis, is even more extreme concerning the asymmetry of the ejecta. The flame burns toward the north pole very quickly but is prevented from propagating around the core almost completely making the south pole deficient of burning products. Furthermore, the ejecta only reach velocities of $\sim 6000 \text{ km s}^{-1}$

toward the south pole and $\sim 10\,000 \text{ km s}^{-1}$ at the north pole. This large-scale anisotropy might introduce significant viewing angle dependencies.

To analyze the chemical composition of the ejecta we have compiled 1D average velocity profiles of the three reference models in Fig. 9. They show that the ejecta are mixed in the sense that IGEs, IMEs and unburned CO fuel are present at all velocities. However, we observe a weak decreasing trend for IGEs (including ^{56}Ni) and IMEs toward high velocities and an increase in C and O. At the very edge of the ejecta, IGEs and ^{56}Ni even begin to rise again. However, these trends are not as strong as predicted by Barna et al. (2018) and the increase of IGEs at very high velocities is in strong conflict with their work. Their abundance tomography study yields similar mass fractions for IMEs, IGEs and O in the inner regions but they find that C is virtually absent in the inner region and O dominates at high velocities. This comparison is, however, not too revealing since Barna et al. (2018) investigate the brightest members of the SN Iax subclass (SNe 2011ay, 2012Z, 2005hk, 2002cx) and our models represent faint and moderate members of the class. In a recent study, Barna et al. (2021) focus on the moderately bright SN Iax SN 2019muj (comparable to r10_d1.0_Z, r82_d1.0_Z, r65_d2.0_Z, r45_d6.0_Z in terms of $M(^{56}\text{Ni})$) and find no significant stratification except for carbon. Although their results are uncertain above $\sim 6500 \text{ km s}^{-1}$ due to a sharp drop-off in density, they conclude that C is virtually absent below this value and steeply increases above in agreement with their earlier

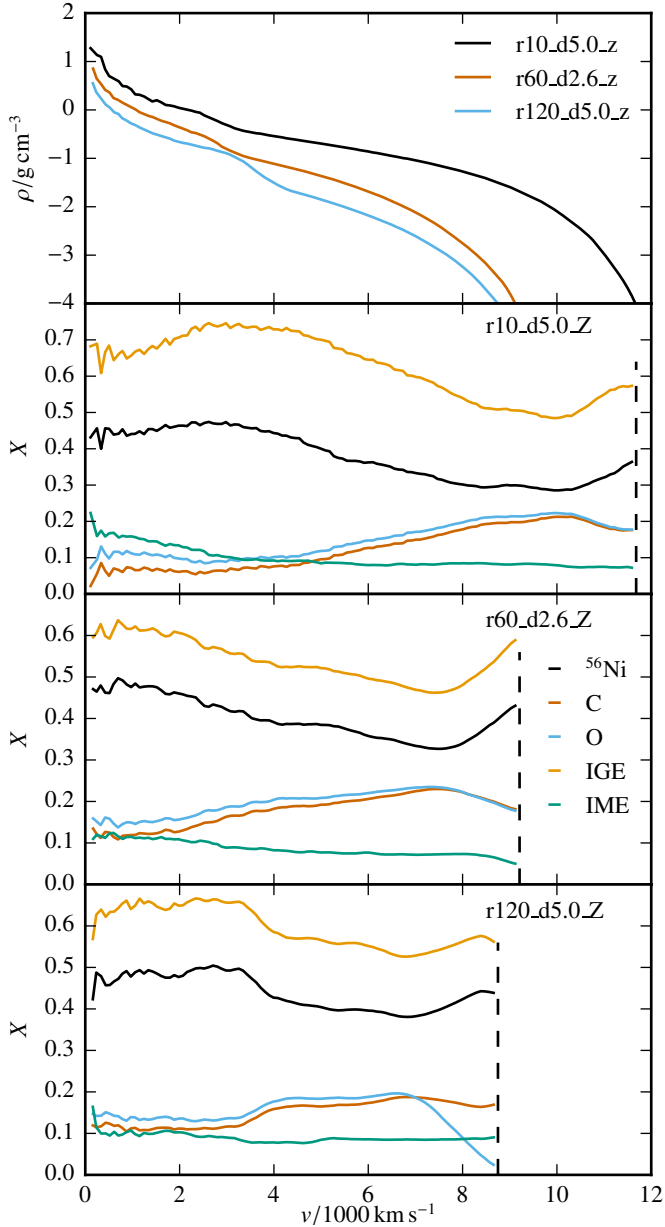


Fig. 9. 1D averaged density profile of the ejecta for Models r10_5.0_Z, r60_2.6_Z, r120_5.0_Z (upper panel). Lower three panels: 1D IGE, ^{56}Ni , IME, C, and O profiles for the respective models. The dashed lines indicate a cutoff at densities below $10^{-4} \text{ g cm}^{-3}$.

work (Barna et al. 2018) and in strong contrast to the models presented here. This conclusion, however, is not really strong since earlier spectra are needed to accurately model the outer layers of the ejecta. Apart from the case of C, a qualitative comparison of Figs. 9–11 in Barna et al. (2021) shows that our abundance profiles are concordant with their abundance tomography models showing a shallow decline of ^{56}Ni and IMEs and an increase in the O mass fraction.

6. Synthetic observables

To determine how the parameters varied in this study impact the synthetic observables, we carried out time-dependent 3D Monte-Carlo RT simulations using the ARTIS code (Sim 2007; Kromer & Sim 2009). Table A.3 lists the models for which RT simulations were carried out along with bolometric band, *BVRI*

Bessel band, and *ugriz* Sloan band light curve parameters. We selected models that cover the range of ^{56}Ni masses produced in the model sequence to explore its full diversity and investigate the impact of the varied parameters. For each RT simulation, 3×10^7 energy packets were tracked through the ejecta for 150 logarithmically spaced time steps between 0.3 and 35 days post explosion. We use the atomic data set described by Gall et al. (2012). A gray approximation is used in cells that are optically thick (cf. Kromer & Sim 2009) and local thermal equilibrium (LTE) is assumed for times earlier than 0.4 days post explosion. Line of sight dependent light curves are calculated for 100 equal solid angle bins.

After the choice of initial conditions we make in the models (e.g., central density, ignition radius, metallicity, rigid rotation), we have a fully self-consistent modeling pipeline. This consists of the hydrodynamic explosion simulations, nucleosynthesis postprocessing step, and, finally, the RT simulations producing synthetic observables. This means we are comparing the predictions of our simulations, given a choice of initial parameters, to measured data. We are not providing any further input parameters (e.g., temperature, luminosity etc.) in order to fit the data and the comparisons we make should be interpreted within this context. Our self consistent pipeline also means it is important to take into account any assumptions made throughout our simulations. Of particular note for these models is the approximate non-LTE treatment of the ionization and excitation conditions in the plasma we adopt for our ARTIS RT simulations (see Kromer & Sim 2009 for more details). The non-LTE treatment of the ionization and excitation conditions in the plasma is an important ingredient in the modeling of SNe Ia (Dessart et al. 2014). No direct comparisons have been made between a M_{Ch} pure deflagration model simulated using approximate non-LTE and full non-LTE treatment in the regime that matches SNe Ia models. It is therefore uncertain how adopting a full non-LTE treatment for our models would change our results. However, previous works employing a full non-LTE treatment of the plasma conditions in models for SNe Ia (e.g., Blondin et al. 2013; Dessart et al. 2014; Shen et al. 2021) indicate that it will have noticeable effects on the synthetic observables produced on scales relevant for detailed comparisons to data. We are currently working on follow-up work in which we will re-simulate a subset of the models from the sequence presented here using the updated version of the ARTIS code developed by Shingles et al. (2020) which implements a full non-LTE treatment of the excitation and ionization conditions in the plasma. The results presented here will help prioritize models for further study.

6.1. Angle-averaged light curves

Our bolometric light curves are shown in Fig. 10. From this, it can be seen that the model light curves show a clear relationship between their bolometric evolution time scales and peak bolometric brightness, that is, the brighter models are slower in rise and decline. This is in agreement with the trend observed in the deflagration study of F14 driven by ^{56}Ni synthesized in the explosion. In addition to this, the trends discussed in Sect. 5 for the choice of initial conditions and varied parameters, that is, ignition radius, central density, and metallicity, are confirmed by the results of the RT simulations: in general for a fixed central density the smaller the ignition radius of the model the brighter and broader its bolometric light curve will be. Additionally, for a fixed ignition radius the higher the central density the brighter and broader the model light curve. These trends, however, are

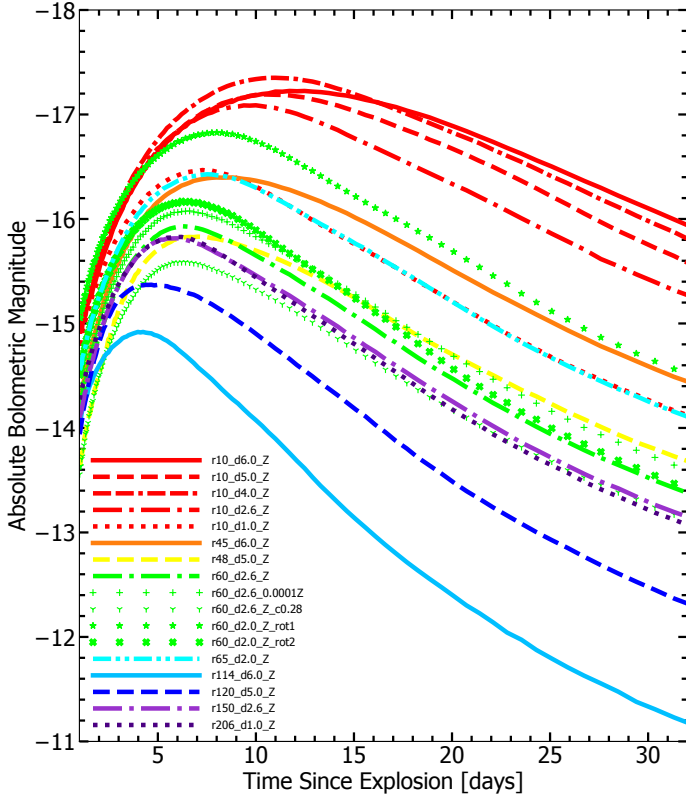


Fig. 10. Angle averaged bolometric light curves for a selection of our models.

not uniform for the whole model sequence and break down for the models with the highest central densities and also for those models which have both high central density and large ignition radius (see Sect. 5 for a more detailed discussion).

Figure 11 shows the *BVRlgr* band light curves for the selected models. Example SNe Iax are included for comparison. We emphasize that while we show observed SNe Iax for comparison here, the primary aim of this section is to comment on the overall light curve properties of the model sequence. In Sect. 6.4 we show a more detailed comparison to an observed SNe Iax. The estimated explosion epochs used for the observed SNe Iax 2005hk, 2012Z, 2019muj, 2008ha, and 2019gsc in Fig. 11 are taken from previous studies, specifically Phillips et al. (2007), Yamanaka et al. (2015), Barna et al. (2021), Valenti et al. (2009), and Srivastav et al. (2020), respectively. We note that this approach of comparing all light curves relative to literature values for explosion date may make the agreement of the model light curves with observed SNe Iax light curves seem relatively poor. However, if we allow the freedom to shift the explosion epochs of the observed SNe Iax later by even ~ 2 days, (which is reasonable on the scale of the uncertainties in the estimated explosion epochs), significantly better agreement can be achieved between model and observed light curves, particularly for intermediate luminosity SNe Iax such as SN 2019muj (see Sect. 6.4 and Fig. 15).

From Fig. 11 it can be seen that the light curves show a similar relationship between their evolution timescales and peak magnitude in all bands as was observed for the bolometric light curves. Some models do show small variations in their band colors. However, these differences are relatively small and have little impact on the overall trends observed for the suite of models. Furthermore, any differences between models are too small

to significantly impact the agreement between the models and observed SNe Iax.

The models show reasonably good agreement between their rise time scales and the data in both red and blue bands, although the red bands do appear to match the rise to peak of observed SNe Iax slightly better. However, the decline post peak of the data is matched much better by the models in the blue bands. The models are significantly too fast in the red bands to compare favorably with the light curve evolution of the data post peak (see also Figs. 14 and 17). This is similar to the trend observed previously in the deflagration study of F14. As noted above, when we move from brighter to fainter models in the sequence the models become faster in both rise and decline. This results in an evolution of the light curves of the fainter models that is significantly too fast to produce good agreement with the faintest members of the SN Iax class such as SN 2008ha and SN 2019gsc.

The choice of initial conditions leads to a variation in the ^{56}Ni mass synthesized in the models and this is the characteristic which overwhelmingly controls the light curve properties of the models in terms of their absolute bolometric and band magnitudes and evolution time scales, regardless of what initial conditions are chosen. However, one parameter which leads to some variation in the light curve evolution is the ^{56}Ni mass to ejecta mass ratio. The model with the lowest value of $M(^{56}\text{Ni})/M_{\text{ej}}$, Model r48_d5.0_Z (see Tables A.1 and A.3, yellow dashed line in Figs. 10 and 11), is slightly slower in both rise and decline in the red bands than models with similar peak absolute band magnitudes (e.g., Model r60_d2.6_Z, green dash-dot line). While this does improve agreement between the model light curve evolution compared to the data in red bands (see *r*-band in Figs. 11 and 17) the red light curves for this model are not slowed down sufficiently to account for the slower light curve evolution of real SNe Iax.

6.2. Angle-averaged spectra

Figure 12 shows spectroscopic comparisons between a selection of models ranging from faintest (r114_d6.0_Z, blue) to brightest (r10_d4.0_Z, red) and three observed SNe Iax which span the diversity in brightness of the SNe Iax class. A variety of epochs from pre-peak to post-peak are chosen such that comparisons between the overall spectroscopic evolution of the model sequence and data can be made. As in Sect. 6.1 we note, that the purpose of this section is not to make detailed comparisons between the spectra of individual observed SNe Iax and the best agreeing model (see instead Sect. 6.4 for such a detailed comparison). Therefore, again for consistency, all times in Fig. 12 are relative to explosion with the same estimates for explosion epochs used for the data as referenced in Sect. 6.1.

From Fig. 12 we see that the bright and intermediate luminosity models show best spectroscopic agreement with the data in terms of their spectroscopic features for later epochs. The brightest model (r10_d4.0_Z, red) shows good agreement with one of the brighter SNe Iax, that is, SN 2012Z, for the latest epoch shown in terms of its spectroscopic features. In addition, the two intermediate luminosity models (r48_d5.0_Z, orange and r206_d1.0_Z, green) agree well with the intermediate luminosity SN Iax, that is, SN 2019muj, in terms of their spectroscopic features for all but the earliest epoch shown. However, while the bright and intermediate luminosity models match the slope and overall flux profile of observed SNe Iax spectra well at earlier epochs (at later times the flux agreement is poorer due

¹ <https://wiserep.weizmann.ac.il>

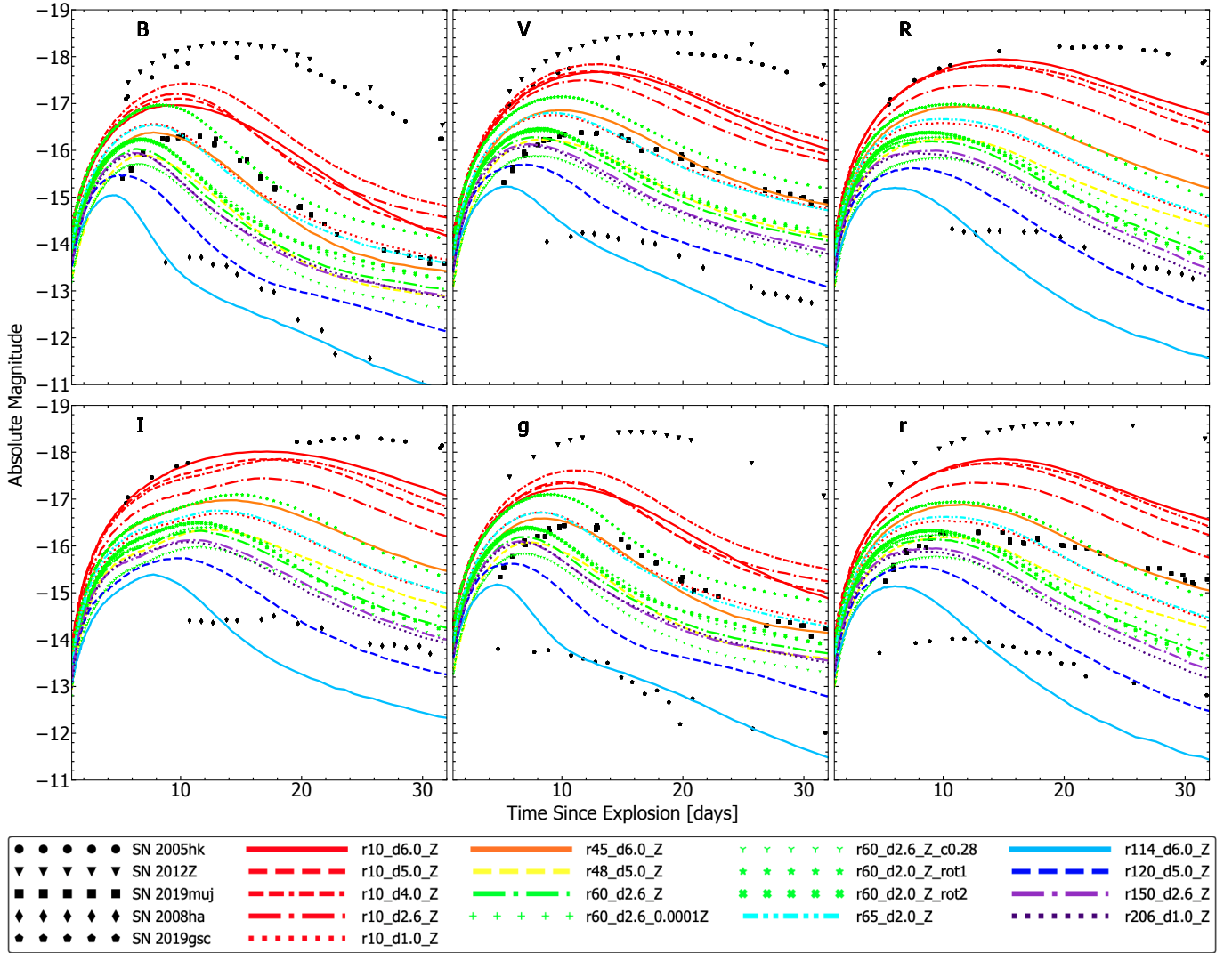


Fig. 11. Angle averaged *BVRIgr* band light curves for selected models. Observed light curves of the SNe Iax SN 2005hk (Phillips et al. 2007), SN 2012Z (Stritzinger et al. 2015), SN 2019muj (Barna et al. 2021), SN 2008ha (Foley et al. 2009) and SN 2019gsc (Srivastav et al. 2020; Tomasella et al. 2020) are included for comparison.

to the model light curves evolving faster than the observed light curves), the synthetic spectra show too many distinct spectral features compared to the data at earlier times (6, 8, and 12 days after explosion for SN 2012Z and 6 days after explosion for SN 2019muj).

The faintest model (r114_d6.0_Z, blue) shows poor spectroscopic agreement with the faint SN Iax, SN 2019gsc. This model has spectra that have significantly too many spectral features compared to the data at all epochs. Therefore, the fainter models provide a much poorer match to the spectroscopic evolution of the data than the bright and intermediate luminosity models. From Fig. 12 it is also clear that Model r114_d6.0_Z is noticeably spectroscopically different to all the other models. This model has significantly more absorption in the blue region of the spectrum and more emission in the red wavelengths compared to the rest of the models which are more typical of the models in the sequence. This difference observed for Model r114_d6.0_Z is due to greater absorption by singly ionized IGEs such as iron, cobalt, nickel, and chromium in the blue region of the spectrum and subsequent re-emission in the red part of the spectrum. Since it is the faintest in the suite of models this characteristic can be attributed to this model having cooler ejecta

which leads to a greater fraction of IGEs being in a lower ionization state.

Overall, we can see that all our models are spectroscopically very similar across all epochs, although the faintest model shows more noticeable differences. Therefore, the spectroscopic differences between models are much smaller than differences between models and data, although spectroscopic agreement between the models and data is reasonably good for bright and intermediate luminosity models particularly at later epochs. However, the poorer spectroscopic agreement at earlier times between models and data, even for the bright and moderate luminosity models shows there is disagreement in the early phase spectroscopic evolution of the models compared to data. This suggests that there are systematic differences in the spectroscopic evolution of the models and data which these simulations do not account for. We also note, that while the brightest model in our sequence does not quite reach the flux level of bright SNe Iax such as SN 2012Z, previous work by K13 and F14 has already shown that pure deflagration models are able to produce reasonable agreement with bright observed SNe Iax (although there are still some spectroscopic systematic differences). To confirm these findings still hold true when using the updated version of the LEAFS code we re-simulated

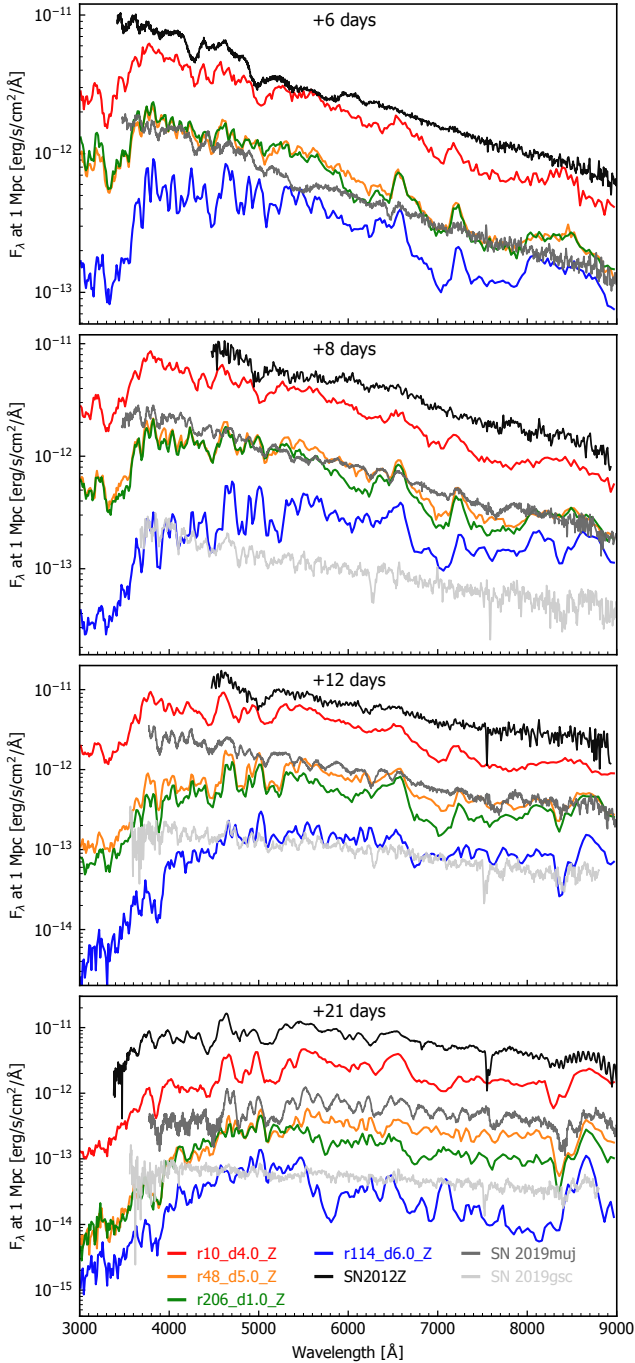


Fig. 12. Spectra over a variety of epochs for selected models which range from the bright to faint end of the model sequence alongside three observed SNe Iax: SN 2012Z (Stritzinger et al. 2015), one of the brighter members of the SN Iax class, SN 2019muj (Barna et al. 2021) which is an intermediate brightness SNe Iax, and SN 2019gsc (Srivastav et al. 2020) which is one of the faintest SNe Iax (see Figs. 13 and 17). The observed spectra shown here were obtained from WISeREP¹ (Yaron & Gal-Yam 2012). All times are relative to explosion and in all cases real flux is plotted on a logarithmic scale. There is no data for SN 2019gsc 6 days after explosion and in the lowest panel the spectra were taken 23 days after explosion for SN 2012Z and SN 2019gsc. All observed spectra are flux calibrated to match the photometry and corrected for distance, red shift and reddening.

the N5def model from K13 and F14 and simulated the RT using ARTIS. The results obtained are consistent with those reported by K13 and F14.

6.3. Viewing-angle dependencies

Figure 13 illustrates the viewing angle dependencies of the bolometric light curve properties (peak absolute bolometric magnitude, bolometric rise time to peak and bolometric decline post peak) for the selection of models for which RT simulations were carried out. In addition, Fig. 14 shows the viewing angle dependencies of *B*-band peak absolute magnitude and rise time for the selected models and includes observed SNe Iax for comparison. As can be seen from Figs. 13 and 14 the models occupy a one-dimensional sequence where the brighter the model the slower its rise to peak and decline post peak (the models of K13 and F14 also lie on this sequence). As discussed in Sect. 6.1 this trend is driven by the ⁵⁶Ni mass synthesized in the models with secondary parameters having little impact on this overall trend. However, there can be variations of up to a magnitude at peak in both the bolometric and band light curves for certain models due to viewing angle effects, as well as significant variation in light curve evolution in both rise and decline. In particular, from Fig. 13 (right panel) we can see that there is a clear correlation between the peak bolometric brightness of the model viewing angles and their rate of decline: the brighter viewing angles have faster declining light curves post peak. An explanation for this is that the brighter viewing angles correspond to those in which there is a higher concentration of ⁵⁶Ni near to the surface of the ejecta. Therefore the radiation due to the decay of this ⁵⁶Ni will have to travel through less material to escape the ejecta leading to a faster evolution post peak.

6.3.1. Viewing-angle dependencies of nonrotating models

The nonrotating model spectra do not show particularly strong viewing angle dependencies. The most noticeable effect is the velocity shifts of spectral lines: spectral features exhibit different blue shifts depending on the direction they are viewed from. The velocity shifts of spectral features can differ by up to $\sim 1000 \text{ km s}^{-1}$. For all models the faint viewing angles have spectral features which are more blue shifted than for the bright viewing angles. Towards the blue wavelengths (less than $\sim 6000 \text{ \AA}$) the bright models show less strong absorption than the faint models which is in better agreement with what is observed in the data (see Fig. 12). However, this effect is still too small to significantly improve the agreement of any of the individual models with the spectra of observed SNe Iax. Conversely, the red wavelengths show only very small differences in their flux when observed from different viewing angles. Variations in flux between different viewing angles can however lead to improved agreement with the overall flux of the spectra of an observed SNe Iax for selected viewing angles.

The nonrotating models also show some viewing angle dependencies in their light curves. Viewing-angles closer to the ignition spark (which is always on the positive *x*-axis for the nonrotating models) tend to be fainter, whereas those viewing angles further from the ignition spark tend to be the brightest. This is the case for all models for which RT simulations were carried out except the two faintest models in the sequence (r114_d6.0_Z and r120_d5.0_Z) which, by contrast, have brighter viewing angles closer to the ignition spark and fainter viewing angles further from the ignition spark. These two models have a noticeably different structure from the other models in the sequence (see r120_d5.0_Z compared to the other models shown in Fig. 7 that have structures more representative of the rest of the models in the sequence).

In general, it is clear that viewing angle effects are modest but noticeable even for well mixed pure deflagration

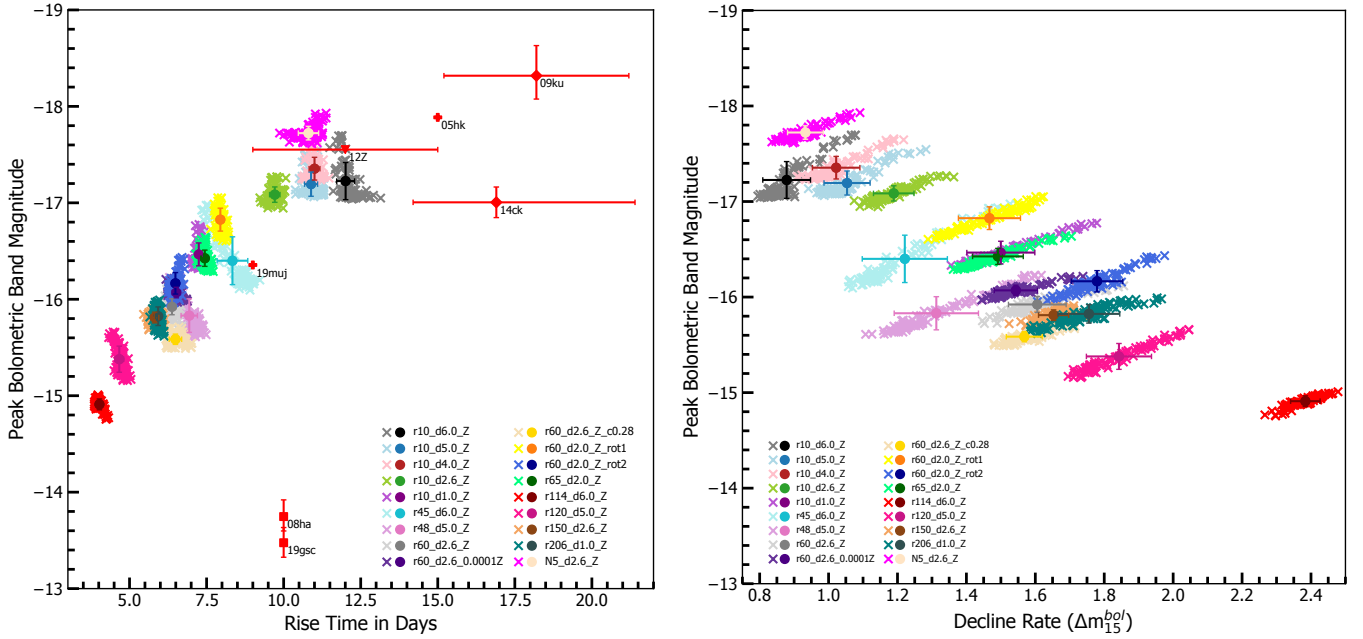


Fig. 13. Viewing angle dependencies of the bolometric light curve properties for selected models. The solid circles represent the angle-averaged values and the crosses represent values from 100 different viewing angles for each model. The error bars depict the standard deviation of the viewing angle distribution for each model. *Left panel:* the peak bolometric-band magnitude is plotted against rise time. Alongside the models, estimates of peak bolometric magnitude and rise times for the observed SNe Iax SN 2019gsc (Srivastav et al. 2020, taking the values calculated for their full blackbody bolometric light curve), SN 2008ha (Foley et al. 2009), SN 2019muj (Barna et al. 2021), SN 2014ck (Tomasella et al. 2016), SN 2012Z (Yamanaka et al. 2015), SN 2005hk (Phillips et al. 2007), and SN 2009ku (Narayan et al. 2011) are included (represented by red markers and labeled by name). The different marker styles representing the SNe Iax of diamond, square, triangle, and plus correspond to SNe Iax where errors were quoted for both rise time and peak bolometric magnitude, only for peak bolometric magnitude, only for rise time and no errors quoted respectively. Where uncertainties were not quoted the uncertainties are still significant, particularly in rise times that can have uncertainties as much as several days. *Right hand panel:* peak bolometric-band magnitude vs. decline rate in terms of $\Delta m_{15}^{\text{bol}}$.

models. These viewing angle effects, while unable to explain all the differences between our models and observed SNe Iax, are relevant on the scale of comparisons between observed SNe Iax and the models. This can clearly be seen from Fig. 14 where the variation of $\Delta m_{15}^{\text{bol}}$ observed for individual models is comparable to the differences in $\Delta m_{15}^{\text{bol}}$ between observed SNe Iax, particularly for the brighter SNe Iax. In addition, the spread of $\Delta m_{15}^{\text{bol}}$ values for the bright models due to viewing angle effects puts certain model viewing angles in better agreement with observed SNe Iax than the angle-averaged values for the models. Finally, we note that neither the models with different metallicity nor the carbon-depleted model show any noticeable differences in their viewing angle dependencies compared to the other models in the sequence.

6.3.2. Viewing-angle dependencies of rigidly rotating models

As discussed in Sect. 5.4 the rigidly rotating models are sensitive to whether the model is ignited perpendicular to the rotation axis (r60_d2.0_Z_rot1) or along the rotation axis (r60_d2.0_Z_rot2). The different choice of the ignition location in the rotational models leads to a variation in their brightnesses and produces a noticeably different ejecta structure for each model (see Fig. 8). The rigidly rotating models exhibit most significant differences with the nonrotating models in their viewing angle dependent spectra. Like the nonrotating models the rigidly rotating models show differences in their spectra depending on what line of sight they are viewed from, with the most noticeable differences in flux being seen in the blue wavelengths. Additionally, as was the case for the nonrotating

models, the rigidly rotating models show spectral features which are more blue shifted for faint viewing angles and less blue shifted for bright viewing angles. However, the rigidly-rotating models show angle dependent differences between the blue shifts of their spectral features of over 2000 km s^{-1} ; double the difference in velocity shifts observed for the spectral features of the nonrotating models. The rigidly rotating models therefore exhibit significantly more asymmetry in their ejecta velocities compared to the nonrotating models. These models do not, however, show larger variations in their viewing angle dependent light curves compared to the nonrotating models.

6.4. Best agreeing model comparisons with SN 2019muj

In this section, we compare the intermediate luminosity SN Iax, SN 2019muj (Barna et al. 2021), with the model from our sequence in best agreement, to allow a more detailed comparisons between the light curves and spectra of one of our models and an observed SNe Iax. We have chosen SN 2019muj as it provides a good brightness match to the intermediate luminosity models in our sequence and also has good quality spectra to compare to (also including earlier epochs). Figure 15 shows the BVr light curves of SN 2019muj and the best agreeing model, r48_d5.0_Z. The angle-averaged as well as light curves for both a faint and bright viewing angle for this model are included. The model light curves are plotted relative to explosion time while we have shifted the band light curves of SN 2019muj such that their explosion epoch occurs 2 days later (MJD 58700) compared to the estimate from Barna et al. (2021) based on early light curve fitting, spectral fitting and bolometric light curve

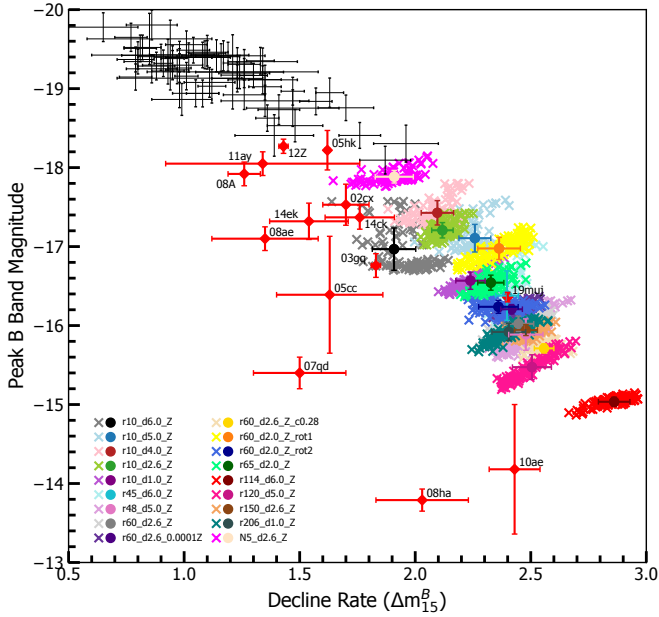


Fig. 14. B -band magnitude vs. Δm_{15}^B plotted in the same way as in Fig. 13. Also included is data compiled by Taubenberger (2017): normal SNe Ia are shown as black crosses and SNe Iax (as in Fig. 13) are labeled by name and represented by red diamonds. Additional SNe Iax have also been added: SN 2014ck, SN 2019muj (see Fig. 13 for references), and SN 2014ek (Li et al. 2018). B -band is chosen as viewing angle effects are easier to identify in the blue bands.

fitting (MJD 58697.5–58698.1). This means the B band peak of SN 2019muj matches the brightest viewing angle shown for Model r48_d5.0_Z (blue). Barna et al. (2021) do not include uncertainties in their estimates of the explosion epoch, however the first ATLAS detection of SN 2019muj is on MJD 58702.5 with only a marginal 1.8σ detection before this on MJD 58700.5. We therefore argue that shifting the explosion epoch 2 days later than what was estimated by Barna et al. (2021) is justified within the uncertainty of the explosion epoch of SN 2019muj. We have flux calibrated the spectra of SN 2019muj to match the photometry and corrected the light curves and spectra of SN 2019muj for redshift, reddening, and distance (taking the values estimated by Barna et al. 2021 of $z = 0.007035$, $E(B-V) = 0.02$, $d = 34.1$ Mpc and using $R_V = 3.1$). As discussed in Sect. 6.1, this model has the lowest value of $M(^{56}\text{Ni})/M_{\text{ej}}$ which results in it being slightly slower to rise and decline in the red bands compared to models with similar peak absolute band magnitudes. This leads to slightly better agreement with SN 2019muj. However, the improvement in agreement for the Model r48_d5.0_Z compared to other models of similar brightness (e.g., Models r10_d1.0_Z, r60_d2.0_Z_rot2, and r45_d6.0_Z) is small and the same conclusions are reached if we compare to one of these models instead.

Figure 15 demonstrates the importance of taking into account the viewing angle dependencies of our models. The brightest viewing angle shown (blue) has band light curves in noticeably better agreement with those of SN 2019muj than both the fainter viewing angle (red) and angle-averaged band light curves (green). Additionally, these brightest viewing angle band light curves are noticeably brighter than both the angle-averaged and faint viewing angle band light curves. This is especially true in B band where it is brighter than the angle averaged light curve by almost half a magnitude and more than this compared to the faint viewing angle shown. From Fig. 15 we see the brightest

viewing angle shown for the r48_d5.0_Z model matches the rise to peak of SN 2019muj very well in all bands. Moreover, this viewing angle matches the decline of SN 2019muj well in all bands until approximately 5 days after B peak. Therefore, until this time, this viewing angle provides a very good match to the colors of SN 2019muj. After this time, the decline of SN 2019muj is matched much better by the model in the B band than the V and particularly r band where the model light curves decline too quickly compared to those of SN 2019muj. As discussed in Sect. 6.1 (see also Sect. 6.5) this is a systematic discrepancy which effects all models in the sequence.

Figure 16 shows spectroscopic comparisons over a variety of epochs between SN 2019muj (black) and the viewing angle for Model r48_d5.0_Z in best agreement with SN 2019muj (blue in Fig. 15). From Fig. 16 we see that the model produces very good agreement in terms of the overall flux and spectral shape compared to SN 2019muj at all epochs apart from the latest epoch shown. For this latest epoch the model is too faint as we move to red wavelengths because the model declines faster than the data in the red bands at later epochs. The model is also able to successfully reproduce a significant proportion of the spectral features observed for SN 2019muj both in terms of their strength and location, although for the earliest epoch shown (4.2 days before B peak) the model does show slightly too many distinct spectral features compared to SN 2019muj (see also discussion in Sect. 6.2). We note that our synthetic spectra produce C features (at 4268, 4746, 6580, and 7234 Å) that are broadly consistent with observations of SN 2019muj (Barna et al. 2021). In particular, unlike the uniform composition model tested by Barna et al. (2021), we do not find the carbon features are significantly too strong at epochs around peak. Overall, from Figs. 15 and 16 it is clear that our models are able to reproduce many of the observed characteristics of the light curves, and, in particular, spectra of intermediate SNe Iax such as SN 2019muj very well, although some systematic differences remain.

6.5. Overall model sequence comparisons to observations

Figure 17 shows peak absolute r -band magnitude with rise time to r -peak (left panel) and decline rate post r -peak (right panel) for our models, models from the F14 and K15 studies as well as observed SNe Iax, and normal SNe Ia for comparison. From Fig. 17 we can see that our models map a significant portion of the wide variety of brightnesses covered by the SNe Iax class. They are, however, unable to reach the luminosities of the very brightest as well as the faintest SNe Iax. The new models extend the 1D sequence previously observed by F14 to more than a magnitude fainter at r -band peak and the new models appear to connect the F14 suite of models to the hybrid CONe models produced in the K15 study as an attempt to reach the faintest members of the Iax class (in particular SN 2008ha).

It is interesting to note that single spark models from our model sequence are very similar to models from the F14 sequence of similar peak brightness both in terms of their light curve evolution (see Figs. 13, 14, and 17 where the N5_d2.6_Z model from the F14 sequence, re-simulated using the newest version of the LEAFS code, is included) and spectra. However, as expected, the single spark models do show greater viewing angle dependencies than the multi-spark models (see Figs. 13 and 14). This suggests that while using a multi-spark ignition is a physically improbable scenario there is relatively little signature of how the models were ignited in the synthetic observables they produce. This also provides some confirmation of the validity of the multipot ignition approach taken by J12,

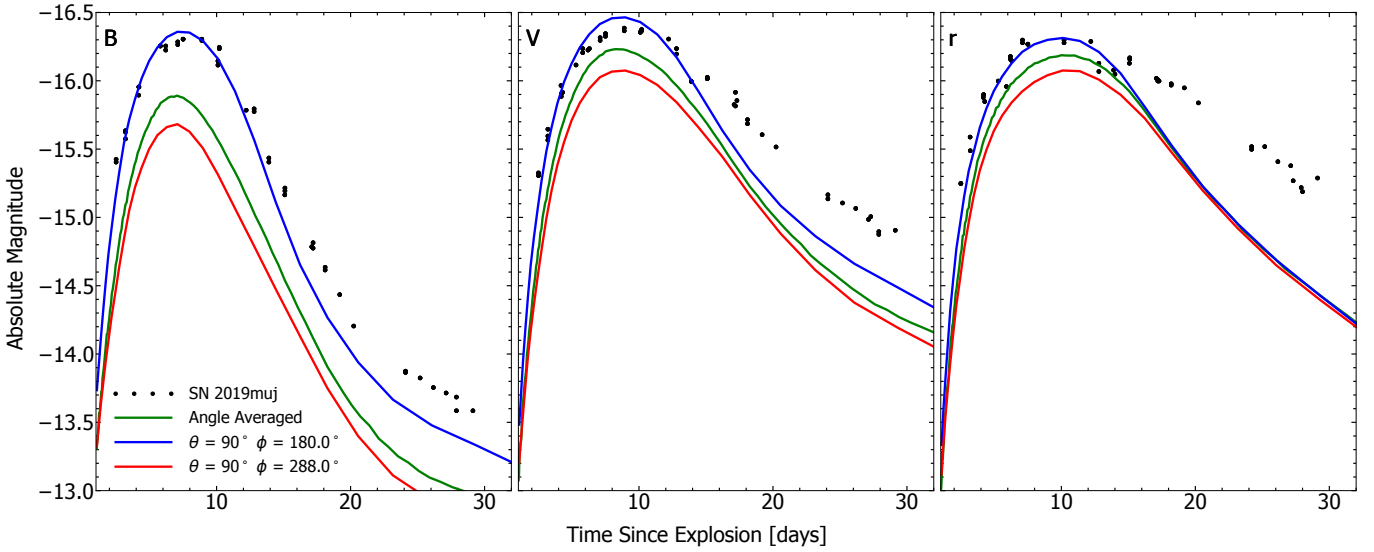


Fig. 15. *BVr* band light curves for Model r48_d5.0_Z (angle-averaged as well as a faint and bright viewing angle) compared with SN 2019muj (Barna et al. 2021). Model r48_d5.0_Z produces the best agreement in terms of its light curve and spectra compared to SN 2019muj. The model light curves are plotted relative to the explosion time predicted by our simulations, whereas the band light curves of SN 2019muj have all been shifted 2 days earlier than the explosion epoch estimated by Barna et al. (2021) such that SN 2019muj matches the brightest viewing angle shown (blue) for the model at B peak. The viewing angle looking along the axis that the ignition spark is placed is $\theta = 90^\circ \phi = 0^\circ$ meaning the fainter viewing angle shown (red) is looking almost along this axis whereas the brighter viewing angle is looking along the axis directly opposite.

L14 and F14 to vary the strength of the deflagration in different models.

The 1D sequence followed by the models of previous works (see Sect. 2) and also our new model sequence is driven by the ^{56}Ni mass synthesized in the explosion. Although the ^{56}Ni mass to M_{ej} ratio may have a small impact (see Sect. 6.1), no secondary parameters appear to have any dramatic impact on the overall behavior of the model sequence. Additionally, further changes to initial setups (such as models with different metallicity, the carbon-depleted model and rigidly rotating models) do not lead to any major break away from the general behavior of the model sequence with these different setups only being a further way in which the ^{56}Ni synthesized in the explosions can be varied.

The sequence occupied by the models means they do not produce good agreement in their light curve evolution time scales, especially in their decline in the red bands (see Fig. 17) where the majority of the flux is observed. The agreement also becomes increasingly poor as we move to the faint models in our sequence because the models become faster in both rise and decline times for decreasing brightness. Faint SNe Iax, on the other hand, do not appear to evolve significantly faster than the brighter members of the SN Iax class (see Figs. 14 and 17). In addition, the model spectra show some systematic differences with observed SNe Iax, especially at early times and as we move to fainter models.

7. Conclusions

In this work we presented an extensive parameter study of 3D explosion simulations of deflagrations in M_{Ch} CO WDs. The aim of this research is to gain insights into the explosion mechanism of SNe Iax, a subluminous subclass of SNe Ia, since the pure deflagration scenario yields results in broad agreement with observations (Long et al. 2014; Fink et al. 2014; Kromer et al. 2013, 2015; Jordan et al. 2012). However, none of the studies carried out to date captures the full range in brightness and

variations in decline rates and rise times, especially for the faint objects among this subclass. Moreover, multispot ignition was used as a tool to vary the explosion strength although the ignition in a single spark seems to be more realistic (Zingale et al. 2009, 2011; Nonaka et al. 2012). Therefore, we restricted the models to single-spot ignition and varied the location of the ignition spark from 10 to 206 km off from the center of the WD. We also employed central densities from 1 to $6 \times 10^9 \text{ g cm}^{-3}$ and metallicities between $1 \times 10^{-4} Z_{\odot}$ and $2 Z_{\odot}$. Finally, two rigidly rotating models and a progenitor with a carbon depleted core were added to the sequence to widen the parameter space and search for additional, physically motivated characteristics of a WD breaking the 1D trends found in previous studies.

We find that the sequence of models covers a large range in bolometric brightness ranging from -14.91 mag to -17.35 mag although the explosion is not controlled via the number of ignition bubbles. This demonstrates that single-spark ignition models can account for a wide range of luminosity as required to match the SN Iax observations. The faintest model is still about one order of magnitude brighter than the faint SN 2008ha and SN 2019gsc. However, a further reduction in brightness, that is, ^{56}Ni mass, is rather easy to achieve by further increasing the ignition radius. On the other hand, it is hard to reach the brightest members of the SN Iax class with the restriction to a single spark ignition. Furthermore, we validate that, regardless of ignition, deflagrations do produce well mixed ejecta apart from some shallow abundance gradients. In addition, we report kick velocities of the bound explosion remnant of up to 369.8 km s^{-1} largely exceeding those reported by Fink et al. (2014). The kick velocity is, however, not a simple function of the deflagration strength. The direction of the natal kick changes by 180° for decreasing energy release leading to a minimum in the absolute value of the kick velocity.

Significant viewing angle effects in rise and decline times as well as variations of up to $\sim 1 \text{ mag}$ in peak brightness further enhance the variations in observational properties. Additionally, both nonrotating and rigidly-rotating models show

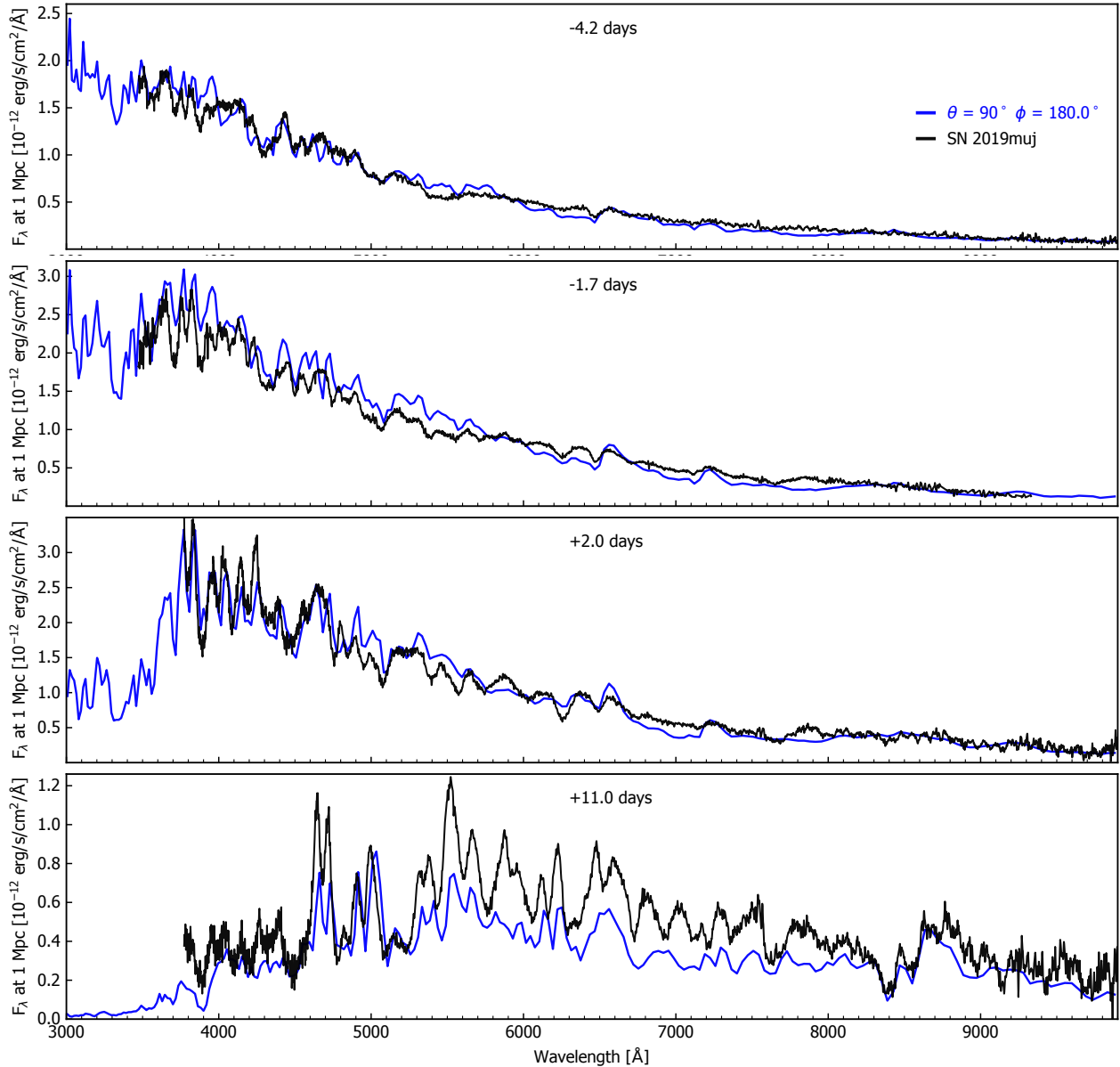


Fig. 16. Spectroscopic comparisons in absolute flux between SN 2019muj and the viewing angle for Model r48_d5.0_Z (blue in Fig. 15). Times are relative to B band maximum.

spectroscopic differences depending on the line of sight with variations in velocity shifts of $\sim 1000 \text{ km s}^{-1}$ and $\sim 2000 \text{ km s}^{-1}$ for the nonrotating and rotating models, respectively. Spectra, rise times and decline rates for the bright models of our sequence are in rough agreement with observations as already found by Fink et al. (2014) and Kromer et al. (2013). The intermediate luminosity models in our sequence also show reasonably good agreement. However, although the model observational properties show a significant diversity introduced by the wide exploration of the parameter space of the initial conditions and viewing angle effects, there are systematic differences between models and data which become increasingly apparent when moving to lower luminosities. For instance, the light curve decline is too fast in the red bands for all models, but as we move to the faint models this worsens and the overall light curve evolution also becomes too fast in all bands. The synthetic spectra of the faint models also show worse agreement across all epochs.

Overall, our findings suggest the pure deflagration scenario remains an appealing explanation for bright and intermediate luminosity SNe Iax. However, some systematic differences remain which need to be addressed. The work presented here, therefore leaves a few open questions. First, it needs to be investigated whether the decline of the model light curves can be slowed down within the framework of the M_{Ch} deflagration model. It seems that strong coupling between the ejected mass of ^{56}Ni and the total ejected mass cannot be overcome easily by varying the parameters of our simulations. The most uncertain assumptions are the ignition conditions which need to be further investigated. Also the RT calculations introduce inaccuracies which need to be quantified and the effects of the new non-LTE version of ARTIS (Shingles et al. 2020) will be tested in future studies, which may help explain some of the systematic differences (particularly in spectral evolution) between models and observed SNe Iax. Another explanation for these systematic differences may be the properties of the models

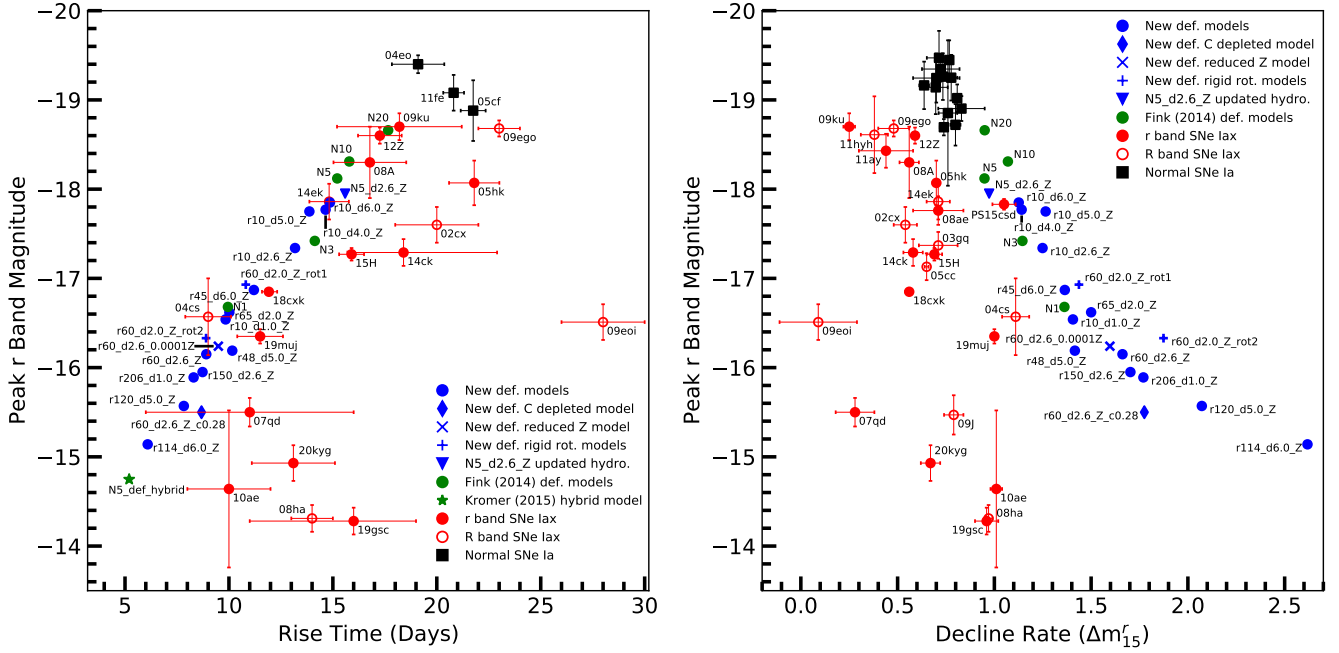


Fig. 17. Peak *r*-band magnitudes vs. rise time (*left*) and peak *r*-band magnitudes vs. decline rate in terms of Δm_{15} (*right*) for the models of F14 (green), our new sequence of models (blue), real SNe Iax (red) and normal SNe Ia (black). The filled red circles represent measurements in the *r*-band while the unfilled red circles represent measurements in the *R*-band. The observations include those compiled by Magee et al. (2016) as well as SN 2014ck (Tomasella et al. 2016), SN 2014ek (Li et al. 2018), SN 2018cck (Yao et al. 2019), SN 2019muj (Barna et al. 2021), SN 2019gsc (Tomasella et al. 2020; Srivastav et al. 2020) and SN 2020kyg (Srivastav et al., in prep.). The blue diamond, cross and plus markers correspond to models which are variations on the standard r60_d2.6_Z model. The blue diamond represents r60_d2.6_Z_c0.28 (carbon depleted model), the cross depicts r60_d2.6_0.0001Z (reduced Z model) and the blue plus signs represent r60_d2.0_Z_rot1 and r60_d2.0_Z_rot2 (rigidly rotating models). The blue triangle represents the N5_d2.6_Z model from the F14 deflagration study simulated again using the updated version of the LEAFS code to quantify the difference caused by using the newer version of the code. The green star represents the hybrid CONE WD model produced by K15.

themselves: perhaps a more stratified ejecta structure as suggested by Stritzinger et al. (2015), Barna et al. (2017, 2018, 2021) may help match the spectral evolution of SNe Iax better. Moreover, we note our simulations do not take into account the possible impacts of the burning products in the bound remnant on the light curves and spectra. While this impact is very uncertain it has been suggested that the contribution of the burned material in the bound core may help to explain the long term evolution of SNe Iax light curves (Kromer et al. 2013; Foley et al. 2014; Shen & Schwab 2017) and their peculiar late time spectra (Foley et al. 2016). In addition, the effects due to the bound remnant could be increasingly relevant for the faint explosions, and, depending on the structure of the bound remnant, could contribute to SNe Iax light curves and spectra at earlier times (Kromer et al. 2015). A greater contribution of the remnant may be expected for fainter explosions as in fainter models the ^{56}Ni mass in the bound remnant is predicted to be significantly higher than in the ejected material (e.g., Model r114_d6.0_Z has bound remnant ^{56}Ni mass which is 5 times higher than the ^{56}Ni mass in the ejected material). The bound remnant, therefore, may help explain some of the systematic differences between our models (particularly the fainter ones) and observed SNe Iax. However, as the impact, if any, of the burned material on top of the bound remnant on observed SNe Iax light curves and spectra is very uncertain future studies which better quantify the possible contribution of the bound remnant are key to understanding if this really can help explain some of the systematic differences between our models and observed SNe Iax.

The fact that the models can match some of the bright and intermediate luminosity events, but the observational trend does

not naturally explain the faint explosions, may suggest that a different scenario might be at work. In particular, Valenti et al. (2009) argue that the most probable explanation for the very faint SNe Iax supernova, SN 2008ha, is that it was produced in the low-energy core-collapse explosion of a hydrogen-deficient massive star. However, the fainter models in our sequence as well as the hybrid CONE deflagration model produced by Kromer et al. (2015) are able to reach luminosities approaching the low luminosities of the faintest SNe Iax such as SN 2008ha. In addition, while Valenti et al. (2009) argue there is a striking resemblance between SN 2008ha and the under-luminous type IIP SN 2005cs (Li et al. 2006; Pastorello et al. 2009) the comparisons they make between the early time spectra of SN 2008ha and those of SN 2002cx and SN 2005hk with their line velocities shifted by -3000 km s^{-1} show similarly good agreement. Moreover, speculations about ONe WD – neutron star mergers as a candidate for faint SNe Iax have been put forward by Bobrick et al. (2022). In summary, it seems likely that SNe Iax can be modeled by a combination of deflagrations in M_{Ch} WDs and other scenarios that may be needed to account for the fainter members of this class of transients.

Acknowledgements. This work was supported by the Deutsche Forschungsgemeinschaft (DFG, German Research Foundation) – Project-ID 138713538 – SFB 881 (“The Milky Way System”, subproject A10), by the ChETEC COST Action (CA16117), and by the National Science Foundation under Grant No. OISE-1927130 (IRENA). FL and FKR acknowledge support by the Klaus Tschira Foundation. FPC acknowledges an STFC studentship and SAS acknowledges funding from STFC Grant Ref: ST/P000312/1. NumPy and SciPy (Oliphant 2007), IPython (Pérez & Granger 2007), and Matplotlib (Hunter 2007) were used for data processing and plotting. The authors gratefully acknowledge the

- Gauss Centre for Supercomputing e.V. (www.gauss-centre.eu) for funding this project by providing computing time on the GCS Supercomputer JUWELS (Jülich Supercomputing Centre 2019) at Jülich Supercomputing Centre (JSC). Part of this work was performed using the Cambridge Service for Data Driven Discovery (CSD3), part of which is operated by the University of Cambridge Research Computing on behalf of the STFC DiRAC HPC Facility (www.dirac.ac.uk). The DiRAC component of CSD3 was funded by BEIS capital funding via STFC capital grants ST/P002307/1 and ST/R002452/1 and STFC operations grant ST/R00689X/1. DiRAC is part of the National e-Infrastructure. We thank James Gillanders for assisting with the flux calibrations of the observed spectra.
- ## References
- Asplund, M., Grevesse, N., Sauval, A. J., & Scott, P. 2009, *ARA&A*, 47, 481
- Barna, B., Szalai, T., Kromer, M., et al. 2017, *MNRAS*, 471, 4865
- Barna, B., Szalai, T., Kerzendorf, W. E., et al. 2018, *MNRAS*, 480, 3609
- Barna, B., Szalai, T., Jha, S. W., et al. 2021, *MNRAS*, 501, 1078
- Bauer, E. B., White, C. J., & Bildsten, L. 2019, *ApJ*, 887, 68
- Blinnikov, S. I., & Khokhlov, A. M. 1986, *Sov. Astron. Lett.*, 12, 131
- Blondin, S., Dessart, L., Hillier, D. J., & Khokhlov, A. M. 2013, *MNRAS*, 429, 1217
- Bobrick, A., Zenati, Y., Perets, H. B., Davies, M. B., & Church, R. 2022, *MNRAS*, 510, 3758
- Brachwitz, F., Dean, D. J., Hix, W. R., et al. 2000, *ApJ*, 536, 934
- Branch, D., Fisher, A., & Nugent, P. 1993, *AJ*, 106, 2383
- Branch, D., Baron, E., Thomas, R. C., et al. 2004, *PASP*, 116, 903
- Branch, D., Dang, L. C., Hall, N., et al. 2006, *PASP*, 118, 560
- Bravo, E. 2019, *A&A*, 624, A139
- Bravo, E., Gil-Pons, P., Gutiérrez, J. L., & Doherty, C. L. 2016, *A&A*, 589, A38
- Bulla, M., Sim, S. A., & Kromer, M. 2015, *MNRAS*, 450, 967
- Catalan, S., Ribas, I., Isern, J., & García-Berro, E. 2008, *A&A*, 477, 901
- Chamulak, D. A., Brown, E. F., & Timmes, F. X. 2007, *ApJ*, 655, L93
- Chamulak, D. A., Brown, E. F., Timmes, F. X., & Dupczak, K. 2008, *ApJ*, 677, 160
- Chornock, R., Filippenko, A. V., Branch, D., et al. 2006, *PASP*, 118, 722
- Colella, P., & Woodward, P. R. 1984, *J. Comput. Phys.*, 54, 174
- Denissenkov, P. A., Herwig, F., Truran, J. W., & Paxton, B. 2013, *ApJ*, 772, 37
- Denissenkov, P. A., Truran, J. W., Herwig, F., et al. 2015, *MNRAS*, 447, 2696
- Dessart, L., Hillier, D. J., Blondin, S., & Khokhlov, A. 2014, *MNRAS*, 441, 3249
- Di Stefano, R., Voss, R., & Claeys, J. S. W. 2011, *ApJ*, 738, L1
- Domínguez, I., Höflich, P., & Straniero, O. 2001, *ApJ*, 557, 279
- Fernández, R., & Metzger, B. D. 2013, *ApJ*, 763, 108
- Fink, M., Kromer, M., Seitenzahl, I. R., et al. 2014, *MNRAS*, 438, 1762
- Fink, M., Kromer, M., Hillebrandt, W., et al. 2018, *A&A*, 618, A124
- Foley, R. J., & Kirshner, R. P. 2013, *ApJ*, 769, L1
- Foley, R. J., Chornock, R., Filippenko, A. V., et al. 2009, *AJ*, 138, 376
- Foley, R. J., Challis, P. J., Chornock, R., et al. 2013, *ApJ*, 767, 57
- Foley, R. J., McCully, C., Jha, S. W., et al. 2014, *ApJ*, 792, 29
- Foley, R. J., Jha, S. W., Pan, Y.-C., et al. 2016, *MNRAS*, 461, 433
- Fryxell, B. A., Müller, E., & Arnett, W. D. 1989, *Hydrodynamics and Nuclear Burning*, MPA Green Report 449 (Garching: Max-Planck-Institut für Astrophysik)
- Gall, E. E. E., Taubenberger, S., Kromer, M., et al. 2012, *MNRAS*, 427, 994
- Gamezo, V. N., Khokhlov, A. M., Oran, E. S., Chtchelkanova, A. Y., & Rosenberg, R. O. 2003, *Science*, 299, 77
- Gamezo, V. N., Khokhlov, A. M., & Oran, E. S. 2005, *ApJ*, 623, 337
- Gronow, S., Cote, B., Lach, F., et al. 2021, *A&A*, 656, A94
- Hamuy, M., Phillips, M. M., Suntzeff, N. B., et al. 1996, *AJ*, 112, 2391
- Hillebrandt, W., Kromer, M., Röpke, F. K., & Ruiter, A. J. 2013, *Front. Phys.*, 8, 116
- Hix, W. R., & Thielemann, F. 1999, *ApJ*, 511, 862
- Höflich, P., & Khokhlov, A. 1996, *ApJ*, 457, 500
- Hunter, J. D. 2007, *Comput. Sci. Eng.*, 9, 90
- Iben, I., Jr., & Tutukov, A. V. 1984, *ApJS*, 54, 335
- Iwamoto, K., Brachwitz, F., Nomoto, K., et al. 1999, *ApJS*, 125, 439
- Jha, S. W. 2017, *Handbook of Supernovae*, 375
- Jha, S., Branch, D., Chornock, R., et al. 2006, *AJ*, 132, 189
- Jha, S., Riess, A. G., & Kirshner, R. P. 2007, *ApJ*, 659, 122
- Jordan, G. C., IV, Perets, H. B., Fisher, R. T., & van Rossum, D. R. 2012, *ApJ*, 761, L23
- Jülich Supercomputing Centre 2019, *Journal of Large-scale Research Facilities*, 5, A171
- Kasen, D. 2006, *ApJ*, 649, 939
- Kashyap, R., Haque, T., Lorén-Aguilar, P., García-Berro, E., & Fisher, R. 2018, *ApJ*, 869, 140
- Kawabata, M., Kawabata, K. S., Maeda, K., et al. 2018, *PASJ*, 70, 111
- Kawabata, M., Maeda, K., Yamanaka, M., et al. 2021, *PASJ*, 73, 1295
- Khokhlov, A. M. 1989, *MNRAS*, 239, 785
- Khokhlov, A. M. 1991, *A&A*, 245, 114
- Khokhlov, A. M. 2000, ArXiv e-prints [arXiv:astro-ph/0008463]
- Kobayashi, C., Umeda, H., Nomoto, K., Tominaga, N., & Ohkubo, T. 2006, *ApJ*, 653, 1145
- Kobayashi, C., Leung, S.-C., & Nomoto, K. 2020, *ApJ*, 895, 138
- Kromer, M., & Sim, S. A. 2009, *MNRAS*, 398, 1809
- Kromer, M., Fink, M., Stanishev, V., et al. 2013, *MNRAS*, 429, 2287
- Kromer, M., Ohlmann, S. T., Pakmor, R., et al. 2015, *MNRAS*, 450, 3045
- Kromer, M., Ohlmann, S. T., & Röpke, F. K. 2017, *Mem. Soc. Astron. It.*, 88, 312
- Kuhlen, M., Woosley, S. E., & Glatzmaier, G. A. 2006, *ApJ*, 640, 407
- Lach, F., Röpke, F. K., Seitenzahl, I. R., et al. 2020, *A&A*, 644, A118
- Langanke, K., & Martínez-Pinedo, G. 2001, *At. Data Nucl. Data Tables*, 79, 1
- Lesaffre, P., Han, Z., Tout, C. A., Podsiadlowski, P., & Martin, R. G. 2006, *MNRAS*, 368, 187
- Leung, S.-C., & Nomoto, K. 2020, *ApJ*, 900, 54
- Li, W., Filippenko, A. V., Chornock, R., et al. 2003, *PASP*, 115, 453
- Li, W., Van Dyk, S. D., Filippenko, A. V., et al. 2006, *ApJ*, 641, 1060
- Li, W., Leaman, J., Chornock, R., et al. 2011, *MNRAS*, 412, 1441
- Li, L., Wang, X., Zhang, J., et al. 2018, *MNRAS*, 478, 4575
- Liu, Z.-W., Kromer, M., Fink, M., et al. 2013, *ApJ*, 778, 121
- Livio, M., & Mazzali, P. 2018, *Phys. Rep.*, 736, 1
- Long, M., Jordan, G. C., IV, Van Rossum, D. R., et al. 2014, *ApJ*, 789, 103
- Lundqvist, P., Mattila, S., Sollerman, J., et al. 2013, *MNRAS*, 435, 329
- Lyman, J., Taddia, F., Stritzinger, M., et al. 2018, *MNRAS*, 473, 1359
- Magée, M. R., Kotak, R., Sim, S. A., et al. 2016, *A&A*, 589, A89
- Magée, M., Sim, S., Kotak, R., Maguire, K., & Boyle, A. 2019, *A&A*, 622, A102
- Marquardt, K. S., Sim, S. A., Ruiter, A. J., et al. 2015, *A&A*, 580, A118
- McClelland, C. M., Garnavich, P. M., Galbany, L., et al. 2010, *ApJ*, 720, 704
- McCully, C., Jha, S. W., Foley, R. J., et al. 2014a, *Nature*, 512, 54
- McCully, C., Jha, S. W., Foley, R. J., et al. 2014b, *ApJ*, 786, 134
- McCully, C., Jha, S. W., Scalzo, R. A., et al. 2022, *ApJ*, 925, 138
- Narayan, G., Foley, R. J., Berger, E., et al. 2011, *ApJ*, 731, L11
- Neunteufel, P. 2020, *A&A*, 641, A52
- Nomoto, K., Kobayashi, C., & Tominaga, N. 2013, *ARA&A*, 51, 457
- Nonaka, A., Aspden, A. J., Zingale, M., et al. 2012, *ApJ*, 745, 73
- Ohlmann, S. T., Kromer, M., Fink, M., et al. 2014, *A&A*, 572, A57
- Oliphant, T. E. 2007, *Comput. Sci. Eng.*, 9, 10
- Osher, S., & Sethian, J. A. 1988, *J. Comput. Phys.*, 79, 12
- Oskinova, L. M., Gvaramadze, V. V., Gräfener, G., Langer, N., & Todt, H. 2020, *A&A*, 644, L8
- Pakmor, R., Röpke, F. K., Weiss, A., & Hillebrandt, W. 2008, *A&A*, 489, 943
- Pakmor, R., Edelmann, P., Röpke, F. K., & Hillebrandt, W. 2012, *MNRAS*, 424, 2222
- Pastorello, A., Valenti, S., Zampieri, L., et al. 2009, *MNRAS*, 394, 2266
- Pérez, F., & Granger, B. E. 2007, *Comput. Sci. Eng.*, 9, 21
- Perlmutter, S., Aldering, G., Goldhaber, G., et al. 1999, *ApJ*, 517, 565
- Pfannes, J. M. M., Niemeyer, J. C., Schmidt, W., & Klingenberg, C. 2010, *A&A*, 509, A74
- Phillips, M. M. 1993, *ApJ*, 413, L105
- Phillips, M. M., Li, W., Frieman, J. A., et al. 2007, *PASP*, 119, 360
- Piro, A. L., & Bildsten, L. 2008, *ApJ*, 673, 1009
- Prantzos, N., Abia, C., Limongi, M., Chieffi, A., & Cristallo, S. 2018, *MNRAS*, 476, 3432
- Provenzal, J. L., Shipman, H., Høg, E., & Thejll, P. 1998, *ApJ*, 494, 759
- Raddi, R., Hollands, M., Koester, D., et al. 2018a, *ApJ*, 858, 3
- Raddi, R., Hollands, M., Gänsicke, B., et al. 2018b, *MNRAS*, 479, L96
- Raddi, R., Hollands, M., Koester, D., et al. 2019, *MNRAS*, 489, 1489
- Rauscher, T., & Thielemann, F.-K. 2000, *At. Data Nucl. Data Tables*, 75, 1
- Reinecke, M., Hillebrandt, W., & Niemeyer, J. C. 1999a, *A&A*, 347, 739
- Reinecke, M., Hillebrandt, W., Niemeyer, J. C., Klein, R., & Gröbl, A. 1999b, *A&A*, 347, 724
- Riess, A. G., Press, W. H., & Kirshner, R. P. 1996, *ApJ*, 473, 88
- Ritter, A., Parker, Q., Lykou, F., et al. 2021, *ApJ*, 918, L33
- Röpke, F. K. 2005, *A&A*, 432, 969
- Röpke, F. K. 2007, *ApJ*, 668, 1103
- Röpke, F. K., & Hillebrandt, W. 2004, *A&A*, 420, L1
- Röpke, F. K., & Hillebrandt, W. 2005, *A&A*, 431, 635
- Röpke, F. K., & Hillebrandt, W. 2006, in *Origin of Matter and Evolution of Galaxies*, eds. S. Kubono, W. Aoki, T. Kajino, T. Motobayashi, & K. Nomoto, *AIP Conf. Ser.*, 847, 190
- Röpke, F. K., & Sim, S. A. 2018, *Space Sci. Rev.*, 214, 72
- Röpke, F. K., Hillebrandt, W., Niemeyer, J. C., & Woosley, S. E. 2006a, *A&A*, 448, 1
- Röpke, F. K., Gieseler, M., Reinecke, M., Travaglio, C., & Hillebrandt, W. 2006b, *A&A*, 453, 203

- Röpke, F. K., Hillebrandt, W., Schmidt, W., et al. 2007, *ApJ*, 668, 1132
- Schmidt, B. P., Suntzeff, N. B., Phillips, M. M., et al. 1998, *ApJ*, 507, 46
- Seitenzahl, I. R., Townsley, D. M., Peng, F., & Truran, J. W. 2009, *At. Data Nucl. Data Tables*, 95, 96
- Seitenzahl, I. R., Ciaraldi-Schoolmann, F., Röpke, F. K., et al. 2013, *MNRAS*, 429, 1156
- Shen, K. J., & Schwab, J. 2017, *ApJ*, 834, 180
- Shen, K. J., Blondin, S., Kasen, D., et al. 2021, *ApJ*, 909, L18
- Shingles, L. J., Sim, S. A., Kromer, M., et al. 2020, *MNRAS*, 492, 2029
- Sim, S. A. 2007, *MNRAS*, 375, 154
- Soker, N. 2019, *New Astron. Rev.*, 87, 101535
- Srivastav, S., Smartt, S. J., Leloudas, G., et al. 2020, *ApJ*, 892, L24
- Stritzinger, M. D., Hsiao, E., Valenti, S., et al. 2014, *A&A*, 561, A146
- Stritzinger, M. D., Valenti, S., Hoefflich, P., et al. 2015, *A&A*, 573, A2
- Taubenberger, S. 2017, *Handbook of Supernovae*, 317
- Thielemann, F.-K., Nomoto, K., & Hashimoto, M.-A. 1996, *ApJ*, 460, 408
- Thielemann, F.-K., Isern, J., Perego, A., & von Ballmoos, P. 2018, *Space Sci. Rev.*, 214, 62
- Timmes, F. X., & Arnett, D. 1999, *ApJS*, 125, 277
- Timmes, F. X., & Woosley, S. E. 1992, *ApJ*, 396, 649
- Timmes, F. X., Brown, E. F., & Truran, J. W. 2003, *ApJ*, 590, L83
- Tomasella, L., Cappellaro, E., Benetti, S., et al. 2016, *MNRAS*, 459, 1018
- Tomasella, L., Stritzinger, M., Benetti, S., et al. 2020, *MNRAS*, 496, 1132
- Townsley, D. M., Jackson, A. P., Calder, A. C., et al. 2009, *ApJ*, 701, 1582
- Travaglio, C., Hillebrandt, W., Reinecke, M., & Thielemann, F.-K. 2004, *A&A*, 425, 1029
- Umeda, H., Nomoto, K., Kobayashi, C., Hachisu, I., & Kato, M. 1999, *ApJ*, 522, L43
- Valenti, S., Pastorello, A., Cappellaro, E., et al. 2009, *Nature*, 459, 674
- Vennes, S., Nemeth, P., Kawka, A., et al. 2017, *Science*, 357, 680
- Wang, B., & Han, Z. 2012, *New Astron. Rev.*, 56, 122
- Whelan, J., & Iben, I. J. 1973, *ApJ*, 186, 1007
- White, C. J., Kasliwal, M. M., Nugent, P. E., et al. 2015, *ApJ*, 799, 52
- Woosley, S. E., Arnett, W. D., & Clayton, D. D. 1973, *ApJS*, 26, 231
- Yamanaka, M., Maeda, K., Kawabata, K. S., et al. 2015, *ApJ*, 806, 191
- Yao, Y., Miller, A. A., Kulkarni, S. R., et al. 2019, *ApJ*, 886, 152
- Yaron, O., & Gal-Yam, A. 2012, *PASP*, 124, 668
- Yoon, S., & Langer, N. 2005, *A&A*, 435, 967
- Zeng, Y., Liu, Z.-W., & Han, Z. 2020, *ApJ*, 898, 12
- Zhang, M., Fuller, J., Schwab, J., & Foley, R. J. 2019, *ApJ*, 872, 29
- Zhou, P., Leung, S.-C., Li, Z., et al. 2021, *ApJ*, 908, 31
- Zingale, M., Almgren, A. S., Bell, J. B., Nonaka, A., & Woosley, S. E. 2009, *ApJ*, 704, 196
- Zingale, M., Nonaka, A., Almgren, A. S., et al. 2011, *ApJ*, 740, 8

Appendix A: Simulation summary tables

Table A.1. Summary of the main properties of the ejected material and the initial conditions.

model	ρ_c (10^9 g cm^{-3})	r_{ign} (km)	Z (Z_{\odot})	E_{nuc} (10^{50} erg)	M_{ej} (M_{\odot})	$M(^{56}\text{Ni})$ (M_{\odot})	M_{IGE} (M_{\odot})	M_{IME} (M_{\odot})	$M(^{56}\text{Ni})/M_{\text{IGE}}$	$E_{\text{kin,ej}}$ (10^{50} erg)
r10_d1.0_Z	1.0	10	1	1.98	0.077	0.033	0.039	0.0072	0.84	0.15
r10_d2.0_Z	2.0	10	1	2.81	0.127	0.049	0.066	0.011	0.74	0.28
r10_d2.6_Z	2.6	10	1	3.15	0.164	0.069	0.094	0.015	0.74	0.41
r10_d3.0_Z	3.0	10	1	3.26	0.174	0.070	0.100	0.014	0.70	0.43
r10_d4.0_Z	4.0	10	1	3.83	0.227	0.092	0.144	0.020	0.64	0.68
r10_d5.0_Z	5.0	10	1	4.07	0.237	0.085	0.150	0.022	0.58	0.75
r10_d6.0_Z	6.0	10	1	4.70	0.301	0.090	0.178	0.027	0.50	0.97
r82_d1.0_Z	1.0	82	1	2.31	0.082	0.033	0.038	0.0071	0.86	0.16
r65_d2.0_Z	2.0	65	1	2.38	0.079	0.033	0.041	0.0074	0.78	0.16
r60_d2.6_0.0001Z	2.6	60	1e-4	1.95	0.053	0.022	0.028	0.0045	0.79	0.089
r60_d2.6_0.001Z	2.6	60	1e-3	1.98	0.052	0.021	0.026	0.0044	0.80	0.088
r60_d2.6_0.01Z	2.6	60	1e-2	1.93	0.048	0.019	0.024	0.0045	0.79	0.084
r60_d2.6_0.1Z	2.6	60	1e-1	1.92	0.049	0.020	0.026	0.0042	0.79	0.79
r60_d2.6_Z	2.6	60	1	1.93	0.050	0.018	0.025	0.0045	0.75	0.082
r60_d2.6_2Z	2.6	60	2	1.97	0.054	0.020	0.028	0.0052	0.71	0.096
r60_d2.6_Z_co0.28	2.6	60	1	1.87	0.036	0.012	0.018	0.0036	0.68	0.039
r57_d3.0_Z	3.0	57	1	1.86	0.054	0.022	0.030	0.0053	0.74	0.093
r51_d4.0_Z	4.0	51	1	1.29	0.033	0.012	0.019	0.0033	0.67	0.042
r48_d5.0_Z	5.0	48	1	1.67	0.054	0.018	0.030	0.0047	0.59	0.072
r45_d6.0_Z	6.0	45	1	2.19	0.093	0.033	0.056	0.0086	0.58	0.19
r206_d1.0_Z	1.0	206	1	1.67	0.041	0.016	0.018	0.0037	0.88	0.064
r163_d2.0_Z	2.0	163	1	1.40	0.029	0.012	0.015	0.0025	0.80	0.038
r150_d2.6_Z	2.6	150	1	1.75	0.039	0.016	0.021	0.0036	0.78	0.061
r143_d3.0_Z	3.0	143	1	1.61	0.031	0.013	0.017	0.0028	0.77	0.041
r129_d4.0_Z	4.0	129	1	1.58	0.031	0.013	0.017	0.0029	0.75	0.047
r120_d5.0_Z	5.0	120	1	1.36	0.024	0.010	0.014	0.0023	0.74	0.034
r114_d6.0_Z	6.0	114	1	0.96	0.014	0.0058	0.0081	0.0012	0.72	0.018
r60_d2.0_Z_rot1	2.0	60	1	2.89	0.095	0.045	0.058	0.0076	0.77	0.23
r60_d2.0_Z_rot2	2.0	60	1	2.44	0.054	0.022	0.028	0.0038	0.78	0.11
N5_d2.6_Z	3.6	N5	1	4.30	0.294	0.136	0.178	0.0352	0.76	0.983

Table A.2. Main properties of the bound remnant and the respective initial conditions.

model	ρ_c (10^9 g cm^{-3})	r_{ign} (km)	Z (Z_{\odot})	M_{bound} (M_{\odot})	$M(^{56}\text{Ni})$ (M_{\odot})	M_{IGE} (M_{\odot})	M_{IME} (M_{\odot})	ρ_{max} (10^5 g cm^{-3})	v_{kick} (km s^{-1})	v_x (km s^{-1})
r10_d1.0_Z	1.0	10	1	1.27	0.053	0.059	0.027	2.19	139.3	-139.3
r10_d2.0_Z	2.0	10	1	1.24	0.073	0.087	0.023	2.17	76.6	-76.3
r10_d2.6_Z	2.6	10	1	1.21	0.064	0.078	0.022	1.49	109.8	-109.4
r10_d3.0_Z	3.0	10	1	1.21	0.064	0.080	0.021	1.30	182.6	-182.0
r10_d4.0_Z	4.0	10	1	1.16	0.054	0.067	0.020	1.27	157.7	-157.7
r10_d5.0_Z	5.0	10	1	1.16	0.057	0.082	0.016	1.43	250.2	-250.0
r10_d6.0_Z	6.0	10	1	1.09	0.058	0.091	0.014	1.12	241.9	-241.8
r82_d1.0_Z	1.0	82	1	1.27	0.070	0.078	0.030	2.48	22.9	-22.3
r65_d2.0_Z	2.0	65	1	1.29	0.073	0.085	0.024	1.92	7.5	-6.9
r60_d2.6_0.0001Z	2.6	60	1e-4	1.33	0.065	0.075	0.020	2.33	53.3	53.2
r60_d2.6_0.001Z	2.6	60	1e-3	1.33	0.068	0.078	0.020	2.62	20.2	16.7
r60_d2.6_0.01Z	2.6	60	1e-2	1.33	0.066	0.077	0.021	2.61	119.9	119.7
r60_d2.6_0.1Z	2.6	60	1e-1	1.33	0.065	0.076	0.020	2.22	46.1	45.9
r60_d2.6_Z	2.6	60	1	1.33	0.064	0.077	0.020	2.34	16.8	16.5
r60_d2.6_2Z	2.6	60	2	1.33	0.066	0.076	0.020	2.62	8.6	-5.4
r60_d2.6_Z_co0.28	2.6	60	1	1.34	0.069	0.088	0.021	3.28	271.6	-271.4
r57_d3.0_Z	3.0	57	1	1.33	0.056	0.069	0.018	2.25	135.1	134.7
r51_d4.0_Z	4.0	51	1	1.36	0.033	0.051	0.011	2.90	365.6	364.0
r48_d5.0_Z	5.0	48	1	1.34	0.038	0.064	0.010	2.02	38.1	38.0
r45_d6.0_Z	6.0	44	1	1.30	0.037	0.070	0.0078	1.98	10.7	6.2
r206_d1.0_Z	1.0	206	1	1.31	0.057	0.062	0.027	2.76	6.4	-2.1
r163_d2.0_Z	2.0	163	1	1.34	0.048	0.056	0.018	3.16	54.8	53.1
r150_d2.6_Z	2.6	150	1	1.34	0.061	0.071	0.019	2.64	86.5	86.2
r143_d3.0_Z	3.0	143	1	1.35	0.058	0.069	0.017	2.70	130.8	130.6
r129_d4.0_Z	4.0	129	1	1.36	0.056	0.068	0.015	2.21	369.8	369.6
r120_d5.0_Z	5.0	120	1	1.37	0.047	0.058	0.014	2.54	225.4	225.2
r114_d6.0_Z	6.0	114	1	1.38	0.030	0.042	0.011	3.63	43.2	-42.6
r60_d2.0_Z_rot1	2.0	60	1	1.34	0.084	0.096	0.027	1.84	232.4	-
r60_d2.0_Z_rot2	2.0	60	1	1.38	0.087	0.101	0.026	2.15	17.6	-
N5_d2.6_Z	2.6	N5	1	1.08	0.050	0.058	0.018	1.11	264.6	-137.0

Table A.3. Angle averaged light curve properties for bolometric band and BVRI Bessel bands (top) as well as ugriz Sloan bands (bottom) for the selection of models for which RT simulations were carried out.

model	t_{rise}^{bol}	M_{peak}^{bol}	Δm_{15}^{bol}	t_{rise}^B	M_{peak}^B	Δm_{15}^B	t_{rise}^V	M_{peak}^V	Δm_{15}^V	t_{rise}^R	M_{peak}^R	Δm_{15}^R	t_{rise}^I	M_{peak}^I	Δm_{15}^I
r_10_d1.0_Z	7.27	-16.47	1.5	7.69	-16.57	2.24	9.07	-16.76	1.49	9.46	-16.59	1.29	13.99	-16.68	1.49
r_10_d2.6_Z	9.7	-17.08	1.19	9.61	-17.21	2.12	11.56	-17.49	1.37	12.88	-17.38	1.13	17.06	-17.45	1.25
r_10_d4.0_Z	11.02	-17.35	1.03	10.42	-17.43	2.09	12.85	-17.83	1.31	14.62	-17.81	1.05	18.35	-17.86	0.98
r_10_d5.0_Z	10.93	-17.19	1.06	9.7	-17.11	2.26	12.25	-17.69	1.41	13.96	-17.81	1.17	17.03	-17.86	1.22
r_10_d6.0_Z	12.07	-17.23	0.89	9.55	-16.97	1.92	13.15	-17.67	1.32	15.04	-17.94	1.02	16.82	-18.02	0.93
r_65_d2.0_Z	7.45	-16.43	1.49	7.63	-16.54	2.33	9.1	-16.8	1.57	9.67	-16.67	1.37	13.84	-16.73	1.52
r_60_d2.6_0.0001Z	6.52	-16.07	1.55	6.79	-16.2	2.42	8.2	-16.42	1.62	9.31	-16.29	1.48	12.31	-16.38	1.53
r_60_d2.6_Z	6.39	-15.92	1.61	6.48	-16.02	2.45	7.84	-16.28	1.66	8.83	-16.2	1.57	11.44	-16.3	1.59
r_60_d2.6_Z_c0.28	6.48	-15.58	1.57	6.58	-15.71	2.56	7.96	-15.89	1.64	9.19	-15.84	1.46	11.53	-15.96	1.48
r_48_d5.0_Z	6.94	-15.83	1.32	6.94	-15.88	2.49	8.53	-16.23	1.57	10.27	-16.25	1.32	12.73	-16.34	1.33
r_45_d6.0_Z	8.35	-16.4	1.22	7.9	-16.38	2.41	9.76	-16.86	1.53	11.26	-16.93	1.26	14.08	-16.97	1.28
r_206_d1.0_Z	5.91	-15.82	1.76	6.3	-15.92	2.41	7.51	-16.1	1.68	8.08	-15.95	1.66	10.54	-16.07	1.61
r_150_d2.6_Z	5.79	-15.81	1.65	6.09	-15.94	2.48	7.45	-16.13	1.67	8.65	-16.0	1.61	11.11	-16.11	1.62
r_120_d5.0_Z	4.68	-15.38	1.84	5.1	-15.47	2.5	6.76	-15.7	1.81	7.81	-15.62	2.01	9.55	-15.74	1.91
r_114_d6.0_Z	4.02	-14.91	2.38	4.17	-15.04	2.84	5.31	-15.21	2.13	6.06	-15.2	2.55	7.72	-15.36	2.38
r_60_d2.0_Z_rot1	7.96	-16.83	1.47	8.41	-16.98	2.37	9.73	-17.15	1.52	10.36	-16.98	1.3	15.1	-17.09	1.57
r_60_d2.0_Z_rot2	6.52	-16.16	1.79	6.76	-16.24	2.36	8.11	-16.46	1.69	8.71	-16.38	1.79	11.47	-16.48	1.83
N5_d2.6_Z	10.81	-17.72	0.93	10.75	-17.89	1.9	13.45	-18.16	1.19	15.37	-17.98	0.87	20.06	-18.06	0.72
model	t_{rise}^u	M_{peak}^u	Δm_{15}^u	t_{rise}^g	M_{peak}^g	Δm_{15}^g	t_{rise}^r	M_{peak}^r	Δm_{15}^r	t_{rise}^i	M_{peak}^i	Δm_{15}^i	t_{rise}^z	M_{peak}^z	Δm_{15}^z
r10_d1.0_Z	6.42	-16.23	4.11	8.20	-16.72	1.83	9.85	-16.54	1.41	9.04	-15.96	0.87	14.65	-16.45	1.30
r10_d2.6_Z	8.14	-16.78	3.69	10.21	-17.38	1.75	13.18	-17.34	1.25	16.88	-16.75	1.12	17.57	-17.22	1.16
r10_d4.0_Z	9.16	-16.9	3.47	11.14	-17.61	1.73	14.65	-17.77	1.14	18.38	-17.21	0.85	18.98	-17.58	0.93
r10_d5.0_Z	8.56	-16.54	3.65	10.45	-17.35	1.88	13.87	-17.75	1.26	16.97	-17.28	1.08	17.63	-17.56	1.12
r10_d6.0_Z	8.02	-16.4	2.78	10.42	-17.23	1.67	14.86	-17.85	1.12	16.73	-17.52	0.85	17.57	-17.68	0.85
r65_d2.0_Z	6.42	-16.11	4.27	8.14	-16.72	1.92	10.00	-16.63	1.5	9.34	-16.02	0.91	14.32	-16.49	1.34
r60_d2.6_0.0001Z	5.64	-15.8	4.47	7.24	-16.36	1.99	9.49	-16.24	1.60	11.08	-15.68	1.30	12.85	-16.12	1.32
r60_d2.6_Z	5.49	-15.61	4.56	6.94	-16.19	2.01	8.92	-16.15	1.66	10.54	-15.62	1.43	12.01	-16.00	1.36
r60_d2.6_Z_c0.28	5.49	-15.34	4.63	7.00	-15.84	2.08	9.13	-15.78	1.54	11.11	-15.33	1.38	12.04	-15.62	1.27
r48_d5.0_Z	5.82	-15.44	4.39	7.39	-16.07	2.04	10.15	-16.19	1.42	12.88	-15.75	1.27	13.03	-15.99	1.18
r45_d6.0_Z	6.64	-15.88	4.02	8.47	-16.59	2.01	11.20	-16.87	1.36	13.99	-16.40	1.18	14.68	-16.65	1.18
r206_d1.0_Z	5.19	-15.57	4.45	6.73	-16.08	1.97	8.32	-15.89	1.77	8.32	-15.38	1.36	11.47	-15.79	1.35
r150_d2.6_Z	4.98	-15.59	4.66	6.55	-16.09	2.03	8.74	-15.95	1.7	10.21	-15.41	1.46	11.68	-15.82	1.38
r120_d5.0_Z	3.78	-15.22	4.84	5.67	-15.63	2.05	7.84	-15.57	2.07	9.01	-15.06	1.92	10.03	-15.42	1.58
r114_d6.0_Z	3.06	-14.74	4.97	4.47	-15.16	2.32	6.09	-15.14	2.62	7.48	-14.7	2.62	8.08	-14.98	1.90
r60_d2.0_Z_rot1	6.91	-16.66	4.18	8.89	-17.11	1.93	10.66	-16.94	1.41	15.01	-16.35	1.48	15.70	-16.85	1.40
r60_d2.0_Z_rot2	5.46	-15.9	4.18	7.21	-16.39	1.93	8.92	-16.33	1.88	9.37	-15.79	1.59	12.22	-16.20	1.55
N5_d2.6_Z	8.83	-17.46	3.01	11.62	-18.05	1.6	15.58	-17.95	0.97	20.63	-17.33	0.57	20.84	-17.86	0.71

Chapter 7

Models of pulsationally assisted gravitationally confined detonations with different ignition conditions

Publication information:

Journal: Astronomy & Astrophysics (A&A)

Reference: F. Lach et al. 2022b, in press

Digital Object Identifier: <https://doi.org/10.1051/0004-6361/202142194>

Status: Accepted for publication in A&A on 15 November 2021

Credit: Florian Lach, A&A, 2022, reproduced with permission ©ESO

Authors:

Florian Lach (FL), Fionntan P. Callan (FPC), Friedrich K. Röpke (FKR), Stuart A. Sim (SAS)

Author's contribution:

The workload was shared similar to Publication 1. While FL wrote the text of the manuscript (including abstract, introduction, and conclusions) FPC added Section 6. FPC also conducted and analyzed the radiative transfer simulations. FL carried out the hydrodynamic and nuclear network simulations and their corresponding analysis. The scientific content of the paper was discussed in close collaboration with FPC, FKR and SAS.

Models of pulsationally assisted gravitationally confined detonations with different ignition conditions

F. Lach^{1,2} , F. P. Callan³ , S. A. Sim³ , and F. K. Röpke^{1,2} 

¹ Heidelberger Institut für Theoretische Studien, Schloss-Wolfsbrunnenweg 35, 69118 Heidelberg, Germany
e-mail: florian.lach@h-its.org

² Zentrum für Astronomie der Universität Heidelberg, Institut für Theoretische Astrophysik, Philosophenweg 12, 69120 Heidelberg, Germany

³ School of Mathematics and Physics, Queen's University Belfast, Belfast BT7 INN, UK

Received 10 September 2021 / Accepted 15 November 2021

ABSTRACT

Over the past decades, many explosion scenarios for Type Ia supernovae have been proposed and investigated including various combinations of deflagrations and detonations in white dwarfs of different masses up to the Chandrasekhar mass. One of these is the gravitationally confined detonation model. In this case a weak deflagration burns to the surface, wraps around the bound core, and collides at the antipode. A subsequent detonation is then initiated in the collision area. Since the parameter space for this scenario, that is, varying central densities and ignition geometries, has not been studied in detail, we used pure deflagration models of a previous parameter study dedicated to Type Iax supernovae as initial models to investigate the gravitationally confined detonation scenario. We aim to judge whether this channel can account for one of the many subgroups of Type Ia supernovae, or even normal events. To this end, we employed a comprehensive pipeline for three-dimensional Type Ia supernova modeling that consists of hydrodynamic explosion simulations, nuclear network calculations, and radiative transfer. The observables extracted from the radiative transfer are then compared to observed light curves and spectra. The study produces a wide range in masses of synthesized ⁵⁶Ni ranging from 0.257 to 1.057 M_{\odot} , and, thus, can potentially account for subluminous as well as overluminous Type Ia supernovae in terms of brightness. However, a rough agreement with observed light curves and spectra can only be found for 91T-like objects. Although several discrepancies remain, we conclude that the gravitationally confined detonation model cannot be ruled out as a mechanism to produce 91T-like objects. However, the models do not provide a good explanation for either normal Type Ia supernovae or Type Iax supernovae.

Key words. hydrodynamics – nuclear reactions, nucleosynthesis, abundances – radiative transfer – methods: numerical – supernovae: general – supernovae: individual: SN 1991T

1. Introduction

Despite several decades of research, the questions of the progenitor systems of Type Ia supernovae (SNe Ia), and their explosion mechanism, remain open. A common basis for modeling different conceivable explosion scenarios is the origin of SNe Ia from the thermonuclear disruptions of carbon-oxygen (CO, [Hoyle & Fowler 1960](#); [Arnett 1969](#)), oxygen-neon (ONe, [Marquardt et al. 2015](#); [Kashyap et al. 2018](#)), hybrid carbon-oxygen-neon (CONE, [Denissenkov et al. 2015](#); [Kromer et al. 2015](#); [Bravo et al. 2016](#)), or helium-carbon-oxygen ([Pakmor et al. 2021](#)) white dwarf (WD) stars in a binary system. Whether the pre-explosion WD has reached the Chandrasekhar mass (M_{Ch}) or whether it remains significantly below this limit is not clear yet. In fact, it may well be possible that more than one progenitor and explosion mechanism is needed to account for the observed sample of SNe Ia given the variety of peculiar subclasses that have been identified ([Taubenberger 2017](#); [Jha 2017](#)). The nature of the binary companion of the exploding WD is yet another open question since it is not clear whether it is a nondegenerate star, for example, a main sequence, red giant, or asymptotic giant branch star ([Whelan & Iben 1973](#)), or another WD ([Iben & Tutukov 1984](#)). Finally, the reason for the explosion and the combustion mechanism are unknown. The

WD might explode due to an interaction with its binary companion via accretion or due to a merger with the latter, and the thermonuclear flame can propagate as a subsonic deflagration or a supersonic detonation front (e.g., [Röpke 2016](#)). These possibilities leave room for a plethora of explosion scenarios (see [Hillebrandt et al. 2013](#), for a review) trying to explain the typical features of the bulk of so-called normal SNe Ia as well as the various subclasses. Here, we focus solely on explosions of M_{Ch} WDs.

Specifically, we extend the models of asymmetric deflagrations in M_{Ch} WDs of [Lach et al. \(2022, hereafter L21\)](#), and trigger detonations in late stages of the explosion. The models presented in that study were ignited asymmetrically in a single spot, and, hence, lead to weak deflagrations ejecting only little mass. The deflagration ashes rush across the still bound object and collide at the opposite side. Therefore, they can serve as a starting point for the investigation of the gravitationally confined detonation (GCD) scenario first investigated by [Plewa et al. \(2004\)](#). In this scenario, a detonation is initiated in the collision region leading to a healthy explosion disrupting the whole star. The goal of our study is to investigate two main properties of these models. First, we explore whether this mechanism is capable of reproducing the brightness variation of normal SNe Ia or even extending to subluminous events. Second, the

effects of the predicted composition inversion in comparison to 1D SN Ia (see e.g., [Nomoto et al. 1984](#); [Khokhlov et al. 1993](#)) models of the canonical delayed detonation (DD) scenario ([Gamezo et al. 2005](#); [Röpke & Niemeyer 2007](#); [Sim et al. 2013](#)) on the predicted observables are examined. By construction, the deflagration products remain in the central parts of the ejecta in 1D models. In 3D DD simulations, the composition is not strictly stratified. Deflagration ashes extend out to high ejecta velocities while material composed of lighter elements sinks down toward the center because of the buoyancy instability during the initial deflagration phase. In the GCD model this effect is most strongly pronounced. A complete inversion of the ejecta composition compared to the 1D models is observed: the deflagration products enshroud the detonation ashes. While [Kasen & Plewa \(2007\)](#) conclude that the spectrum of SN 1994D can be matched by their GCD model, [Baron et al. \(2008\)](#) and [Seitenzahl et al. \(2016\)](#) find it difficult to bring the large abundances of iron group elements (IGEs) in the outer layers in agreement with observations (see discussion in Sect. 2).

Because of the restricted spatial resolution of the regions where the detonation potentially triggers, the mechanism for the initiation of the detonation wave cannot be followed consistently within this study. According to [Seitenzahl et al. \(2009a\)](#) a resolution of at least a few 100 meters per cell is required. We emphasize that the numerical methods used in this work are not appropriate to conclusively verify whether a detonation is ignited or not (see Sect. 4). Therefore, we only give plausibility arguments and follow a what-if-approach to explore the consequences of an assumed detonation initiation. Because of this uncertainty, the occurrence of a detonation is not necessarily a contradiction to the notion that Type Iax supernovae (SNe Iax) may arise from weak deflagrations in M_{Ch} WDs [Branch et al. \(2004\)](#), [Phillips et al. \(2007\)](#), [Kromer et al. \(2013\)](#), [Long et al. \(2014\)](#), [Fink et al. \(2014\)](#), [L21](#). Although a detonation is possible in the collision region it is not guaranteed that it also occurs in every realization in nature. Furthermore, we note that the GCD mechanism relies on the absence of a spontaneous deflagration-to-detonation transition (DDT) before the deflagration breaks out of the surface. Also in this case, the question – whether DDTs occur in unconfined media remains an open issue and topic of active research ([Oran & Gamezo 2007](#); [Woodsley et al. 2009](#); [Poludnenko et al. 2011](#), but see [Poludnenko et al. 2019](#) for a recently suggested mechanism).

The paper is structured in the following way: we first discuss the GCD explosion mechanism and its implications in detail in Sect. 2, and, then give a brief overview of the employed codes and our initial setup in Sect. 3. This is followed by a description of the detonation initiation mechanism and conditions relevant for this study in Sect. 4. Section 5 then covers the results of the hydrodynamic simulations and the postprocessing step. In Sect. 6 we present synthetic observables and compare them to observations. Finally, our conclusions can be found in Sect. 7.

2. Explosion model

As mentioned above, in a previous study ([L21](#)), we investigate explosions of M_{Ch} WDs that result from ignitions of a deflagration flame in a single spot off-center of the star as suggested by simmering phase simulations by [Zingale et al. \(2009, 2011\)](#) and [Nonaka et al. \(2012\)](#). Such models had been proposed to explain the class of SNe Iax and we confirm that a large part of the luminosity range observed for these objects can be reproduced in the context of the assumed explosion scenario. The overall agreement of those models with observational data of

SNe Iax (light curves and spectra) is reasonable, but not perfect. In particular, the observables of the lowest-luminosity members of the SN Iax class are not satisfactorily reproduced by our models. In the scenario of a subsonic deflagration ignited in a single (or a few) spark(s) off-center in a M_{Ch} WD star, the energy released by the nuclear burning does not completely unbind the object and a bound remnant is left behind. But even multispot ignition scenarios – also capable of unbinding the entire WD star – produce ^{56}Ni masses and explosion energies reaching the faint end of normal SNe Ia at best ([Fink et al. 2014](#)). A DD in such models can produce brighter events and approximately cover the range of observed normal SNe Ia ([Gamezo et al. 2005](#); [Maeda et al. 2010a](#); [Röpke & Niemeyer 2007](#); [Seitenzahl et al. 2013a](#)). Observables predicted from these models are again in reasonable agreement with data, however, important trends and relations such as the width-luminosity relation employed to calibrate SNe Ia as cosmological distance indicators ([Phillips 1993](#)) are not fully reproduced by current multidimensional models ([Kasen et al. 2009](#); [Sim et al. 2013](#)). We note, however, that it has been demonstrated that a full treatment of nonlocal thermodynamic equilibrium (NLTE) effects is important for detailed modeling, including at phases relevant to studying the width-luminosity relation (e.g., [Blondin et al. 2013](#); [Dessart et al. 2014](#); [Shen et al. 2021](#)). Since multidimensional studies currently lack full NLTE treatments further work is therefore still needed to fully quantify the extent to which such models can agree with observations. As mentioned above, the mechanism triggering the required spontaneous transition of the combustion wave from deflagration to detonation remains unclear.

For the single-spot off-center ignited M_{Ch} WD models considered by [L21](#), triggering of a detonation in a late phase of the explosion process is also a possibility. Such scenarios have been discussed by [Plewa et al. \(2004\)](#) as gravitationally confined detonations and were later investigated in more detail by [Plewa \(2007\)](#), [Townsend et al. \(2007\)](#), [Röpke et al. \(2007\)](#), [Jordan et al. \(2008, 2009\)](#), [Meakin et al. \(2009\)](#), [Seitenzahl et al. \(2009b, 2016\)](#), [García-Senz et al. \(2016\)](#), and [Byrohl et al. \(2019\)](#). The idea is that the deflagration flame rises toward the surface of the WD and sweeps around the gravitationally bound core. Subsequently, the ashes collide on the opposite side and a detonation is ignited in the collision region. There, an inward and outward moving jet form and material is compressed and heated at the head of the inward moving jet until necessary conditions for a detonation are reached. This leads to the following problem: the less energy released in the initial asymmetric deflagration, the less the WD star expands and the stronger the collision of the deflagration wave at the antipode of its ignition. This increases the chances of triggering a detonation. But a weak expansion of the WD prior to this moment also implies that the detonation produces a substantial amount of ^{56}Ni , and, therefore, such explosion models are very bright. In contrast, a too strong deflagration may pre-expand the WD so much that the antipodal collision of the deflagration ashes is too weak to trigger a detonation.

The immediate triggering of the detonation in the GCD model only works if the collision of ashes is strong, that is, the deflagration is weak. This seems too restrictive to reproduce the brightness range covered by normal SNe Ia, especially the fainter events. Some additional dynamics is introduced by models that take into account the pulsation phase ensuing in the distorted, but still bound, WD after the deflagration phase if a detonation is not triggered immediately. The predecessor to such models is the pulsating delayed detonation (PDD) mechanism (see [Khokhlov 1991](#); [Khokhlov et al. 1993](#); [Höflich et al. 1995](#)) in which a deflagration is ignited centrally in a one-dimensional

(1D) setup that is too weak to unbind the WD. Hence, the star subsequently pulsates and eventually a detonation is triggered inside a mixing zone of ashes and heated fuel. A multi-dimensional variant of this is the “pulsationally assisted” GCD (PGCD, [Jordan et al. 2012a](#)). Here, the initiation of the detonation results from the coincidence of the contraction of the bound core during its pulsation and the collision of the ashes. In the pulsating reverse detonation (PRD) mechanism proposed by [Bravo & García-Senz \(2006, 2009\)](#), the detonation does not necessarily happen near the collision spot of the deflagration waves but is caused by an accretion shock as the burned material falls back onto the WD core. Most probably, these detonation initiation mechanisms coexist legitimately and highly depend on the details of the model and the ignition conditions. Moreover, it seems reasonable to assume that there is a continuous transition between the GCD and the PGCD mechanism (see also [Byrohl et al. 2019](#)).

All model variations mentioned above, except the original 1D PDD scenario, predict similar ejecta structures: well mixed or even clumpy outer layers containing IGEs and intermediate mass elements (IMEs) typical for a deflagration and a stratified inner region caused by the detonation of the core. There is no composition inversion in the PDD, that is, the deflagration ashes stay in the center of the ejecta, but this is an artifact of its restriction to one spatial dimension.

As mentioned earlier, the actual brightness of the event is determined by the state (density) of the WD core at detonation initiation. This depends on the pre-expansion due to the deflagration but also on the phase of the pulsation. Models presented to date (see references above) either result in brightnesses comparable to luminous normal SNe Ia, 91T-like events, or transients significantly too bright to account for most known SNe Ia. The masses of ^{56}Ni lie in the range of $\sim 0.7\text{--}1.2 M_{\odot}$. The faint end of the distribution of normal SNe Ia or even bright SNe Iax, such as SN 2012Z ([Stritzinger et al. 2015](#)), cannot be reproduced by this scenario to date. [Fisher & Jumper \(2015\)](#) discuss the fate of the M_{Ch} scenario and state that sparsely ignited models most probably produce overluminous events, such as SN 1991T. The same conclusion is reached by [Byrohl et al. \(2019\)](#) who study the impact of different deflagration ignition radii with 3D hydrodynamic simulations and find that the GCD mechanism either fails (central ignition) or produces ^{56}Ni masses in excess of $1 M_{\odot}$.

Observational properties of the GCD model were first investigated by [Kasen & Plewa \(2005\)](#). They focused on the Ca II IR triplet at high velocities observed in some SNe Ia, for example, SN 2001el, showing that this can be explained by deflagration ashes in the outer layers of the ejecta. In a later study, [Kasen & Plewa \(2007\)](#) present radiative transfer (RT) calculations of a GCD model taken from [Plewa \(2007\)](#). Although the model is slightly too bright, they find a rough agreement with SN 2001el regarding the shape of the light curve and the color evolution. Moreover, the spectra qualitatively match those of SN 1994D, a normal SN Ia, and they find strong viewing angle dependencies of the decline rate and the Si II $\lambda 6150$ line velocities. [Baron et al. \(2008\)](#) have examined a PRD model and find that it matches the typical Si II absorption feature at maximum light in SN 1994D quite well while the S II “W” feature, a defining characteristic of normal SNe Ia, is totally absent. Furthermore, the large amount of IGEs in the outer layers leads to very red colors not compatible with normal SNe Ia. In a later work, [Bravo et al. \(2009\)](#) find that due to the asymmetry in the deflagration ashes the spectra are not too red for all viewing angles in the PRD models from [Bravo & García-Senz \(2009\)](#). In addition,

some bright models of their sequence agree favorably with the $[M(^{56}\text{Ni})-\Delta m_{15}]$ -relation of normal SNe Ia. The GCD model of [Seitenzahl et al. \(2016\)](#) yields $M(^{56}\text{Ni})$ close to that observed in SN 1991T. They find, however, that the amount of stable IGEs in the deflagration ashes is too large and that features of IMEs (Ca II, S II, Si II) are too pronounced at premaximum and too weak, in contrast, at later epochs to match SN 1991T. Finally, significant viewing angle effects are found, especially in the bluer bands reducing the UV-blocking effect of IGEs in the outer layers at the detonation initiation side. These studies show that a rough agreement of the GCD observational properties with SNe Ia can be found although there still are several shortcomings. Therefore, a large parameter study of the GCD scenario is necessary to judge whether some of the discrepancies between theory and observations can be remedied.

3. Numerical methods and initial setup

The numerical methods and the initial setup are the same as in [L21](#). Therefore, we only give a brief review here, and refer the reader to [L21](#) and references therein for more details.

The LEAFS code employed for the hydrodynamic simulations solves the reactive Euler equations using the piecewise parabolic finite difference scheme of [Colella & Woodward \(1984\)](#). It utilizes the level-set technique ([Sethian 1999](#)) to capture flame fronts and two nested, expanding grids to follow the ejecta to homologous expansion ([Röpke 2005](#)). Gravity is treated using a fast Fourier transform based gravity solver and the Helmholtz equation of state by [Timmer & Arnett \(1999\)](#) is employed. Nucleosynthesis yields are calculated via the tracer particle method ([Travaglio et al. 2004](#)) with the nuclear network code YANN ([Pakmor et al. 2012](#)). To obtain synthetic spectra and light curves we carry out RT simulations using the three-dimensional (3D) Monte Carlo RT code ARTIS ([Sim 2007](#); [Kromer & Sim 2009](#)) allowing comparisons to be made directly with observational data.

We used a selection of M_{Ch} deflagration models from [L21](#) as initial models for GCD explosions. CO white dwarfs with equal amounts of C and O but different central densities ρ_c between $1 \times 10^9 \text{ g cm}^{-3}$ and $6 \times 10^9 \text{ g cm}^{-3}$ were ignited in a single bubble consisting of eight overlapping spheres with a radius of 5 km (see [L21](#) for a visualization) with varying offset radii r_{off} . The latter was varied between 10 and 150 km from the center of the star. Furthermore, the central temperature is $6 \times 10^8 \text{ K}$ decreasing adiabatically to $1 \times 10^8 \text{ K}$. In contrast to our previous [L21](#) deflagration study, the metallicity was kept constant at the solar value since this parameter has shown to be of minor importance for the synthetic observables and the deflagration strength. Therefore, we abbreviate the model names and label them rX_dY, where X encodes the offset radius (r) in km and Y the central density (d) in 10^9 g cm^{-3} . Moreover, the cell size of the inner grid tracking the flame is $\sim 2 \text{ km}$ at the beginning of the simulation and increases to $\sim 200 \text{ km}$ at detonation initiation. Our explosion models are summarized in [Table 1](#). We omit some of the [L21](#) explosion models ignited at large radii since they do not extend the range in nuclear energy release of the deflagration $E_{\text{nuc}}^{\text{def}}$, and, therefore, do not introduce further variations to our set of GCD models.

4. Detonation initiation

The spontaneous initiation of a detonation in a WD environment is a complicated process and the mechanism that modern

supernova research is built on is the gradient mechanism proposed by Zel'dovich et al. (1970). The relevant properties of a hotspot are its temperature, composition, density and size (alternatively its mass). Studies on the initiation process have been carried out by Khokhlov et al. (1997), Niemeyer & Woosley (1997), Dursi & Timmes (2006), and Röpke et al. (2007), for instance. Seitenzahl et al. (2009a) also study different functional forms of the temperature profile in two dimensions and find that the ambient temperature also has an impact on the initiation process. All these studies suggest that a detonation is robustly ignited as soon as a density of $\rho_{\text{crit}} > 1 \times 10^7 \text{ g cm}^{-3}$ and a temperature of $T_{\text{crit}} > 2 \times 10^9 \text{ K}$ are reached simultaneously on length scales of approximately 10 km. Moreover, this critical length scale increases for decreasing C mass fraction suggesting a value of at least $X(\text{C}) \sim 0.4$ is needed.

In simulations of SNe Ia the resolution is not sufficient to capture the details of the detonation initiation process, and, thus, the studies of GCDs mentioned in Sect. 2 ignite a detonation as soon as critical values are reached. Seitenzahl et al. (2016), for example, use a rather optimistic condition of $\rho_{\text{crit}} > 1 \times 10^6 \text{ g cm}^{-3}$ and $T_{\text{crit}} > 1 \times 10^9 \text{ K}$ while Jordan et al. (2012a) and Byrohl et al. (2019) resort to the conservative values of $\rho_{\text{crit}} > 1 \times 10^7 \text{ g cm}^{-3}$ and $T_{\text{crit}} > 2 \times 10^9 \text{ K}$. In this work, we also stuck to these conservative conditions, and, in addition, imposed a limit for the mass fraction of fuel, that is, $X(\text{CO}) \geq 0.8$. The detonation is then initiated in a spherical bubble with a radius of two cell sizes by initializing a second levelset. Since the LEAFS code tracks the ejecta via two nested, expanding grids the resolution in the inner parts becomes worse with ongoing expansion. The size of one cell in the detonation region is $\sim 200 \text{ km}$ in the simulations presented here, and, therefore, highly exceeds the critical length scale necessary for a detonation initiation. Furthermore, no volume burning is included in our simulation, and, thus, its feedback on the hydrodynamic evolution is neglected. The low resolution at late times and the lack of an actively coupled nuclear network therefore make it impossible to definitely predict a detonation. However, a detailed high resolution (up to 125 m per cell) study of the collision region in the GCD scenario has been carried out by Seitenzahl et al. (2009a). They show that a detonation may indeed be ignited as the result of a complex interplay of internal shocks, compression waves and Kelvin-Helmholtz instabilities associated with an inward moving jet near the collision area.

5. Results

5.1. Hydrodynamic evolution

We find that the conditions necessary for initiating a detonation in the context of the PGCD scenario (see Sect. 4) are achieved in most of the models from L21. Only the models ignited at $r_{\text{off}} = 10 \text{ km}$ with central densities in excess of $2.6 \times 10^9 \text{ g cm}^{-3}$ and the rigidly rotating models do not reach the detonation initiation conditions in the collision area. In high central density models (r10_d3.0_Z, r10_d4.0_Z, r10_d5.0_Z, and r10_d6.0_Z from L21), the deflagration is too powerful, that is, high values of $E_{\text{nuc}}^{\text{def}}$, and the pre-expansion of the star is very strong. Hence, the high densities needed for the initiation of a detonation are not reached. For the highest central densities the expansion is so strong that the ashes hardly collide at the antipode (see also discussion in L21). The rigidly rotating models of L21 do not detonate although their nonrotating counterpart, Model r60_d2.0, detonates via the PGCD mechanism. This supports

the work of García-Senz et al. (2016) stating that rotation breaks the symmetry and leads to a weaker focusing of the colliding deflagration products. In summary, high temperatures and densities sufficient to initiate a detonation are found in 23 of the 29 single-spark ignition models presented in L21. We, however, only simulated the detonation phase for eleven models to capture the whole variety in explosion energies and production of ^{56}Ni , respectively. The models omitted are very weak deflagrations resulting in very bright events if a detonation was taken into account.

The evolution of the explosions is similar to that described in earlier works (Plewa 2007; Townsley et al. 2007; Röpke et al. 2007; Seitenzahl et al. 2016; Byrohl et al. 2019): after the ignition of the deflagration, the flame buoyantly rises to the surface of the star accelerated further by turbulent motions (Rayleigh-Taylor and Kelvin-Helmholtz instabilities). Subsequently, the hot ashes race across the surface of the bound core and clash at the side opposite to the deflagration ignition. A stagnation region, that is, a region of almost zero velocity, then develops and two jets are launched inward and outward. They are sustained by the ongoing inflow of material from all lateral directions. A 3D visualization of this process is shown in Fig. 1. As the jet moves inward it compresses and heats matter ahead of it until ρ_{crit} and T_{crit} are reached. These conditions are achieved during the first pulsation phase of the core, and, therefore, all our models belong to the PGCD scenario (Jordan et al. 2012a). Figure 2 shows the central density as a function of time where the detonation initiation of each model is marked with a filled circle. In general, for the weak deflagrations the detonation already occurs before the maximum compression of the core is reached and shifts to later points in time for the stronger ones marking the transition from the PGCD to the GCD scenario. Model r10_d2.6 even ignites during the onset of the expansion phase after the maximum central density was reached in the first pulsation cycle (see Fig. 2). This special situation is shown in Fig. 3. At $t = 6.21 \text{ s}$ (upper row) the core is contracting (inside the white contour) and the inward moving jet pushes material toward the center, and, thus, compresses and heats it. The temperature in the compression region is still low around $1 \times 10^8 \text{ K}$. About 1.5 s later, the core has reached its maximum density and begins to expand again (see the second white contour emerging in the dense core, middle row). The temperature is already near $1 \times 10^9 \text{ K}$. Right before the initiation of the detonation at 8.31 s the infalling material further heats the expanding innermost parts of the core. This heating is strongest where the inward directed jet penetrates into the core until the detonation conditions are reached. The initiation location is indicated by a scatter point in the last row of Fig. 3. The detonation then burns the remaining CO fuel at supersonic velocities in less than $\sim 0.5 \text{ s}$ and the whole star is disrupted.

We emphasize that although many of our simulations robustly ignite a detonation, this is not proof for the mechanism since the resolution in the area of interest is not fine enough to track the turbulent motions and shock waves inside the collision region (see Seitenzahl et al. 2009a) due to the expanding grid approach to track the ejecta. Moreover, we did not employ a reaction network in parallel with the hydrodynamics to capture the nuclear energy generation outside the flame. Therefore, the detonation location as well as t_{det} can be subject to slight variations within a specific model which may introduce some more diversity among the presented PGCD models. The energetic and nucleosynthesis yields as well as the synthetic observables of our simulations, however, are expected to largely capture the characteristics of these explosions.

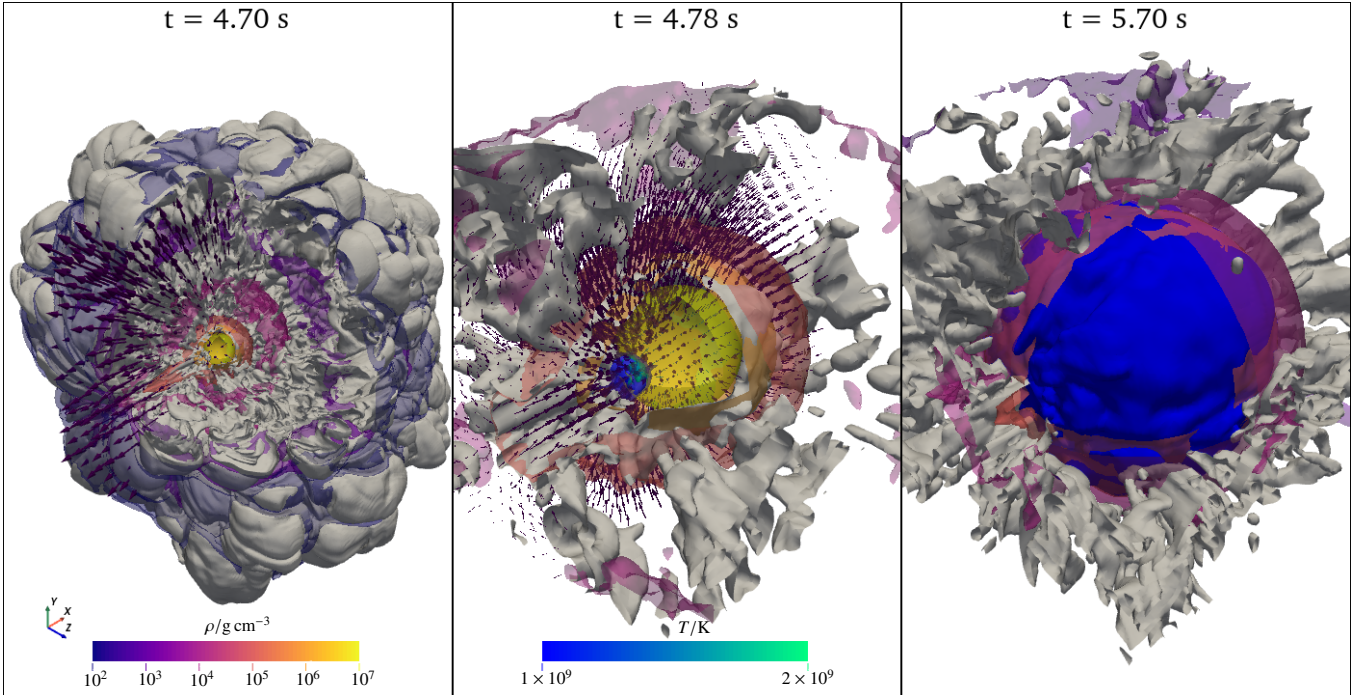


Fig. 1. Flame surface (gray) and density isosurfaces of $\rho = 10^2, 10^3, 10^4, 10^5, 10^6, 10^7 \text{ g cm}^{-3}$ (see colorbar) for model r60_d2.6. *Left panel:* situation prior to detonation initiation at $t = 4.7 \text{ s}$. *Middle panel:* zoom in on the core at $t = 4.78 \text{ s}$. The hotspot with temperatures above $1 \times 10^9 \text{ K}$ is marked by the blue-green contour. *Right panel:* detonation front (blue surface) $\sim 1 \text{ s}$ after initiation. The illustration is not to scale.

5.2. Energetics and nucleosynthesis yields

The total nuclear energy E_{nuc} released during the explosion is sufficient to unbind the whole WD in all simulations of this work. The disruption of the whole star was verified by checking that the kinetic energy of each cell exceeds its gravitational energy at the end of the simulations ($t = 100 \text{ s}$). The ejecta expand homologously. While E_{nuc} ranges from 1.61 to $1.96 \times 10^{51} \text{ erg}$ the energy released in the deflagration $E_{\text{nuc}}^{\text{def}}$ lies between 1.29 and $3.15 \times 10^{50} \text{ erg}$ (see Table 1) which corresponds to 24.1 to 61.4% of the initial binding energy E_{bind} of the star. There is a clear trend that for an increasing deflagration strength ($E_{\text{nuc}}^{\text{def}}$) the time until detonation t_{det} increases and the central density ρ_{det} at t_{det} , E_{nuc} and with it the total kinetic energy E_{kin} decrease. This behavior is well in line with previous studies of the GCD scenario (see Sect. 1). A little scatter is added to these trends by the different initial central densities of the models. As an extreme example, Model r45_d6.0 and Model r82_d1.0 release a comparable amount of nuclear energy in the deflagration but differ significantly in their total energy release E_{nuc} , and, especially in the amount of ^{56}Ni produced. The high initial central density of Model r45_d6.0 also leads to a high value for ρ_{det} of $8.8 \times 10^7 \text{ g cm}^{-3}$ more than twice the value found for Model r82_d1.0. Moreover, the total amount of matter at high densities above 10^7 g cm^{-3} at the detonation initiation sums up to $0.98 M_{\odot}$ in Model r45_d6.0 and to $0.64 M_{\odot}$ in Model r82_d1.0, respectively.

The parameter driving the luminosity of SNe Ia is the mass of ^{56}Ni ejected since it deposits energy into the expanding material via its decay to ^{56}Co , and, subsequently, to ^{56}Fe . The model sequence presented here covers a wide range of luminosities resulting from $M(^{56}\text{Ni})$ ranging between 0.257 and $1.057 M_{\odot}$. This includes ^{56}Ni masses appropriate for faint normal SNe Ia (see e.g. Stritzinger et al. 2006; Scalzo et al. 2014) but also the bright end of the SN Ia subclass (e.g., SN 2012Z eject-

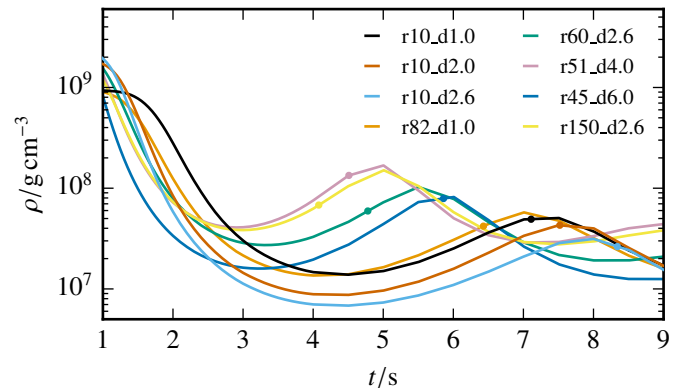


Fig. 2. Central density over time for a representative selection of models. The scatter points indicate the time of the detonation initiation.

ing $\sim 0.2\text{--}0.3 M_{\odot}$ of ^{56}Ni and $\sim M_{\text{Ch}}$ in total Stritzinger et al. 2015 or SN 2011ay Szalai et al. 2015) and O2es-like objects (see SN 2006bt also ejecting $\sim 0.2\text{--}0.3 M_{\odot}$ of ^{56}Ni Foley et al. 2010). On the bright end, luminous normal SNe Ia, the slightly overluminous 91T-like objects (Filippenko et al. 1992) and the transitional events like SN 2000cx (Li et al. 2001) can also be accounted for by our models in terms of $M(^{56}\text{Ni})$ ejected.

The result that models ignited at $r_{\text{off}} = 10 \text{ km}$ do detonate pushes the transition between PGCDs and failed detonations, that is, pure deflagrations, to lower ignition radii compared to the works of Fisher & Jumper (2015) and Byrohl et al. (2019). These studies conclude that below $\sim 16 \text{ km}$ a detonation initiation becomes unlikely, and, thus, the GCD mechanism produces mostly bright explosions. Indeed, the faintest model in our study, Model r10_d2.6, exhausts the viability of the PGCD mechanism since critical conditions for a detonation initiation are only reached at the very end of the contraction phase. However,

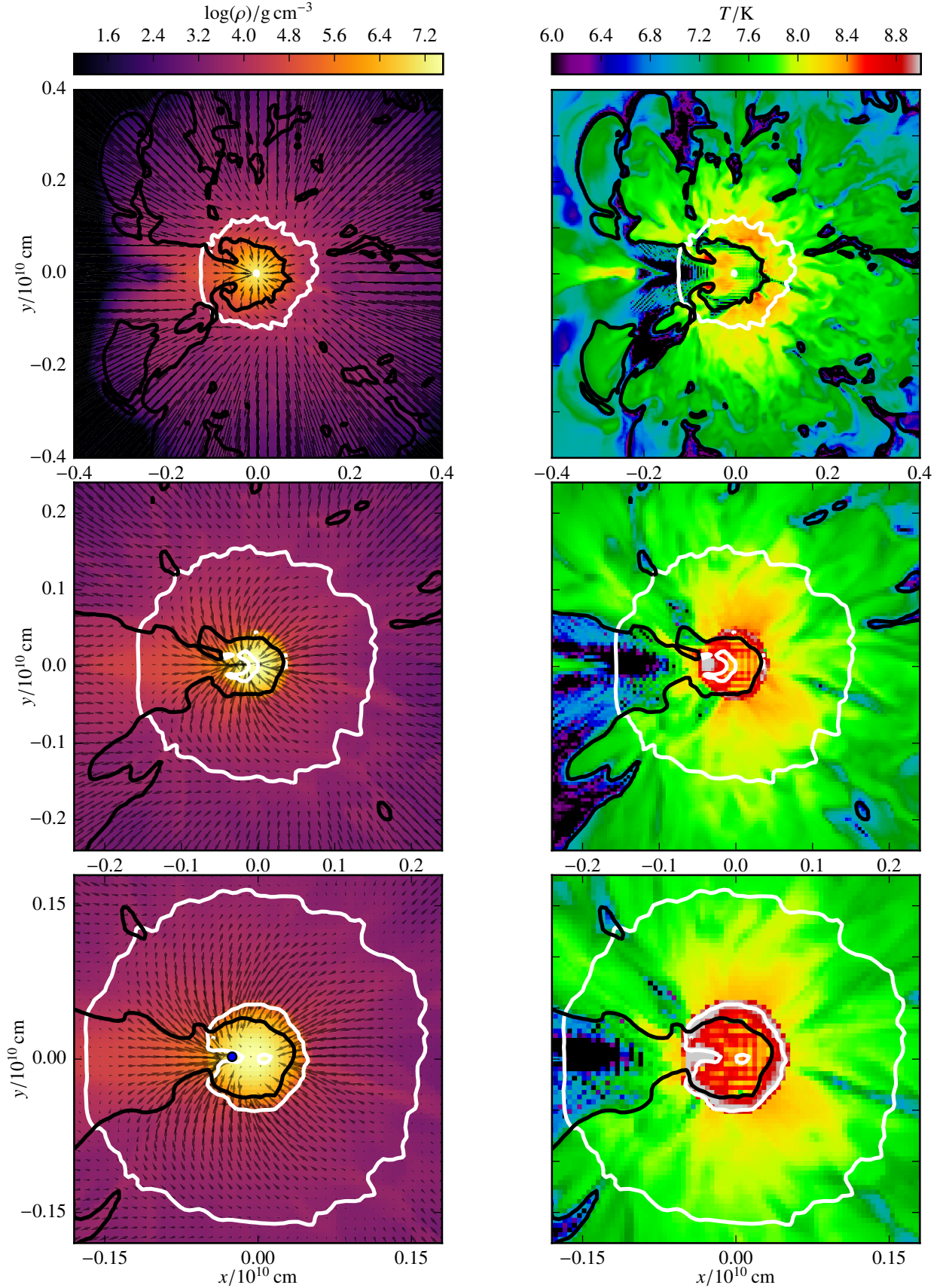


Fig. 3. Slices of the x - y -plane at $z = 0$ showing the density (left column) and the temperature (right column) of Model r10_d2.6 for three points in time: 6.21 s, 7.71 s and 8.31 s (from top to bottom). The white contour marks the zero level of the radial velocity, i.e., it separates regions of expansion and contraction and the black contour indicates $X(\text{CO}) = 0.8$. The blue point in the bottom left panel shows the location of the detonation initiation.

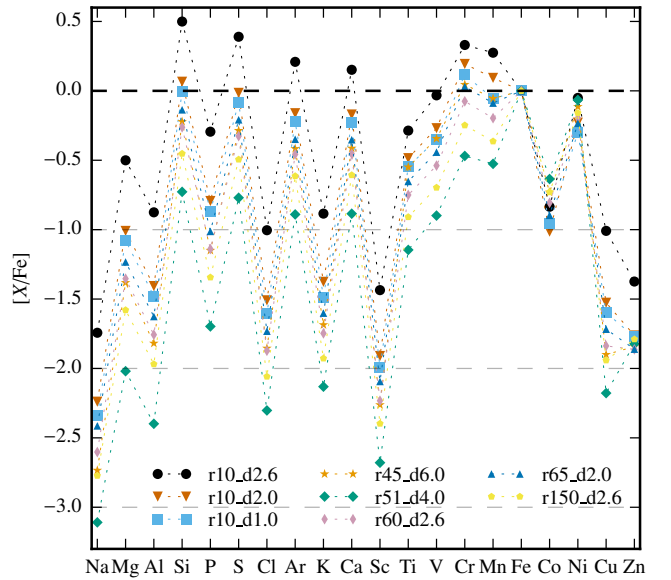
Table 1. Summary of the main properties of the ejected material and the initial conditions.

Model	ρ_c (10^9 g cm^{-3})	r_{ign} (km)	$E_{\text{nuc}}^{\text{def}}$ (10^{50} erg)	E_{nuc} (10^{51} erg)	t_{det} (s)	ρ_c^{det} (10^7 g cm^{-3})	$M(^{56}\text{Ni})$ (M_{\odot})	M_{IGE} (M_{\odot})	M_{IME} (M_{\odot})	$E_{\text{kin,ej}}$ (10^{51} erg)
r10_d1.0	1.0	10	1.98	1.70	7.11	5.12	0.596	0.662	0.521	1.24
r10_d2.0	2.0	10	2.81	1.69	7.52	4.37	0.532	0.612	0.561	1.21
r10_d2.6	2.6	10	3.15	1.61	8.34	2.96	0.257	0.328	0.782	1.14
r82_d1.0	1.0	82	2.31	1.63	6.43	4.12	0.592	0.657	0.507	1.17
r65_d2.0	2.0	65	2.38	1.74	5.65	4.86	0.695	0.773	0.451	1.24
r60_d2.6	2.6	60	1.93	1.79	4.78	5.86	0.793	0.876	0.386	1.30
r57_d3.0	3.0	57	1.86	1.85	4.97	7.00	0.850	0.936	0.346	1.36
r51_d4.0	4.0	51	1.29	1.96	4.51	13.4	1.057	1.164	0.175	1.48
r48_d5.0	5.0	48	1.67	1.96	5.05	11.7	0.916	1.024	0.288	1.47
r45_d6.0	6.0	45	2.19	1.93	5.86	8.80	0.760	0.876	0.412	1.45
r150_d2.6	2.6	150	1.75	1.81	4.09	6.73	0.914	0.999	0.289	1.29

subluminous SNe Ia resulting from the GCD scenario should still be considered rare events as pointed out by [Byrohl et al. \(2019\)](#). They extract a probability density function (PDF) for the ignition radius using data from [Nonaka et al. \(2012\)](#) to interpret their results. The PDF peaks at approximately 50 km and suggests that ignition below ~ 20 km and above ~ 100 km is a scarce event. In detail, they state that only 2.2% of M_{Ch} explosions are ignited below $r_{\text{off}} = 16$ km.

[Flörs et al. \(2020\)](#) examine features of stable Ni, mostly in the form of ^{58}Ni , and Fe in late-time spectra of SNe Ia. They then compare their measured Ni to Fe ratios ($M_{\text{Ni}}/M_{\text{Fe}}$) to theoretical models and conclude that most SNe Ia probably originate from sub- M_{Ch} WDs. In detail, they find that $M_{^{58}\text{Ni}}/M_{^{56}\text{Ni}} < 6\%$ for sub- M_{Ch} models (see references in [Flörs et al. 2020](#)) and larger for M_{Ch} explosions. The reason for this is that more neutron-rich isotopes are favored in nuclear statistical equilibrium at high densities which are reached in M_{Ch} WDs only. We find values of $M_{^{58}\text{Ni}}/M_{^{56}\text{Ni}}$ between 2.4% and 5.1% making it hard to distinguish the PGCD models¹ from sub- M_{Ch} explosions based on this ratio. Moreover, [Flörs et al. \(2020\)](#) state that $M_{^{57}\text{Ni}}/M_{^{56}\text{Ni}}$ is expected to lie above 2% and $M_{^{54,56}\text{Fe}}/M_{^{56}\text{Ni}}$ above 10% for M_{Ch} models. Again, the nucleosynthesis yields of our simulations predict lower values of $M_{^{57}\text{Ni}}/M_{^{56}\text{Ni}} = 1.7\text{--}2.4\%$ and $M_{^{54,56}\text{Fe}}/M_{^{56}\text{Ni}} = 1.8\text{--}14.6\%$. The obvious reason for this finding is that PGCD models exhibit characteristics of a deflagration at high densities and a detonation of a sub- M_{Ch} CO core. Finally, the significant amounts of IMEs produced in Model r10_d2.6 even exceed the mass of IGEs.

The elemental ratios to Fe compared to their solar value $[X/\text{Fe}]$ (isotopes decayed to 2 Gyr) also include characteristics of both M_{Ch} deflagrations and detonations in low-mass WDs. First, supersolar values of $[\text{Mn}/\text{Fe}]$ are achieved in models with a strong deflagration, for instance, Model r10_d2.6 and r10_d2.0 (see Fig. 4). This is in agreement with the commonly accepted fact that M_{Ch} explosions are responsible for a substantial amount of Mn in the Universe ([Seitenzahl et al. 2013b](#); [Lach et al. 2020](#)). For decreasing deflagration strength the contribution of the detonation becomes larger and $[\text{Mn}/\text{Fe}]$ falls below the solar value. Second, we observe high values of $[\text{Cr}/\text{Fe}]$ in some explosions which is a direct imprint of low-mass ($\lesssim 0.8 M_{\odot}$) CO detonation models (compare also Fig. 3 in [Lach et al. 2020](#)) but special


Fig. 4. Elemental abundances over Fe in relation to their solar value for a few representative models of the parameter study.

for M_{Ch} models. Third, the usual overproduction of stable Ni in M_{Ch} deflagrations is suppressed by the detonation yields. Finally, Fig. 4 also shows signs of the strong odd-even effect in the detonation IME yields smoothed out by the deflagration products (compare again Fig. 3 in [Lach et al. 2020](#)). The α -elements Si, S, Ar and Ca are even synthesized in supersolar amounts in the core detonation of Model r10_d2.6. The rest of the models show rather low values of $[\alpha/\text{Fe}]$ more typical for M_{Ch} deflagrations. In summary, the nucleosynthesis yields of faint (r10_d2.6) to intermediately bright (r10_d2.0) models show characteristics of low-mass CO detonations as well as M_{Ch} explosions. As the deflagration strength decreases, the total elemental yields more and more resemble those of a pure CO detonation in a WD of approximately $1 M_{\odot}$. Nevertheless, the pollution of the outer layers with deflagration products still has some impact on the observables (see Sect. 6).

5.3. Ejecta structure

The expelled material is spherically symmetric on large scales, especially the deflagration ashes which reach maximum

¹ The full set of isotopic yields and also the angle averaged optical spectral time series and UVOIR bolometric light curves calculated in the radiative transfer simulations will be published on HESMA [Kromer et al. \(2017\)](#).

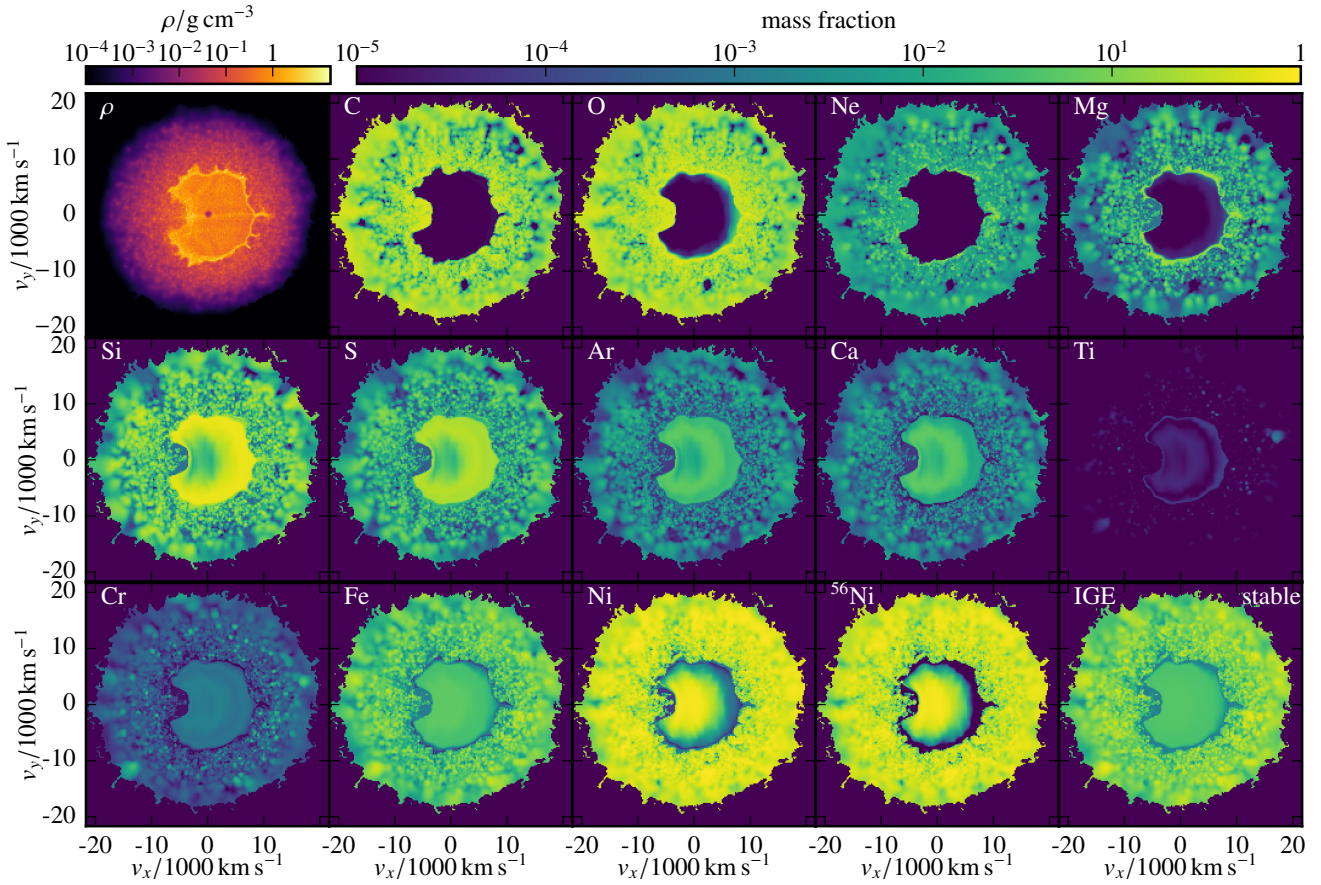


Fig. 5. Color-coded density and elemental abundance slices in the v_x - v_y -plane for Model r10_d2.6.

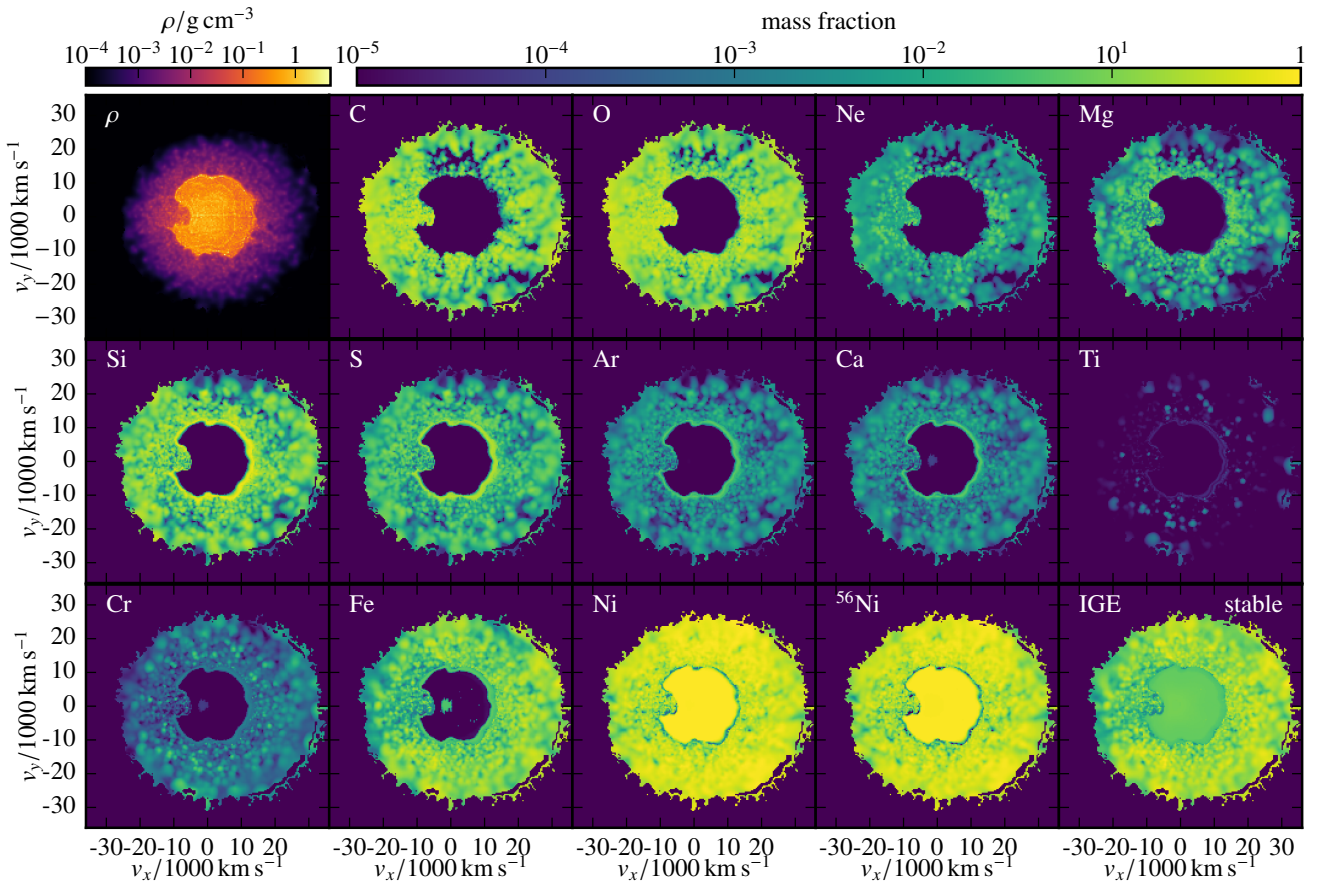


Fig. 6. Same as Fig. 5, but for Model r51_d4.0.

velocities from $\sim 19\,000\text{ km s}^{-1}$ (r10_d2.6, see Fig. 5) up to $\sim 29\,000\text{ km s}^{-1}$ (r51_d4.0, see Fig. 6). The shell of well mixed deflagration products extends down to $\sim 8000\text{ km s}^{-1}$ in Model r10_d2.6 and $\sim 11\,000\text{ km s}^{-1}$ for Model r51_d4.0. The outer boundary of the detonation products, primarily consisting of IMEs, is not exactly spherical but slightly elliptical and more elongated along the y -axis (perpendicular to the line connecting the deflagration and the detonation initiation). This structure is more pronounced in Model r82_d1.0 (see Fig. 7) and only very subtle in the most energetic explosion, that is, the strongest detonation, r51_d4.0. Moreover, the detonation region exhibits a cusp of deflagration products on the detonation side (left-hand side) disturbing the spherical structure. This is the region of the jet of ashes penetrating into the core until the detonation conditions are reached.

A comparison of the ejecta structure to Fig. 4 of Seitenzahl et al. (2016) reveals an important difference: In their work the detonating core is not centered inside the deflagration ashes. This means that the envelope of burned material is thicker on the deflagration ignition side than on the detonation side leading to significant viewing angle effects. In our work the detonation products lie relatively well centered inside the shell of deflagration ashes (see Figs. 5–8). Only a very close inspection of Model r51_d4.0 (brightest) and Model r10_d2.6 (faintest) reveals that the deflagration envelope is slightly thicker on the deflagration side in Model r51_d4.0 than on the antipode. The opposite holds for Model r10_d2.6: the deflagration envelope is slightly thicker on the deflagration side in Model r51_d4.0 than on the antipode. The opposite holds for Model r10_d2.6. In addition to this minor asymmetry, viewing angle effects can be expected to originate from the irregularly shaped core detonation. This difference between our models and the model of Seitenzahl et al. (2016) is very likely due to the distinct detonation initiation conditions. Since Seitenzahl et al. (2016) use optimistic values of $\rho = 10^6\text{ g cm}^{-3}$ and $T = 10^9\text{ K}$ the detonation is ignited very early ($t_{\text{det}} = 2.37\text{ s}$) almost immediately after the ashes have collided. Therefore, the amount of ashes on the detonation side has not piled up significantly and the detonation also ignites more off-center than found in this study. In our models the detonation only ignites after a prolonged period of contraction and the penetration of a jet into the core ($t_{\text{det}} > 4.5\text{ s}$) providing enough time for the deflagration products to engulf the core homogeneously.

The 1D-averaged velocity profiles of various elements and ^{56}Ni are shown in Fig. 9 for a faint (r10_d2.6), a moderately bright (r10_d2.0) and an overluminous (r51_d3.0) model. All explosions are characterized by mixed deflagration products at high velocities dominated by ^{56}Ni . The second most abundant elements are unburned C and O followed by Fe and Si. Less abundant IMEs present in the outer ejecta are S, Mg, and Ca while the mass fractions of Ar, Ti and Cr stay below 10^{-3} . Going to lower velocities, the IMEs individually (from light to heavy) rise to a maximum and Fe and ^{56}Ni exhibit a local minimum. This stratified region was burned in the detonation at rather low densities via incomplete silicon burning. The innermost regions are then dominated by ^{56}Ni . The central density at detonation in Model r10_d2.6, however, is so low that even a significant fraction of IMEs is present at low velocities.

From the ejecta structure it is evident that all of these models will display IGEs in their early-time spectra. This characteristic is in agreement with SNe Iax Foley et al. (2013), Jha (2017) as well as the overluminous 91T-like events. Normal SNe Ia, however, are dominated by IMEs around maximum light. Moreover, the fact that stable IGE are primarily found in the outer lay-

ers at high velocity neither matches the properties of 91T-like (Sasdehli et al. 2014; Seitenzahl et al. 2016) objects nor normal SNe Ia (Mazzali et al. 2007). The distribution of stable IGEs is also a problem for the method used in Flörs et al. (2020) (see also Sect. 5.2) to distinguish between M_{Ch} and sub- M_{Ch} mass models since only a small fraction of stable IGEs will be visible in late-time spectra.

6. Synthetic observables

To obtain synthetic spectra and light curves for our sequence of PGCD models we carried out time-dependent 3D Monte-Carlo RT simulations using the ARTIS code (Sim 2007; Kromer & Sim 2009). For each RT simulation we remapped the ejecta structure to a 50^3 grid. 10^8 photon packets were then tracked through the ejecta for 450 logarithmically spaced time steps between 0.1 and 100 days since explosion. We used the atomic data set described by Gall et al. (2012). We adopted a gray approximation in optically thick cells (cf. Kromer & Sim 2009) and for times earlier than 0.12 days post explosion local thermal equilibrium (LTE) is assumed. After this, we adopted our approximate NLTE description as presented by Kromer & Sim (2009). We calculated line of sight dependent light curves for 100 bins of equal solid-angle and line of sight dependent spectra for 10 different observer orientations of equal angle spacing that lie on the x - y -plane. The viewing angle dependent spectra we present here were calculated with the method described by Bulla et al. (2015) utilizing “virtual packets” leading to a significant reduction in the Monte-Carlo noise.

Figure 10 shows the bolometric and *UBVRI* band angle-averaged light curves for a selection of our PGCD models spanning from the faintest to the brightest model in our sequence. Observed light curves representing different subclasses of SNe Ia relevant for comparison to our model sequence are included for comparison: SN 1991T after which the luminous 91T-like subclass is named, SN 2011fe, a normal SN Ia and SN 2012Z, which is one of the bright members of the subluminous subclass of SNe Iax. We have shifted the explosion epochs of the observed light curves to better compare to the light curve evolution of the PGCD models. The explosion epochs we adopted are JD 2448359.5 for SN 1991T (2 days later than estimated by Filippenko et al. 1992), JD 2455800.2 for SN 2011fe (3 days later than estimated by Nugent et al. 2011) and JD 2455955.9 for SN 2012Z (2 days later than estimated by Yamanaka et al. 2015).

From Fig. 10 we can see that a feature of our PGCD model light curves is a relatively sharp initial rise over approximately the first 5 days post explosion (particularly in the *U* and *B* bands). After this, the light curves become quite flat and complex, with the exception of the faintest PGCD model r10_d2.6 (blue in Fig. 10), which shows an initial rapid decline post peak in the *U* and *B* bands. One of the intermediate brightness models shown in Fig. 10, Model r10_d1.0 (green), even exhibits a double peak in its *U* and *B* band light curves. This peculiar light curve behavior is driven by the interplay between the detonation ash at the center of the models and the deflagration ash which surrounds it. In all bands the radiation emitted from the decay of ^{56}Ni in the deflagration ash dominates the initial rapid rise. However, as the band light curves approach peak, the contribution from the radiation emitted from the deflagration ash begins to diminish while the contribution of the radiation emitted from the detonation ash increases to become the dominant source of the luminosity for the band light curves. Such interplay between the deflagration and detonation ash distinguishes these PGCD models from pure detonation models (e.g., Sim et al. 2010; Blondin et al. 2017;

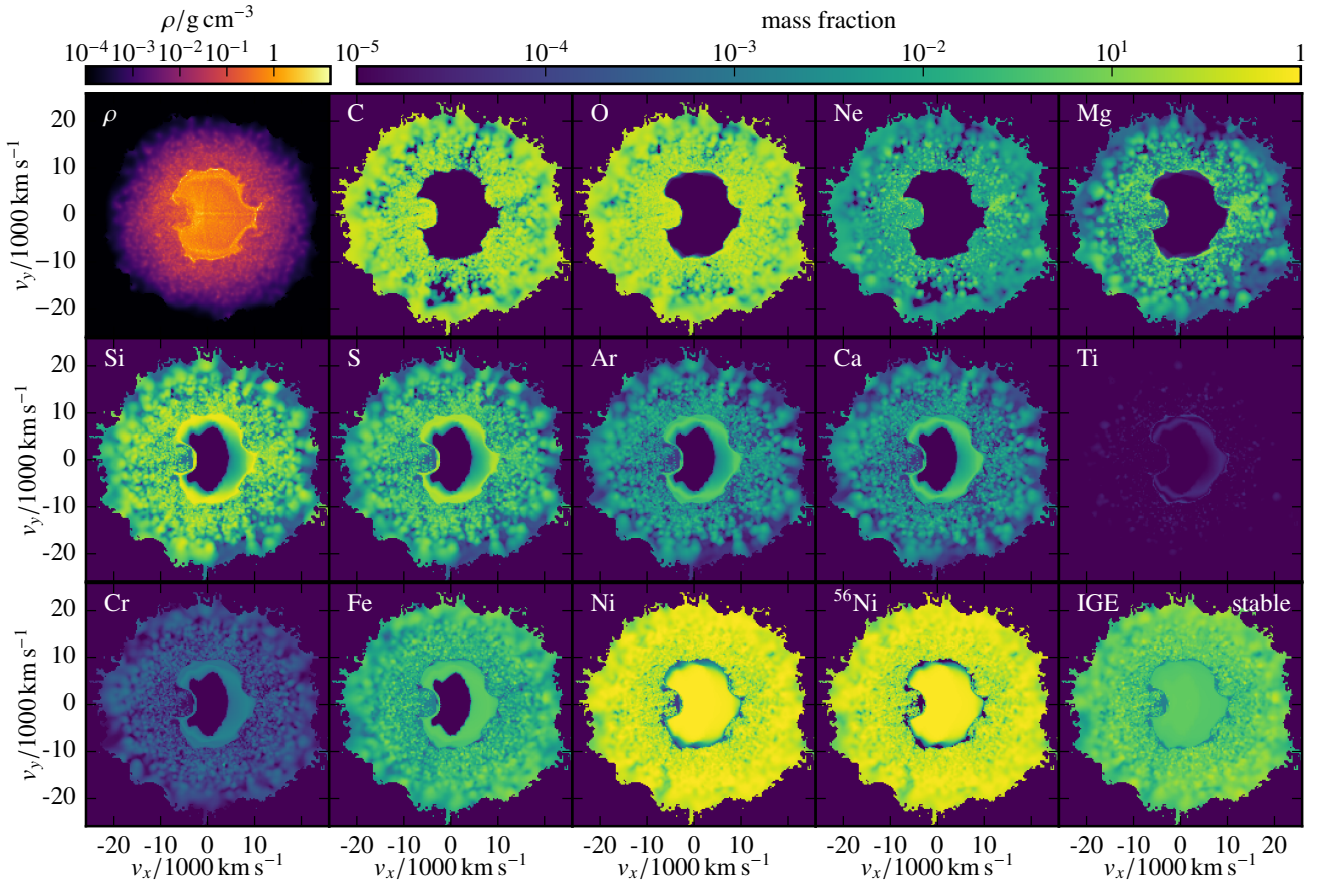


Fig. 7. Same as Fig. 5, but for Model r82_d1.0.

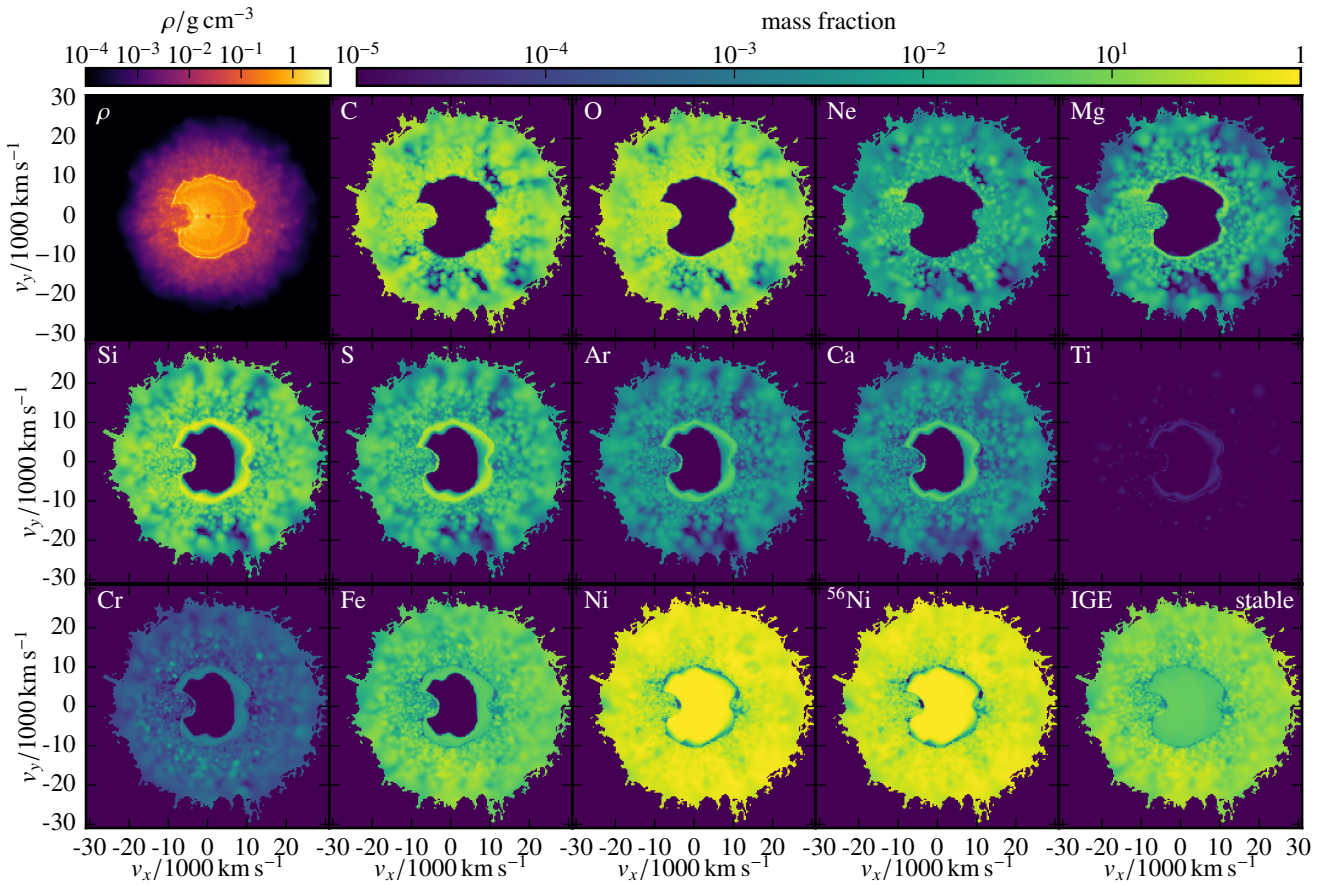


Fig. 8. Same as Fig. 5, but for Model r60_d2.6.

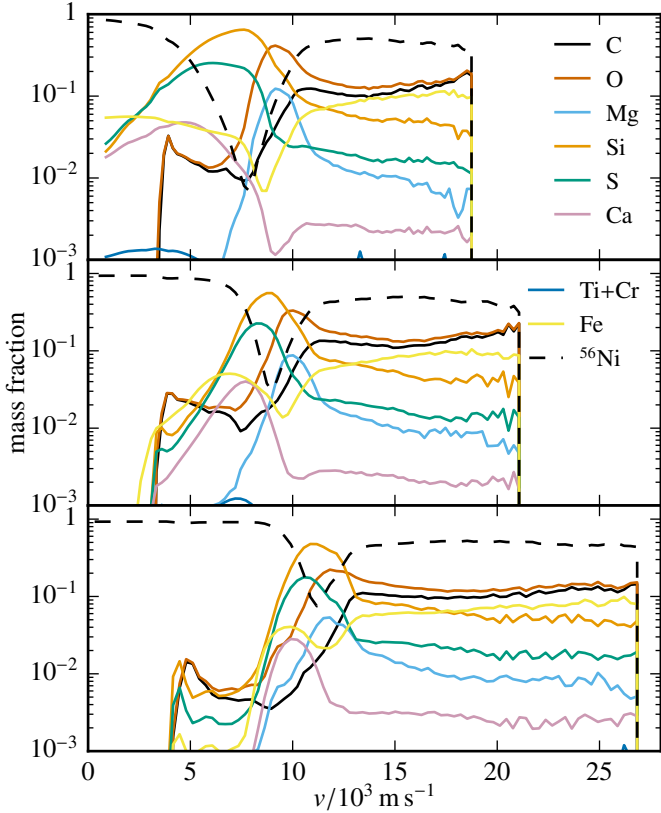


Fig. 9. 1D-averaged velocity profiles for C, O, Mg, Si, S, Ca, Ti+Cr, Fe and ^{56}Ni . *Upper panel:* data for Model r10_d2.6, *middle panel:* Model r10_d2.0 and *lower panel:* Model r57_d3.0.

Shen et al. 2018) and DD models (e.g., Gamezo et al. 2005; Röpke & Niemeyer 2007; Maeda et al. 2010b; Seitenzahl et al. 2013a).

It is clear from Fig. 10 that the best match is found between the band light curves of the brightest PGCD model in our sequence, Model r51_d4.0 (red) and SN 1991T. This is consistent with the results of Seitenzahl et al. (2016) who found the best match between their GCD model and SN 1991T. Model r51_d4.0 reproduces the initial rise of SN 1991T well in all bands until approximately 10 days post explosion with good agreement continuing to later times for certain bands. In particular, the model shows good agreement in *B* band with SN 1991T across all epochs shown. However, the band light curves of the model become too red as we move to later times. In particular, Model r51_d4.0 predicts a secondary peak that is approximately half a magnitude brighter than the first peak. A secondary peak of this size in *I* band is not observed for SN 1991T leading to a difference of over half a magnitude between the model and SN 1991T around the time of this secondary peak.

The band light curves of our PGCD models span a wide range of peak brightnesses (variations of almost 2 mag are predicted for the models in *U*, *B* and *V* bands). The models therefore cover a range of brightnesses which encompasses luminous SNe Ia such as those in the 91T-like subclass, normal SNe Ia and bright members of the subluminous SNe Iax class. However, the band light curves of our PGCD models show poor agreement with the normal SNe Ia, SN 2011fe and the bright SNe Iax, SN 2012Z in terms of colors and overall light curve evolution. Therefore, while we are able to reach lower brightnesses with our sequence compared to previous works the disagreement in

the predicted light curves disfavors them as an explanation for either normal SNe Ia or SNe Iax.

From our light curve comparisons discussed above our PGCD models appear best suited to explain the 91T-like subclass (if any). In Fig. 11 we compare a selection of viewing angle dependent spectra, over a variety of epochs, for our brightest model (r51_d4.0, red), this is the model which produces best overall agreement in terms of light curves and spectra with SN 1991T. As was the case for the GCD model of Seitenzahl et al. (2016), our PGCD models are almost symmetric about the axis defined by the center of the star and the position of the initial deflagration ignition spark (located on the positive *x*-axis in Figs. 5–8). Therefore, we focus on different observer orientations that lie in the *x*-*y*-plane to demonstrate the viewing angle effects here. In Fig. 11 we identify these with ϕ , the angle made between the observer orientation and the *x*-axis. The $\phi = 0^\circ$ direction corresponds to the observer viewing from the side where the initial deflagration spark was placed while the $\phi = 180^\circ$ direction corresponds to the side where the detonation occurred. The viewing angles shown in Fig. 11 are representative of the range of brightness exhibited by this model depending on the line of sight. Model spectra are shown relative to explosion as labeled. As in Fig. 10 we adopted an explosion date of JD 2448359.5 for the SN 1991T spectra we compare to.

From Fig. 11 we can see that there are noticeable viewing angle variations in the spectra of Model r51_d4.0, for wavelengths of $\sim 5000 \text{ \AA}$ or less, at all epochs. This viewing angle dependency is driven by the asymmetric distribution of the deflagration ashes in the model that are rich in IGEs. As we can see from Fig. 6, which shows the ejecta structure of slices along the *x*-*y*-plane for Model r51_d4.0, the deflagration ashes extend over a greater range of velocities toward the side where the initial deflagration was ignited at $\phi = 0^\circ$, (positive *x*-axis in Fig. 6). This leads to increased line blanketing by IGEs for lines of sight looking close to this initial deflagration spark (e.g., $\phi = 0^\circ$ spectra, red in Fig. 11), and, thus, the flux in the blue and UV is significantly reduced. The deflagration ashes, however, only cover a significantly greater velocity range for a relatively small window of viewing angles. Looking along $\phi = 72^\circ$ (green in Fig. 11), we already see the line blanketing by IGEs in the blue and UV is significantly reduced and the flux at wavelengths less than $\sim 5000 \text{ \AA}$ is already quite similar to what is observed for the viewing angle looking toward where the detonation is first ignited ($\phi = 180^\circ$, blue in Fig. 11). Wavelengths greater than $\sim 5000 \text{ \AA}$ are less impacted by line blanketing due to IGEs, and, thus, do not show significant viewing angle dependencies. Additionally, as we move to later times, the viewing angle effects become less noticeable for the model as the outer layers become more optically thin. We find the same viewing angle dependency is observed in the *B* and *U* band light curves of Model r51_d4.0. The *U* band peak magnitudes vary between -19.5 to -20.5 while the *B* band peak magnitudes vary between -19.4 to -19.9 . There is only very minimal viewing angle variation in the *VRI* band light curves. Overall, Model r51_d4.0 exhibits viewing angle dependencies comparable to those shown by the GCD model of Seitenzahl et al. (2016). Indeed, we find significant viewing angle dependencies for all of our models, with all models showing the largest viewing angle variation in the *U* and *B* bands. However, for fainter models the viewing angle variations in the *VRI* bands become increasingly prominent. We also find that the brightest and faintest viewing angles can correspond to significantly different observer orientations depending on the distribution of deflagration ash and differences between the irregularly shaped core detonations in each individual model.

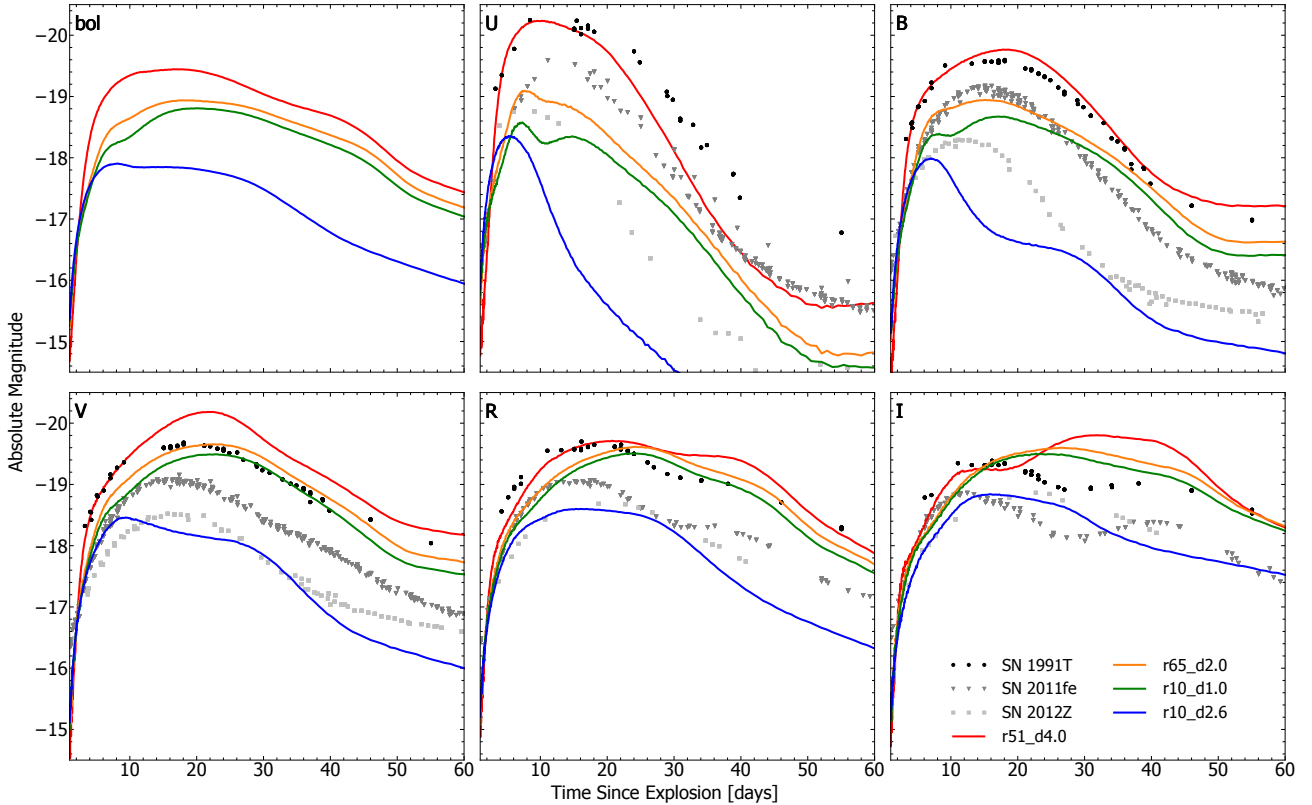


Fig. 10. Angle averaged bolometric and *UBVRI* band light curves for a subset of our PGCD models. Observed light curves representing different subclasses of SNe Ia are also included. SN 1991T (Lira et al. 1998), SN 2011fe (Richmond & Smith 2012; Tsvetkov et al. 2013; Munari et al. 2013; Brown et al. 2014; Stahl et al. 2019) and SN 2012Z (Stritzinger et al. 2015; Brown et al. 2014; Stahl et al. 2019). We made use of the Open Supernova Catalogue (Guillochon et al. 2017) to obtain the observed photometry.

The two brighter viewing angles shown in Fig. 11 (blue and green) show best spectroscopic agreement with SN 1991T, in particular at 9.1 and 12.9 days since explosion where they produce a good match to the overall flux of SN 1991T across all wavelengths. However, these viewing angles provide a poor match to the blue and UV flux at the earliest epoch shown and also have significantly too much flux in the red wavelengths for the last two epochs shown. Therefore, although promising, we find no individual viewing angles which provide a consistently good match to the spectra of SN 1991T over multiple epochs. Additionally, as noted above and already found for the GCD model of Seitenzahl et al. (2016), none of the PGCD models produce good spectroscopic agreement with normal SNe Ia, showing IME features which are too weak and spectra which are too red particularly toward later epochs.

As we have discussed above the band light curves of the faintest PGCD model in our sequence do not produce good agreement with those of bright SNe Iax such as SN 2012Z. However, our faintest model has a brightness similar to bright SNe Iax. As 91T-like SNe Ia and SNe Iax are known to be spectroscopically similar before peak and a more stratified ejecta structure as opposed to pure deflagration models is suggested for bright SNe Iax (Barna et al. 2017; Stritzinger et al. 2015) we briefly explore the spectroscopic comparisons between our faintest PGCD model and the bright SN Iax, SN 2012Z. In particular, we investigated whether our PGCD model spectra might compare more favorably than the pure deflagration models of L21. Figure 12 shows spectroscopic comparisons between the bright SN Iax, SN 2012Z, the angle-averaged spectra for our faintest PGCD model (r10_d2.6, red) and the brightest

model in our sequence of pure deflagration models from L21 (r10_d4.0_Z, blue). We compare these models to SN 2012Z as they are the models from each sequence that match the brightness of SN 2012Z most closely. From Fig. 12 we see that the spectra of our PGCD and pure deflagration models show significantly different flux in both the epochs shown as well as a different evolution in their flux between the two epochs. However, they do predict many of the same spectral features, although the line velocities of these features are noticeably more blue shifted for our PGCD model. This is to be expected as the PGCD model is more energetic than the pure deflagration model leading to higher ejecta velocities. For the earlier epoch shown (8.1 days since explosion) the pure deflagration model (blue) shows better spectroscopic agreement with SN 2012Z as it matches the overall flux profile of SN 2012Z much better. At this epoch our PGCD model (red) shows a large amount of emission between ~ 5000 to 6000 \AA as a result of the re-emission of radiation absorbed by IGEs in the UV. This is not observed in the spectrum of SN 2012Z at this epoch. For the later spectra shown (22.7 days post explosion) the PGCD model shows better overall flux agreement with the spectra of SN 2012Z than the deflagration model. This is because the deflagration model is too fast in decline compared to SN 2012Z which is a general issue that is encountered when we compare pure deflagration models to SNe Iax (see L21 for more details). However, the deflagration model reproduces the locations of individual spectral features of SN 2012Z at least as successfully as the PGCD model and in particular provides a better match for the location of the Ca II infrared triplet than the PGCD model. Previous work, presented by L21, has also shown that we are able to produce reasonably

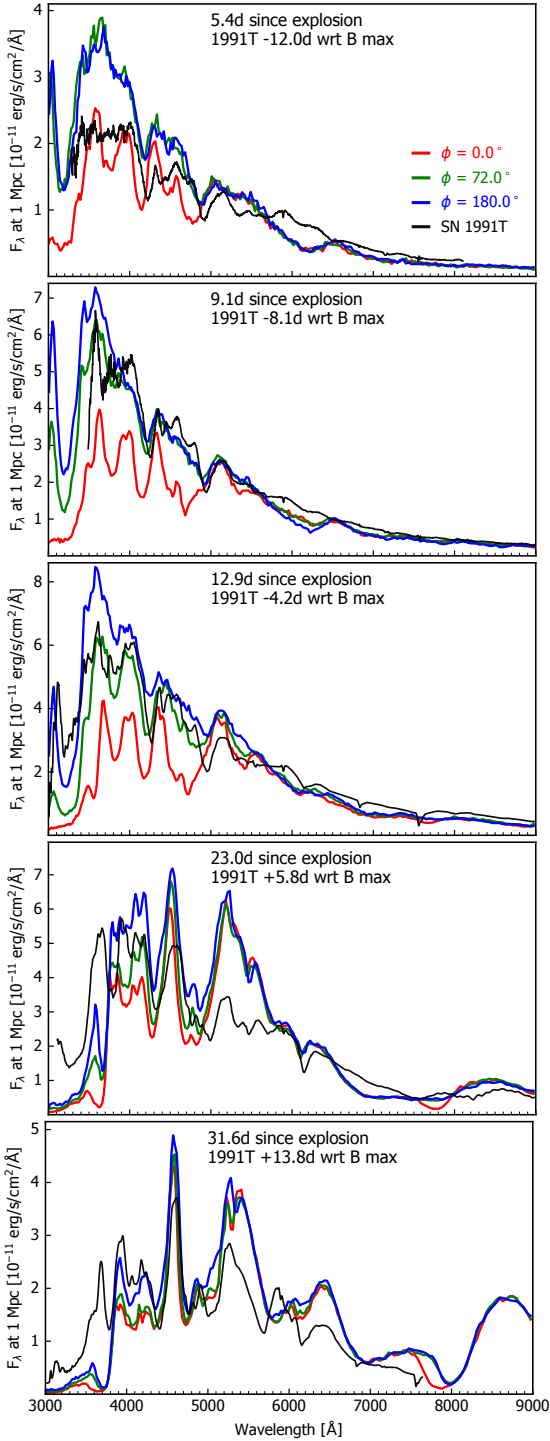


Fig. 11. Spectra over a variety of epochs for a selection of viewing angles for our brightest PGCD model (r51_d4.0). Observed spectra of SN 1991T (Ruiz-Lapuente et al. 1992; Phillips et al. 1992; Filippenko et al. 1992) are included for comparison. The observed spectra have been flux calibrated to match the photometry, dereddened using $E(B-V) = 0.13$ as estimated by Phillips et al. (1992) and deredshifted taking $z = 0.006059$ from interstellar Na. We take 30.76 as the distance modulus to SN 1991T (Saha et al. 2006).

good spectroscopic and light curve agreement with intermediate luminosity SNe Iax using our sequence of pure deflagration models. However, none of our PGCD models presented here are faint enough to produce agreement with intermediate luminosity SNe Iax. Therefore, our pure deflagration models

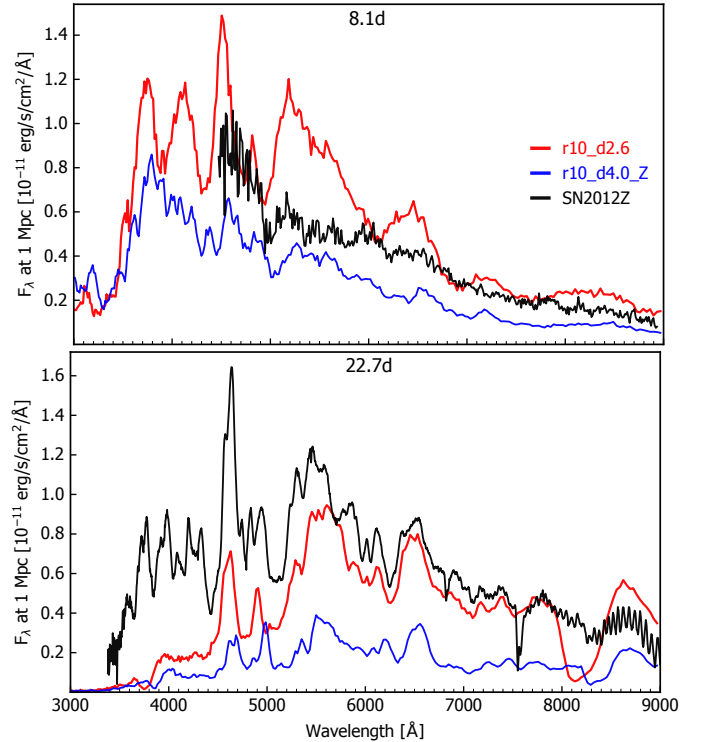


Fig. 12. Spectroscopic comparisons between the bright SN Iax, SN 2012Z (Stritzinger et al. 2015), along with angle-averaged spectra for our faintest PGCD model (r10_d2.6, red) and the brightest pure deflagration model from our previous pure deflagration study, L21 (r10_d4.0_Z, blue). Times displayed are relative to explosion for all spectra. We take the explosion time estimated for SN 2012Z by Yamanaka et al. (2015). The observed spectra of SN 2012Z have been flux calibrated to match the photometry. Additionally, they have been corrected for distance, red shift and reddening assuming a distance of 33.0 Mpc, $z = 0.007125$ and $E(B-V) = 0.11$ (Stritzinger et al. 2015).

do appear more promising to explain SNe Iax than our PGCD models.

7. Conclusions

We used the pure deflagration simulations of L21 as initial models for a parameter study of the GCD scenario containing 11 models. The initial models used in this work were ignited in a single spark off-center at varying radii r_{off} between 10 and 150 km. Moreover, different central densities of $\rho_c = 1, 2, 2.6, 3, 4, 5, 6 \times 10^9 \text{ g cm}^{-3}$ were explored. The suite of models presented here constitutes one of the largest systematic studies of the GCD scenario to date.

Our explosions proceed similar to the models presented in earlier works (Plewa et al. 2004; Plewa 2007; Townsley et al. 2007; Röpke et al. 2007; Jordan et al. 2008; Meakin et al. 2009; Seitenzahl et al. 2016), and Byrohl et al. (2019): The deflagration front burns toward the surface, burned ashes spread around the WD and collide at the opposite side of the star. This collision produces an inwardly directed jet which compresses and heats material ahead and leads to the initiation of a detonation. In the case of our models, this compression is aided by the coincidence of the first pulsation phase of the WD and the collision of the ashes, and, thus, our models resemble the “pulsationally assisted gravitationally confined detonation” scenario presented by Jordan et al. (2012b).

We find that all but the most energetic models from L21 satisfy the conditions for a detonation, that is, they simultaneously reach values of $\rho_{\text{crit}} > 1 \times 10^7 \text{ g cm}^{-3}$ and $T_{\text{crit}} > 2 \times 10^9 \text{ K}$ in one grid cell. Moreover, we can corroborate the results of García-Senz et al. (2016) who state that rotation disturbs the focus of the collision, and, therefore, suppresses the initiation of a detonation in the GCD mechanism. In addition, the combination of different central densities and ignition locations introduces some diversity to the inverse proportionality of deflagration strength and synthesized mass of ^{56}Ni .

The set of models produces a wide range of ^{56}Ni masses, that is, brightnesses, from 1.057 down to 0.257 M_{\odot} which is the faintest GCD model published to date. This range comprises the subluminous SNe Iax, normal SNe Ia as well as the slightly overluminous 91T-like objects. We also study, inspired by Flörs et al. (2020), the ratio of stable IGEs to ^{56}Ni in the ejecta and find that the GCD scenario blurs the boundaries between typical nucleosynthesis products of the sub- M_{Ch} and M_{Ch} scenario. Since our models contain a deflagration as well as a detonation a mixture of characteristics of both channels is reasonable. The same holds for the [Mn/Fe] value which ranges from subsolar to supersolar values. (Detailed nucleosynthesis yields will be published on HESMA (Kromer et al. 2017) as will the angle-averaged optical spectral time series and UVOIR bolometric light curves calculated in the radiative transfer simulations).

Furthermore, the *UBVRI* band light curves show a complex evolution reflecting the transition to a detonation at various states of the pre-expanded WD core. We compare model light curves to the bright SN 1991T, the normal event SN 2011fe and the SN Iax SN 2012Z finding that only SN 1991T can be reproduced for early times up to 10 d after explosion. At later epochs (≥ 20 d), the light curves exhibit an unusually prominent secondary maximum. The *B* band, however, shows good agreement with SN 1991T at all times. While there is still some disagreement between observations and models the GCD or PGCD scenario is still the most promising scenario for 91T-like SNe presented to date.

We also report a strong viewing angle dependency (our analysis presented here focuses on the brightest model in the sequence) showing line blanketing due to the prominent deflagration ashes on the ignition side, and, hence, a suppressed flux at blue wavelengths below $\sim 5000 \text{ \AA}$. A spectral comparison to SN 1991T reveals that good agreement is only found for intermediate times (9.1 and 12.9 d after explosion) for viewing angles away from the deflagration ignition spot. For late times, however, these viewing angle dependencies vanish since the detonation products dominate the spectra.

Despite the poor agreement of the light curve evolution, we compared the spectra of the faintest model in the study to SN 2012Z. In addition, we add the brightest pure deflagration model of L21 and conclude that deflagrations still provide a better match to these transients and that SNe Iax are most probably not the result of the GCD scenario.

Since our simulations are not able to predict whether a detonation is really initiated we speculate that SNe Iax and 91T-like SNe might originate from the same progenitor system. In the case of a failed detonation (more likely for strong deflagrations) a SN Iax arises and in the case of a successful detonation (more likely for weak deflagrations) the result is a 91T-like transient. This is a reasonable explanation for their similar spectra near maximum light and their very different luminosity and post-maximum evolution. It should be noted that the ignition of a deflagration in a M_{Ch} WD is a stochastic process, and that strong deflagrations resulting from an ignition near the center can be

considered a rare event (Nonaka et al. 2012; Byrohl et al. 2019). However, more simmering phase simulations with different WD models are still needed to validate the findings of Nonaka et al. (2012). Finally, although our fainter models do not reproduce any observations of SNe Ia, these might still occur in nature as rare events not detected to date and they could be identified due to their characteristic observables.

Acknowledgements. This work was supported by the Deutsche Forschungsgemeinschaft (DFG, German Research Foundation) – Project-ID 138713538 – SFB 881 (“The Milky Way System”, subproject A10), by the ChETEC COST Action (CA16117), and by the National Science Foundation under Grant No. OISE-1927130 (IRENA). FL and FKR acknowledge support by the Klaus Tschira Foundation. FPC acknowledges an STFC studentship and SAS acknowledges funding from STFC Grant Ref: ST/P000312/1. NumPy and SciPy (Oliphant 2007), IPython (Pérez & Granger 2007), and Matplotlib (Hunter 2007) were used for data processing and plotting. The authors gratefully acknowledge the Gauss Centre for Supercomputing e.V. (www.gauss-centre.eu) for funding this project by providing computing time on the GCS Supercomputer JUWELS (Jülich Supercomputing Centre 2019) at Jülich Supercomputing Centre (JSC). Part of this work was performed using the Cambridge Service for Data Driven Discovery (CSD3), part of which is operated by the University of Cambridge Research Computing on behalf of the STFC DiRAC HPC Facility (www.dirac.ac.uk). The DiRAC component of CSD3 was funded by BEIS capital funding via STFC capital grants ST/P002307/1 and ST/R002452/1 and STFC operations grant ST/R00689X/1. DiRAC is part of the National e-Infrastructure. We thank James Gillanders for assisting with the flux calibrations of the observed spectra.

References

- Arnett, W. D. 1969, *Ap&SS*, 5, 180
- Barna, B., Szalai, T., Kromer, M., et al. 2017, *MNRAS*, 471, 4865
- Baron, E., Jeffery, D. J., Branch, D., et al. 2008, *ApJ*, 672, 1038
- Blondin, S., Dessart, L., Hillier, D. J., & Khokhlov, A. M. 2013, *MNRAS*, 429, 2127
- Blondin, S., Dessart, L., Hillier, D. J., & Khokhlov, A. M. 2017, *MNRAS*, 470, 157
- Branch, D., Baron, E., Thomas, R. C., et al. 2004, *PASP*, 116, 903
- Bravo, E., & García-Senz, D. 2006, *ApJ*, 642, L157
- Bravo, E., & García-Senz, D. 2009, *ApJ*, 695, 1244
- Bravo, E., García-Senz, D., Cabezón, R. M., & Domínguez, I. 2009, *ApJ*, 695, 1257
- Bravo, E., Gil-Pons, P., Gutiérrez, J. L., & Doherty, C. L. 2016, *A&A*, 589, A38
- Brown, P. J., Breeveld, A. A., Holland, S., Kuin, P., & Pritchard, T. 2014, *Ap&SS*, 354, 89
- Bulla, M., Sim, S. A., & Kromer, M. 2015, *MNRAS*, 450, 967
- Byrohl, C., Fisher, R., & Townsley, D. 2019, *ApJ*, 878, 67
- Colella, P., & Woodward, P. R. 1984, *J. Comput. Phys.*, 54, 174
- Denissenkov, P. A., Truran, J. W., Herwig, F., et al. 2015, *MNRAS*, 447, 2696
- Dessart, L., Blondin, S., Hillier, D. J., & Khokhlov, A. 2014, *MNRAS*, 441, 532
- Dursi, L. J., & Timmes, F. X. 2006, *ApJ*, 641, 1071
- Filippenko, A. V., Richmond, M. W., Matheson, T., et al. 1992, *ApJ*, 384, L15
- Fink, M., Kromer, M., Seitenzahl, I. R., et al. 2014, *MNRAS*, 438, 1762
- Fisher, R., & Jumper, K. 2015, *ApJ*, 805, 150
- Flörs, A., Spyromilio, J., Taubenberger, S., et al. 2020, *MNRAS*, 491, 2902
- Foley, R. J., Narayan, G., Challis, P. J., et al. 2010, *ApJ*, 708, 1748
- Foley, R. J., Challis, P. J., Chornock, R., et al. 2013, *ApJ*, 767, 57
- Gall, E. E. E., Taubenberger, S., Kromer, M., et al. 2012, *MNRAS*, 427, 994
- Gamezo, V. N., Khokhlov, A. M., & Oran, E. S. 2005, *ApJ*, 623, 337
- García-Senz, D., Cabezón, R. M., Domínguez, I., & Thielemann, F. K. 2016, *ApJ*, 819, 132
- Guillochon, J., Parrent, J., Kelley, L. Z., & Margutti, R. 2017, *ApJ*, 835, 64
- Hillebrandt, W., Kromer, M., Röpke, F. K., & Ruiter, A. J. 2013, *Front. Phys.*, 8, 116
- Höflich, P., Khokhlov, A., & Wheeler, J. 1995, *ApJ*, 444, 831
- Hoyle, F., & Fowler, W. A. 1960, *ApJ*, 132, 565
- Hunter, J. D. 2007, *Comput. Sci. Eng.*, 9, 90
- Iben, I., Jr., & Tutukov, A. V. 1984, *ApJS*, 54, 335
- Jha, S. W. 2017, in *Handbook of Supernovae*, (Springer) 375
- Jordan, G. C., IV, Fisher, R. T., Townsley, D. M., et al. 2008, *ApJ*, 681, 1448
- Jordan, G. C., Meakin, C. A., Hearn, N., et al. 2009, in Numerical Modeling of Space Plasma Flows: ASTRONUM-2008, eds. N. V. Pogorelov, E. Audit, P. Colella, & G. P. Zank, *ASP Conf. Ser.*, 406, 92
- Jordan, G. C., IV, Graziani, C., Fisher, R. T., et al. 2012a, *ApJ*, 759, 53

- Jordan, G. C., IV, Perets, H. B., Fisher, R. T., & van Rossum, D. R. 2012b, *ApJ*, 761, L23
- Jülich Supercomputing Centre 2019, *Journal of Large-scale Research Facilities*, 5, A171
- Kasen, D., & Plewa, T. 2005, *ApJ*, 622, L41
- Kasen, D., & Plewa, T. 2007, *ApJ*, 662, 459
- Kasen, D., Röpke, F. K., & Woosley, S. E. 2009, *Nature*, 460, 869
- Kashyap, R., Haque, T., Lorén-Aguilar, P., García-Berro, E., & Fisher, R. 2018, *ApJ*, 869, 140
- Khokhlov, A. M. 1991, *A&A*, 245, L25
- Khokhlov, A., Mueller, E., & Hoefflich, P. 1993, *A&A*, 270, 223
- Khokhlov, A. M., Oran, E. S., & Wheeler, J. C. 1997, *ApJ*, 478, 678
- Kromer, M., & Sim, S. A. 2009, *MNRAS*, 398, 1809
- Kromer, M., Fink, M., Stanishev, V., et al. 2013, *MNRAS*, 429, 2287
- Kromer, M., Ohlmann, S. T., Pakmor, R., et al. 2015, *MNRAS*, 450, 3045
- Kromer, M., Ohlmann, S. T., & Röpke, F. K. 2017, *Mem. Soc. Astron. It.*, 88, 312
- Lach, F., Röpke, F. K., Seitzzahl, I. R., et al. 2020, *A&A*, 644, A118
- Lach, F., Callan, F. P., Bubeck, D., et al. 2022, *A&A*, 658, A179
- Li, W., Filippenko, A. V., Treffers, R. R., et al. 2001, *ApJ*, 546, 734
- Lira, P., Suntzeff, N. B., Phillips, M. M., et al. 1998, *AJ*, 115, 234
- Long, M., Jordan, G. C., IV, Van Rossum, D. R., et al. 2014, *ApJ*, 789, 103
- Maeda, K., Taubenberger, S., Sollerman, J., et al. 2010a, *ApJ*, 708, 1703
- Maeda, K., Röpke, F. K., Fink, M., et al. 2010b, *ApJ*, 712, 624
- Marquardt, K. S., Sim, S. A., Ruiter, A. J., et al. 2015, *A&A*, 580, A118
- Mazzali, P. A., Röpke, F. K., Benetti, S., & Hillebrandt, W. 2007, *Science*, 315, 825
- Meakin, C. A., Seitzzahl, I., Townsley, D., et al. 2009, *ApJ*, 693, 1188
- Munari, U., Henden, A., Belligoli, R., et al. 2013, *New Astron.*, 20, 30
- Niemeyer, J. C., & Woosley, S. E. 1997, *ApJ*, 475, 740
- Nomoto, K., Thielemann, F.-K., & Yokoi, K. 1984, *ApJ*, 286, 644
- Nonaka, A., Aspden, A. J., Zingale, M., et al. 2012, *ApJ*, 745, 73
- Nugent, P. E., Sullivan, M., Cenko, S. B., et al. 2011, *Nature*, 480, 344
- Oliphant, T. E. 2007, *Comput. Sci. Eng.*, 9, 10
- Oran, E. S., & Gamezo, V. N. 2007, *Combust. Flame*, 148, 4
- Pakmor, R., Edelmann, P., Röpke, F. K., & Hillebrandt, W. 2012, *MNRAS*, 424, 2222
- Pakmor, R., Zenati, Y., Perets, H. B., & Toonen, S. 2021, *MNRAS*, 503, 4734
- Pérez, F., & Granger, B. E. 2007, *Comput. Sci. Eng.*, 9, 21
- Phillips, M. M. 1993, *ApJ*, 413, L105
- Phillips, M. M., Wells, L. A., Suntzeff, N. B., et al. 1992, *AJ*, 103, 1632
- Phillips, M. M., Li, W., Frieman, J. A., et al. 2007, *PASP*, 119, 360
- Plewa, T. 2007, *ApJ*, 657, 942
- Plewa, T., Calder, A. C., & Lamb, D. Q. 2004, *ApJ*, 612, L37
- Poludnenko, A. Y., Gardiner, T. A., & Oran, E. S. 2011, *Phys. Rev. Lett.*, 107, 054501
- Poludnenko, A. Y., Chambers, J., Ahmed, K., Gamezo, V. N., & Taylor, B. D. 2019, *Science*, 366, 7365
- Richmond, M. W., & Smith, H. A. 2012, *J. Am. Assoc. Var. Star*, 40, 872
- Röpke, F. K. 2005, *A&A*, 432, 969
- Röpke, F. K. 2016, in *Handbook of Supernovae*, eds. A. Alsabti, & P. Murdin (Springer), 1185
- Röpke, F. K., & Niemeyer, J. C. 2007, *A&A*, 464, 683
- Röpke, F. K., Woosley, S. E., & Hillebrandt, W. 2007, *ApJ*, 660, 1344
- Ruiz-Lapuente, P., Cappellaro, E., Turatto, M., et al. 1992, *ApJ*, 387, L33
- Saha, A., Thim, F., Tammann, G. A., Reindl, B., & Sandage, A. 2006, *ApJS*, 165, 108
- Saselli, M., Mazzali, P. A., Pian, E., et al. 2014, *MNRAS*, 445, 711
- Scalzo, R., Aldering, G., Antilogus, P., et al. 2014, *MNRAS*, 440, 1498
- Seitzzahl, I. R., Meakin, C. A., Townsley, D. M., Lamb, D. Q., & Truran, J. W. 2009a, *ApJ*, 696, 515
- Seitzzahl, I. R., Meakin, C. A., Lamb, D. Q., & Truran, J. W. 2009b, *ApJ*, 700, 642
- Seitzzahl, I. R., Ciaraldi-Schoolmann, F., Röpke, F. K., et al. 2013a, *MNRAS*, 429, 1156
- Seitzzahl, I. R., Cescutti, G., Röpke, F. K., Ruiter, A. J., & Pakmor, R. 2013b, *A&A*, 559, L5
- Seitzzahl, I. R., Kromer, M., Ohlmann, S. T., et al. 2016, *A&A*, 592, A57
- Sethian, J. A. 1999, *Level Set Methods and Fast Marching Methods* (Cambridge: Cambridge University Press)
- Shen, K. J., Kasen, D., Miles, B. J., & Townsley, D. M. 2018, *ApJ*, 854, 52
- Shen, K. J., Blondin, S., Kasen, D., et al. 2021, *ApJ*, 909, L18
- Sim, S. A. 2007, *MNRAS*, 375, 154
- Sim, S. A., Röpke, F. K., Hillebrandt, W., et al. 2010, *ApJ*, 714, L52
- Sim, S. A., Seitzzahl, I. R., Kromer, M., et al. 2013, *MNRAS*, 436, 333
- Stahl, B. E., Zheng, W., de Jaeger, T., et al. 2019, *MNRAS*, 490, 3882
- Stritzinger, M., Mazzali, P. A., Sollerman, J., & Benetti, S. 2006, *A&A*, 460, 793
- Stritzinger, M. D., Valentí, S., Hoefflich, P., et al. 2015, *A&A*, 573, A2
- Szalai, T., Vinkó, J., Sárneczky, K., et al. 2015, *MNRAS*, 453, 2103
- Taubenberger, S. 2017, *Handbook of Supernovae*, 317
- Timmer, F. X., & Arnett, D. 1999, *ApJS*, 125, 277
- Townsley, D. M., Calder, A. C., Asida, S. M., et al. 2007, *ApJ*, 668, 1118
- Travaglio, C., Hillebrandt, W., Reinecke, M., & Thielemann, F.-K. 2004, *A&A*, 425, 1029
- Tsvetkov, D. Y., Shugarov, S. Y., Volkov, I. M., et al. 2013, *Contrib. Astron. Obs. Skaln. Pleso*, 43, 94
- Whelan, J., & Iben, I., Jr. 1973, *ApJ*, 186, 1007
- Woosley, S. E., Kerstein, A. R., Sankaran, V., Aspden, A. J., & Röpke, F. K. 2009, *ApJ*, 704, 255
- Yamanaka, M., Maeda, K., Kawabata, K. S., et al. 2015, *ApJ*, 806, 191
- Zel'dovich, Y. B., Librovich, V. B., Makhviladze, G. M., & Sivashinskii, G. I. 1970, *J. Appl. Mech. Tech. Phys.*, 11, 264
- Zingale, M., Almgren, A. S., Bell, J. B., Nonaka, A., & Woosley, S. E. 2009, *ApJ*, 704, 196
- Zingale, M., Nonaka, A., Almgren, A. S., et al. 2011, *ApJ*, 740, 8

Chapter 8

Nucleosynthesis imprints from different Type Ia supernova explosion scenarios and implications for galactic chemical evolution

Publication information:

Journal: Astronomy & Astrophysics (A&A), Volume 644, December 2020

Reference: F. Lach et al. 2020, A&A, 644, A118

Digital Object Identifier: <https://doi.org/10.1051/0004-6361/202038721>

Status: Published on 09 December 2020

Credit: Florian Lach, A&A, 644, A118, 2020, reproduced with permission ©ESO

Authors:

Florian Lach (FL), Friedrich K. Röpke (FKR), Ivo R. Seitenzahl (IRS), Benoit Côté (BC), Sabrina Gronow (SG), Ashley J. Ruiter (AJR)

Author's contribution:

All sections of the manuscript except one paragraph in Section 3.1 about the STARTRACK code (provided by AJR) were written by FL. Moreover, FL produced all the figures, carried out the GCE simulations using the OMEGA code, and analyzed the SN Ia nucleosynthesis yields. The SN explosion models investigated are the result of work within the research group of FKR during the past decade. One model (R60) has also been provided by FL and is also part of Publication 1 (Chapter 6). All authors have read the manuscript, participated in discussions and gave relevant suggestions during submission and reviewing process.

Nucleosynthesis imprints from different Type Ia supernova explosion scenarios and implications for galactic chemical evolution

F. Lach^{1,2}, F. K. Röpké^{1,3}, I. R. Seitenzahl⁴, B. Côté^{5,6,7}, S. Gronow^{1,2}, and A. J. Ruiter⁴

¹ Heidelberger Institut für Theoretische Studien, Schloss-Wolfsbrunnenweg 35, 69118 Heidelberg, Germany
e-mail: florian.lach@h-its.org

² Zentrum für Astronomie der Universität Heidelberg, Astronomisches Rechen-Institut, Mönchhofstr. 12-14, 69120 Heidelberg, Germany

³ Zentrum für Astronomie der Universität Heidelberg, Institut für Theoretische Astrophysik, Philosophenweg 12, 69120 Heidelberg, Germany

⁴ School of Science, University of New South Wales, Australian Defence Force Academy, Canberra, ACT 2600, Australia

⁵ Konkoly Observatory, Research Centre for Astronomy and Earth Sciences, MTA Centre for Excellence, Konkoly Thege Miklos 15-17, 1121 Budapest, Hungary

⁶ ELTE Eötvös Lorénd University, Institute of Physics, Pázmány Péter Sétány 1/A, Budapest 1117, Hungary

⁷ National Superconducting Cyclotron Laboratory, Michigan State University, East Lansing, MI 48824, USA

Received 23 June 2020 / Accepted 19 October 2020

ABSTRACT

We analyze the nucleosynthesis yields of various Type Ia supernova explosion simulations including pure detonations in sub-Chandrasekhar mass white dwarfs; double detonations and pure helium detonations of sub-Chandrasekhar mass white dwarfs with an accreted helium envelope; a violent merger model of two white dwarfs; and deflagrations and delayed detonations in Chandrasekhar mass white dwarfs. We focus on the iron peak elements Mn, Zn, and Cu. To this end, we also briefly review the different burning regimes and production sites of these elements, as well as the results of abundance measurements and several galactic chemical evolution studies. We find that super-solar values of $[\text{Mn}/\text{Fe}]$ are not restricted to Chandrasekhar mass explosion models. Scenarios including a helium detonation can significantly contribute to the production of Mn, in particular the models proposed for calcium-rich transients. Although Type Ia supernovae are often not accounted for as production sites of Zn and Cu, our models involving helium shell detonations can produce these elements in super-solar ratios relative to Fe. Our results suggest a re-consideration of Type Ia supernova yields in galactic chemical evolution models. A detailed comparison with observations can provide new insight into the progenitor and explosion channels of these events.

Key words. nuclear reactions, nucleosynthesis, abundances – methods: numerical – stars: abundances – supernovae: general – white dwarfs – Galaxy: abundances

1. Introduction

Over the past two decades Type Ia supernovae (SNe Ia) have been the focus of interest of astrophysical studies primarily because of their application as distance indicators (Riess et al. 1998; Perlmutter et al. 1999) via the Phillips relation (Phillips 1993). As one of the significant sources for heavy elements in the Universe, however, they are also important as a main contributor to cosmic nucleosynthesis (Matteucci & Greggio 1986; Matteucci & Recchi 2001; Matteucci et al. 2006; Kobayashi et al. 2006, 2015, 2020; Kobayashi & Nomoto 2009). Although SNe Ia have been intensely studied in observational and theoretical approaches, the questions concerning their progenitors and explosion mechanisms remain open.

There is broad agreement that SNe Ia originate from the thermonuclear explosions of carbon-oxygen white dwarf (WD) stars (Hoyle & Fowler 1960). In some cases, however, also oxygen-neon WDs (Marquardt et al. 2015) or hybrid carbon-oxygen-neon WDs (Kromer et al. 2015; Willcox et al. 2016) may give rise to similar events. In most scenarios the explosion is triggered by the interaction with a binary companion. This rather

unsharp characterization leaves room for a “zoo” of possible progenitor (e.g., Wang & Han 2012) and explosion scenarios (see, e.g., Hillebrandt & Niemeyer 2000; Hillebrandt et al. 2013). Potential progenitors can be subdivided into the single-degenerate (SD) scenario involving one WD accompanied by a main sequence, giant, or helium star (Whelan & Iben 1973) and the double-degenerate (DD) scenario consisting of a binary system of two WDs (Iben & Tutukov 1984). Another possibility, the core-degenerate scenario, has been proposed by Kashi & Soker (2011). Here a WD merges with a post-asymptotic giant branch (AGB) core already during the common envelope phase, and forms a new WD above the Chandrasekhar mass (M_{Ch}) that is stabilized by rotation. As the rotation slows down it might explode as a SN Ia.

From the explosion modeling point of view and the implied nucleosynthesis output, however, the mass of the WD at the time of explosion is the fundamental parameter (Seitenzahl et al. 2017). Generally, near- M_{Ch} models are distinguished from models in which the exploding WDs are significantly below the Chandrasekhar mass limit of approximately $1.4 M_{\odot}$. Finally, the characteristics of the explosion is governed by the combustion

mechanism. A thermonuclear combustion wave is formed via a runaway process during convective burning, due to dynamical interaction in a WD merger, or by converging shock waves. In the first case a subsonic deflagration propagates via heat conduction. The two other cases may lead to the formation of a supersonic detonation where, in contrast, the fuel is heated and burned by the compression of a shock wave (see, e.g., Röpke et al. 2017 for a review of thermonuclear combustion in SNe Ia).

It is not clear yet which of the various possible explosion mechanisms can account for SNe Ia. In addition to the bulk of normal SNe Ia obeying the Phillips relation, a variety of subclasses of SNe Ia have been identified (see Taubenberger 2017 for a review), and therefore it is plausible that more than one scenario contributes to the overall class of SNe Ia.

One approach to check the validity of a certain scenario is to conduct multidimensional hydrodynamical simulations of the explosion phase together with the subsequent calculation of synthetic observables, such as light curves and spectra. These can then be compared to observations of SNe Ia and the initial model can be accepted, discarded, or adjusted accordingly. This exercise has been carried out during the past years for a variety of explosion scenarios, and although suitable explanations of subclasses could be identified, there is no fully convincing model for the bulk of normal SNe Ia yet (Blinnikov et al. 2006; Kasen & Plewa 2007; Blondin et al. 2011; Röpke et al. 2012; Seitzzahl et al. 2013a; Sim et al. 2013; Fink et al. 2014; Kromer et al. 2013; Townsley et al. 2019; Gronow et al. 2020).

Another test of the realization of specific explosion scenarios are abundance measurements in stars combined with galactic chemical evolution (GCE) models (Matteucci et al. 2006; Travaglio et al. 2014; Kobayashi et al. 2011). Among other ingredients, these models assume certain rates, delay-time distributions, and nucleosynthesis yields for various kinds of SNe Ia and core-collapse supernovae (CCSNe). The enrichment of the investigated stellar population or galaxy with metals is then compared to stellar abundances derived from spectroscopy and thus allows us to infer the origin of a particular element or group of elements. This is the reason why the characteristic imprints of a certain explosion scenario are of great interest.

A prominent example is the case of the element manganese. It is widely accepted that the primary contribution to Mn stems from SNe Ia since the observed values of $[\text{Mn}/\text{Fe}]$ in the Galaxy increase from $[\text{Fe}/\text{H}] \approx -1$ to the solar value, and CCSN yields predict sub-solar values for $[\text{Mn}/\text{Fe}]$ (Timmer et al. 1995; McWilliam 1997; Kobayashi et al. 2006, 2011, 2020; Kobayashi & Nomoto 2009; Weinberg et al. 2019). This “SN Ia knee” has already been explained by Tinsley (1979), Greggio & Renzini (1983), and Matteucci & Greggio (1986) since it coincides nicely with the decrease in the α -elements (i.e., $[\alpha/\text{Fe}]$) produced by CCSNe from their super-solar plateau at lower $[\text{Fe}/\text{H}]$. Seitzzahl et al. (2013b) picked this up arguing that Mn is produced at high burning densities in normal freeze-out from nuclear statistical equilibrium (NSE; see Sect. 2), and therefore it predominantly originates from M_{Ch} explosions. The best agreement with the data is achieved if SNe Ia arise equally from sub- M_{Ch} and M_{Ch} progenitors. These results have been further refined in the recent work of Eitner et al. (2020). Their non-LTE measurements of Mn in a sample of 42 stars in the Galaxy show a rather flat evolution of $[\text{Mn}/\text{Fe}]$ near the solar value lowering the contribution of M_{Ch} SNe Ia to about 25%. The trend in $[\text{Mn}/\text{Fe}]$ is not so clear in dwarf spheroidal galaxies (dSphs), but various works also find that a SN Ia contribution to Mn is required to explain observations (Cescutti et al. 2008; North et al. 2012; Cescutti & Kobayashi 2017). Another

study carried out by McWilliam et al. (2018) claims that the most metal-rich star in Ursa Minor, COS 171, was enriched by a low-metallicity, low-mass sub- M_{Ch} detonation. In particular, its low $[\text{Mn}/\text{Fe}]$ and $[\text{Ni}/\text{Fe}]$ values exclude a M_{Ch} origin. Furthermore, the sub-solar amounts of Cu and Zn in COS 171 are also a hint for a low-mass progenitor of the SN explosion which has enriched the star since these elements are produced in strong α -rich freeze-out. Moreover, de los Reyes et al. (2020) attribute different $[\text{Mn}/\text{Fe}]$ values in dSphs to their specific star formation history. The combination of sub-solar $[\text{Mn}/\text{Fe}]$ and a short star burst, as seen in Sculptor, indicates a dominant role of sub- M_{Ch} explosions. In contrast, Fornax and Leo I show a long-lasting star formation and $[\text{Mn}/\text{Fe}]$ around the solar value, which points to an increasing enrichment via near- M_{Ch} SNe Ia.

Our work analyzes the nucleosynthetic yields of various models for SNe Ia, namely pure deflagrations and delayed detonations in M_{Ch} WDs, as well as pure detonations and double detonations of sub- M_{Ch} WDs. The aim is not to go into detail about the observational implications of specific isotopes or to evaluate whether the model matches any observed SN Ia, but to identify specific abundance patterns that are characteristic for particular explosion scenarios, and therefore to constrain whether this scenario is required to produce the observed elemental and isotopic abundances. The key discriminant is the initial mass of the WD that sets its central density, mainly determining the freeze-out regime reached by the burning region. Normal freeze-out from NSE, for instance, requires high densities only reached in M_{Ch} WDs, and the presence of a helium detonation yields unique abundance patterns not produced in explosive carbon-oxygen burning. Moreover, electron capture significantly reduces the electron fraction at high densities, and therefore shifts the nucleosynthesis yields in NSE to more neutron rich isotopes (see Sect. 2.2). Thus, the occurrence of iron group elements (IGEs) with a considerable neutron excess suggests the Chandrasekhar mass scenario (Yamaguchi et al. 2015).

This work is structured in the following way. In Sect. 2 we first review the different burning regimes and then summarize the explosion models investigated. Section 3 presents the results of our nucleosynthesis analysis, and we discuss the implications of these results for the nature of the progenitor for SNe Ia. The elements Mn, Zn, and Cu are of particular interest. Because we find substantial amounts of the unstable radionuclides ^{68}Ge , ^{68}Ga , and ^{65}Zn , we briefly test their potential impact on the observables. In Sect. 4 we summarize our findings.

2. Explosion models and burning regimes

2.1. Explosive silicon burning

In a thermonuclear supernova explosion the innermost (i.e., densest) part of the WD star reaches temperatures sufficiently high for silicon burning, and thus significantly contributes to the production of IGEs. Woosley et al. (1973) divide the parameter space of this burning regime into three regions: the regime of incomplete silicon burning, α -rich freeze-out, and normal freeze-out from NSE (see Fig. 1). In NSE all the abundances from protons, neutrons, and α -particles up to the iron peak have reached an equilibrium (i.e., the forward and reverse reactions cancel each other). In addition to the peak temperature T_{peak} and density ρ_{peak} , the timescale on which a particular fluid element cools after the crossing of the burning front also determines the nucleosynthesis yields. Adiabatic cooling can be written as

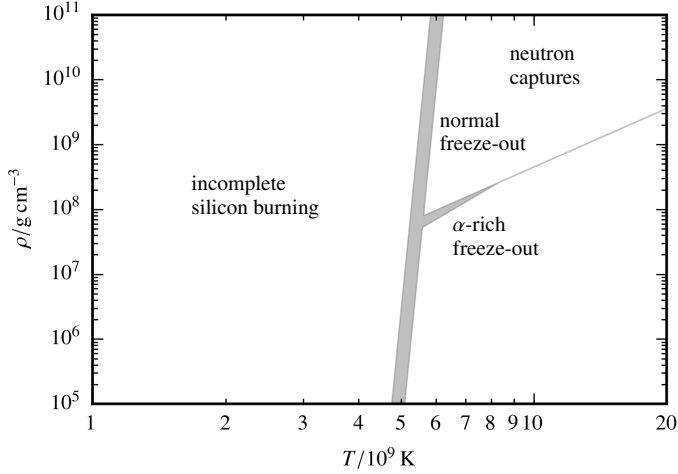


Fig. 1. Burning regimes in the $T - \rho$ plane according to Woosley et al. (1973). Below a certain temperature the burning of silicon is incomplete. At high temperatures the state of nuclear statistical equilibrium is achieved and silicon is transformed into iron peak elements. This region is subdivided in the regime of normal freeze-out and α -rich freeze-out. The shaded area covers values of χ between 1 and 10 according to Eqs. (3) and (4).

(Woosley et al. 1973)

$$\rho(t) = \rho_{\text{peak}} e^{-t/\tau_{\text{HD}}}, \quad (1)$$

$$T_9(t) = T_{9,\text{peak}} \left(\frac{\rho(t)}{\rho_{\text{peak}}} \right)^{\gamma-1}. \quad (2)$$

Here γ denotes the adiabatic exponent and $\tau_{\text{HD}} = 446\chi\rho_{\text{peak}}^{-1/2}$ is the hydrodynamical timescale. With the help of the scaling parameter χ , the dependence of the results on the timescale can be examined.

Meakin et al. (2009) present an updated prescription for the density evolution in SNe Ia. They employ an exponential temperature decay and ensure adiabaticity by fixing the entropy to the post-burning state. The entropy S is a function of temperature, density, and averaged values of the mass number \bar{A} and the proton number \bar{Z} . Thus, the density can be obtained from $S = S(T(t), \rho(t), \bar{A}, \bar{Z})$. However, for demonstration purposes we stick to the formulation of Woosley et al. (1973) in the following since the main statements about freeze-out from NSE are not affected by the exact choice of the expansion prescription.

Incomplete silicon burning is characterized by the presence of two quasi-equilibrium clusters, i.e., only certain regions in the chart of nuclei that have reached equilibrium states, centered around ^{28}Si and ^{56}Ni , respectively. They are separated by the bottleneck at a mass number of $A \approx 45$ (e.g., Ti and Sc). These elements are weakly bound compared to Ca and are therefore low in abundance. Hence, there is only little flow of material through the bottleneck and intermediate-mass elements (IMEs), and IGEs remain present after the burning is quenched. At higher temperatures the bottleneck is removed. The equilibrium clusters merge and matter achieves the state of NSE, ultimately converting silicon to IGEs almost completely. The temperature necessary for silicon exhaustion, $X(^{28}\text{Si}) \lesssim 5 \times 10^{-3}$, can be approximated by (Woosley et al. 1973)

$$T_{9,\text{peak}} \gtrsim 4.3 \left(\frac{\rho_{\text{peak}}}{\chi^2} \right)^{1/68}. \quad (3)$$

In NSE, the abundance distribution is uniquely determined by density, temperature, and electron fraction Y_e . The composition

changes as soon as the first reactions drop out of equilibrium due to decreasing temperature. At high densities matter is characterized by a low fraction of light and of free particles such as neutrons, protons, and α -particles. Therefore, the composition during this normal freeze-out or particle-poor freeze-out is not altered significantly by the capture of light particles during expansion. At lower densities, in contrast, light particles are more abundant and thus react with the prevailing iron group nuclei and bring matter out of NSE composition. Due to the high mass fraction of α -particles, this drop-out of equilibrium is called alpha-rich freeze-out. Woosley et al. (1973) derive the approximate relation

$$\rho_{\text{peak}} \lesssim \min \left\{ \begin{array}{l} 4.5 \times 10^5 T_{9,\text{peak}}^3 \\ 2.5 \times 10^5 T_{9,\text{peak}}^4 \chi^{-2/3} \end{array} \right. \quad (4)$$

for the density separating α -rich freeze-out and normal freeze-out using $\gamma = 4/3$ in Eqs. (1) and (2).

Therefore, the $T_{\text{peak}} - \rho_{\text{peak}}$ -plane is split into three regions by Eqs. (3) and (4), as illustrated in Fig. 1 (see also Fig. 20 of Woosley et al. 1973). These regions produce different chemical compositions after the last reactions have frozen out. This is also visualized in Fig. 2 for the different explosion models explained in the next section. The separation of the different regions can be shifted continuously by a variation of the scaling parameter χ . The gray shaded areas in Figs. 1 and 2 cover values of χ between 1 and 10.

2.2. Neutronization in high-density material

We discuss in the previous section how the NSE composition is altered in the two different freeze-out regimes, but the NSE composition itself is determined by the electron fraction Y_e (related to the neutron excess $\eta = 1 - 2Y_e$). In NSE, but also in quasi-statistical equilibrium (QSE), the most abundant nuclei after freeze-out are those with the highest binding energy and an electron fraction close to that of the initial fuel. For symmetric matter (i.e., $Y_e = 0.5$) the most abundant nucleus is ^{56}Ni . As Y_e decreases, isotopes like $^{57-60}\text{Ni}$ and $^{54-58}\text{Fe}$ become more abundant depending on the actual electron fraction and their binding energies. The value of Y_e is determined and altered by three mechanisms.

First, the electron fraction of the WD is set by the metallicity Z of the progenitor main sequence star. Most important are the abundances of ^{56}Fe and CNO nuclei which are mostly converted to ^{14}N in hydrogen burning (CNO cycle) and subsequently to ^{22}Ne in helium burning. These two isotopes, ^{56}Fe and ^{22}Ne , provide the dominant part of the surplus of neutrons in the exploding WD. Timmes et al. (2003) derive an approximate relation for the mass of ^{56}Ni as a function of metallicity. It shows a decreasing trend for ^{56}Ni with increasing Z , and a variation of 25% if Z is varied by a factor of three.

Second, the initial Y_e of the WD is altered during convective carbon burning (“simmering”) preceding the thermonuclear runaway in a M_{Ch} WD. The number of neutrons is increased via the capture of free electrons onto the highly ionized atoms (Bahcall 1964):



These endoergic reactions require high electron energies, and therefore only become important at high densities. Chamulak et al. (2008) study the behavior of Y_e during carbon burning and find that the reaction chain $^{12}\text{C}(p, \gamma)^{13}\text{N}(e^-, \nu)^{13}\text{C}$ is

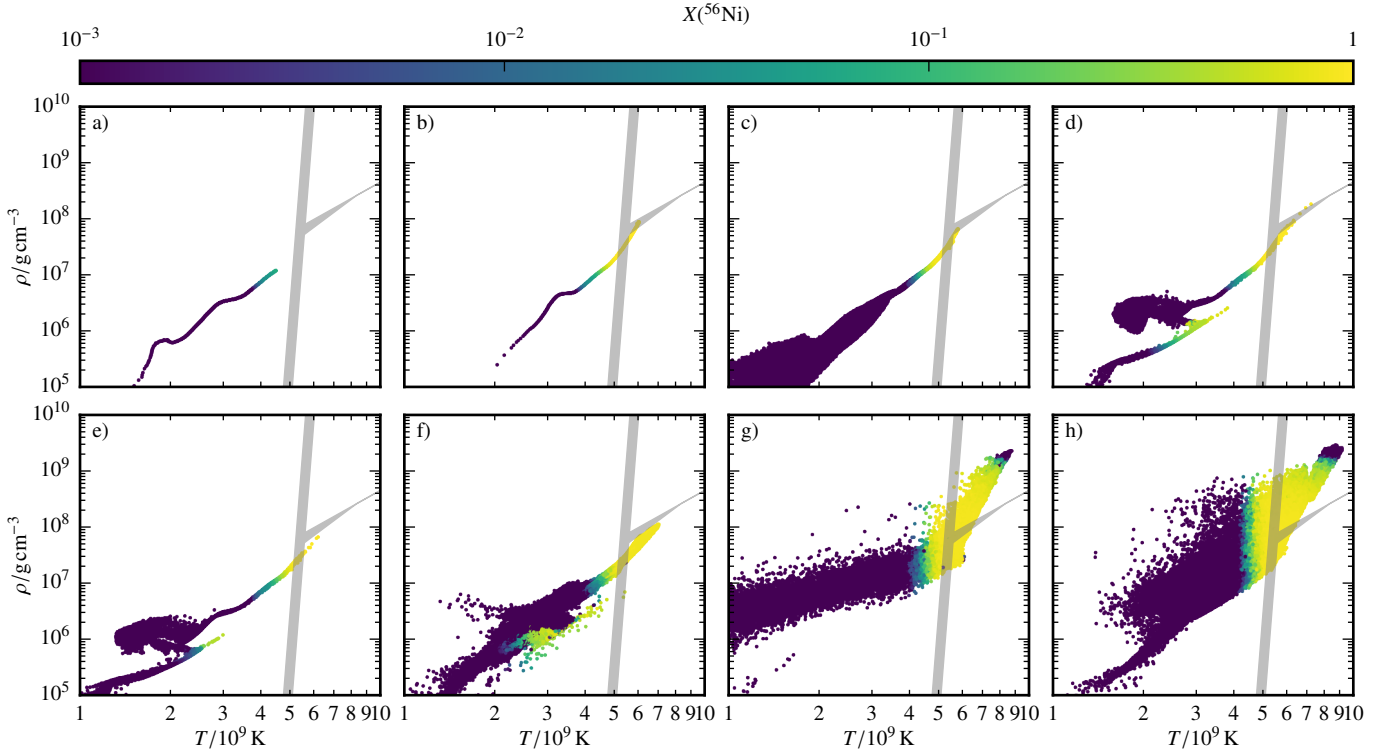


Fig. 2. Distribution of the tracer particles in the $T_{\text{peak}} - \rho_{\text{peak}}$ plane with color-coded mass fraction of ^{56}Ni 100 s after triggering the explosion. The panels show (a) PD081, (b) PD115, (c) VM, (d) CSDD-S, (e) CSDD-L, (f) M2a $_{\odot}$, (g) R60, (h) N100ddt. The gray shaded regions separate incomplete (*left*) from complete silicon burning (*right*) and normal freeze-out (*upper right*) from α -rich freeze-out (*lower right*) according to Eqs. (3) and (4). The area covered corresponds to a varying scaling parameter: $1 < \chi < 10$.

the dominant mechanism for reducing Y_e for densities of approximately $1 \times 10^9 \text{ g cm}^{-3}$. The electron capture on ^{13}N is gradually replaced by $^{12}\text{C}(^{12}\text{C}, p)^{23}\text{Na}(e^-, \nu)^{23}\text{Ne}$ for $\rho > 1.7 \times 10^9 \text{ g cm}^{-3}$. Chamulak et al. (2008) estimate a maximum reduction in Y_e by 6.3×10^{-4} , and Piro & Bildsten (2008) suggest a carbon-dependent value of $|\Delta Y_{e,\text{max}}| = 1.7 \times 10^{-3} X(^{12}\text{C})$.

Finally, the most dramatic changes to the electron fraction happen during the explosion itself. In NSE, electrons are mostly captured by free protons at high temperatures. Subsequently, as the temperature drops, IGEs capture most of the electrons. This leads to a decrease in Y_e to $Y_e \approx 0.44$ in the most extreme cases in the central regions of the exploding WD star. Therefore, the regions with the highest density do not contribute significantly to the production of ^{56}Ni (Brachwitz et al. 2000), but to more neutron-rich IGEs. In general, the nucleosynthesis results then depend on the central density and the corresponding density gradient. Detailed studies of the nucleosynthesis in Chandrasekhar-mass models and the effect of neutronization have been carried out by Thielemann et al. (1986), Iwamoto et al. (1999), and, with updated electron capture rates (Langanke & Martinez-Pinedo 2000), by Brachwitz et al. (2000) and Bravo (2019). When 3D effects in deflagration models are taken into account the final abundance stratification are smoothed out compared to the theoretical prediction based on density, metallicity, and neutronization (Seitenzahl et al. 2013a).

In summary, the neutronization due to electron capture is an effect restricted to the high densities reached only in WDs close to M_{Ch} , and hence the abundances of very neutron-rich isotopes are a hint to the Chandrasekhar-mass scenario. The abundance ratio of nickel to iron, for instance, measured in late-time spectra of SNe Ia can be taken as a proxy for the quotient $^{58}\text{Ni}/^{56}\text{Ni}$, and thus for neutronization. This is used by Flörs et al. (2020)

to infer the contribution of sub- M_{Ch} progenitors to SNe Ia in relation to M_{Ch} progenitors.

2.3. Explosive helium burning

In addition to explosive silicon burning, the burning of helium is another source of nucleosynthesis products in the double-detonation scenario (see Sect. 1). Explosive helium burning was studied by Khokhlov (1984) and Khokhlov & Érgma (1985). They found that in general the burning is characterized by a competition between the triple- α reaction and α -captures on heavier nuclei. First, ^{12}C is synthesized by the reaction $3\alpha \rightarrow ^{12}\text{C}$, and subsequently heavier α -elements (^{16}O , ^{20}Ne , ^{24}Mg , ^{28}Si , ^{32}S , ^{36}Ar , ^{40}Ca , ^{44}Ti , ...) are produced. The timescale for the capture of an α -particle increases for higher mass numbers A due to the higher Coulomb barriers. These are penetrated more easily at higher particle energies, and the timescale is therefore temperature dependent. Consequently, the α -chain stops as soon as the timescale for the triple- α -reaction is shorter than for the next α -capture. However, above a certain density-dependent temperature of approximately $2 \times 10^9 \text{ K}$ at $\rho = 5 \times 10^6 \text{ g cm}^{-3}$, ^{56}Ni is always the most abundant isotope since it has the highest binding energy at $Y_e = 0.5$ (see Sect. 2.1). These temperatures are usually surpassed in helium detonations, and therefore most of the material is converted to ^{56}Ni . Nevertheless, there is a way to stop the α -chain before ^{56}Ni is reached, even at high temperatures. If the initial fuel is polluted with carbon, oxygen, or nitrogen, for instance, the slow triple- α reaction is bypassed by α -capture on these seed nuclei. This leads to a very fast depletion of α -particles and the nucleosynthesis stops below $A = 56$ once the material runs out of α -particles (see also Wosley & Kasen 2011, Shen & Moore 2014; Gronow et al. 2020).

Beyond $A = 56$, the reverse reactions become increasingly important and start to balance the α -captures to some extent. Nevertheless, a high abundance of α -particles results in an enhanced production of elements beyond Ni, such as Cu and Zn, compared to their NSE abundance. The timescale to reach NSE is about 1 s at a temperature of 5×10^9 K. However, conditions necessary for NSE are not achieved in most of the helium detonations, and thus nucleosynthesis exhibits interesting differences in the burning products of the CO core.

2.4. Models

In this work we investigate three distinct kinds of explosion models. The first class consists of pure detonations of sub-Chandrasekhar mass CO WDs. We closely examine the violent merger (VM) of a $0.9 M_{\odot}$ with a $1.1 M_{\odot}$ WD simulated by

Pakmor et al. (2012a). In addition, two pure detonations of CO WDs with total masses of the progenitor of 0.81 (PD081) and $1.15 M_{\odot}$ (PD115) of Sim et al. (2010) are included in our analysis.

We then study models including a detonation of a helium shell on top of a sub- M_{Ch} mass WD (also labeled “Ia-SN”, Bildsten et al. 2007; Shen & Bildsten 2009; Shen et al. 2010) eventually triggering a second detonation burning the CO core (double detonation). Two models are taken from Sim et al. (2012) that follow the explosion of low-mass CO cores (0.58 and $0.45 M_{\odot}$) with a prominent helium shell of $0.21 M_{\odot}$ (hereafter CSDD-S and CSDD-L, respectively). The second detonation is triggered via the converging shock mechanism not far from the center of the WD (Fink et al. 2007). The HeD-S model follows the same setup as CSDD-S, but the detonation of the core is suppressed. These pure helium detonations are a possible explosion mechanism for Ca-rich transients (e.g., Inserra et al. 2015). Moreover, a double detonation in the core of a $1.05 M_{\odot}$ WD with a carbon-enriched helium shell of $0.073 M_{\odot}$ (Model M2a of Gronow et al. 2020) is included. In this case, a detonation in the core is triggered at its outer edge when the helium detonation front converges on the far side of its ignition. In addition, an equivalent model to M2a at solar metallicity M2a $_{\odot}$ is investigated. This model is set up as a WD with a total mass of $1.06 M_{\odot}$. Its core consists of ^{12}C , ^{16}O , and, to reproduce the metallicity, 1.34% of ^{22}Ne . In the ^4He shell ($M_{\text{shell}} = 0.075 M_{\odot}$) an admixture of 0.34% by mass of ^{14}N accounts for solar metallicity in the hydrodynamical explosion simulation.

Finally, the M_{Ch} scenario is analyzed. We add the N5def model of Fink et al. (2014) as an example of a pure deflagration, the N100ddt delayed detonation identical with model N100 of Seitzzahl et al. (2013a), as well as a pure deflagration in a M_{Ch} WD with central density of $2.6 \times 10^9 \text{ g cm}^{-3}$. The latter (R60) is ignited in a single spot 60 km off-center and, like N5def, does not disrupt the whole star but leaves behind a bound remnant. The model produces a very faint explosion ejecting only $0.018 M_{\odot}$ of ^{56}Ni and $0.049 M_{\odot}$ of material in total. Moreover, the kinetic energy of the ejecta amounts to 8.17×10^{48} erg and an intact WD of $1.33 M_{\odot}$ is left behind after the explosion. This model has been calculated for this paper with methods similar to Fink et al. (2014) but with an updated equation of state (Timmer & Arnett 1999) and a gravity solver based on fast Fourier transforms.

More details concerning the individual setups and the employed codes can be found in the references above. Moreover, data for the models VM, CSDD-S, CSDD-L, HeD-S, N5def, N100ddt, and M2a have been made publicly available in the online model database HESMA (Kromer et al. 2017). It should be noted that all hydrodynamic explosion simulations were done

using the LEAFS code (Reinecke et al. 1999, 2002; Röpke 2005) except for the double detonations M2a and M2a $_{\odot}$, which were computed with AREPO (Springel 2010).

Because solving a large nuclear network in parallel with the actual explosion simulation goes beyond the scope of the current computational resources, the nucleosynthesis yields are calculated in a post-processing step. To this end, virtual tracer particles are placed into the exploding WD star and advected passively with the fluid flow recording their thermodynamic history. Subsequently, this data is used to determine the isotopic abundances produced by the explosion.

Because we partially work with models from HESMA but also add new explosion simulations, the postprocessing and the treatment of metallicity in it follows different approaches: Models CSDD-L, CSDD-S, HeD-S, PD081, and PD115 were post-processed at zero metallicity and VM, N100ddt, and N5def at solar metallicity using the methods described in Travaglio et al. (2004). In the latter models, solar metallicity was mimicked by including 2.5% of ^{22}Ne to approximately adjust Y_e to the solar value (see also Seitzzahl et al. 2013a). All other simulations, i.e., M2a, M2a $_{\odot}$, and R60, use the YANN code (Pakmor et al. 2012b) for postprocessing. The metallicity of the material in M2a is assumed to be zero, while M2a $_{\odot}$ and R60 apply solar metallicity. To this end, the abundances of all isotopes in the core material (carbon and oxygen) are set according to Asplund et al. (2009) except for elements lighter than fluorine. While H and He are ignored, all CNO isotopes are converted to ^{22}Ne , thus accounting for their processing in H and He burning. In the shell material of M2a $_{\odot}$ carbon and oxygen are instead converted to ^{14}N . To check the effect of the different metallicity implementations we also post-processed R60 and M2a $_{\odot}$ with the appropriate amounts of ^{22}Ne in CO material and ^{14}N in the helium shell, but no other isotopes present. These variants are labeled R60 $_{\text{Ne}}$ and M2a $_{\text{Ne}}$. In all cases the 384 species network of Travaglio et al. (2004) is utilized. Reaction rates were taken from the REACLIB database (Rauscher & Thielemann 2000, updated 2009) and only for our most recent simulations (e.g., R60, M2a) the version of 2014 is applied.

3. Discussion of the nucleosynthesis yields

An instructive way to illustrate the burning regimes reached by a specific model is the distribution of the tracer particles in the $T_{\text{peak}} - \rho_{\text{peak}}$ diagram shown in Fig. 1.

In the case of the sub-Chandrasekhar mass pure detonations (VM, PD081, PD115) the important characteristic from the nucleosynthesis point of view is the low central density ($\rho_c \lesssim 10^8 \text{ g cm}^{-3}$) of the WD. Therefore, IGEs are produced in alpha-rich freeze-out and incomplete silicon burning only (see Fig. 2). While the higher-mass CO core (PD115) produces ^{56}Ni also in NSE (α -rich freeze-out), the low-mass core model (PD081) synthesizes all of its ^{56}Ni in incomplete silicon burning. In addition, the fuel in the VM model stays below densities of $8 \times 10^7 \text{ g cm}^{-3}$, and therefore it burns to NSE in the α -rich freeze-out regime. In the merger process the structure of the primary is not much affected, but the disruption of the secondary causes the larger scatter in the thermodynamic properties of the tracer particles at lower densities (see Fig. 2).

In addition to this, the double-detonation models (CSDD-S, CSDD-L, M2a $_{\odot}$) clearly show that ^{56}Ni is also produced in the helium shell detonation. The tracer particles located in the shell cover an area in the parameter space shown in Fig. 2 that is slightly below that of the core detonation. The scatter in the M_{Ch} deflagration models is larger due to the turbulent

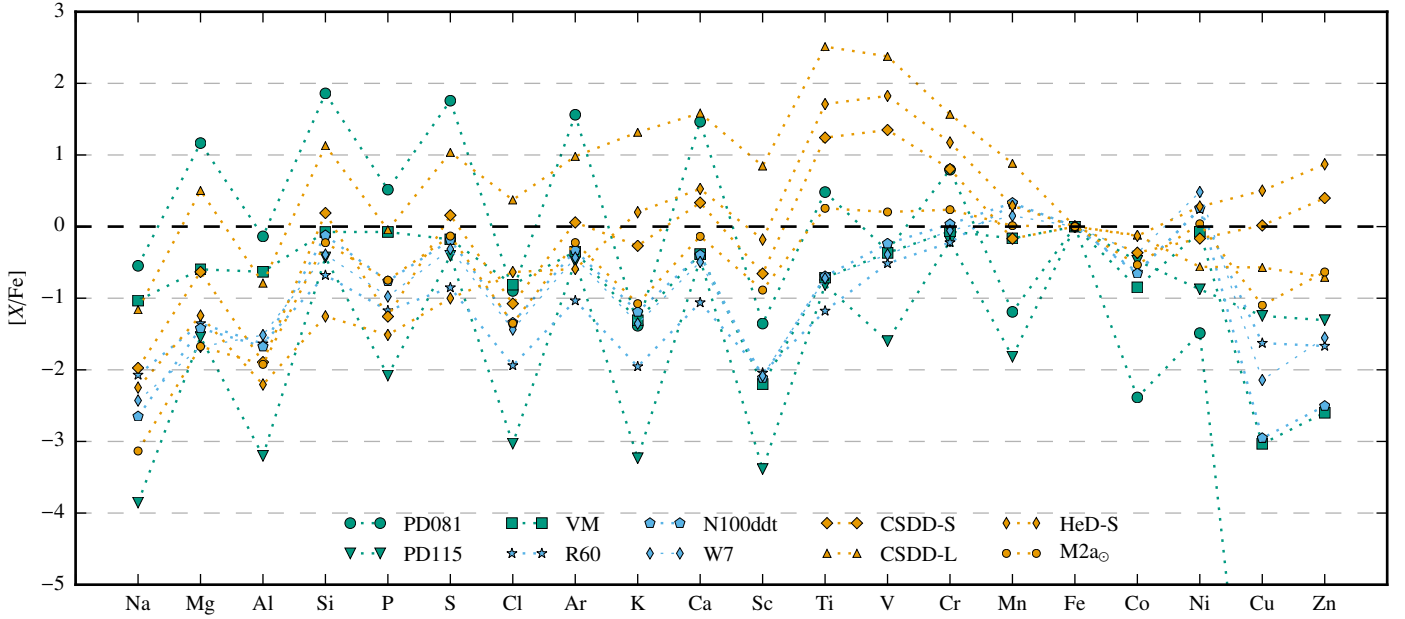


Fig. 3. Elemental ratios to Fe (with radioactive isotopes decayed to 2×10^9 yr) compared to their solar ratios for three sub- M_{Ch} detonations (VM, PD081, PD115), three double detonations (M2a $_{\odot}$, CSDD-S, CSDD-L), one helium detonation (HeD-S), two pure M_{Ch} deflagrations (R60, W7), and a delayed detonation (N100ddt).

motion of the flame and the pre-expansion of the WD during the burning phase. This is even more obvious in the delayed detonation model since some tracers might be affected first by the deflagration and subsequently by the detonation. We note that for the single-spot ignited Model R60 the WD is not disrupted completely, and hence Fig. 2 only shows ejected tracers. Because only such massive WDs reach high densities of $\rho \gtrsim 10^9 \text{ g cm}^{-3}$ and consequently their nucleosynthesis yields originate mainly from normal freeze-out, these kinds of explosions contribute to elements not synthesized in sub- M_{Ch} models.

The gross nucleosynthesis yields are summarized in Fig. 3, which displays the elemental ratio to iron compared to the solar ratio according to [Asplund et al. \(2009\)](#). Since the PD081 model does not burn to NSE, it synthesizes super-solar amounts of IMEs showing a strong odd-even effect. Furthermore, it exhibits a rather high Cr abundance and drops off steeply for higher mass IGEs. CSDD-S also produces super-solar abundances of some IMEs, such as Si, S, Ar, and Ca which is not surprising as it shares the characteristics of a low-mass CO core with the PD081 model. However, the helium shell detonation adds substantial amounts of light IGEs (Ti, V, Cr) as well as Cu and Zn to the mix. These elements are most abundant in HeD-S since they are primarily produced in the helium detonation. Moreover, it should be noted that HeD-S and CSDD-L yield super-solar amounts of Mn. The VM yields are rather inconspicuous for not showing any overproduction, but instead significant underproduction of Mn, Co, Cu, and Zn. Interestingly, the M2a $_{\odot}$ simulation exhibits characteristics similar to those seen in pure detonations (a strong odd-even effect for IMEs, an underproduction of Co, a drop-off for Cu and Zn) as well as helium shell detonation features (super-solar values of Ti, V, Cr and solar abundance of Mn). Finally, the pure deflagration explosions R60 and W7 (we included the W7 model from [Iwamoto et al. 1999](#) because it has been widely used in GCE calculations) and the delayed detonation N100ddt display low abundances of the light IGEs V and Cr and super-solar abundances of Mn and stable Ni. Moreover, the produced

amounts of Cu and Zn are negligible, as is also the case for the pure detonations VM and PD081.

We summarize that all SNe Ia models included here underproduce Co compared to the solar value. Moreover, we confirm the known facts that M_{Ch} explosions can produce Mn at super-solar values and that they also overproduce stable Ni. These have been used to discriminate between M_{Ch} and sub- M_{Ch} explosions in nebular spectra ([Flörs et al. 2020](#)). The theoretical reason for this distinction is that stable Ni ($^{58,60}\text{Ni}$) is produced at higher densities due to the lower electron fraction (see Sect. 2.2). However, we also find the double-detonation models can overproduce Mn and Ni, which makes the nucleosynthetic distinction between M_{Ch} and sub- M_{Ch} explosions not as straightforward as expected. The lighter elements Ti, V, and Cr stem either from He detonations or from the incomplete silicon burning region in low-mass CO cores. The heaviest IGEs Cu and Zn are synthesized in He detonations only, and therefore test the double-detonation scenario: any observations and GCE calculations finding Cu or Zn to be produced by SNe Ia would hint to the occurrence of this explosion mechanism.

3.1. Manganese

The only stable isotope of Mn, ^{55}Mn , is produced in CCSNe and in SNe Ia in incomplete silicon burning primarily via the channel $^{55}\text{Co} \rightarrow ^{55}\text{Fe} \rightarrow ^{55}\text{Mn}$. As already pointed out by [Seitenzahl et al. \(2013b\)](#), a super-solar production of Mn is required to explain the rise in $[\text{Mn}/\text{Fe}]$ for $[\text{Fe}/\text{H}] \gtrsim -1$ to its solar value. Although the CCSN contribution to Mn is uncertain, all current models predict $[\text{Mn}/\text{Fe}]$ ratios below the solar value. Therefore, M_{Ch} explosions must be added to the mix of SNe Ia. Only these WDs reach densities high enough for normal freeze-out, and thus offer an additional site of production to the regime of incomplete silicon burning. The production of ^{55}Co is illustrated in Fig. 4 for the pure deflagration model R60, the violent merger model VM, and the double-detonation model M2a $_{\odot}$. It clearly shows that ^{55}Co is synthesized in normal

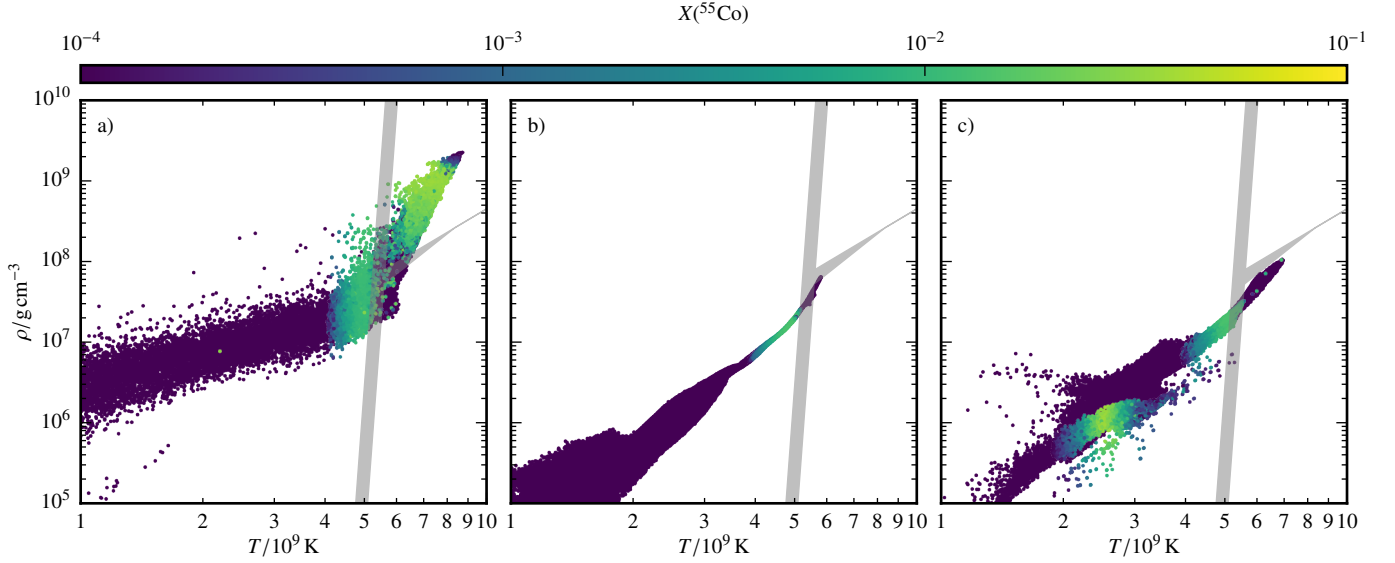


Fig. 4. Same as Fig. 2 with a color-coded mass fraction of ^{55}Co . The panels show (a) R60, (b) VM, (c) $M2a_{\odot}$.

Table 1. Mn-to-Fe ratio compared to solar for the total explosion at 100 s after ignition and to shell and core material only, the total amount of stable Mn in M_{\odot} , and the radioactive and stable isotopes from which ^{55}Mn originates (shown as percentages).

Model	[Mn/Fe]	[Mn/Fe] _{shell}	[Mn/Fe] _{core}	Mn	^{55}Co	^{55}Fe	^{55}Mn
PD081	-1.19	–	–	4.90e-06	99.3	0.7	–
PD115	-1.82	–	–	1.04e-06	97.6	2.4	–
VM	-0.16	–	–	3.74e-03	97.9	2.1	–
$M2a_{\odot}$	-0.03	0.81	-0.07	4.57e-03	98.9	1.1	–
$M2a_{\text{Ne}}$	-0.15	0.81	-0.21	3.46e-03	99.5	0.5	–
$M2a$	-1.00	0.53	-1.63	4.94e-04	99.7	0.3	–
CSDD-L	0.88	1.69	-1.19	1.47e-03	99.6	0.4	–
CSDD-S	-0.17	0.29	-1.37	1.27e-03	99.9	0.1	–
HeD-S	0.29	0.29	–	1.21e-03	99.9	0.1	–
N5def	0.35	–	–	4.03e-03	87.5	12.3	0.2
N100ddt	0.33	–	–	1.33e-02	85.8	14.0	0.2
R60	0.11	–	–	2.30e-04	85.0	14.8	0.2
$R60_{\text{Ne}}$	0.11	–	–	2.30e-04	85.1	14.7	0.2
W7	0.16	–	–	8.87e-03	–	–	–

freeze-out in the R60 model in contrast to VM and $M2a_{\odot}$. Furthermore, it can be seen that Mn also originates from the He detonation in Model $M2a_{\odot}$. Table 1 summarizes the Mn yields and also gives the fraction of the isotopes contributing to the final Mn abundance. It reveals that only M_{Ch} deflagrations (N5def, N100ddt, R60, $R60_{\text{Ne}}$, W7), the double detonation CSDD-L, and the helium detonation HeD-S achieve super-solar [Mn/Fe] ratios. For model R60 the [Mn/Fe] values are somewhat lower compared to N100ddt and N5def due to the newer set of reaction rates employed in the postprocessing. While $M2a_{\odot}$ roughly reaches the solar value of [Mn/Fe], the other double detonations ($M2a$, $M2a_{\text{Ne}}$ and CSDD-S) exhibit a sub-solar production of [Mn/Fe].

The value of [Mn/Fe] in the double-detonation models is governed by three fundamental parameters of the initial model:

(i) The ratio of shell to core mass ($M_{\text{shell}}/M_{\text{core}}$) is a crucial factor. Most Mn is produced in the helium detonation which is reflected by the super-solar value of 0.29 for HeD-S (see Table 1). In contrast to that [Mn/Fe] is below solar in CSDD-S due to the sub-solar value of the core detonation. The WD in Model CSDD-L, however, has a very low core mass ($0.45 M_{\odot}$)

and a helium shell of $0.2 M_{\odot}$ (the same as CSDD-S), and therefore the contribution of the core detonation to [Mn/Fe] is less significant.

(ii) The density of the helium shell also affects [Mn/Fe]. ^{55}Co is produced in a well-defined range of initial densities in the helium envelope above approximately $6 \times 10^5 \text{ g cm}^{-3}$. The density at the base of the helium shell for the low-mass progenitors in CSDD-L ($\rho_c = 5.92 \times 10^5 \text{ g cm}^{-3}$) and for CSDD-S ($\rho_c = 12 \times 10^5 \text{ g cm}^{-3}$) is sufficient to synthesize ^{55}Co . Thus, the amount of Mn is quite similar in both models. However, the amount of Fe is much lower in CSDD-L due to the lower density in the envelope, and therefore the discrepancy between CSDD-L and CSDD-S in [Mn/Fe] mainly originates from the yields of the shell detonation. Model CSDD-L gives a value of 1.69 for [Mn/Fe] from the helium shell detonation compared to 0.29 in Model CSDD-S.

(iii) The progenitor metallicity plays an essential role for the production of Mn.

Following argument (i) from above, a very low value of [Mn/Fe] could be expected for Model $M2a_{\odot}$ because of the

low-mass helium shell and the $\sim 1 M_{\odot}$ core. The data, in contrast, show an approximately solar value. The reason is that it has been calculated at solar metallicity, which leads to $[\text{Mn}/\text{Fe}]_{\text{core}} = -0.07$ (comparable to Model VM) for core material and $[\text{Mn}/\text{Fe}]_{\text{shell}} = 0.81$ for the shell. Since the production of nuclei more neutron-rich than ^{56}Ni is enhanced for lower Y_e , this shift in $[\text{Mn}/\text{Fe}]$ is reasonable. The yields of model M2a_{Ne} fall into line with this analysis. The $[\text{Mn}/\text{Fe}]$ value in the core material slightly decreases, however, indicating a low dependence on the initial distribution of nuclei. Furthermore, Model M2a at zero metallicity from Gronow et al. (2020) gives $[\text{Mn}/\text{Fe}] = -1.00$, which supports the explanations given above.

It is generally found that CO detonations at zero metallicity (also the core detonations of CSDD-L and CSDD-S) produce less Mn than models at higher metallicity (VM, M2a_o, M2a_{Ne}). In addition, the pure detonation models (PD081, PD115) not only underproduce Mn with respect to Fe (like VM), but also eject a total amount of Mn roughly three orders of magnitude below all other explosions. Although we do not have solar counterparts of CSDD-L, CSDD-S, PD081, PD115 nor zero-metallicity versions of VM, the comparison between the individual CO detonations still indicates a metallicity-dependent Mn production.

In addition, some Mn is made via ^{55}Fe directly only in the M_{Ch} models. In Fig. 4 we can observe that ^{55}Co is not produced at the very tip of the high-density end of the tracer particle distribution in Model R60. These are exactly the conditions where the even more neutron rich element ^{55}Fe is synthesized. In contrast to M2a_{Ne}, we do not observe any changes in the yields of R60_{Ne} compared to R60. This is most likely because almost all of ^{55}Co and ^{55}Fe is synthesized in normal freeze-out from NSE. Thus, the products largely depend on the neutronization due to electron capture during the explosion phase (see Sec. 2.2) and only weakly on the initial metallicity.

It should be noted that explosions such as M2a do not resemble normal SNe Ia in some aspects (see also Fink et al. 2010; Gronow et al. 2020). A solution to this problem might be to further decrease the mass of the helium shell (Townsley et al. 2019), but this also reduces the production of Mn in its detonation. However, explosions such as HeD-S are candidates for Ca-rich transients, a sub-luminous class of SNe residing between normal SNe Ia and classical novae in terms of absolute magnitude. Frohmaier et al. (2018) estimate rather high rates for Ca-rich transients of about 33%–94% of the rate of normal SNe Ia. If this proves to be correct, such explosions may substantially contribute to the production of Mn in the Universe.

To estimate the effect of Ca-rich SNe on the evolution of $[\text{Mn}/\text{Fe}]$ in the Milky Way we carried out a chemical evolution simulation using the code One-zone Model for the Evolution of GALaxies (OMEGA; Côté et al. 2017). We calculate an open-box model and employ the Côté et al. (2017) star formation model to control the in- and outflows of gas. These are linked to the star formation rate M_{\star} via a mass loading factor η . The total mass of gas inside the Galaxy is determined by the star formation efficiency f_{\star} : $M_{\star} = f_{\star} M_{\text{gas}}$. The star formation rate is taken from Chiappini et al. (2001), yields for massive stars are from Limongi & Chieffi (2018) (we use averaged values of their different rotating and non-rotating models), and yields of AGB stars are extracted from Karakas (2010). We find reasonable agreement with observational data for Mn using different SN Ia scenarios (see below) and fixing the star formation efficiency to $f_{\star} = 0.006$, the mass loading factor to $\eta = 0.7$, and the proportional constant connecting the star formation timescale and the dynamical timescale to $f_{\text{dyn}} = 0.004$. Moreover, the mass

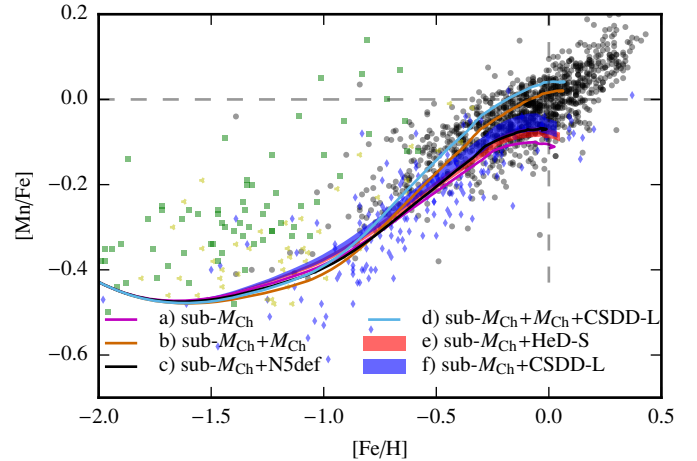


Fig. 5. Evolution of $[\text{Mn}/\text{Fe}]$ for different SNe Ia scenarios. The sub- M_{Ch} scenario is represented by the Model VM, the M_{Ch} scenario by N100ddt, and N5def is used as a proxy for SNe Iax. The shaded areas in the runs sub- M_{Ch} +CSDD-L and sub- M_{Ch} +HeD-S correspond to a range in the rate of Ca-rich transients between 33% and 94%. Black dots show observational data of Adibekyan et al. (2012), blue diamonds the data of Reddy et al. (2006), yellow triangles the data of Gratton et al. (2003), and red squares the data of Ishigaki et al. (2012, 2013). The data is from the STELLAr ABundances (STELLAB) library (Ritter & Côté 2016). The non-LTE data by Eitner et al. (2020) are not included in this simple approach.

transition between AGB yields and massive star yields is chosen to be $10.5 M_{\odot}$. Finally, the rate of SNe Ia is chosen to be $1.3 \times 10^{-3} M_{\odot}^{-1}$, and the total number of SNe Ia is distributed according to the chosen contribution of each channel (see cases below).

For the Chandrasekhar mass delayed detonations (N100ddt), helium-shell double-detonations (CSDD-L, HeD-S), and violent WD mergers (VM), we use delay time distributions calculated with the STARTRACK binary evolution code (e.g., Belczynski et al. 2008; Ruiter et al. 2009). For this work we assume Chandrasekhar mass exploding CO WDs that have a hydrogen-rich donor (in most cases a subgiant or giant star) that produces delayed-detonations. For violent WD mergers, we include any merger between two CO WDs that has at least one component WD mass $\geq 0.9 M_{\odot}$. For double-detonations with helium shells we employ the WD mass-dependent helium shell prescription of Ruiter et al. (2014).

We implemented the following combinations of SN Ia channels. Combinations (a), (b), and (c) have also been investigated by Seitzzahl et al. (2013b):

- (a) sub- M_{Ch} : 100% Model VM;
- (b) sub- $M_{\text{Ch}} + M_{\text{Ch}}$: 50% Model VM + 50% Model N100ddt;
- (c) sub- $M_{\text{Ch}} + \text{Iax}$: 80% Model VM + 20% N5def;
- (d) sub- $M_{\text{Ch}} + M_{\text{Ch}} + \text{CSDD-L}$: same as case (b) with 50% of CSDD-L added, which increases the number of SNe Ia per stellar mass formed to $1.95 M_{\odot}^{-1}$;
- (e) sub- $M_{\text{Ch}} + \text{HeD-S}$: the SN Ia rate consists of 100% of Model VM, and 33%-94% of Model HeD-S are included;
- (f) sub- $M_{\text{Ch}} + \text{CSDD-L}$: same as case (e) with Model CSDD-L instead of HeD-S.

Combinations (a), (b), and (c) confirm the results described above. The solar value of $[\text{Mn}/\text{Fe}]$ can only be reached when including a significant fraction of M_{Ch} explosions. In addition, a rather high fraction of 20% of failed deflagrations (N5def) represented by case (c) is not sufficient to match the increasing

trend. However, we note that the upward trend in $[\text{Mn}/\text{Fe}]$ is not only due to the contribution of M_{Ch} -mass SNe Ia. CCSNe also exhibit an increasing trend in $[\text{Mn}/\text{Fe}]$ with increasing metallicity. This is illustrated in scenario (a) where SNe Ia have virtually no contribution to Mn. However, despite the CCSN-caused increase in Mn, a solar ratio is not reached. Moreover, we find that helium detonations (HeD-S, CSDD-L) are as effective in increasing the final value of $[\text{Mn}/\text{Fe}]$ as N5def with our choice of rates (see variations (e) and (f)). Furthermore, case (d) demonstrates that CSDD-L also raises $[\text{Mn}/\text{Fe}]$ in the presence of N100ddt. This indicates that Ca-rich transients are able to reduce the need for M_{Ch} explosions to reproduce the evolution of $[\text{Mn}/\text{Fe}]$. We find that a reduction in M_{Ch} explosions to 30% of the SN Ia rate in scenario (d) yields $[\text{Mn}/\text{Fe}]$ values similar to those in case (b). Replacing CSDD-L with HeD-S allows a reduction to 40%. Thus, the occurrence rate of M_{Ch} SNe Ia needed to explain why $[\text{Mn}/\text{Fe}]$ versus $[\text{Fe}/\text{H}]$ can be reduced but not eliminated by the consideration of helium detonation models.

We note that this simple approach cannot replace future more elaborate GCE studies. It is only intended to give an impression of the contribution of helium shell detonation models compared to other SNe Ia scenarios given their low ejected mass per event. The delay-time distribution for explosions such as CSDD-L and HeD-S is not very well constrained, for instance. Fortunately, this does not challenge our conclusion since different DTDs only alter the shape of the $[\text{Mn}/\text{Fe}]$ evolution and leave the final value at $[\text{Fe}/\text{H}] = 0$ largely unaffected. While there is still much uncertainty associated with the evolution and explosive outcome of helium shell double-detonation binaries, we note that in our binary evolution models progenitors of double-detonation SN Ia explosions are more similar in physical configuration to the models of Gronow et al. (2020) (in terms of core and shell mass), rather than the earlier models computed by Sim et al. (2012). However, it turns out that regardless of whether low to moderate shell mass systems (Gronow) or high shell mass systems (Sim) are actually contributing to the SN Ia population, it will not have any noticeable effect on the delay-time distribution of these explosions since the timescale on which these WDs accumulate helium is insignificant by comparison (on the order of ~ 10 Myr).

In addition, a large number of helium detonations would lead to tensions in $[\text{Ti}/\text{Fe}]$ and $[\text{V}/\text{Fe}]$ since these elements are produced in super-solar amounts in them (see Fig. 3). This is yet another argument excluding helium shell detonations or double detonations as a replacement for M_{Ch} SNe Ia models producing a solar $[\text{Mn}/\text{Fe}]$ value. As Ti and V are, however, underproduced over the whole metallicity range in current GCE studies (see Prantzos et al. 2018 and references therein), their site of production is not yet completely clarified. The yields derived from helium detonation models do not solve the problem. They imply an increased production at $[\text{Fe}/\text{H}] \approx 0$ and fail to provide a good fit to the $[\text{Ti}/\text{Fe}]$ and $[\text{V}/\text{Fe}]$ evolution at low metallicities. We find that a decrease in the CSDD-L rate to approximately 10% of the SN Ia rate resolves this tension and yields the solar value for $[\text{Ti}/\text{Fe}]$ and $[\text{V}/\text{Fe}]$ in scenario d). However, this only allows for a reduction in the M_{Ch} events to 45% compared to 30% mentioned above.

3.2. Zinc

The element zinc ranges right beyond the iron peak and is of high interest for GCE since its origin has not been clarified yet. It has four stable isotopes, namely ^{64}Zn , ^{66}Zn , ^{67}Zn , and ^{68}Zn , of

which ^{64}Zn is the most abundant in the solar neighborhood. The production mechanisms are therefore more diverse than in the case of Mn. Zinc abundances in the Galaxy have been measured already by Sneden et al. (1991) and later by Mishenina et al. (2002), Cayrel et al. (2004), and Nissen et al. (2007). All agree on its evolution: Zn exhibits high values of $[\text{Zn}/\text{Fe}] \approx 0.6$ at $[\text{Fe}/\text{H}] \approx -4$, which drop to solar at around $[\text{Fe}/\text{H}] \approx -2$. From there on they remain at $[\text{Zn}/\text{Fe}] \approx 0$. Some of the Zn abundance is synthesized during He or C burning via the s-process in massive stars, but the major contribution comes from explosive nucleosynthesis in supernovae. Standard CCSNe models (see, e.g., the yields of Woosley & Weaver 1995) fall short in the production of Zn. Only the introduction of hypernovae (HNe) can account for the solar value of $[\text{Zn}/\text{Fe}]$ (Kobayashi et al. 2006), but the high values at very low metallicities are not reached within this model either.

The most commonly used SN Ia model for GCE calculations is the W7 model (Iwamoto et al. 1999): a 1D pure deflagration in a M_{Ch} CO WD. This particular simulation yields only negligible amounts of Zn (see Table 2). Therefore, it has been a goal to explain the evolution of Zn with other production sites, although 1D double-detonation and pure helium detonation models calculated by Woosley & Kasen (2011) show substantial amounts of Zn. The recent work by Hirai et al. (2018) tries to explain the evolution of Zn with metallicity-dependent yields of CCSNe as well as HNe from Nomoto et al. (2013). They find that the inclusion of electron capture supernovae (ECSNe, yields from Wanajo et al. 2018) is necessary to match the high $[\text{Zn}/\text{Fe}]$ values at low metallicity. Jones et al. (2019a) presented nucleosynthesis yields of thermonuclear ECSNe (tECSNe), i.e., the explosion of oxygen-neon WDs at densities around $10^{10} \text{ g cm}^{-3}$. These models overproduce neutron-rich isotopes such as ^{48}Ca , ^{50}Ti , and ^{54}Cr , as well as ^{66}Zn and other elements beyond the iron peak. In a follow-up study Jones et al. (2019b) showed that these models complement nicely the contribution of ECSNe to the chemical evolution of the Milky Way. Prantzos et al. (2018) cannot reproduce the evolution of Zn using the nucleosynthesis yields of rotating massive stars by Limongi & Chieffi (2018).

In spite of this, a high contribution of SNe Ia to Zn was proposed by Matteucci et al. (1993) and later on by François et al. (2004). Mishenina et al. (2002) claim that SNe Ia are responsible for as much as 67% of the Zn production. Tsujimoto & Nishimura (2018) investigate the evolution of Zn in the Galaxy using Mg instead of Fe as the reference element. Magnesium is an α -element assumed to be solely produced in CCSNe, and thus it is more sensitive in detecting the contribution of sources other than CCSNe to a specific element. They discover a decreasing trend for $[\text{Zn}/\text{Mg}]$ for $[\text{Zn}/\text{Mg}] \lesssim -1$ and an increasing trend for higher metallicities. This increasing behavior coincides with the well-known kick-in of SNe Ia at $[\text{Fe}/\text{H}] = -1$. Consequently, they conclude that SNe Ia must be responsible for this behavior and suggest a scenario including a He detonation with strong α -rich freeze-out. The decreasing trend at low metallicities is explained in their GCE model by the incorporation of magnetorotational SNe (MR SNe), whose rate decreases with increasing metallicity.

No matter which combination of supernova scenarios accounts for the observed abundances at $[\text{Fe}/\text{H}] \lesssim -1$, it is very likely that SNe Ia also contribute to Zn in a non-negligible way, i.e., a significant underproduction would require an even larger contribution from CCSNe to keep $[\text{Zn}/\text{Fe}]$ near the solar value. The question is which scenario for SNe Ia synthesizes $[\text{Zn}/\text{Fe}]$ at around the solar ratio or higher and therefore contributes to the enrichment of galaxies with Zn.

Table 2. Total amount of stable Zn in M_{\odot} and the radioactive and stable isotopes from which Zn originates (shown as percentages) at 100 s.

Model	Zn	^{64}Zn	^{66}Zn	^{68}Zn	^{64}Ga	^{64}Ge	^{66}Ge	^{67}Ge	^{68}Ge	^{67}Cu	^{66}Ni
PD081	3.49e-16	97.9	–	–	1.5	–	–	–	–	–	–
PD115	5.42e-05	99.1	–	–	–	–	–	–	–	–	–
VM	2.21e-06	1.6	–	–	9.4	28.3	60.6	–	–	–	–
M2a $_{\odot}$	1.71e-04	4.2	10.3	–	7.8	39.1	34.0	1.2	2.1	–	–
M2a $_{\text{Ne}}$	1.35e-04	–	–	–	11.1	58.4	29.1	–	–	–	–
M2a	4.44e-04	–	–	–	13.0	79.9	5.4	–	–	–	–
CSDD-L	6.05e-06	1.6	–	–	12.7	21.2	36.7	12.7	14.4	–	–
CSDD-S	7.49e-04	–	–	–	7.0	85.4	6.9	–	–	–	–
HeD-S	7.41e-04	–	–	–	6.8	85.5	7.0	–	–	–	–
N5def	6.58e-07	8.5	–	–	6.0	28.5	56.2	–	–	–	–
N100ddt	3.12e-06	5.6	–	–	5.9	30.9	57.2	–	–	–	–
R60	1.80e-07	4.7	2.9	–	4.1	33.6	53.0	–	–	–	–
R60 $_{\text{Ne}}$	1.92e-06	–	–	–	3.9	31.6	49.6	–	–	–	14.1
W7	4.93e-07	–	–	–	–	–	–	–	–	–	–

Notes. Only contributions larger than 1% are listed.

Table 3. Ratio of Zn to Fe compared to solar for the total explosion, to shell and core material only, and to stable zinc isotopes decayed at 2×10^9 yr.

Model	[Zn/Fe]	[Zn/Fe] $_{\text{shell}}$	[Zn/Fe] $_{\text{core}}$	^{64}Zn	^{66}Zn	^{67}Zn	^{68}Zn
PD081	-10.54	–	–	3.48e-16	–	–	–
PD115	-1.31	–	–	5.38e-05	3.57e-07	–	–
VM	-2.60	–	–	8.67e-07	1.34e-06	–	–
M2a $_{\odot}$	-0.66	0.82	-0.92	8.72e-05	7.59e-05	2.48e-06	5.11e-06
M2a $_{\text{Ne}}$	-0.77	0.77	-1.09	9.46e-05	3.92e-05	5.60e-07	3.45e-07
M2a	-0.25	1.02	-0.48	4.16e-04	2.46e-05	1.52e-06	1.64e-06
CSDD-L	-0.71	0.07	-1.77	2.14e-06	2.25e-06	7.86e-07	8.73e-07
CSDD-S	0.40	0.87	-1.44	6.94e-04	5.19e-05	–	–
HeD-S	0.87	0.87	–	6.86e-04	5.18e-05	–	–
N5def	-2.64	–	–	2.83e-07	3.74e-07	–	–
N100ddt	-2.51	–	–	1.32e-06	1.79e-06	–	–
R60	-1.20	–	–	7.67e-07	1.02e-06	5.76e-09	8.67e-09
R60 $_{\text{Ne}}$	-1.17	–	–	6.96e-07	1.22e-06	1.48e-09	3.80e-10
W7	-1.66	–	–	–	–	–	–

Table 2 lists the total production of Zn in solar masses as well as the fraction of isotopes via which it is produced. In addition, Table 3 shows [Zn/Fe] for the whole explosion and for the helium shell and core detonation separately in the case of a double detonation. It reveals that all models, except for those including a helium detonation (M2a $_{\odot}$, M2a, CSDD-S, CSDD-L, and HeD-S), severely underproduce [Zn/Fe] compared to its solar value. While M2a $_{\odot}$, M2a $_{\text{Ne}}$, M2a, and CSDD-L exhibit only a moderate underproduction, the remaining models synthesize super-solar ratios [Zn/Fe]. The [Zn/Fe] value of the helium detonation is quite similar in M2a $_{\odot}$, CSDD-S, and HeD-S, but the result of the whole explosion is dominated by the core detonation for model M2a $_{\odot}$. In contrast to the case of Mn, the values of [Zn/Fe] in M2a are higher than its solar metallicity counterpart. The most important production channel is via the symmetric nucleus ^{64}Ge , as is also the case for CSDD-S and HeD-S. In Model CSDD-L the [Zn/Fe] yield of the helium shell detonation is significantly lower than in the other models. The reason for this is the lower density of the envelope (see argument (ii) in Sect. 3.1) because most Zn is produced above an initial density of $5.0 \times 10^5 \text{ g cm}^{-3}$. The lower density is also responsible for the difference in the contribution of ^{64}Ge compared to

the other double detonations as it is produced at higher densities than ^{66}Ge , for example.

Furthermore, it can be seen that the main production channels are $^{64}\text{Ga} \rightarrow ^{64}\text{Zn}$, $^{64}\text{Ge} \rightarrow ^{64}\text{Ga} \rightarrow ^{64}\text{Zn}$, and $^{66}\text{Ge} \rightarrow ^{66}\text{Ga} \rightarrow ^{66}\text{Zn}$ for the majority of models except for PD081 and PD115. These isotopes are produced either in α -rich freeze-out from NSE or in the helium detonation (see Fig. 6).

Figure 6 also shows that Zn is primarily produced in the helium shell at relatively high densities. This region is not reached by CSDD-L, as discussed above. A direct production of Zn in the form of a high contribution from ^{64}Zn can only be observed in the pure detonations PD081 and PD115 and, to a much lesser extent, in the M_{Ch} models. However, the total amount of Zn falls short of that of Models CSDD-S, HeD-S, and M2a $_{\odot}$ by about two orders of magnitude. R60 and M2a $_{\odot}$ are the only models to directly produce a non-negligible amount of ^{66}Zn . Moreover, the direct production of Zn isotopes ($^{64,66}\text{Zn}$) is clearly a metallicity effect. The corresponding simulations at lower metallicity shift the production of Zn to the symmetric isotope. This behavior is not observed for the other models at solar metallicity (N5def, N100ddt, VM). In contrast to our most recent simulations (M2a $_{\odot}$ and R60, where the solar value for each

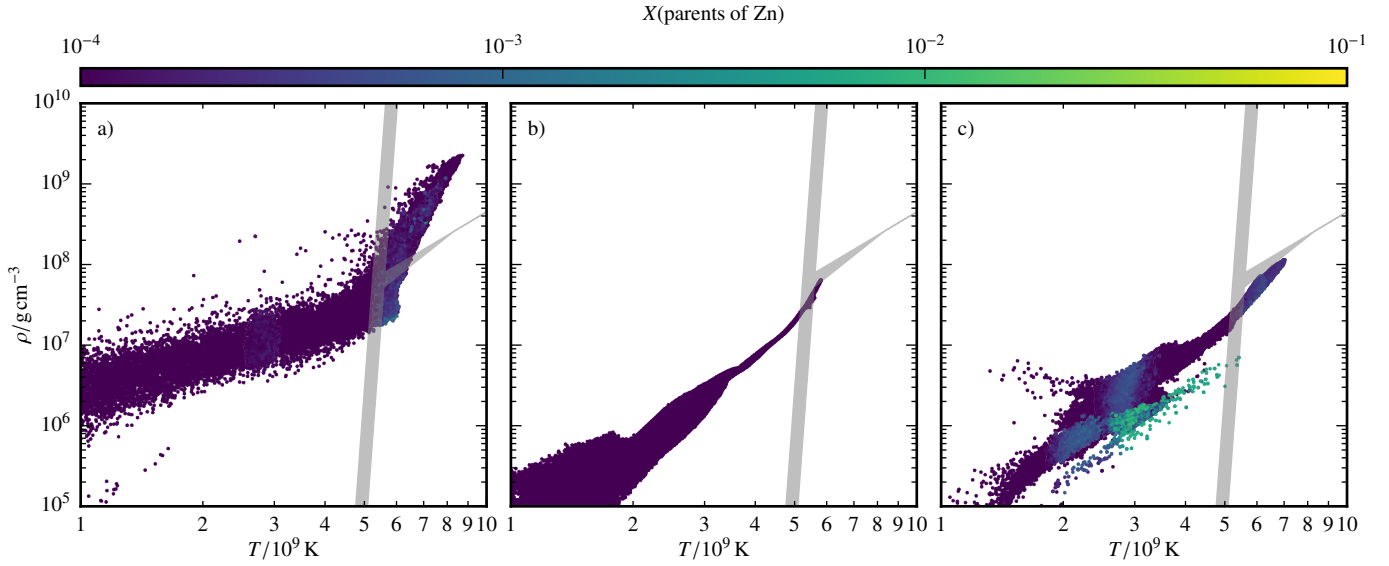


Fig. 6. Same as Fig. 2 with a color-coded mass fraction of the parent nuclei of Zn listed in Table 2. The panels show (a) R60, (b) VM, (c) M2a_⊙.

isotope according to [Asplund et al. 2009](#) is used as input for the postprocessing), the metallicity is set by adding only ²²Ne to adjust the electron fraction. Therefore, the lack of seed nuclei in the investigated region might affect the detailed nucleosynthesis results. This is confirmed by models R60_{Ne} and M2a_{Ne}. They do not produce any Zn isotopes and also show differences in the production of various other species.

In summary, any SN Ia scenario noticeably contributing to the enrichment of the Galaxy with Zn is required to include a prominent helium detonation. The production of Zn can be explained by the same three arguments used for the case of Mn. However, here CSDD-L shows the lowest ratio to iron since the initial shell density is too low to synthesize Zn in sufficient amounts. We abstain from adding an investigation of the galactic evolution of [Zn/Fe] since we have already shown for the case of Mn that low-mass double detonations and pure helium shell detonations do contribute significantly to [Mn/Fe] despite their low ejecta masses. This result holds analogously for [Zn/Fe].

Instead, we briefly estimate the influence of ⁶⁸Ge on the light curve. All other isotopes listed in Table 2 are short-lived with a maximum half-life¹ of 61.8 h for ⁶⁷Cu. Although compared to ⁵⁶Ni long-lived isotopes are not produced in large amounts, they can modify the shape of the light curve at late times ([Seitenzahl et al. 2009](#)). Furthermore, γ rays or X-rays emitted in their decay might be detectable.

⁶⁸Ge decays to ⁶⁸Ga via electron capture with a half-life of $T_{1/2} = 270.95$ d. The two most relevant X-rays emitted have energies of $E_1 = 9.225$ and $E_2 = 9.252$ keV with an emission probability of $I_1 = 0.131$ and $I_2 = 0.258$, respectively. As an example, we consider Model M2a_⊙, which ejects $3.554 \times 10^{-6} M_{\odot}$ of ⁶⁸Ge. Assuming transparent ejecta after $t = 100$ d and a very close SN explosion at a distance of $d = 1$ Mpc, we arrive at a flux on Earth of

$$F_i = \frac{1}{4\pi d^2} \cdot I \lambda N_0 e^{-\lambda t} \cdot E_i$$

$$= \begin{cases} 2.325 \times 10^{-17} \text{ erg s}^{-1} \text{ cm}^{-2} & i = 1 \\ 4.592 \times 10^{-17} \text{ erg s}^{-1} \text{ cm}^{-2} & i = 2, \end{cases} \quad (6)$$

¹ All nuclear decay data is taken from <https://www.nndc.bnl.gov/nudat2/>

where λ is the decay constant and N_0 the number of nuclei at $t = 0$, which can be derived dividing the ejected mass by the corresponding atomic mass². The X-ray telescope *NuSTAR* ([Harrison et al. 2013](#)) has a sensitivity of 2×10^{-15} erg s⁻¹ cm⁻² in the considered energy range. Therefore, the added flux of the two X-ray emissions is about a factor of 35 below the detection limit, and thus a higher production of ⁶⁸Ge would be necessary for a potential detection even under the rather favorable conditions assumed here. We note that this statement is by no means conclusive since the sensitivity of *NuSTAR* also depends on the line shape and on the observation time.

Subsequently, ⁶⁸Ga decays to ⁶⁸Zn via positron emission very quickly ($T_{1/2} = 67.71$ min). Assuming an instantaneous energy deposition, we calculated the contributions of ⁶⁸Ga, ⁴⁴Sc, ⁵⁶Co, ⁵⁷Co, and ⁵⁵Fe positrons, conversion electrons, and Auger electrons to the SN light curve for Models HeD-S (same amount of ⁶⁸Ge as CSDD-S), CSDD-L, and M2a_⊙. In the cases of ⁶⁸Ga and ⁴⁴Sc the electrons emitted by their long-lived parents are included as well. Figure 7 shows that with less than 0.4% of the energy generation per second ϵ , the ⁶⁸Ga decay plays only a minor role in model M2a_⊙. Its contribution is even lower in the HeD-S and CSDD-L models.

3.3. Copper

Copper directly follows nickel in the periodic table and its elemental solar abundance consists of two stable isotopes, namely ⁶³Cu and ⁶⁵Cu. Of these, about 69% are attributed to ⁶³Cu ([Asplund et al. 2009](#)). The first extensive measurements and an analysis of Cu abundances have been carried out by [Snedden et al. \(1991\)](#). The general trend of an increasing value of [Cu/Fe] with [Fe/H] in the Galaxy was established in that work. [Cu/Fe] increases from a value of approximately -1 at $[\text{Fe}/\text{H}] \approx -3$ to the solar value at $[\text{Fe}/\text{H}] \approx 0$.

As for Zn, the origin of Cu is still very uncertain. The largest contributors are believed to be the weak component of the s-process in massive stars (a secondary process) and the direct fusion as a primary element simultaneous to IGEs in CCSNe and SNe Ia. [Matteucci et al. \(1993\)](#) carried out detailed GCE

² The atomic mass is taken from <https://www-nds.iaea.org/>

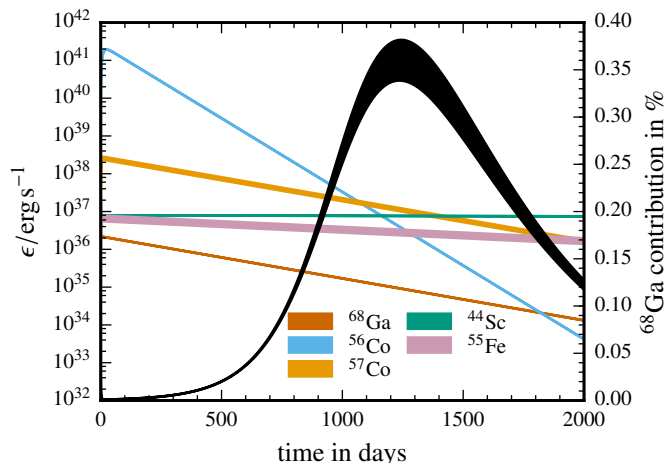


Fig. 7. Energy generation rate ϵ of the emission of positrons, conversion electrons, and Auger electrons in model M2a $_{\odot}$. Shaded areas show the range between no X-ray trapping and full X-ray trapping. The black curve depicts the contribution of the ^{68}Ga decay relative to the total energy generation.

calculations. Comparing their data to the [Snedden et al. \(1991\)](#) data, they conclude that a best fit is achieved if the SNe Ia yields for Cu are increased by an order of magnitude. Moreover, they claim that SNe Ia start contributing to the enrichment of the Galaxy starting from $[\text{Fe}/\text{H}] \approx -1.7$ (i.e., already in the halo phase). [Mishenina et al. \(2002\)](#) provide a large upgrade to the Cu abundance data by measuring Cu and Zn in 90 metal-poor stars in the Galaxy. They arrive at the conclusion that the increase in $[\text{Cu}/\text{Fe}]$ is due to a significant contribution of SNe Ia. As a guideline they also provide a very rough estimate of the relative contributions of Cu from different production sites to the solar abundance. They assign 7.5% to SNe II (primary process in massive stars), 25% to secondary processes in massive stars, 5% to the s-process in AGB stars, and 62.5% to SNe Ia. The overall trend of the Cu-to-Fe ratio, i.e., a sub-solar plateau at low metallicities and an increase to the solar value, which is reached at $[\text{Fe}/\text{H}] \approx -0.8$, has also been confirmed by [Reddy et al. \(2003\)](#). In contrast, [Prantzos et al. \(2018\)](#) show that by including the yields of [Limongi & Chieffi \(2018\)](#) the evolution of $[\text{Cu}/\text{Fe}]$ can be modeled with CCSNe alone (they use W7 for SNe Ia). [Nissen & Schuster \(2011\)](#) also confirm sub-solar $[\text{Cu}/\text{Fe}]$ values for their low- α population of dwarf stars in the solar neighborhood. These stars are thought to be primarily enriched by SNe Ia, and therefore they conclude that they are not main contributors to Cu. [Simmerer et al. \(2003\)](#) investigate the Cu abundances in various globular clusters and draw the opposite conclusion, that SNe Ia are likely to be the main contributors to Cu, because $[\text{Cu}/\text{Fe}]$ in globular clusters follows the trend seen in field stars. However, the only cluster spanning a significant range in metallicity ($-1.8 < [\text{Fe}/\text{H}] < 0.8$) is ω -Centauri and there the $[\text{Cu}/\text{Fe}]$ curve is rather flat. This suggests a different chemical evolution history. In contrast to the previously mentioned results, [Romano & Matteucci \(2007\)](#) find that their GCE model can fit both the Galaxy and ω -Centauri if the s-process yields are enhanced and the SN Ia yields are reduced. [Cunha et al. \(2002\)](#) investigate in more detail the evolution of ω -Centauri. They attribute the strong enhancement of α -elements relative to Fe and the constant evolution of $[\text{Cu}/\text{Fe}]$ at a rather low value of -0.5 to an enrichment via CCSNe. However, a final explanation for the lack of SNe Ia enrichment is not given. Recent non-LTE Cu abundance measurements are

presented by [Yan et al. \(2015, 2016\)](#). They show that non-LTE effects raise the previously measured values by about 0.2 dex and that this difference is also metallicity dependent. The impact of the non-LTE treatment is higher for lower $[\text{Fe}/\text{H}]$, and therefore flattens the whole curve. Furthermore, the plateau at lower metallicities is extended compared to older works, and reaches up to $[\text{Fe}/\text{H}] \approx -1$ and then rises to solar. However, [Yan et al. \(2015\)](#) note that due to the uncertainties in the main production site of Cu and to the peculiar evolution of Cu in Ursa Major, ω -Centauri, the Sagittarius dwarf galaxy, and the halo subpopulation ([Nissen & Schuster 2011](#)), further GCE models should be postponed until the trend of $[\text{Cu}/\text{Fe}]$ is clearly established by using non-LTE measurements.

Similar to the discussion on Zn (see Sect. 3.2), it is now interesting to see which SN Ia scenario is able to synthesize Cu in significant amounts. Table 4 displays the Cu yields together with the relative contribution of the most important production channels. In Table 5 the $[\text{Cu}/\text{Fe}]$ values and the remaining stable Cu isotopes can be found.

The overall result is the same as for the Zn case: Cu is largely underproduced compared to solar in all simulations except for two models including a He detonation, in this case HeD-S and CSDD-S. However, $[\text{Cu}/\text{Fe}]$ values are lower than $[\text{Zn}/\text{Fe}]$ for the helium shell, which also diminishes the total $[\text{Cu}/\text{Fe}]$ yields. M2a $_{\odot}$, M2a $_{\text{Ne}}$, and M2a even approach the pure detonation PD115 due to the low ratio of shell mass to core mass (argument (i) in Sect. 3.1). A comparison between M2a $_{\odot}$ and M2a shows that the metallicity has little impact on the total value of $[\text{Cu}/\text{Fe}]$. It only slightly changes the fractions of the parent nuclei that decay to stable Cu. In particular, we find that the direct production of ^{63}Cu and ^{65}Cu is favored for higher metallicity and that the inclusion of only ^{22}Ne leads to a decrease in $[\text{Cu}/\text{Fe}]$ (see R60 $_{\text{Ne}}$, M2a $_{\text{Ne}}$). Moreover, the difference in $[\text{Cu}/\text{Fe}]$ from the helium shell between CSDD-L and the other double detonations is less significant than for $[\text{Zn}/\text{Fe}]$. ^{63}Ga , for example, is mainly produced at an initial density higher than the density at the base of the shell in CSDD-L, and therefore the relative contribution to stable Cu is shifted to ^{65}Ga and ^{65}Ge compared to Models CSDD-S and HeD-S.

In contrast to Zn, a main production channel for Cu cannot be identified. While most models, except R60, produce some Cu via ^{63}Zn , the helium detonations additionally show a major contribution from ^{63}Ga , ^{65}Ga , and ^{65}Ge . The M_{Ch} simulations and PD115 also synthesize considerable amounts of ^{63}Cu , and M2a $_{\odot}$ exhibits contributions from almost every parent isotope listed in Table 4. This suggests that neither the core nor the helium detonation dominates the total Cu yields.

To sum up, the creation of a large amount of Cu in relation to Fe requires an even more prominent helium detonation than in the case of Zn. We find in addition that a density at the base of the helium envelope exceeding that in Model CSDD-L of $5.92 \times 10^5 \text{ g cm}^{-3}$ is essential. From a GCE point of view the contribution of helium detonations to Cu is less significant than in the case of Mn or Zn among the investigated models. The only model expected to contribute considerably to $[\text{Cu}/\text{Fe}]$ is HeD-S. Also in this case we postpone detailed GCE modeling to future work.

Similar to the discussion of long-lived radioactive isotopes in Sect. 3.2 we take a brief look at ^{65}Zn . The only other long-lived isotope in Table 4 is ^{63}Ni . However, it is only produced in very small amounts in model R60, and its half-life of 101.2 y implies a very low rate of decay. ^{65}Zn , in contrast, has a half-life of $T_{1/2} = 243.93 \text{ d}$ and emits an energetic γ ray with an energy of $E = 1115.539 \text{ keV}$ and an emission probability of $I = 0.5004$.

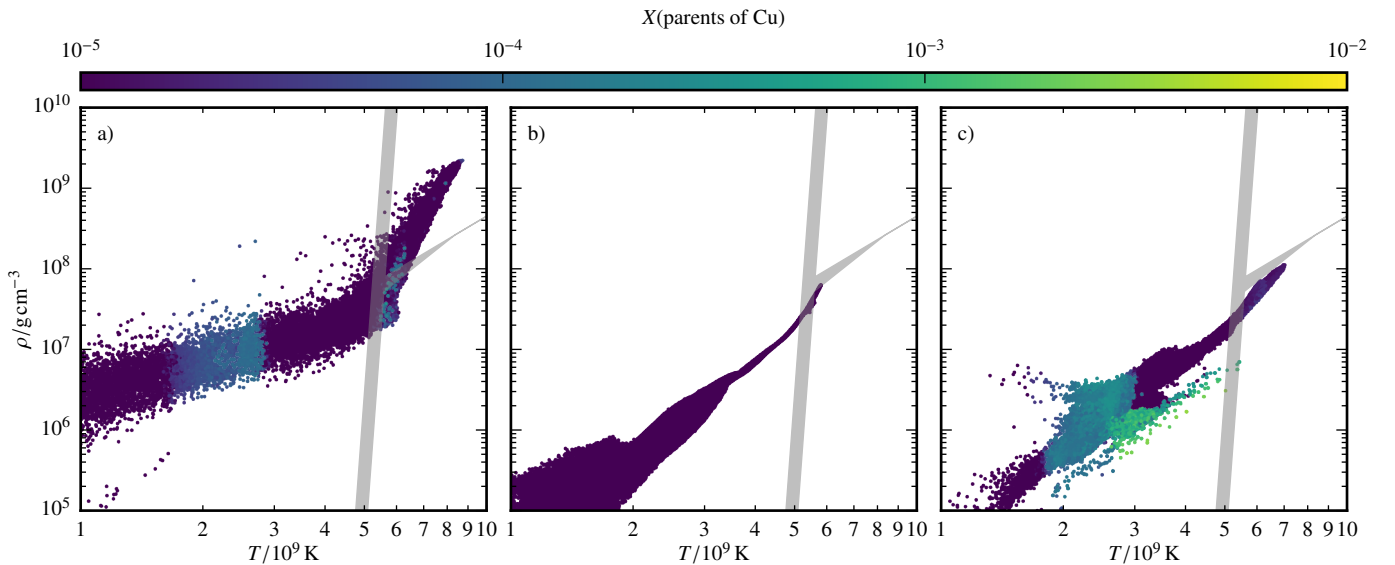
Table 4. Total amount of stable Cu in M_{\odot} and the radioactive and stable isotopes from which Cu originates (shown as percentages) at 100 s.

Model	Cu	^{63}Cu	^{65}Cu	^{63}Zn	^{65}Zn	^{63}Ga	^{65}Ga	^{65}Ge	^{63}Ni	^{65}Ni	^{63}Co
PD081	1.66e-15	33.4	–	66.0	–	–	–	–	–	–	–
PD115	2.48e-05	34.2	–	64.9	–	–	–	–	–	–	–
VM	3.37e-07	–	–	74.2	–	8.8	13.9	2.0	–	–	–
M2a $_{\odot}$	2.43e-05	10.6	10.8	15.5	3.6	10.5	33.4	12.6	2.2	–	–
M2a $_{\text{Ne}}$	1.60e-05	–	–	20.2	–	16.9	45.1	17.3	–	–	–
M2a	3.03e-05	–	–	18.2	3.0	23.5	41.9	14.1	–	–	–
CSDD-L	3.44e-06	–	–	27.0	–	16.0	26.2	30.4	–	–	–
CSDD-S	1.29e-04	–	–	18.8	–	57.7	9.9	13.6	–	–	–
HeD-S	1.31e-04	–	–	17.9	–	59.1	9.4	13.6	–	–	–
N5def	1.15e-07	38.9	1.4	30.8	–	8.3	9.5	4.5	6.7	–	–
N100ddt	4.58e-07	29.6	–	38.9	–	10.1	11.5	5.0	3.8	–	–
R60	2.54e-07	22.3	8.3	9.3	3.1	3.5	12.5	16.6	13.3	2.3	8.9
R60 $_{\text{Ne}}$	1.13e-07	2.3	–	20.7	–	7.8	28.1	37.2	–	–	2.4
W7	3.21e-07	–	–	–	–	–	–	–	–	–	–

Notes. Only contributions larger than 1% are listed.

Table 5. Ratio of Cu to Fe compared to solar for the total explosion, and for shell and core material only and stable copper isotopes decayed at 2×10^9 yr.

Model	[Cu/Fe]	[Cu/Fe] $_{\text{shell}}$	[Cu/Fe] $_{\text{core}}$	^{63}Cu	^{65}Cu
PD081	-9.48	–	–	1.65e-15	9.78e-18
PD115	-1.25	–	–	2.55e-05	2.33e-07
VM	-3.03	–	–	2.82e-08	5.44e-08
M2a $_{\odot}$	-1.13	0.43	-1.48	9.62e-06	1.47e-05
M2a $_{\text{Ne}}$	-1.31	0.39	-1.93	5.95e-06	1.01e-05
M2a	-1.04	0.43	-1.51	1.29e-05	1.75e-05
CSDD-L	-0.57	0.21	-1.69	1.49e-06	1.95e-06
CSDD-S	0.02	0.48	-1.31	9.86e-05	3.02e-05
HeD-S	0.50	0.50	–	1.01e-04	3.01e-05
N5def	-3.01	–	–	9.76e-07	1.77e-08
N100ddt	-2.95	–	–	3.78e-07	8.04e-08
R60	-1.67	–	–	1.45e-07	1.09e-07
R60 $_{\text{Ne}}$	-2.02	–	–	3.84e-08	7.50e-08
W7	-1.46	–	–	–	–


Fig. 8. Same as Fig. 2, with a color-coded mass fraction of ^{64}Ge . The panels show (a) R60, (b) VM, (c) M2a $_{\odot}$.

Most ^{65}Zn is synthesized via the fast decaying isotopes ^{65}Ge and ^{65}Ga (see Table 2). Under the same assumptions as in Sect. 3.2, we arrive at a flux on Earth for Model CSDD-S (highest amount of ^{65}Zn among our models with $3.019 \times 10^{-5} M_{\odot}$) of

$$F = 1.031 \times 10^{-13} \text{ erg s}^{-1} \text{ cm}^{-2}. \quad (7)$$

Although this value is four orders magnitude higher than for the ^{68}Ge X-rays (see Sect. 3.2), it is still at least an order of magnitude below the expected sensitivity of the planned γ -ray telescope e-ASTROGAM (De Angelis et al. 2018), and therefore a detection is very unlikely.

4. Summary

We investigated the nucleosynthesis yields of a variety of SN Ia models from the HESMA (Kromer et al. 2017) archive as well as two new explosion simulations, M2a $_{\odot}$ and R60. These models include double-detonation models from Sim et al. (2012) and Gronow et al. (2020). Furthermore, we examined the pure detonations in sub- M_{Ch} WDs of Sim et al. (2010) and a set of M_{Ch} explosions from Seitenzahl et al. (2013a) and Fink et al. (2014).

Our aim was to identify elements characteristic of a certain explosion mechanism. In combination with GCE calculations and abundance measurements in stellar atmospheres, this can help to identify SN Ia progenitors. A well-known example is the element manganese. Its abundance relative to iron increases from $[\text{Fe}/\text{H}] \approx -1$ and it is not produced by CCSNe in sufficiently high ratios relative to Fe. Therefore, it is attributed to thermonuclear explosions of M_{Ch} WDs (Seitenzahl et al. 2013b). In this study we find that super-solar amounts of Mn are additionally synthesized in helium detonations and that the actual result depends on the interplay of three parameters: the metallicity, the helium shell mass compared to the CO core, and the density of the helium envelope. A variation in these values gives rise to sub-solar values of $[\text{Mn}/\text{Fe}]$ (as seen in Models M2a and CSDD-S) up to highly super-solar results (CSDD-L). This also brings the double-detonation scenario into play as a potential source of Mn. Therefore, the sole distinction between sub- M_{Ch} and M_{Ch} mass models when investigating the source of Mn is insufficient. The details of the underlying model employed for the sub- M_{Ch} channel have to be defined in addition. Our GCE calculation corroborates this result and demonstrates that double-detonation models with massive helium shells can significantly reduce but not completely remove the need for M_{Ch} explosions to explain the solar $[\text{Mn}/\text{Fe}]$ ratio. Their actual rate is limited, however, due to their super-solar $[\text{Ti}/\text{Fe}]$ and $[\text{V}/\text{Fe}]$ values.

Moreover, the elements zinc and copper have received little attention when studying the contribution of SNe Ia to galactic chemical evolution, although Matteucci et al. (1993) already pointed out the potential relevance of these events as a production site. We find that double-detonation models are able to produce Zn and Cu in super-solar ratios with respect to Fe. Since a sophisticated GCE modeling and a comprehensive analysis of the contribution of massive stars is beyond the scope of this work, we did not include models for the evolution of $[\text{Zn}/\text{Fe}]$ and $[\text{Cu}/\text{Fe}]$. However, the general results from the case of Mn carry over to Zn and Cu. The same three parameters as in the case of Mn also affect the creation of Zn and Cu. Essentially, any value of $[\text{Mn}/\text{Fe}]$, $[\text{Zn}/\text{Fe}]$, or $[\text{Cu}/\text{Fe}]$ can be realized using different combinations of helium shell mass, core mass, shell density and metallicity. However, in this study we find that the models from Sim et al. (2012) affect the evolution of Mn, Zn and Cu the most. These models follow explosions in a system of a low-mass CO

cores covered by a massive helium shell. They were intended to resemble a subluminous subclass of SNe Ia, namely calcium-rich transients, but do not account for normal SNe Ia. Their significance for GCE therefore depends on the realization frequency of Ca-rich transients, which is currently subject to large uncertainties. Ongoing and planned transient searches hold promise to clarify this aspect.

We thus emphasize that SNe Ia, or, in general thermonuclear explosions, should be treated more carefully in GCE studies. It seems necessary to include a variety of thermonuclear explosion models rather than sticking to only one or two scenarios. SNe Ia should be considered as a source of Zn and Cu in GCE simulations if the double-detonation scenario is used to represent either normal SNe Ia (see, however, Kromer et al. 2010, for potential problems with the predicted spectral observables) or the faint class of calcium-rich transients. M_{Ch} explosions might not be the only relevant source of Mn.

Acknowledgements. This work was supported by the Deutsche Forschungsgemeinschaft (DFG, German Research Foundation) – Project-ID 138713538 – SFB 881 (“The Milky Way System”, subproject A10), by the ChETEC COST Action (CA16117), and by the National Science Foundation under Grant No. OISE-1927130 (iReNA). F. L., F. K. R. and S. G. acknowledge support by the Klaus Tschira Foundation. IRS was supported by the Australian Research Council through Grant FT160100028. A. J. R. was supported by the Australian Research Council through Grant FT170100243. NumPy and SciPy (Oliphant 2007), IPython (Pérez & Granger 2007), and Matplotlib (Hunter 2007) were used for data processing and plotting. The authors gratefully acknowledge the Gauss Centre for Supercomputing e.V. (www.gauss-centre.eu) for funding this project by providing computing time on the GCS Supercomputer JUWELS (Jülich Supercomputing Centre 2019) at Jülich Supercomputing Centre (JSC). Part of this research was undertaken with the assistance of resources and services from the National Computational Infrastructure (NCI), which is supported by the Australian Government, through the National Computational Merit Allocation Scheme and the UNSW HPC Resource Allocation Scheme. BC acknowledges support from the ERC Consolidator Grant (Hungary) funding scheme (project RADIOSSTAR, G.A. n. 724560) and from the National Science Foundation (USA) under Grant No. PHY-1430152 (JINA Center for the Evolution of the Elements).

References

- Adibekyan, V. Z., Sousa, S., Santos, N., et al. 2012, *A&A*, 545, A32
 Asplund, M., Grevesse, N., Sauval, A. J., & Scott, P. 2009, *ARA&A*, 47, 481
 Bahcall, J. N. 1964, *ApJ*, 139, 318
 Belczynski, K., Kalogera, V., Rasio, F. A., et al. 2008, *ApJS*, 174, 223
 Bildsten, L., Shen, K. J., Weinberg, N. N., & Nelemans, G. 2007, *ApJ*, 662, L95
 Blinnikov, S. I., Röpke, F. K., Sorokina, E. I., et al. 2006, *A&A*, 453, 229
 Blondin, S., Kasen, D., Röpke, F. K., Kirshner, R. P., & Mandel, K. S. 2011, *MNRAS*, 417, 1280
 Brachwitz, F., Dean, D. J., Hix, W. R., et al. 2000, *ApJ*, 536, 934
 Bravo, E. 2019, *A&A*, 624, A139
 Cayrel, R., Depagne, E., Spite, M., et al. 2004, *A&A*, 416, 1117
 Cescutti, G., & Kobayashi, C. 2017, *A&A*, 607, A23
 Cescutti, G., Matteucci, F., Lanfranchi, G. A., & McWilliam, A. 2008, *A&A*, 491, 401
 Chamulak, D. A., Brown, E. F., Timmes, F. X., & Dupczak, K. 2008, *ApJ*, 677, 160
 Chiappini, C., Matteucci, F., & Romano, D. 2001, *ApJ*, 554, 1044
 Côté, B., O’Shea, B. W., Ritter, C., Herwig, F., & Venn, K. A. 2017, *ApJ*, 835, 128
 Cunha, K., Smith, V. V., Suntzeff, N. B., et al. 2002, *ApJ*, 124, 379
 De Angelis, A., Tatischeff, V., Grenier, I. A., et al. 2018, *J. High Energy Astrophys.*, 19, 1
 de los Reyes, M. A., Kirby, E. N., Seitenzahl, I. R., & Shen, K. J. 2020, *ApJ*, 891, 85
 Eitner, P., Bergemann, M., Hansen, C. J., et al. 2020, *A&A*, 635, A38
 Fink, M., Hillebrandt, W., & Röpke, F. K. 2007, *A&A*, 476, 1133
 Fink, M., Röpke, F. K., Hillebrandt, W., et al. 2010, *A&A*, 514, A53
 Fink, M., Kromer, M., Seitenzahl, I. R., et al. 2014, *MNRAS*, 438, 1762
 Flörs, A., Spyromilio, J., Taubenberger, S., et al. 2020, *MNRAS*, 491, 2902
 François, P., Matteucci, F., Cayrel, R., et al. 2004, *A&A*, 421, 613
 Frohmaier, C., Sullivan, M., Maguire, K., & Nugent, P. 2018, *ApJ*, 858, 50

- Gratton, R. G., Carretta, E., Claudi, R., Lucatello, S., & Barbieri, M. 2003, *A&A*, **404**, 187
- Greggio, L., & Renzini, A. 1983, *A&A*, **118**, 217
- Gronow, S., Collins, C., Ohlmann, S. T., et al. 2020, *A&A*, **635**, A169
- Harrison, F. A., Craig, W. W., Christensen, F. E., et al. 2013, *ApJ*, **770**, 103
- Hillebrandt, W., & Niemeyer, J. C. 2000, *ARA&A*, **38**, 191
- Hillebrandt, W., Kromer, M., Röpke, F. K., & Ruiter, A. J. 2013, *Front. Phys.*, **8**, 116
- Hirai, Y., Saitoh, T. R., Ishimaru, Y., & Wanajo, S. 2018, *ApJ*, **855**, 63
- Hoyle, F., & Fowler, W. A. 1960, *ApJ*, **132**, 565
- Hunter, J. D. 2007, *Comput. Sci. Eng.*, **9**, 90
- Iben, I., Jr, & Tutukov, A. V. 1984, *ApJS*, **54**, 335
- Insera, C., Sim, S. A., Wyrzykowski, L., et al. 2015, *ApJ*, **799**, L2
- Ishigaki, M. N., Chiba, M., & Aoki, W. 2012, *ApJ*, **753**, 64
- Ishigaki, M. N., Aoki, W., & Chiba, W. 2013, *ApJ*, **771**, 67
- Iwamoto, K., Brachwitz, F., Nomoto, K., et al. 1999, *ApJS*, **125**, 439
- Jones, S., Côté, B., Röpke, F. K., & Wanajo, S. 2019a, *ApJ*, **882**, 170
- Jones, S., Röpke, F., Fryer, C., et al. 2019b, *A&A*, **622**, A74
- Jülich Supercomputing Centre 2019, *J. Large-scale Res. Facil.*, **5**, Karakas, A. I. 2010, *MNRAS*, **403**, 1413
- Kasen, D., & Plewa, T. 2007, *ApJ*, **662**, 459
- Kashi, A., & Soker, N. 2011, *MNRAS*, **417**, 1466
- Khokhlov, A. M. 1984, *Sov. Astron. Lett.*, **10**, 123
- Khokhlov, A. M., & Érgma, É. V. 1985, *Astrofizika*, **23**, 605
- Kobayashi, C., & Nomoto, K. 2009, *ApJ*, **707**, 1466
- Kobayashi, C., Umeda, H., Nomoto, K., Tominaga, N., & Ohkubo, T. 2006, *ApJ*, **653**, 1145
- Kobayashi, C., Karakas, A. I., & Umeda, H. 2011, *MNRAS*, **414**, 3231
- Kobayashi, C., Nomoto, K., & Hachisu, I. 2015, *ApJ*, **804**, L24
- Kobayashi, C., Leung, S.-C., & Nomoto, K. 2020, *ApJ*, **895**, 138
- Kromer, M., Sim, S. A., Fink, M., et al. 2010, *ApJ*, **719**, 1067
- Kromer, M., Pakmor, R., Taubenberger, S., et al. 2013, *ApJ*, **778**, L18
- Kromer, M., Ohlmann, S. T., Pakmor, R., et al. 2015, *MNRAS*, **450**, 3045
- Kromer, M., Ohlmann, S., & Röpke, F. K. 2017, *Mem. Soc. Astron. It.*, **88**, 312
- Langanke, K., & Martinez-Pinedo, G. 2000, *Nucl. Phys. A*, **673**, 481
- Limongi, M., & Chieffi, A. 2018, *ApJS*, **237**, 13
- Marquardt, K. S., Sim, S. A., Ruiter, A. J., et al. 2015, *A&A*, **580**, A118
- Matteucci, F., & Greggio, L. 1986, *A&A*, **154**, 279
- Matteucci, F., & Recchi, S. 2001, *ApJ*, **558**, 351
- Matteucci, F., Raiteri, C., Busson, M., Gallino, R., & Gratton, R. 1993, *A&A*, **272**, 421
- Matteucci, F., Panagia, N., Pipino, A., et al. 2006, *MNRAS*, **372**, 265
- McWilliam, A. 1997, *ARA&A*, **35**, 503
- McWilliam, A., Piro, A. L., Badenes, C., & Bravo, E. 2018, *ApJ*, **857**, 97
- Meakin, C. A., Seitzzahl, I., Townsley, D., et al. 2009, *ApJ*, **693**, 1188
- Mishenina, T., Kovtyukh, V., Soubiran, C., Travaglio, C., & Busso, M. 2002, *A&A*, **396**, 189
- Nissen, P. E., & Schuster, W. J. 2011, *A&A*, **530**, A15
- Nissen, P. E., Akerman, C., Asplund, M., et al. 2007, *A&A*, **469**, 319
- Nomoto, K., Kobayashi, C., & Tominaga, N. 2013, *ARA&A*, **51**, 457
- North, P., Cescutti, G., Jablonka, P., et al. 2012, *A&A*, **541**, A45
- Oliphant, T. E. 2007, *Comput. Sci. Eng.*, **9**, 10
- Pakmor, R., Edelmann, P., Röpke, F. K., & Hillebrandt, W. 2012a, *MNRAS*, **424**, 2222
- Pakmor, R., Kromer, M., Taubenberger, S., et al. 2012b, *ApJ*, **747**, L10
- Pérez, F., & Granger, B. E. 2007, *Comput. Sci. Eng.*, **9**, 21
- Perlmutter, S., Aldering, G., Goldhaber, G., et al. 1999, *ApJ*, **517**, 565
- Phillips, M. M. 1993, *ApJ*, **413**, L105
- Piro, A. L., & Bildsten, L. 2008, *ApJ*, **673**, 1009
- Prantzos, N., Abia, C., Limongi, M., Chieffi, A., & Cristallo, S. 2018, *MNRAS*, **476**, 3432
- Rauscher, T., & Thielemann, F.-K. 2000, *At. Data Nucl. Data Tables*, **75**, 1
- Reddy, B. E., Tomkin, J., Lambert, D. L., & Allende Prieto, C. 2003, *MNRAS*, **340**, 304
- Reddy, B. E., Lambert, D. L., & Prieto, C. A. 2006, *MNRAS*, **367**, 1329
- Reinecke, M., Hillebrandt, W., & Niemeyer, J. C. 1999, *A&A*, **347**, 739
- Reinecke, M., Hillebrandt, W., & Niemeyer, J. C. 2002, *A&A*, **386**, 936
- Riess, A. G., Filippenko, A. V., Challis, P., et al. 1998, *AJ*, **116**, 1009
- Ritter, C., & Côté, B. 2016, *NuPyCEE: NuGrid Python Chemical Evolution Environment* (Astrophysics Source Code Library)
- Romano, D., & Matteucci, F. 2007, *MNRAS*, **378**, L59
- Röpke, F. K. 2005, *A&A*, **432**, 969
- Röpke, F. K. 2017, in *Handbook of Supernovae*, eds. A. Alsabti, & P. Murdin (Springer)
- Röpke, F. K., Kromer, M., Seitzzahl, I. R., et al. 2012, *ApJ*, **750**, L19
- Ruiter, A. J., Belczynski, K., & Fryer, C. 2009, *ApJ*, **699**, 2026
- Ruiter, A. J., Belczynski, K., Sim, S. A., Seitzzahl, I. R., & Kwiatkowski, D. 2014, *MNRAS*, **440**, L101
- Seitzzahl, I. R., & Townsley, D. M. 2017, in *Nucleosynthesis in Thermonuclear Supernovae*, eds. A. W. Alsabti, & P. Murdin (Springer), 1955
- Seitzzahl, I. R., Taubenberger, S., & Sim, S. A. 2009, *MNRAS*, **400**, 531
- Seitzzahl, I. R., Cescutti, G., Röpke, F. K., Ruiter, A. J., & Pakmor, R. 2013a, *A&A*, **559**, L5
- Seitzzahl, I. R., Ciaraldi-Schoolmann, F., Röpke, F. K., et al. 2013b, *MNRAS*, **429**, 1156
- Shen, K. J., & Bildsten, L. 2009, *ApJ*, **699**, 1365
- Shen, K. J., & Moore, K. 2014, *ApJ*, **797**, 46
- Shen, K. J., Kasen, D., Weinberg, N. N., Bildsten, L., & Scannapieco, E. 2010, *ApJ*, **715**, 767
- Sim, S. A., Röpke, F. K., Hillebrandt, W., et al. 2010, *ApJ*, **714**, L52
- Sim, S. A., Fink, M., Kromer, M., et al. 2012, *MNRAS*, **420**, 3003
- Sim, S. A., Seitzzahl, I. R., Kromer, M., et al. 2013, *MNRAS*, **436**, 333
- Simmerer, J., Sneden, C., Ivans, I. I., et al. 2003, *ApJ*, **125**, 2018
- Sneden, C., Gratton, R., & Crocker, D. 1991, *A&A*, **246**, 354
- Springel, V. 2010, *MNRAS*, **401**, 791
- Taubenberger, S. 2017, *Handbook of Supernovae* (Springer), 317
- Thielemann, F.-K., Nomoto, K., & Yokoi, K. 1986, *A&A*, **158**, 17
- Timmes, F. X., & Arnett, D. 1999, *ApJS*, **125**, 277
- Timmes, F. X., Woosley, S. E., & Weaver, T. A. 1995, *ApJS*, **98**, 617
- Timmes, F. X., Brown, E. F., & Truran, J. W. 2003, *ApJ*, **590**, L83
- Tinsley, B. 1979, *ApJ*, **229**, 1046
- Townsley, D. M., Miles, B. J., Shen, K. J., & Kasen, D. 2019, *ApJ*, **878**, L38
- Travaglio, C., Hillebrandt, W., Reinecke, M., & Thielemann, F.-K. 2004, *A&A*, **425**, 1029
- Travaglio, C., Gallino, R., Rauscher, T., et al. 2014, *ApJ*, **795**, 141
- Tsujimoto, T., & Nishimura, N. 2018, *ApJ*, **863**, L27
- Wanajo, S., Müller, B., Janka, H.-T., & Heger, A. 2018, *ApJ*, **852**, 40
- Wang, B., & Han, Z. 2012, *New Astron. Rev.*, **56**, 122
- Weinberg, D. H., Holtzman, J. A., Hasselquist, S., et al. 2019, *ApJ*, **874**, 102
- Whelan, J., & Iben, I. J. 1973, *ApJ*, **186**, 1007
- Willcox, D. E., Townsley, D. M., Calder, A. C., Denissenkov, P. A., & Herwig, F. 2016, *ApJ*, **832**, 13
- Woosley, S. E., & Kasen, D. 2011, *ApJ*, **734**, 38
- Woosley, S. E., & Weaver, T. A. 1995, *ApJS*, **101**, 181
- Woosley, S. E., Arnett, W. D., & Clayton, D. D. 1973, *ApJS*, **26**, 231
- Yamaguchi, H., Badenes, C., Foster, A. R., et al. 2015, *ApJ*, **801**, L31
- Yan, H., Shi, J., & Zhao, G. 2015, *ApJ*, **802**, 36
- Yan, H., Shi, J., Nissen, P. E., & Zhao, G. 2016, *A&A*, **585**, A102

Part III
Discussion

Chapter 9

Summary of the scientific results

9.1 Publication 1: Type Iax supernovae from deflagrations in Chandrasekhar mass white dwarfs

This study comprises the largest set of full-star 3D SN explosion simulations published in the astrophysical literature to date. It includes 30 hydrodynamic models computed with LEAFS (see Section 5.1), 30 nuclear network calculations carried out with YANN (see Section 5.2, the data will be published on the Heidelberg Supernova Model Archive HESMA, [Kromer et al. 2017](#)) and a selection of 18 radiative transfer models produced with ARTIS (see Section 5.3). Moreover, the explored parameter space is huge, covering variations in central density ρ_c of the initial CO WD from 1 to $6 \times 10^9 \text{ g cm}^{-3}$, metallicities Z from 10^{-4} to 2 times the solar metallicity Z_\odot and ignition radii r_{off} (single spot ignition) from 10 to 206 km from the center of the WD. Moreover, the C mass fraction in the center of the WD was reduced for one model and two rigidly rotating WD models were included to investigate whether these parameters can introduce further diversity to the suite of models. To check the consistency of the updated version of the LEAFS code the N5 model of [Fink et al. \(2014\)](#) was reproduced.

In particular, the systematic examination of the ignition geometry constitutes an essential contribution to the search for the explosion mechanism of SNe Iax. Since the exact ignition geometry, i.e., the number, location, and shape of the ignition sparks, is unknown, it has been treated as a free parameter to control the strength of the deflagration. To produce brighter events in agreement with normal SNe Ia a larger number of centrally distributed ignition sparks was needed. However, it turned out that these pure deflagration models neither reach the luminosities required to account for normal events nor do their photometric and spectroscopic properties agree with observational data of normal SNe Ia. In contrast, the faint explosions, i.e., sparsely or off-center ignited models, have shown to be in reasonable agreement with the class of SNe Iax. In addition, it seems unnatural to assume the simultaneous ignition of a deflagration in hundreds or even thousands of points. This has been corroborated by studies of the convective burning phase preceding the TNR (simmering phase) in M_{Ch} WDs ([Höflich and Stein 2002](#); [Kuhlen et al. 2006](#); [Zingale et al. 2009, 2011](#); [Nonaka et al. 2012](#)). According to these studies, the ignition in a single point located at $r_{\text{off}} \sim 50 \text{ km}$ away from the center of the star is most likely. Of course, the exact value of r_{off} can vary since the ignition is a stochastic process. Therefore, a study dedicated to the effects of varying r_{off} and its interplay with other parameters such as ρ_c was overdue. In the following, the main takeaway points of interest for SN Ia research presented in

Publication 1 (Chapter 6) are listed.

1. It is shown that the production of ^{56}Ni and, thus, the brightness of the explosion can vary significantly among single-spark ignition models. The peak bolometric magnitude, for instance, shows a range of ~ 2.4 mag ($M_{\text{peak}}^{\text{bol}} = -14.91$ to -17.35 mag). This significantly extends the range of CO deflagration models toward the fainter members of the SN Iax class compared to previous studies (Fink et al. 2014; Long et al. 2014; Jordan et al. 2012b). Moreover, the brightest model only falls ~ 0.4 mag short of the N5 model (Fink et al. 2014) (ignited in 5 sparks) which has been shown to be in good agreement with SN 2005hk (Kromer et al. 2013a). To cover the whole class, however, the range in brightness is still too narrow.
2. The LC evolution of the faintest SNe Iax, e.g., SN 2019gsc and SN 2008ha, deviates strongly from the numerical models presented here. While model rise times t_{R} decrease and decline rates increase toward lower luminosities, this trend is not observed for the very faintest SNe Iax, especially in the redder bands. SN 2019gsc has a longer rise time than SN 2019muj although it is approximately 3 mag fainter (bolometric). Since the trend in the deflagration models is plausible from a theoretical point of view and naturally explained by the explosion dynamics, these results suggest that the possibility of a different mechanism for faint SNe Iax has to be taken into account¹.
3. Secondary parameters such as metallicity, rotation, and the C/O ratio do not considerably change the appearance of the modeled explosions. While there is reasonable agreement between theory and observations for intermediately-bright to bright SNe Iax, some discrepancies such as the fast decline in red bands remain. It was suspected by Kromer et al. (2013a, 2015) that a higher amount of mass ejected in total at constant ^{56}Ni would bring the models and observation into agreement. Although the parameters mentioned above slightly modify the ejecta properties including the ^{56}Ni to ejecta mass ratio, the variations introduced are only minor.
4. The recoil velocity of the bound WD remnant due to the asymmetric explosion is not a monotonous function of the deflagration strength. In fact it shows a convex behavior with a corresponding change in direction. Furthermore, the results of Jordan et al. (2012b) are corroborated showing that the kick velocity can amount to a few hundred km s^{-1} . This strengthens the connection of bound WD remnants to the observed peculiar high velocity WDs (see e.g., Raddi et al. 2019). Finally, the importance of solving the full Poisson equation is demonstrated via a recalculation of the N5 model by Fink et al. (2014) which shows almost no recoil compared to the new version which exhibits a kick velocity of 264.6 km s^{-1} .

¹The recent detection of SN 2021fcg (Karambelkar et al. 2021) strengthens the speculation that faint SNe Iax are the result of an alternative mechanism. Since SN 2021fcg is even fainter than SN 2008ha and SN 2019muj but exhibits similar photometric and spectroscopic properties it can hardly be reproduced by current pure deflagration models.

9.2 Publication 2: Models of pulsationally assisted gravitationally confined detonations with different ignition conditions

The work presented in Publication 2 (Chapter 7) contains an extensive study (eleven 3D models) of the GCD scenario employing different initial central densities and deflagration ignition locations to examine the range of luminosities achievable in this scenario. Earlier studies (Plewa et al. 2004; Plewa 2007; Townsley et al. 2007; Kasen and Plewa 2007; Jordan et al. 2008; Meakin et al. 2009; Seitenzahl et al. 2016; Byrohl et al. 2019) explored the general feasibility of the mechanism or presented only very few models without an extensive discussion of nucleosynthesis yields and 3D radiative transfer calculations except for Seitenzahl et al. (2016). Their work, however, only includes one model.

Therefore, the models of deflagrations in M_{Ch} CO WDs of Publication 1 were used as initial models for a comprehensive parameter study of the GCD scenario. In this work, a detonation in the collision region is ignited as soon as critical values of density (10^7 g cm^{-3}) and temperature ($2 \times 10^9 \text{ K}$) are reached inside a grid cell (same approach as in Seitenzahl et al. 2016). Since the LEAFS code is not coupled to a nuclear network, matter is burned only in burning fronts and volume burning within the compression zone is not covered. Moreover, the resolution within a full-star SN explosion simulation is too low to explore a potential self-consistent initiation of a detonation. It was, however, shown by Seitenzahl et al. (2009a) that the ignition of a detonation in the GCD scenario is very likely. Thus, this study (Publication 2) approximately predicts the detonation location and time and yields characteristic observables and nucleosynthesis yields under the assumption that the GCD scenario works in general. The main results of this work can be summarized as follows:

1. Most of the initial models from Publication 1 do reach critical conditions for a detonation except the most energetic deflagrations and the rigidly rotating WDs. The latter finding is an important validation of the results of García-Senz et al. (2016) that the Coriolis force breaks the spherical symmetry, and, thus, weakens the focus of the deflagration ashes. This makes it harder to initiate a detonation. Moreover, the explosions presented rely on the contraction of the bound WD remnant (after an initial expansion due to the deflagration), and, therefore, belong to the class of “pulsationally assisted gravitationally confined detonations” (PGCD, Jordan et al. 2012a).
2. The range in ^{56}Ni masses is extended significantly toward lower values compared to earlier studies. The minimum found is $M(^{56}\text{Ni}) = 0.257 M_{\odot}$. This, in principle, brings the scenario in the range of faint normal SNe Ia and subluminous subclasses such as SNe Iax. It should, however, be noted that these faint GCD models rely on a strong pre-expansion of the WD during the deflagration phase, and, therefore, an ignition near the center. According to Nonaka et al. (2012) and Byrohl et al. (2019) these ignition conditions should be considered as rare events.
3. The isotopic yields of neutron-rich elements, e.g., $^{58,57}\text{Ni}$ and ^{55}Mn , are not typical for M_{Ch} explosions for all models. This is due to the fact that characteristics of sub- M_{Ch} detonations and M_{Ch} deflagrations are mixed in the GCD model. Therefore, an unambiguous

assignment using measurements of neutron-rich elements in the ejecta is not possible if the GCD scenario is realized in nature.

4. While the observational characteristics of normal SNe Ia and bright objects of the SN Iax² class cannot be reproduced within the GCD/PGCD scenario it might account for 91T-like objects. However, although several discrepancies remain which call for further investigations no alternative explosion scenario for 91T-like SNe has been suggested to date.

9.3 Publication 3: Nucleosynthesis imprints from different Type Ia supernova explosion scenarios and implications for galactic chemical evolution

A thorough introduction to the burning stages relevant for SNe Ia is laid out in Publication 3 (Chapter 8). Si burning including quasi-statistical equilibrium, nuclear statistical equilibrium, and the physics of neutron captures in high density material are reviewed in addition to explosive He burning. This theory is then brought into context by analyzing the nucleosynthesis yields of various SN Ia explosion models published in earlier works as well as one explosion model taken from Publication 1. These scenarios include M_{Ch} deflagrations and delayed detonations, pure detonations in sub- M_{Ch} WDs of different masses, double detonations of WDs with an accreted He envelope, pure detonations in He shells and a violent merger model of two CO WDs.

Each of these scenarios shows characteristic nucleosynthesis yields governed by the respective burning mechanism and the density profile of the exploding star. Thus, they influence the temporal evolution of the elements captured by GCE simulations in different ways. A prominent example is the element Mn which is attributed to M_{Ch} explosions since a neutron-rich environment, i.e., burning at high densities, is required for its production (Seitenzahl et al. 2013a). This notion is also frequently used as an argument for the SD scenario including the explosion of a M_{Ch} WD. The major results of this work are:

1. The elements Mn, Zn, and Cu are identified as a key characteristic imprint of He detonations. The total value of [Mn/Fe], [Zn/Fe], and [Cu/Fe] is then governed by the ratio of core-to-shell mass, the density at the base of the He envelope, and metallicity.
2. A GCE simulation carried out within this work suggests that the contribution of M_{Ch} explosions (here a delayed detonation model) to the total SN Ia rate can be reduced by 5 – 20 % if pure He detonations are included. These results carry over to the cases of Zn and Cu.
3. The authors strongly suggest that nucleosynthesis yields of SNe Ia need to be implemented into GCE codes more carefully. In many cases only one explosion scenario is incorporated, neglecting the diversity in characteristic nucleosynthesis yields among SN Ia

²The idea that bright SNe Iax also include a detonation was brought forward by Stritzinger et al. (2015) who detect some potential abundance stratification in SN 201Z. Recently, however, it was shown by Magee et al. (2021) that well mixed models capture the spectroscopic properties of SNe Iax much better than stratified ones. This is in line with the findings in Publication 2 that the GCD scenario does not produce explosions in agreement with observations of bright SNe Iax.

models. In particular, Mn is usually solely attributed to M_{Ch} explosions and Zn and Cu are believed to originate from CCSNe although their evolution is not convincingly reproduced in most GCE studies published to date (Prantzos et al. 2018).

9.4 The broader picture

All publications used in this thesis provide scientific information helping toward the understanding of SNe Ia and inferring their progenitor system. To this end, they primarily make use of two methods described in Section 4.6. A schematic figure showing the routes toward the progenitor star with contributions from the author of this thesis is shown in Figure 9.1.

Publications 1 and 2 employ the well-established supernova modeling pipeline consisting of successive hydrodynamic explosion simulations, nuclear network computations, and radiative transfer calculations. Subsequently, the synthetic observables are contrasted with measured LCs and spectra. While the modeling pipeline consists of self-consistent numerical simulations, the initial WD model, the ignition geometry, and the combustion mechanism act as free parameters. Publication 1 supports the commonly accepted notion that SNe Iax originate from pure deflagrations in M_{Ch} WDs but questions that also the faintest members of the class originate from the same explosion mechanism. Publication 2 excludes the GCD scenario for normal SNe Ia and bright SNe Iax but still leaves some room to interpret it as a 91T-like explosion. Since there are no convincing alternative scenarios for SNe Iax and 91T-like SNe, the following hypothesis seems plausible: Both subclasses originate from the same kind of progenitor star, i.e., a M_{Ch} CO WD. While the GCD mechanism works for weak deflagrations and produces a 91T-like event, the strong deflagrations do not lead to a detonation and resemble SNe Iax. First, due to the similar spectra of SNe Iax and 91T-like SNe at early times deflagration products in the outer layers seem reasonable in both cases. Second, the chances for the initiation of a detonation in the GCD scenario are higher for less energetic deflagrations. At the same time the faintest pure deflagration models do not fit the characteristics of the SN Iax class.

In Publication 3 the nucleosynthesis yields of explosion simulations are inserted into a GCE code (see Section 4.6.2) instead of conducting radiative transfer calculations. It is found that thermonuclear SNe including a He detonation (pure He detonations are candidates for Ca-rich transients) also contribute to the abundance of Mn in the Universe in addition to M_{Ch} models. This reduces the required rate for this scenario to explain the evolution of [Mn/Fe]. Furthermore, it was shown in Publication 2 that a M_{Ch} explosion in the GCD scenario does not necessarily produce supersolar amounts of Mn. If the SN Iax channel is the only one producing significantly supersolar values of [Mn/Fe], another Mn-rich scenario is needed since the total ejecta mass in a SN Iax in combination with realistic rates is too low to explain the Mn abundance evolution. Moreover, Zn and Cu are also synthesized in the He detonation in significant amounts. The authors criticize the simple treatment of SNe Ia in GCE studies mostly including only one explosion scenario which does not live up to the diversity among thermonuclear SNe.

In addition to the methods above, the author also touched the field of SN rates and delay time distributions by incorporating files provided by Ashley J. Ruiter into the OMEGA GCE code (Ritter and Côté 2016; Côté et al. 2017, Publication 3). The influence of the rates of the SD and DD channel was tested and rates for Ca-rich transients were taken from Frohmaier et al. (2018) to describe pure He detonations. Finally, the author prepared the input data for the SNR morphology study of Ferrand et al. (2021) and produced figures for the paper. In this work it

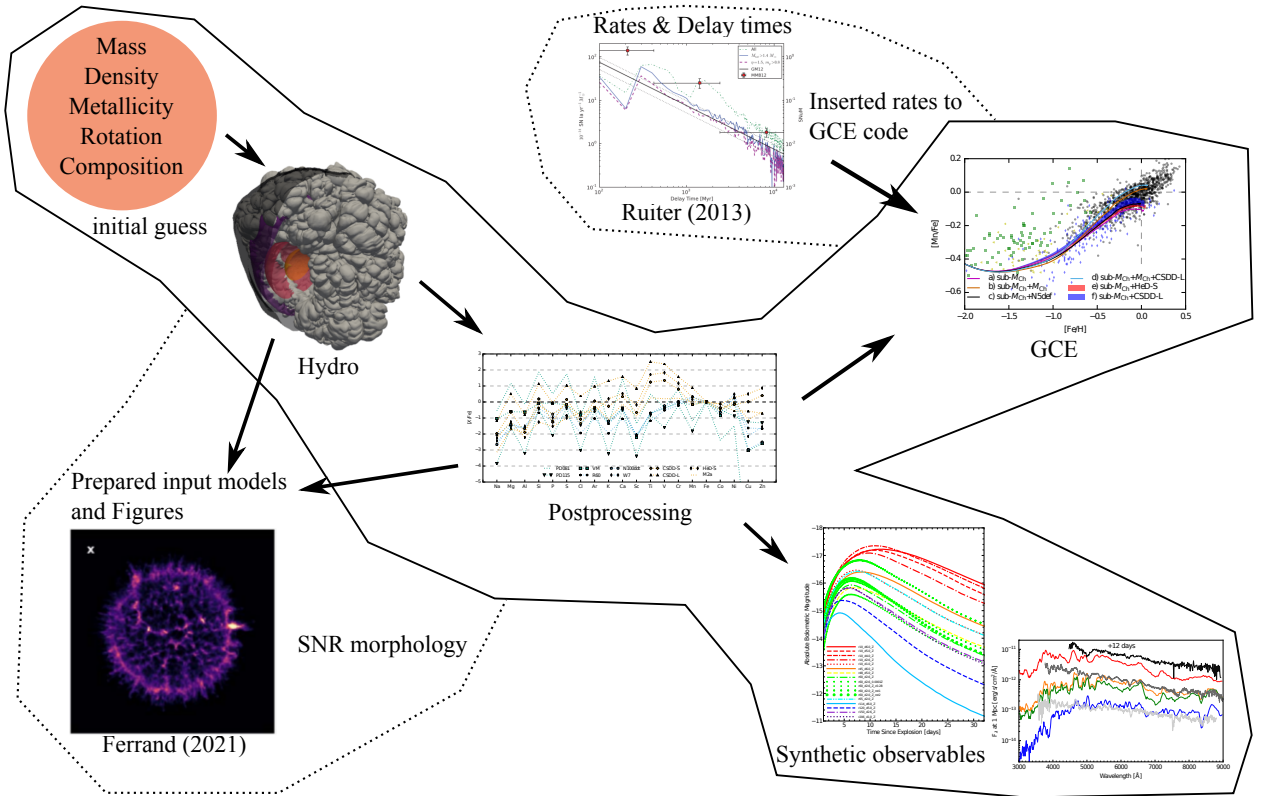


Figure 9.1: Chart of the SN modeling pipeline with contributions from the author. Images without reference are taken from Publications 1, 2, and 3.

is shown that the explosion mechanism can be inferred from young SNRs according to their characteristic ejecta structure. This is yet another way to shed light on the progenitor problem of SNe Ia.

Chapter 10

Summary and possible future work

This thesis provides an overview of the field of SNe Ia, starting from the earliest observations of newly appearing stars and the development of the supernova theory in the first part of the 20th century to modern supernova research.

First, the observational characteristics such as LCs and spectra of the homogeneous class of normal SNe Ia were reviewed. This was complemented by an explanation of how to use normal SNe Ia to measure cosmic distances (standardizable candles) and their application to cosmology. Subsequently, the most relevant subclasses of SNe Ia were summarized. Since all types of SNe Ia contribute to cosmic nucleosynthesis and SNe Ia, in general, are believed to be the primary source of IGEs and some neutron-rich isotopes such as ^{55}Mn , it is important to study all these sub-categories.

Due to the extreme conditions inside stars, experiments on Earth to unveil some of the phenomena observed are not possible. Instead, the only exploitable information comes from observations and numerical simulations. A few ways how to combine a series of simulations to shed light on the explosion mechanism of SNe Ia were discussed. Two of these modeling pipelines are employed in Publications 1, 2, and 3, which form the main part of this work.

Although the ongoing research during the past decades including the development of sophisticated numerical models and an exponential growth in computing resources, the nature of the progenitor system of SNe Ia is not revealed conclusively, yet. The major problem is that all simulations are prone to numerical uncertainties and need to employ simplified models of various physical effects due to the still restricted computing power. Hydrodynamic simulations with LEAFS are restricted, for instance, by the coarse spatial resolution making it impossible to fully resolve turbulent motions. Therefore, an approximate subgrid model has to be employed. Moreover, no actively coupled nuclear network is available. While this has only minor impact on the flame propagation it neglects the energy injection by nuclear reactions away from the flame front. Moreover, a calibration of the conversion of fuel to ash in deflagration and detonation fronts is necessary. Furthermore, magnetic fields are neglected although they may have an impact on the propagation of a deflagration front (Stone and Gardiner 2007; Hristov et al. 2018). The postprocessing via a nuclear network suffers from the uncertainty in many cross sections of nuclear reactions. As stated above, experiments on Earth at these extreme conditions are not feasible. In addition, the radiative transfer calculations also suffer from the low spatial resolution since the results of the hydrodynamics are mapped to a 50^3 Cartesian grid. Furthermore, it is impossible to include the complete atomic data (number of transition lines). In particular, the IGEs (all ionization states) contain thousands of transition lines per isotope

and ionization state. Finally, non-thermal processes need to be included, and the abolishment of local thermodynamic equilibrium is of vital importance for the late-time observables of the SN ejecta.

Assumptions made about the initial model also influence the outcome of the explosions. There is a large parameter space to be explored including different total WD masses, central densities, compositions, initial velocity fields, deflagration ignition geometries, He shell masses, etc. The question to be raised is: Is there a need for fundamentally different initial models or are the uncertainties in the numerical modeling the major limiting factor?

It is the believe of the author that, after hundreds of numerical simulations over the past decades, the gross characteristics of the individual explosion channels are matched by the models presented to date. This, in particular, holds for deflagration studies. Therefore, more simulations with only slight modifications to the initial models or input physics are not going to lead to the ultimate goal: the unambiguous identification of the progenitor and explosion mechanism of SNe Ia. First, a systematic and critical assessment of the uncertainties in the numerical models is required. Based on the results one can then decide on the most urgent developments. This is even more crucial for GCE codes since the uncertainties of many fields of research pile up there.

New simulations should be carried out as soon as significant changes to the numerical codes or initial models have been made. The inclusion of magnetic fields to deflagration models or an initial velocity field mimicking convective burning prior to the TNR are important additions to the hydrodynamic simulations. Furthermore, the modeling of detonation fronts is subject to various uncertainties (see e.g., [Kushnir 2019](#)) which need to be resolved. For the radiation transport full non-LTE studies are of vital importance to be able to compare synthetic nebular spectra to observations. Fortunately, the ARTIS code has recently been updated by [Shingles et al. \(2020\)](#) and such studies are under way.

Glossary

1D	one-dimensional	UV	ultraviolet
3D	three-dimensional	WD	white dwarf
C	carbon	WLR	width-luminosity relation
CCSN	core collapse supernova		
CJ	Chapman-Jouguet		
CN	classical nova		
CO	carbon-oxygen		
CSM	circumstellar material		
DD	double-degenerate		
EoS	equation of state		
GCD	gravitationally confined detonation		
PGCD	pulsationally assisted gravitationally confined detonation		
GCE	galactic chemical evolution		
H	hydrogen		
He	helium		
ISM	interstellar matter		
IGE	iron group element		
IME	intermediate mass element		
LC	light curve		
NSE	nuclear statistical equilibrium		
NIR	near-infrared		
O	oxygen		
ONe	oxygen-neon		
Si	silicon		
SGS	subgrid scale		
SN	supernova		
SN I	Type I supernova		
SN II	Type II supernova		
SN Ia	Type Ia supernova		
SN Iax	Type Iax supernova		
SD	single-degenerate		
SNR	supernova remnant		
TNR	thermonuclear runaway		

Publications

The following publications include a contribution from the author of this thesis:

F. Lach, F. K. Röpke, I. R. Seitenzahl, B. Coté, S. Gronow and A. J. Ruiter. Nucleosynthesis imprints from different Type Ia supernova explosion scenarios and implications for galactic chemical evolution. *A&A Volume 641:A118, December 2020*

Gilles Ferrand, Donald C. Warren, Masaomi Ono, Shigehiro Nagataki, Friedrich K. Röpke, Ivo R. Seitenzahl, **Florian Lach**, Hiroyoshi Iwasaki, and Toshiki Sato. From Supernova to Supernova Remnant: Comparison of Thermonuclear Explosion Models. *The Astrophysical Journal, 906:93(26pp), 2021 January 10*

Sabrina Gronow, Benoit Coté, **Florian Lach**, Ivo R. Seitenzahl, Christine E. Collins, Stuart A. Sim, Friedrich K. Röpke. Metallicity-dependent nucleosynthetic yields of Type Ia supernovae originating from double detonations of sub-MCh white dwarfs. *A&A Volume 656:A94, December 2021*

F. Lach, F. P. Callan, D. Bubeck, F. K. Röpke, S. A. Sim, M. Schrauth, S. T. Ohlmann, and M. Kromer. Type Iax Supernovae from Deflagrations in Chandrasekhar-mass White Dwarfs. *A&A Volume 658:A179, February 2022*

F. Lach, F. P. Callan, S. A. Sim, and F. K. Röpke. Models of pulsationally assisted gravitationally confined detonations with different ignition conditions. arXiv:2111.14394. Accepted for publication in *Astronomy & Astrophysics (A&A)*.

Bibliography

- Althaus, L. G., Córscico, A. H., Isern, J., & García-Berro, E. Evolutionary and pulsational properties of white dwarf stars. *A&A Rev.*, 18(4):471–566, 2010.
- Arnett, D. & Livne, E. The delayed-detonation model of a type Ia supernovae. I. The deflagration phase. *ApJ*, 427:315–329, May 1994a.
- Arnett, D. & Livne, E. The delayed-detonation model of Type Ia supernovae. II. The detonation phase. *ApJ*, 427:330–341, May 1994b.
- Arnett, W. D. A possible model of supernovae: Detonation of ^{12}C . *Ap&SS*, 5:180–212, Oct. 1969.
- Arnett, W. D. Type I supernovae. I. analytic solutions for the early part of the light curve. *ApJ*, 253:785–797, Feb. 1982.
- Arnett, W. D., Truran, J. W., & Woosley, S. E. Nucleosynthesis in supernova models. II. The ^{12}C detonation model. *ApJ*, 165:87–103, Apr. 1971.
- Baade, W. & Zwicky, F. Cosmic rays from super-novae. *Proceedings of the National Academy of Sciences*, 20(5):259–263, 1934a.
- Baade, W. & Zwicky, F. Remarks on super-novae and cosmic rays. *Physical Review*, 46(1):76, 1934b.
- Baade, W. & Zwicky, F. On super-novae. *Proceedings of the National Academy of Sciences*, 20(5):254–259, 1934c.
- Bader, G. & Deuffhard, P. A semi-implicit mid-point rule for stiff systems of ordinary differential equations. *Numerische Mathematik*, 41(3):373–398, Oct. 1983.
- Bertola, F. The supernovae in ngc 1073 and ngc 1058. In *Annales d'Astrophysique*, volume 27, page 319, 1964.
- Bertola, F., Mammano, A., & Perinotto, M. Spectroscopic and photographic observations of supernovae. *Contributi dell'Osservatorio Astrofisica dell'Universita di Padova in Asiago*, 174:3, 1965.
- Bessell, M. S. UBVRI passbands. *PASP*, 102:1181–1199, Oct. 1990.
- Bethe, H. A. & Wilson, J. R. Revival of a stalled supernova shock by neutrino heating. *ApJ*, 295:14–23, 1985.

- Bildsten, L., Shen, K. J., Weinberg, N. N., & Nelemans, G. Faint thermonuclear supernovae from an canum venaticorum binaries. *ApJ*, 662:L95–L98, June 2007.
- Blondin, S., Dessart, L., Hillier, D. J., & Khokhlov, A. M. One-dimensional delayed-detonation models of Type Ia supernovae: confrontation to observations at bolometric maximum. *MNRAS*, 429(3):2127–2142, 12 2012. ISSN 0035-8711.
- Borst, L. B. Supernovae. *Physical Review*, 78(6):807, 1950.
- Botyánszki, J. & Kasen, D. How do type ia supernova nebular spectra depend on explosion properties? insights from systematic non-lte modeling. *ApJ*, 845(2):176, 2017.
- Branch, D. & Venkatakrisna, K. On the ultraviolet spectra of type i supernovae. *ApJ*, 306: L21–L23, 1986.
- Bravo, E., Gil-Pons, P., Gutiérrez, J. L., & Doherty, C. L. Explosion of white dwarfs harboring hybrid CONe cores. *A&A*, 589:A38, May 2016.
- Brooks, J., Bildsten, L., Schwab, J., & Paxton, B. Carbon Shell or Core Ignitions in White Dwarfs Accreting from Helium Stars. *ApJ*, 821(1):28, Apr. 2016.
- Buchler, J. R. Classical Cepheids - a Review. In Ferlet, R., Maillard, J.-P., & Raban, B., editors, *Variables Stars and the Astrophysical Returns of the Microlensing Surveys*, page 181, Jan. 1997.
- Buchler, J.-R., Wheeler, J. C., & Barkat, Z. Thermonuclear Detonations in Evolved Stellar Cores. *ApJ*, 167:465, Aug. 1971.
- Burns, C. R., Stritzinger, M., Phillips, M., et al. The carnegie supernova project: light-curve fitting with snoopy. *ApJ*, 141(1):19, 2010.
- Burns, C. R., Stritzinger, M., Phillips, M., et al. The carnegie supernova project: intrinsic colors of type ia supernovae. *ApJ*, 789(1):32, 2014.
- Byrohl, C., Fisher, R., & Townsley, D. The intrinsic stochasticity of the ^{56}Ni distribution of single-degenerate near-chandrasekhar-mass sn ia. *ApJ*, 878(1):67, 2019.
- Cao, Y., Kulkarni, S. R., Howell, D. A., et al. A strong ultraviolet pulse from a newborn type Ia supernova. *Nature*, 521:328–331, May 2015.
- Chandrasekhar, S. The Maximum Mass of Ideal White Dwarfs. *ApJ*, 74:81, July 1931.
- Childress, M., Scalzo, R., Sim, S. A., et al. Spectroscopic observations of sn 2012fr: A luminous, normal type ia supernova with early high-velocity features and a late velocity plateau. *ApJ*, 770(1):29, 2013.
- Childress, M. J., Hillier, D. J., Seitzzahl, I., et al. Measuring nickel masses in type ia supernovae using cobalt emission in nebular phase spectra. *MNRAS*, 454(4):3816–3842, 2015.
- Clifford, F. E. & Tayler, R. J. The equilibrium distribution of nuclides in matter at high temperatures. *MmRAS*, 69:21–+, 1965.

- Colella, P. & Glaz, H. M. Efficient solution algorithms for the riemann problem for real gases. *Journal of Computational Physics*, 59:264–289, June 1985.
- Colella, P. & Woodward, P. R. The Piecewise Parabolic Method (PPM) for gas-dynamical simulations. *Journal of Computational Physics*, 54:174–201, Sept. 1984.
- Colgate, S. A. & McKee, C. Early supernova luminosity. *ApJ*, 157:623–643, Aug. 1969.
- Colgate, S. A. & White, R. H. The hydrodynamic behavior of supernovae explosions. *The astrophysical journal*, 143:626, 1966.
- Conley, A., Howell, D. A., Howes, A., et al. The Rise Time of Type Ia Supernovae from the Supernova Legacy Survey. *AJ*, 132:1707–1713, Oct. 2006.
- Contardo, G., Leibundgut, B., & Vacca, W. D. Epochs of maximum light and bolometric light curves of type Ia supernovae. *A&A*, 359:876–886, July 2000.
- Contreras, C., Phillips, M., Burns, C. R., et al. Sn 2012fr: ultraviolet, optical, and near-infrared light curves of a type ia supernova observed within a day of explosion. *ApJ*, 859(1):24, 2018.
- Copeland, R. On Hartwig’s Nova Andromeda. *MNRAS*, 47(2):49–61, 12 1886. ISSN 0035-8711.
- Côté, B., Ritter, C., O’Shea, B. W., et al. Uncertainties in Galactic Chemical Evolution Models. *ApJ*, 824:82, June 2016.
- Côté, B., O’Shea, B. W., Ritter, C., Herwig, F., & Venn, K. A. The Impact of Modeling Assumptions in Galactic Chemical Evolution Models. *ApJ*, 835(2):128, Feb. 2017.
- Courant, R., Friedrichs, K. O., & Lewy, H. Über die partiellen Differentialgleichungen der mathematischen Physik. *Math. Ann.*, 100:32–74, 1928.
- Cousins, A. W. J. Standard stars for vri photometry with s25 response photocathodes. *Monthly Notes of the Astronomical Society of Southern Africa*, 33:149, 12 1974.
- Dado, S. & Dar, A. Analytical expressions for light-curves of ordinary and superluminous supernovae type ia. *arXiv preprint arXiv:1301.3333*, 2013.
- Denissenkov, P. A., Herwig, F., Truran, J. W., & Paxton, B. The C-flame Quenching by Convective Boundary Mixing in Super-AGB Stars and the Formation of Hybrid C/O/Ne White Dwarfs and SN Progenitors. *ApJ*, 772:37, July 2013.
- Denissenkov, P. A., Truran, J. W., Herwig, F., et al. Hybrid C-O-Ne white dwarfs as progenitors of Type Ia supernovae: dependence on Urca process and mixing assumptions. *MNRAS*, 447: 2696–2705, Mar. 2015.
- Dessart, L., Blondin, S., Hillier, D. J., & Khokhlov, A. Constraints on the explosion mechanism and progenitors of Type Ia supernovae. *MNRAS*, 441:532–550, June 2014a.
- Dessart, L., Hillier, D. J., Blondin, S., & Khokhlov, A. Critical ingredients of Type Ia supernova radiative-transfer modelling. *MNRAS*, 441:3249–3270, July 2014b.

- Diehl, R. & Timmes, F. X. Gamma-ray line emission from radioactive isotopes in stars and galaxies. *Publications of the Astronomical Society of the Pacific*, 110(748):637, 1998.
- Dimitriadis, G., Sullivan, M., Kerzendorf, W., et al. The late-time light curve of the Type Ia supernova SN 2011fe. *MNRAS*, 468(4):3798–3812, 03 2017. ISSN 0035-8711.
- Dimitriadis, G., Foley, R., Rest, A., et al. K2 observations of sn 2018oh reveal a two-component rising light curve for a type ia supernova. *ApJ*, 870(1):L1, 2018.
- Döring, W. Über den Detonationsvorgang in Gasen. *Annalen der Physik*, 435:421–436, 1943.
- Elias, J., Matthews, K., Neugebauer, G., & Persson, S. Type i supernovae in the infrared and their use as distance indicators. *Astrophysical Journal*, 296:379–389, 1985.
- Falta, D. & Fisher, R. Stochastic gravitational wave background from the single-degenerate channel of type ia supernovae. *Phys. Rev. D*, 84(12):124062, Dec. 2011.
- Falta, D., Fisher, R., & Khanna, G. Gravitational wave emission from the single-degenerate channel of type ia supernovae. *Physical Review Letters*, 106(20):201103, May 2011.
- Feast, M. Cepheids as distance indicators. *Publications of the Astronomical Society of the Pacific*, 111(761):775, 1999.
- Feast, M. & Walker, A. Cepheids as distance indicators. *Annual review of astronomy and astrophysics*, 25(1):345–375, 1987.
- Ferrand, G., Warren, D. C., Ono, M., et al. From supernova to supernova remnant: comparison of thermonuclear explosion models. *ApJ*, 906(2):93, 2021.
- Fickett, W. & Davis, C. *Detonation*. Los Alamos Series in Basic and Applied Sciences. University of California Press, 1979.
- Filippenko, A. V. Optical spectra of supernovae. *ARA&A*, 35:309–355, 1997.
- Filippenko, A. V., Richmond, M. W., Branch, D., et al. The subluminous, spectroscopically peculiar type Ia supernova 1991bg in the elliptical galaxy NGC 4374. *AJ*, 104:1543–1556, Oct. 1992a.
- Filippenko, A. V., Richmond, M. W., Matheson, T., et al. The peculiar Type Ia SN 1991T – Detonation of a white dwarf? *ApJ*, 384:L15–L18, Jan. 1992b.
- Fink, M. *Modeling detonations in Type Ia supernovae*. Dissertation, Technische Universität München, 2010.
- Fink, M., Hillebrandt, W., & Röpke, F. K. Double-detonation supernovae of sub-Chandrasekhar mass white dwarfs. *A&A*, 476:1133–1143, Dec. 2007.
- Fink, M., Röpke, F. K., Hillebrandt, W., et al. Double-detonation sub-Chandrasekhar supernovae: can minimum helium shell masses detonate the core? *A&A*, 514:A53, May 2010.
- Fink, M., Kromer, M., Seitenzahl, I. R., et al. Three-dimensional pure deflagration models with nucleosynthesis and synthetic observables for Type Ia supernovae. *MNRAS*, 438:1762–1783, Feb. 2014.

- Finzi, A. & Wolf, R. A. Type I Supernovae. *ApJ*, 150:115, Oct. 1967.
- Folatelli, G., Phillips, M., Morrell, N., et al. Unburned material in the ejecta of type ia supernovae. *ApJ*, 745(1):74, 2011.
- Foley, R. J., Challis, P. J., Filippenko, A. V., et al. Very Early Ultraviolet and Optical Observations of the Type Ia Supernova 2009ig. *ApJ*, 744:38, Jan. 2012.
- Forcada, R., Garcia-Senz, D., & José, J. Single point off-center helium ignitions as origin of some Type Ia supernovae. In *International Symposium on Nuclear Astrophysics - Nuclei in the Cosmos*, 2006.
- Freedman, W. L., Burns, C. R., Phillips, M., et al. The carnegie supernova project: first near-infrared hubble diagram to $z \approx 0.7$. *ApJ*, 704(2):1036, 2009.
- Frohmaier, C., Sullivan, M., Maguire, K., & Nugent, P. The volumetric rate of calcium-rich transients in the local universe. *ApJ*, 858(1):50, 2018.
- Fryxell, B. A., Müller, E., & Arnett, W. D. Hydrodynamics and nuclear burning. MPA Green Report 449, Max-Planck-Institut für Astrophysik, Garching, 1989.
- Gal-Yam, A. *Observational and Physical Classification of Supernovae*, pages 1–43. Springer International Publishing, Cham, 2017. ISBN 978-3-319-20794-0.
- Gamezo, V. N., Wheeler, J. C., Khokhlov, A. M., & Oran, E. S. Multilevel Structure of Cellular Detonations in Type IA Supernovae. *ApJ*, 512:827–842, Feb. 1999.
- Gamezo, V. N., Khokhlov, A. M., & Oran, E. S. Deflagrations and detonations in thermonuclear supernovae. *Physical Review Letters*, 92(21):211102, May 2004.
- Gamezo, V. N., Khokhlov, A. M., & Oran, E. S. Three-dimensional delayed-detonation model of Type Ia supernovae. *ApJ*, 623:337–346, Apr. 2005.
- García-Senz, D., Bravo, E., & Woosley, S. E. Single and multiple detonations in white dwarfs. *A&A*, 349:177–188, Sept. 1999.
- García-Senz, D., Cabezón, R. M., Domínguez, I., & Thielemann, F. K. Type Ia Supernovae: Can Coriolis Force Break the Symmetry of the Gravitational Confined Detonation Explosion Mechanism? *ApJ*, 819(2):132, Mar. 2016.
- Germano, M. Turbulence: The filtering approach. *Journal of Fluid Mechanics*, 238:325–336, May 1992.
- Gilmozzi, R., Cassatella, A., Clavel, J., et al. The progenitor of SN1987A. *Nature*, 328:318–320, July 1987.
- Godunov, S. K. Finite difference method for numerical computation of discontinuous solution of the equations of fluid dynamics. *Matematicheskii Sbornik*, 47:271, 1959.
- Green, D. Historical supernovae and their remnants. *Highlights of Astronomy*, 12:350–353, 2002.

- Green, D. A. *Historical Supernovae in the Galaxy from AD 1006*, pages 37–48. Springer International Publishing, Cham, 2017. ISBN 978-3-319-21846-5.
- Gronow, S., Collins, C., Ohlmann, S. T., et al. Sne ia from double detonations: Impact of core-shell mixing on the carbon ignition mechanism. *Astronomy & Astrophysics*, 635:A169, 2020.
- Gronow, S., Collins, C. E., Sim, S. A., & Röpke, F. K. Double detonations of sub- M_{Ch} CO white dwarfs: variations in Type Ia supernovae due to different core and He shell masses. *A&A*, 649:A155, May 2021.
- Guy, J., Astier, P., Nobili, S., Regnault, N., & Pain, R. SALT: a spectral adaptive light curve template for type Ia supernovae. *A&A*, 443:781–791, Dec. 2005.
- Hachinger, S., Mazzali, P. A., Taubenberger, S., Pakmor, R., & Hillebrandt, W. Spectral analysis of the 91bg-like Type Ia SN 2005bl: low luminosity, low velocities, incomplete burning. *MNRAS*, 399:1238–1254, Nov. 2009.
- Hamuy, M., Phillips, M., Suntzeff, N. B., et al. The morphology of type ia supernovae light curves. *The Astronomical Journal*, 112:2438, 1996.
- Hamuy, M., Phillips, M. M., Suntzeff, N. B., et al. The hubble diagram of the calan/tololo type Ia supernovae and the value of h_0 . *AJ*, 112:2398–2407, Dec. 1996.
- Han, Z., Podsiadlowski, P., & Eggleton, P. P. The formation of bipolar planetary nebulae and close white dwarf binaries. *MNRAS*, 272:800–820, Feb. 1995.
- Han, Z.-W., Ge, H.-W., Chen, X.-F., & Chen, H.-L. Binary population synthesis. *Research in Astronomy and Astrophysics*, 20(10):161, oct 2020.
- Hillebrandt, W. & Hoflich, P. The supernova 1987a in the large magellanic cloud. *Reports on progress in Physics*, 52(11):1421, 1989.
- Hoefflich, P., Hsiao, E., Ashall, C., et al. Light and color curve properties of type ia supernovae: theory versus observations. *ApJ*, 846(1):58, 2017.
- Höflich, P. & Khokhlov, A. Explosion models for type Ia supernovae: A comparison with observed light curves, distances, h_0 , and q_0 . *ApJ*, 457:500–528, Feb. 1996.
- Höflich, P. & Stein, J. On the thermonuclear runaway in Type Ia supernovae: How to run away? *ApJ*, 568:779–790, Apr. 2002.
- Höflich, P., Müller, E., & Khokhlov, A. Light curve models for type Ia supernovae: Physical assumptions, their influence and validity. *A&A*, 268:570–590, Feb. 1993.
- Höflich, P., Khokhlov, A., & Wheeler, J. Delayed detonation models for normal and subluminous type ia supernovae: Absolute brightness, light curves, and molecule formation. *ApJ*, 444:831–847, 1995.
- Horesh, A., Kulkarni, S. R., Fox, D. B., et al. Early Radio and X-Ray Observations of the Youngest nearby Type Ia Supernova PTF 11kly (SN 2011fe). *ApJ*, 746:21, Feb. 2012.

- Horiuchi, S. & Beacom, J. F. Revealing type ia supernova physics with cosmic rates and nuclear gamma rays. *ApJ*, 723(1):329, 2010.
- Hosseinzadeh, G., Sand, D. J., Valenti, S., et al. Early blue excess from the type ia supernova 2017cbv and implications for its progenitor. *ApJ*, 845(2):L11, 2017.
- Hoyle, F. & Fowler, W. A. Nucleosynthesis in supernovae. *ApJ*, 132:565–590, Nov. 1960.
- Hristov, B., Collins, D. C., Hoefflich, P., Weatherford, C. A., & Diamond, T. R. Magnetohydrodynamical effects on nuclear deflagration fronts in type ia supernovae. *ApJ*, 858(1):13, 2018.
- Hubble, E. A Relation between Distance and Radial Velocity among Extra-Galactic Nebulae. *Proceedings of the National Academy of Science*, 15:168–173, Mar. 1929.
- Hubeny, I. & Mihalas, D. *Theory of stellar atmospheres: an introduction to astrophysical non-equilibrium quantitative spectroscopic analysis*, volume 26. Princeton University Press, 2014.
- Iben, Jr., I. & Tutukov, A. V. Supernovae of type I as end products of the evolution of binaries with components of moderate initial mass (M not greater than about 9 solar masses). *ApJS*, 54:335–372, Feb. 1984.
- Iben, Jr., I. & Tutukov, A. V. Model stars with degenerate dwarf cores and helium-burning shells - A stationary-burning approximation. *ApJ*, 342:430–448, July 1989.
- Iben, Icko, J. & Tutukov, A. V. Helium-accreting Degenerate Dwarfs as Presupernovae and Scenarios for the Ultrasoft X-Ray Sources. *ApJ*, 431:264, Aug. 1994.
- Iliadis, C. Nuclear physics of stars, 2007.
- Ivanova, L. N., Imshennik, V. S., & Chechetkin, V. M. Pulsation regime of the thermonuclear explosion of a star's dense carbon core. *Ap&SS*, 31:497–514, Dec. 1974.
- Iwamoto, K., Brachwitz, F., Nomoto, K., et al. Nucleosynthesis in chandrasekhar mass models for type Ia supernovae and constraints on progenitor systems and burning-front propagation. *ApJS*, 125:439–462, Dec. 1999.
- Jack, D., Hauschildt, P. H., & Baron, E. Near-infrared light curves of type Ia supernovae. *A&A*, 538:A132, Feb. 2012.
- Janka, H.-T. Neutrino-driven explosions. *Handbook of Supernovae*, page 1095, 2017.
- Jerkstrand, A. *Spectra of Supernovae in the Nebular Phase*, pages 1–48. Springer International Publishing, Cham, 2017.
- Jha, S., Riess, A. G., & Kirshner, R. P. Improved distances to type ia supernovae with multicolor light-curve shapes: Mlcs2k2. *ApJ*, 659(1):122, 2007.
- Jha, S. W. Type iax supernovae. *Handbook of Supernovae*, pages 375–401, 2017.

- Jiang, J.-a., Doi, M., Maeda, K., & Shigeyama, T. Surface radioactivity or interactions? multiple origins of early-excess type ia supernovae and associated subclasses. *ApJ*, 865(2):149, 2018.
- Johnson, H. L. & Morgan, W. W. Fundamental stellar photometry for standards of spectral type on the revised system of the Yerkes spectral atlas. *ApJ*, 117:313–+, May 1953.
- Jones, S., Röpke, F. K., Pakmor, R., et al. Do electron-capture supernovae make neutron stars?. First multidimensional hydrodynamic simulations of the oxygen deflagration. *A&A*, 593: A72, Sept. 2016.
- Jordan, IV, G. C., Fisher, R. T., Townsley, D. M., et al. Three-dimensional simulations of the deflagration phase of the gravitationally confined detonation model of Type Ia supernovae. *ApJ*, 681:1448–1457, July 2008.
- Jordan, IV, G. C., Graziani, C., Fisher, R. T., et al. The detonation mechanism of the pulsationally assisted gravitationally confined detonation model of type Ia supernovae. *ApJ*, 759:53, Nov. 2012a.
- Jordan, IV, G. C., Perets, H. B., Fisher, R. T., & van Rossum, D. R. Failed-detonation Supernovae: Subluminous Low-velocity Ia Supernovae and their Kicked Remnant White Dwarfs with Iron-rich Cores. *ApJ*, 761:L23, Dec. 2012b.
- Jordi, K., Grebel, E. K., & Ammon, K. Empirical color transformations between sdss photometry and other photometric systems. *Astronomy & Astrophysics*, 460(1):339–347, 2006.
- Karambelkar, V. R., Kasliwal, M. M., Maguire, K., et al. Faintest of them all: Ztf 21aaoryiz/sn 2021fcg - discovery of an extremely low luminosity type iax supernova. *The Astrophysical Journal Letters*, 921(1):L6, 2021.
- Kasen, D. Secondary Maximum in the Near-Infrared Light Curves of Type Ia Supernovae. *ApJ*, 649:939–953, Oct. 2006.
- Kasen, D. Seeing the Collision of a Supernova with Its Companion Star. *ApJ*, 708:1025–1031, Jan. 2010.
- Kasen, D. & Plewa, T. Detonating failed deflagration model of thermonuclear supernovae. ii. comparison to observations. *ApJ*, 662:459–471, June 2007.
- Kasen, D., Thomas, R. C., & Nugent, P. Time-dependent monte carlo radiative transfer calculations for three-dimensional supernova spectra, light curves, and polarization. *ApJ*, 651: 366–380, Nov. 2006.
- Kasen, D., Röpke, F. K., & Woosley, S. E. The diversity of type Ia supernovae from broken symmetries. *Nature*, 460:869–872, Aug. 2009.
- Kato, M. & Hachisu, I. Mass accumulation efficiency in helium shell flashes for various white dwarf masses. *The Astrophysical Journal Letters*, 613(2):L129, 2004.
- Khatami, D. K. & Kasen, D. N. Physics of luminous transient light curves: A new relation between peak time and luminosity. *ApJ*, 878(1):56, 2019.

- Khokhlov, A. M. Delayed detonation model for type Ia supernovae. *A&A*, 245:114–128, May 1991a.
- Khokhlov, A. M. Nucleosynthesis in delayed detonation models of Type Ia supernovae. *A&A*, 245:L25–L28, May 1991b.
- Khokhlov, A. M. Mechanisms for the initiation of detonations in the degenerate matter of supernovae. *A&A*, 246:383–396, June 1991c.
- Khokhlov, A. M. Propagation of turbulent flames in supernovae. *ApJ*, 449:695–713, Aug. 1995.
- Kippenhahn, R., Weigert, A., & Weiss, A. *Stellar Structure and Evolution*. Springer-Verlag, Berlin Heidelberg, 2012. ISBN 978-3-642-30255-8.
- Kobayashi, C. & Nomoto, K. The role of type ia supernovae in chemical evolution. i. lifetime of type ia supernovae and metallicity effect. *ApJ*, 707:1466–1484, Dec. 2009.
- Kobayashi, C., Umeda, H., Nomoto, K., Tominaga, N., & Ohkubo, T. Galactic Chemical Evolution: Carbon through Zinc. *ApJ*, 653:1145–1171, Dec. 2006.
- Kobayashi, C., Leung, S.-C., & Nomoto, K. New type ia supernova yields and the manganese and nickel problems in the milky way and dwarf spheroidal galaxies. *ApJ*, 895(2):138, 2020.
- Koenig, T. Fritz zwicky: Novae become supernovae. In *1604-2004: Supernovae as Cosmological Lighthouses*, volume 342, page 53, 2005.
- Kolmogorov, A. N. The local structure of turbulence in incompressible viscous fluid for very large reynolds numbers. *Dokl. Akad. Nauk SSSR*, 30:299–303, 1941. in Russian.
- Kolmogorov, A. N. A refinement of previous hypotheses concerning the local structure of turbulence in a viscous incompressible fluid at high reynolds number. *Journal of Fluid Mechanics*, 13:82–85, 1962.
- Krisciunas, K. The infrared hubble diagram of type ia supernovae. *Handbook of Supernovae*, page 2593, 2017.
- Krisciunas, K., Phillips, M. M., & Suntzeff, N. B. Hubble diagrams of Type Ia supernovae in the near-infrared. *ApJ*, 602:L81–L84, Feb. 2004.
- Kromer, M. & Sim, S. A. Time-dependent three-dimensional spectrum synthesis for Type Ia supernovae. *MNRAS*, 398:1809–1826, Aug. 2009.
- Kromer, M., Sim, S. A., Fink, M., et al. Double-detonation Sub-Chandrasekhar Supernovae: Synthetic Observables for Minimum Helium Shell Mass Models. *ApJ*, 719:1067–1082, Aug. 2010.
- Kromer, M., Fink, M., Stanishev, V., et al. 3D deflagration simulations leaving bound remnants: a model for 2002cx-like Type Ia supernovae. *MNRAS*, 429:2287–2297, Mar. 2013a.
- Kromer, M., Pakmor, R., Taubenberger, S., et al. SN 2010lp—a Type Ia Supernova from a Violent Merger of Two Carbon-Oxygen White Dwarfs. *ApJ*, 778:L18, Nov. 2013b.

- Kromer, M., Ohlmann, S. T., Pakmor, R., et al. Deflagrations in hybrid CO/Ne white dwarfs: a route to explain the faint Type Ia supernova 2008ha. *MNRAS*, 450:3045–3053, July 2015.
- Kromer, M., Ohlmann, S. T., & Roepke, F. K. Simulating the observed diversity of type Ia supernovae-introducing a model data base. *arXiv preprint arXiv:1706.09879*, 2017.
- Kuchner, M. J., Kirshner, R. P., Pinto, P. A., & Leibundgut, B. Evidence for $^{56}\text{Ni} \rightarrow ^{56}\text{Co} \rightarrow ^{56}\text{Fe}$ decay in type Ia supernovae. *ApJ*, 426:L89–L92, May 1994.
- Kuhlen, M., Woosley, S. E., & Glatzmaier, G. A. Carbon ignition in Type Ia supernovae. II. A three-dimensional numerical model. *ApJ*, 640:407–416, Mar. 2006.
- Kunugise, T. & Iwamoto, K. Neutrino emission from type Ia supernovae. *PASJ*, 59:L57+, Dec. 2007.
- Kushnir, D. The structure of detonation waves in supernovae revisited. *MNRAS*, 483(1):425–457, 2019.
- Kushnir, D., Livne, E., & Waxman, E. Imploding ignition waves. i. one-dimensional analysis. *ApJ*, 752:89, June 2012.
- Langanke, K. & Martínez-Pinedo, G. Rate Tables for the Weak Processes of pf-SHELL Nuclei in Stellar Environments. *Atomic Data and Nuclear Data Tables*, 79:1–46, Sept. 2001.
- Leibundgut, B. Type Ia supernovae. *A&A Rev.*, 10:179–209, 2000.
- Leibundgut, B. History of supernovae as distance indicators. *Handbook of Supernovae*, page 2525, 2017.
- Leung, S.-C. & Nomoto, K. Explosive nucleosynthesis in near-chandrasekhar mass white dwarf models for type Ia supernovae: Dependence on model parameters. *ApJ*, 900(1):54, 2020.
- LeVeque, R. J. *Finite volume methods for hyperbolic problems*, volume 31. Cambridge university press, Cambridge, 2002.
- Li, L., Zhang, J., Dai, B., et al. Sn 2015bq: A luminous type Ia supernova with early flux excess. *arXiv preprint arXiv:2110.08752*, 2021.
- Li, W., Filippenko, A. V., Treffers, R. R., et al. A High Intrinsic Peculiarity Rate among Type Ia Supernovae. *ApJ*, 546:734–743, Jan. 2001.
- Li, W., Filippenko, A. V., Chornock, R., et al. SN 2002cx: The most peculiar known Type Ia supernova. *PASP*, 115:453–473, Apr. 2003.
- Li, W., Leaman, J., Chornock, R., et al. Nearby supernova rates from the lick observatory supernova search – II. the observed luminosity functions and fractions of supernovae in a complete sample. *MNRAS*, 412:1441–1472, Apr. 2011.
- Li, W., Wang, X., Vinkó, J., et al. Photometric and spectroscopic properties of type Ia supernova 2018oh with early excess emission from the kepler 2 observations. *ApJ*, 870(1):12, 2018.

- Li, W., Wang, X., Vinko, J., Hosseinzadeh, G., & Sand, D. Constraints on the ejecta properties of sn 2018oh with early excess emission from k2 observation. *Supernova Remnants: An Odyssey in Space after Stellar Death II*, page 85, 2019.
- Lippuner, J. & Roberts, L. F. Skynet: a modular nuclear reaction network library. *ApJS*, 233 (2):18, 2017.
- Lira, P., Suntzeff, N. B., Phillips, M. M., et al. Optical light curves of the Type IA supernovae SN 1990N and 1991T. *AJ*, 115:234–+, Jan. 1998.
- Livne, E. Successive detonations in accreting white dwarfs as an alternative mechanism for type I supernovae. *ApJ*, 354:L53–L55, May 1990.
- Livne, E. Numerical simulations of the convective flame in white dwarfs. *ApJ*, 406:L17–L20, Mar. 1993a.
- Livne, E. An implicit method for two-dimensional hydrodynamics. *ApJ*, 412:634–647, Aug. 1993b.
- Livne, E. & Arnett, D. Explosions of sub-Chandrasekhar mass white dwarfs in two dimensions. *ApJ*, 452:62–74, Oct. 1995.
- Livne, E. & Glasner, A. S. Geometrical effects in off-center detonation of helium shells. *ApJ*, 361:244–250, Sept. 1990.
- Livne, E., Asida, S. M., & Höflich, P. On the sensitivity of deflagrations in a Chandrasekhar mass white dwarf to initial conditions. *ApJ*, 632:443–449, Oct. 2005.
- Long, M., Jordan, George C., I., van Rossum, D. R., et al. Three-dimensional Simulations of Pure Deflagration Models for Thermonuclear Supernovae. *ApJ*, 789(2):103, July 2014.
- Lorén-Aguilar, P., Isern, J., & García-Berro, E. High-resolution smoothed particle hydrodynamics simulations of the coalescence of double white dwarfs. *American Institute of Physics Conference Series*, 1122:320–323, May 2009.
- Lucy, L. B. Monte carlo techniques for time-dependent radiative transfer in 3-d supernovae. *A&A*, 429:19–30, Jan. 2005.
- Lundmark, K. The motions and the distances of spiral nebulae.:(plates 18, 19.). *MNRAS*, 85(8): 865–894, 1925.
- Ma, H., Woosley, S. E., Malone, C. M., Almgren, A., & Bell, J. Carbon deflagration in type ia supernova. i. centrally ignited models. *ApJ*, 771:58, July 2013.
- Madej, J., Należyty, M., & Althaus, L. G. Mass distribution of DA white dwarfs in the First Data Release of the Sloan Digital Sky Survey. *A&A*, 419:L5–L8, May 2004.
- Magee, M. & Maguire, K. An investigation of ^{56}Ni shells as the source of early light curve bumps in type ia supernovae. *Astronomy & Astrophysics*, 642:A189, 2020.
- Magee, M., Sim, S., Kotak, R., & Kerzendorf, W. Modelling the early time behaviour of type ia supernovae: effects of the ^{56}Ni distribution. *Astronomy & Astrophysics*, 614:A115, 2018.

- Magee, M. R., Maguire, K., Kotak, R., & Sim, S. A. Exploring the diversity of double-detonation explosions for Type Ia supernovae: effects of the post-explosion helium shell composition. *MNRAS*, 502(3):3533–3553, Apr. 2021.
- Malone, C. M., Nonaka, A., Woosley, S. E., et al. The Deflagration Stage of Chandrasekhar Mass Models for Type Ia Supernovae. I. Early Evolution. *ApJ*, 782:11, Feb. 2014.
- Maoz, D., Mannucci, F., & Brandt, T. D. The delay-time distribution of Type Ia supernovae from Sloan II. *MNRAS*, 426:3282–3294, Nov. 2012.
- Marquardt, K. S., Sim, S. A., Ruiter, A. J., et al. Type Ia supernovae from exploding oxygen-neon white dwarfs. *A&A*, 580:A118, Aug. 2015.
- Marschall, L. A. *The supernova story*. Springer, 1988.
- Matteucci, F. Galaxy Evolution. *Fund. Cosmic Phys.*, 17:283–396, Jan. 1996.
- Matteucci, F. & Greggio, L. Relative roles of type I and II supernovae in the chemical enrichment of the interstellar gas. *A&A*, 154:279–287, Jan. 1986.
- Matteucci, F., Panagia, N., Pipino, A., et al. A new formulation of the Type Ia supernova rate and its consequences on galactic chemical evolution. *MNRAS*, 372:265–275, Oct. 2006.
- Mazzali, P. A., Benetti, S., Altavilla, G., et al. High-velocity features: A ubiquitous property of Type Ia supernovae. *ApJ*, 623:L37–L40, Apr. 2005.
- McCully, C., Jha, S. W., Foley, R. J., et al. A luminous, blue progenitor system for the type Iax supernova 2012Z. *Nature*, 512:54–56, Aug. 2014.
- Meakin, C. A., Seitenzahl, I., Townsley, D., et al. Study of the detonation phase in the gravitationally confined detonation model of Type Ia supernovae. *ApJ*, 693:1188–1208, Mar. 2009.
- Meng, X. & Podsiadlowski, P. A common-envelope wind model for Type Ia supernovae - I. Binary evolution and birth rate. *MNRAS*, 469(4):4763–4787, Aug. 2017.
- Miles, R. A light history of photometry: from Hipparchus to the Hubble Space Telescope. *Journal of the British Astronomical Association*, 117:172–186, Aug. 2007.
- Milisavljevic, D. & Fesen, R. A. The supernova-supernova remnant connection. *Handbook of Supernovae*, page 2211, 2017.
- Minkowski, R. Spectra of supernovae. *PASP*, 53:224–225, Aug. 1941.
- Nadyozhin, D. K. The properties of Ni to Co to Fe decay. *ApJS*, 92:527–531, June 1994.
- Niemeyer, J. C. & Hillebrandt, W. Turbulent nuclear flames in type Ia supernovae. *ApJ*, 452:769–778, Oct. 1995.
- Nobili, S., Amanullah, R., Garavini, G., et al. Restframe I-band Hubble diagram for type Ia supernovae up to redshift $z \sim 0.5$. *A&A*, 437:789–804, July 2005.

- Noebauer, U., Kromer, M., Taubenberger, S., et al. Early light curves for type ia supernova explosion models. *MNRAS*, 472(3):2787–2799, 2017.
- Nomoto, K. Accreting white dwarf models for type I supernovae. II. Off-center detonation supernovae. *ApJ*, 257:780–792, June 1982.
- Nomoto, K. & Kondo, Y. Conditions for accretion-induced collapse of white dwarfs. *ApJ*, 367:L19–L22, Jan. 1991.
- Nomoto, K. & Sugimoto, D. Rejuvenation of Helium White Dwarfs by Mass Accretion. *PASJ*, 29:765–780, Jan. 1977.
- Nomoto, K., Sugimoto, D., & Neo, S. Carbon deflagration supernova, an alternative to carbon detonation. *Ap&SS*, 39:L37–L42, Feb. 1976.
- Nomoto, K., Nariai, K., & Sugimoto, D. Rapid Mass Accretion onto White Dwarfs and Formation of an Extended Envelope. *PASJ*, 31:287–298, Jan. 1979.
- Nomoto, K., Thielemann, F.-K., & Yokoi, K. Accreting white dwarf models of Type I supernovae. III. carbon deflagration supernovae. *ApJ*, 286:644–658, Nov. 1984.
- Nomoto, K., Saio, H., Kato, M., & Hachisu, I. Thermal stability of white dwarfs accreting hydrogen-rich matter and progenitors of type ia supernovae. *ApJ*, 663:1269–1276, July 2007.
- Nonaka, A., Aspden, A. J., Zingale, M., et al. High-resolution simulations of convection preceding ignition in Type Ia supernovae using adaptive mesh refinement. *ApJ*, 745:73, Jan. 2012.
- Nugent, P. E., Sullivan, M., Cenko, S. B., et al. Supernova SN 2011fe from an exploding carbon-oxygen white dwarf star. *Nature*, 480:344–347, Dec. 2011.
- Odrzywolek, A. & Plewa, T. Probing thermonuclear supernova explosions with neutrinos. *A&A*, 529:A156, May 2011.
- Ohlmann, S. T., Kromer, M., Fink, M., et al. The white dwarf’s carbon fraction as a secondary parameter of Type Ia supernovae. *A&A*, 572:A57, 2014.
- Oke, J. B. & Searle, L. The spectra of supernovae. *ARA&A*, 12:315–329, Jan. 1974.
- Osher, S. & Sethian, J. A. Fronts propagating with curvature-dependent speed: Algorithms based on Hamilton–Jacobi formulations. *Journal of Computational Physics*, 79:12–49, Nov. 1988.
- Osterbrock, D. E. Who Really Coined the Word Supernova? Who First Predicted Neutron Stars? In *American Astronomical Society Meeting Abstracts*, volume 199 of *American Astronomical Society Meeting Abstracts*, page 15.01, Dec. 2001.
- Paczynski, B. Evolution of Single Stars. V. Carbon Ignition in Population I Stars. *AcA*, 21:271, Jan. 1971.
- Paczynski, B. & Zytkow, A. N. Hydrogen shell flashes in a white dwarf with mass accretion. *ApJ*, 222:604, June 1978.

- Pakmor, R., Kromer, M., Röpke, F. K., et al. Sub-luminous type ia supernovae from the mergers of equal-mass white dwarfs with mass $\sim 0.9m_{\odot}$. *Nature*, 463:61–64, Jan. 2010.
- Pakmor, R., Hachinger, S., Röpke, F. K., & Hillebrandt, W. Violent mergers of nearly equal-mass white dwarf as progenitors of subluminous Type Ia supernovae. *A&A*, 528:A117+, Apr. 2011.
- Pakmor, R., Kromer, M., Taubenberger, S., et al. Normal Type Ia supernovae from violent mergers of white dwarf binaries. *ApJ*, 747:L10, Mar. 2012.
- Panagia, N., Van Dyk, S. D., Weiler, K. W., et al. A search for radio emission from Type Ia supernovae. *ApJ*, 646:369–377, July 2006.
- Parrent, J., Friesen, B., & Parthasarathy, M. A review of type Ia supernova spectra. *Ap&SS*, 351:1–52, May 2014.
- Parrent, J. T., Thomas, R., Fesen, R. A., et al. A study of carbon features in type ia supernova spectra. *ApJ*, 732(1):30, 2011.
- Perivolaropoulos, L. & Skara, F. Challenges for Λ CDM: An update. *arXiv preprint arXiv:2105.05208*, 2021.
- Perlmutter, S., Aldering, G., Goldhaber, G., et al. Measurements of Omega and Lambda from 42 high-redshift supernovae. *ApJ*, 517:565–586, June 1999.
- Persson, S., Murphy, D., Krzeminski, W. a., Roth, M., & Rieke, M. A new system of faint near-infrared standard stars. *The Astronomical Journal*, 116(5):2475, 1998.
- Pfannes, J. M. M., Niemeyer, J. C., Schmidt, W., & Klingenberg, C. Thermonuclear explosions of rapidly rotating white dwarfs. I. Deflagrations. *A&A*, 509:A74, Jan. 2010.
- Phillips, M. M. The absolute magnitudes of Type Ia supernovae. *ApJ*, 413:L105–L108, Aug. 1993.
- Phillips, M. M., Wells, L. A., Suntzeff, N. B., et al. SN 1991T – Further evidence of the heterogeneous nature of type Ia supernovae. *AJ*, 103:1632–1637, May 1992.
- Phillips, M. M., Lira, P., Suntzeff, N. B., et al. The reddening-free decline rate versus luminosity relationship for Type Ia supernovae. *AJ*, 118:1766–1776, Oct. 1999.
- Pinto, P. A. & Eastman, R. G. The physics of Type Ia supernova light curves. II. Opacity and diffusion. *ApJ*, 530:757–776, Feb. 2000.
- Piro, A. L. Radioactively powered rising light curves of type ia supernovae. *ApJ*, 759:83, Nov. 2012.
- Piro, A. L. & Morozova, V. S. Exploring the potential diversity of early type ia supernova light curves. *ApJ*, 826(1):96, 2016.
- Plewa, T. Detonating failed deflagration model of thermonuclear supernovae. I. Explosion dynamics. *ApJ*, 657:942–960, Mar. 2007.

- Plewa, T., Calder, A. C., & Lamb, D. Q. Type Ia supernova explosion: Gravitationally confined detonation. *ApJ*, 612:L37–L40, Sept. 2004.
- Polin, A., Nugent, P., & Kasen, D. Nebular models of sub-chandrasekhar mass type ia supernovae: Clues to the origin of ca-rich transients. *The Astrophysical Journal*, 906(1):65, 2021.
- Prantzos, N., Abia, C., Limongi, M., Chieffi, A., & Cristallo, S. Chemical evolution with rotating massive star yields–i. the solar neighbourhood and the s-process elements. *MNRAS*, 476(3):3432–3459, 2018.
- Pskovskii, I. P. Light curves, color curves, and expansion velocity of type I supernovae as functions of the rate of brightness decline. *Soviet Astronomy*, 21:675–682, Dec. 1977.
- Raddi, R., Hollands, M., Koester, D., et al. Partly burnt runaway stellar remnants from peculiar thermonuclear supernovae. *MNRAS*, 489(2):1489–1508, 2019.
- Raskin, C., Timmes, F. X., Scannapieco, E., Diehl, S., & Fryer, C. On Type Ia supernovae from the collisions of two white dwarfs. *MNRAS*, 399:L156–L159, Oct. 2009.
- Rauscher, T. & Thielemann, F.-K. Astrophysical reaction rates from statistical model calculations. *Atomic Data and Nuclear Data Tables*, 75:1–2, May 2000.
- Reinecke, M., Hillebrandt, W., & Niemeyer, J. C. Thermonuclear explosions of Chandrasekhar-mass C+O white dwarfs. *A&A*, 347:739–747, July 1999a.
- Reinecke, M., Hillebrandt, W., Niemeyer, J. C., Klein, R., & Gröbl, A. A new model for deflagration fronts in reactive fluids. *A&A*, 347:724–733, July 1999b.
- Reinecke, M., Hillebrandt, W., & Niemeyer, J. C. Refined numerical models for multidimensional type Ia supernova simulations. *A&A*, 386:936–943, May 2002a.
- Reinecke, M., Hillebrandt, W., & Niemeyer, J. C. Three-dimensional simulations of type Ia supernovae. *A&A*, 391:1167–1172, Sept. 2002b.
- Reinecke, M., Hillebrandt, W., Niemeyer, J. C., et al. Recent progress in multidimensional SN Ia simulations. In Hillebrandt, W. & Müller, E., editors, *Proceedings of the 11th Workshop on "Nuclear Astrophysics", Ringberg Castle*, MPA/P13, pages 54–56, Garching, Apr. 2002c. Max-Planck-Institut für Astrophysik.
- Reynolds, S. P. Dynamical evolution and radiative processes of supernova remnants. *Handbook of Supernovae*, page 1981, 2017.
- Reynolds, S. P., Borkowski, K. J., Hwang, U., et al. A deep chandra observation of kepler’s supernova remnant: A type ia event with circumstellar interaction. *ApJ*, 668(2):L135, 2007.
- Riess, A. G., Press, W. H., & Kirshner, R. P. A precise distance indicator: Type Ia supernova multicolor light-curve shapes. *ApJ*, 473:88–109, Dec. 1996.
- Riess, A. G., Filippenko, A. V., Challis, P., et al. Observational evidence from supernovae for an accelerating universe and a cosmological constant. *AJ*, 116:1009–1038, Sept. 1998.

- Riess, A. G., Filippenko, A. V., Li, W., et al. The rise time of nearby type Ia supernovae. *AJ*, 118:2675–2688, Dec. 1999.
- Ritter, C. & Côté, B. NuPyCEE: NuGrid Python Chemical Evolution Environment, Oct. 2016.
- Röpke, F. K. Following multi-dimensional type Ia supernova explosion models to homologous expansion. *A&A*, 432:969–983, Mar. 2005.
- Röpke, F. K. Flame-driven deflagration-to-detonation transitions in Type Ia supernovae? *ApJ*, 668:1103–1108, Oct. 2007.
- Röpke, F. K. Combustion in thermonuclear supernova explosions. In Alsabti, A. & Murdin, P., editors, *Handbook of Supernovae*. Springer, Mar. 2017.
- Röpke, F. K. & Hillebrandt, W. The case against the progenitor’s carbon-to-oxygen ratio as a source of peak luminosity variations in type Ia supernovae. *A&A*, 420:L1–L4, June 2004.
- Röpke, F. K. & Hillebrandt, W. Full-star type Ia supernova explosion models. *A&A*, 431: 635–645, Feb. 2005.
- Röpke, F. K. & Niemeyer, J. C. Delayed detonations in full-star models of type Ia supernova explosions. *A&A*, 464:683–686, Mar. 2007.
- Röpke, F. K. & Sim, S. A. Models for type ia supernovae and related astrophysical transients. *Space Science Reviews*, 214(4):72, 2018.
- Röpke, F. K., Gieseler, M., Reinecke, M., Travaglio, C., & Hillebrandt, W. Type Ia supernova diversity in three-dimensional models. *A&A*, 453:203–217, July 2006.
- Röpke, F. K., Hillebrandt, W., Schmidt, W., et al. A three-dimensional deflagration model for Type Ia supernovae compared with observations. *ApJ*, 668:1132–1139, Oct. 2007a.
- Röpke, F. K., Woosley, S. E., & Hillebrandt, W. Off-center ignition in Type Ia supernovae. I. initial evolution and implications for delayed detonation. *ApJ*, 660:1344–1356, May 2007b.
- Rosswog, S., Kasen, D., Guillochon, J., & Ramirez-Ruiz, E. Collisions of white dwarfs as a new progenitor channel for Type Ia supernovae. *ApJ*, 705:L128–L132, Nov. 2009.
- Ruiter, A. J. Type ia supernova sub-classes and progenitor origin. *Proceedings of the International Astronomical Union*, 15(S357):1–15, 2019.
- Ruiter, A. J., Belczynski, K., & Fryer, C. Rates and delay times of type ia supernovae. *ApJ*, 699:2026–2036, July 2009.
- Russell, B. R. & Immler, S. Swift x-ray upper limits on type ia supernova environments. *ApJ*, 748(2):L29, 2012.
- Schmidt, W., Niemeyer, J. C., & Hillebrandt, W. A localised subgrid scale model for fluid dynamical simulations in astrophysics. I. Theory and numerical tests. *A&A*, 450:265–281, Apr. 2006a.

- Schmidt, W., Niemeyer, J. C., Hillebrandt, W., & Röpke, F. K. A localised subgrid scale model for fluid dynamical simulations in astrophysics. II. Application to type Ia supernovae. *A&A*, 450:283–294, Apr. 2006b.
- Schrauth, M. Massively parallel non-uniform poisson solver and its application to thermonuclear supernova modeling. Master's thesis, Universität Würzburg, 2015.
- Seitenzahl, I. R., Meakin, C. A., Lamb, D. Q., & Truran, J. W. Initiation of the detonation in the gravitationally confined detonation model of type Ia supernovae. *ApJ*, 700:642–653, July 2009a.
- Seitenzahl, I. R., Taubenberger, S., & Sim, S. A. Late-time supernova light curves: the effect of internal conversion and Auger electrons. *MNRAS*, 400:531–535, Nov. 2009b.
- Seitenzahl, I. R., Townsley, D. M., Peng, F., & Truran, J. W. Nuclear statistical equilibrium for type Ia supernova simulations. *Atomic Data and Nuclear Data Tables*, 95:96–114, Jan. 2009c.
- Seitenzahl, I. R., Röpke, F. K., Fink, M., & Pakmor, R. Nucleosynthesis in thermonuclear supernovae with tracers: convergence and variable mass particles. *MNRAS*, 407:2297–2304, Oct. 2010.
- Seitenzahl, I. R., Cescutti, G., Röpke, F. K., Ruiter, A. J., & Pakmor, R. Solar abundance of manganese: a case for near Chandrasekhar-mass type Ia supernova progenitors. *A&A*, 559:L5, Nov. 2013a.
- Seitenzahl, I. R., Ciaraldi-Schoolmann, F., Röpke, F. K., et al. Three-dimensional delayed-detonation models with nucleosynthesis for Type Ia supernovae. *MNRAS*, 429:1156–1172, Feb. 2013b.
- Seitenzahl, I. R., Herzog, M., Ruiter, A. J., et al. Neutrino and gravitational wave signal of a delayed-detonation model of type Ia supernovae. *Phys. Rev. D*, 92(12):124013, Dec. 2015.
- Seitenzahl, I. R., Kromer, M., Ohlmann, S. T., et al. Three-dimensional simulations of gravitationally confined detonations compared to observations of SN 1991T. *A&A*, 592:A57, July 2016.
- Shapiro, S. L. & Teukolsky, S. A. *Black holes, white dwarfs, and neutron stars: The physics of compact objects*. Wiley-VCH, 2004.
- Shappee, B., Holoien, T.-S., Drout, M. R., et al. Seeing double: Asassn-18bt exhibits a two-component rise in the early-time k2 light curve. *ApJ*, 870(1):13, 2018.
- Sharpe, G. J. The structure of steady detonation waves in Type Ia supernovae: pathological detonations in C-O cores. *MNRAS*, 310:1039–1052, Dec. 1999.
- Shchigolev, V. Calculating luminosity distance versus redshift in FLRW cosmology via homotopy perturbation method. *Gravitation and Cosmology*, 23(2):142–148, 2017.
- Shen, K. J. & Bildsten, L. Thermally stable nuclear burning on accreting white dwarfs. *ApJ*, 660:1444–1450, May 2007.

- Shingles, L., Sim, S., Kromer, M., et al. Monte carlo radiative transfer for the nebular phase of type ia supernovae. *MNRAS*, 492(2):2029–2043, 2020.
- Siebert, M., Foley, R., Jones, D., et al. Investigating the diversity of type ia supernova spectra with the open-source relational data base kaepora. *MNRAS*, 486(4):5785–5808, 2019.
- Sienkiewicz, R. Stability of white dwarfs undergoing spherically symmetric steady-state accretion. *A&A*, 85(3):295–301, May 1980.
- Siess, L. Evolution of massive AGB stars. II. model properties at non-solar metallicity and the fate of Super-AGB stars. *A&A*, 476(2):893–909, Dec. 2007.
- Silverman, J. M. & Filippenko, A. V. Berkeley supernova ia program–iv. carbon detection in early-time optical spectra of type ia supernovae. *MNRAS*, 425(3):1917–1933, 2012.
- Silverman, J. M., Kong, J. J., & Filippenko, A. V. Berkeley Supernova Ia Program - II. Initial analysis of spectra obtained near maximum brightness. *MNRAS*, 425:1819–1888, Sept. 2012.
- Silverman, J. M., Ganeshalingam, M., & Filippenko, A. V. Berkeley Supernova Ia Program – V. Late-time spectra of Type Ia Supernovae. *MNRAS*, 430(2):1030–1041, 01 2013. ISSN 0035-8711.
- Sim, S. A. Multidimensional simulations of radiative transfer in type ia supernovae. *MNRAS*, 375:154–162, Feb. 2007.
- Sim, S. A. Spectra of supernovae during the photospheric phase. *Handbook of Supernovae*, page 769, 2017.
- Sim, S. A., Kromer, M., Röpke, F. K., et al. Monte Carlo Radiative Transfer Simulations: Applications to Astrophysical Outflows and Explosions. In Pogorelov, N. V., Audit, E., & Zank, G. P., editors, *Numerical Modeling of Space Plasma Flows, Astronom-2009*, volume 429 of *Astronomical Society of the Pacific Conference Series*, page 148, Sept. 2010.
- Sim, S. A., Fink, M., Kromer, M., et al. 2D simulations of the double-detonation model for thermonuclear transients from low-mass carbon–oxygen white dwarfs. *MNRAS*, 420:3003–3016, Mar. 2012.
- Sim, S. A., Seitzzahl, I. R., Kromer, M., et al. Synthetic light curves and spectra for three-dimensional delayed-detonation models of type ia supernovae. *MNRAS*, 436:333–347, Nov. 2013.
- Smiljanovski, V., Moser, V., & Klein, R. A capturing–tracking hybrid scheme for deflagration discontinuities. *Combustion Theory Modelling*, 1:183–215, June 1997.
- Sobolev, V. V. The Diffusion of $L\alpha$ Radiation in Nebulae and Stellar Envelopes. *Soviet Ast.*, 1: 678, Oct. 1957.
- Soker, N. Supernovae ia in 2019 (review): A rising demand for spherical explosions. *New Astronomy Reviews*, 87:101535, 2019.

- Starrfield, S., Iliadis, C., Timmes, F. X., et al. Theoretical studies of accretion of matter onto white dwarfs and the single degenerate scenario for supernovae of Type Ia. *Bulletin of the Astronomical Society of India*, 40:419, Sept. 2012.
- Starrfield, S., Iliadis, C., & Hix, W. The thermonuclear runaway and the classical nova outburst. *Publications of the Astronomical Society of the Pacific*, 128(963):051001, 2016.
- Stone, J. M. & Gardiner, T. The magnetic rayleigh-taylor instability in three dimensions. *ApJ*, 671(2):1726, 2007.
- Stritzinger, M. & Leibundgut, B. Lower limits on the hubble constant from models of type Ia supernovae. *A&A*, 431:423–431, Feb. 2005.
- Stritzinger, M., Mazzali, P. A., Sollerman, J., & Benetti, S. Consistent estimates of ^{56}Ni yields for type Ia supernovae. *A&A*, 460:793–798, Dec. 2006.
- Stritzinger, M. D., Valenti, S., Hoefflich, P., et al. Comprehensive observations of the bright and energetic Type Iax SN 2012Z: Interpretation as a Chandrasekhar mass white dwarf explosion. *A&A*, 573:A2, Jan. 2015.
- Taam, R. E. The long-term evolution of accreting carbon white dwarfs. *ApJ*, 242:749–755, Dec. 1980.
- Tammann, G. A., Loeffler, W., & Schroeder, A. The Galactic Supernova Rate. *ApJS*, 92:487, June 1994.
- Taubenberger, S. The extremes of thermonuclear supernovae. *Handbook of Supernovae*, pages 317–373, 2017.
- Timmes, F. X. & Arnett, D. The accuracy, consistency, and speed of five equations of state for stellar hydrodynamics. *ApJS*, 125:277–294, Nov. 1999.
- Timmes, F. X. & Swesty, F. D. The accuracy, consistency, and speed of an electron-positron equation of state based on table interpolation of the Helmholtz free energy. *ApJS*, 126:501–516, Feb. 2000.
- Timmes, F. X. & Woosley, S. E. The conductive propagation of nuclear flames. I. degenerate C+O and O+Ne+Mg white dwarfs. *ApJ*, 396:649–667, Sept. 1992.
- Timmes, F. X., Zingale, M., Olson, K., et al. On the Cellular Structure of Carbon Detonations. *ApJ*, 543:938–954, Nov. 2000.
- Toonen, S., Nelemans, G., & Portegies Zwart, S. Supernova type ia progenitors from merging double white dwarfs. using a new population synthesis model. *A&A*, 546:A70, Oct. 2012.
- Toro, E. F. *Riemann Solvers and Numerical Methods for Fluid Dynamics: A Practical Introduction*. Springer, Berlin Heidelberg, 2009. ISBN 9783540498346.
- Townsley, D. M., Calder, A. C., Asida, S. M., et al. Flame evolution during Type Ia supernovae and the deflagration phase in the gravitationally confined detonation scenario. *ApJ*, 668: 1118–1131, Oct. 2007.

- Townsley, D. M., Miles, B. J., Shen, K. J., & Kasen, D. Double detonations with thin, modestly enriched helium layers can make normal type ia supernovae. *ApJ*, 878(2):L38, 2019.
- Trimble, V. Supernovae. part i: the events. *Reviews of Modern Physics*, 54(4):1183, 1982.
- Trimble, V. The 1920 shapley-curtis discussion: Background, issues, and aftermath. *Publications of the Astronomical Society of the Pacific*, 107(718):1133, 1995.
- Truran, J. W., Arnett, W. D., & Cameron, A. G. W. Nucleosynthesis in supernova shock waves. *Can. J. Phys.*, 45:2315–2332, 1967.
- Tutukov, A. & Yungelson, L. Double-degenerate semidetached binaries with helium secondaries: cataclysmic variables, supersoft x-ray sources, supernovae and accretion-induced collapses. *MNRAS*, 280:1035–1045, June 1996.
- van Kerkwijk, M. H., Chang, P., & Justham, S. Sub-chandrasekhar white dwarf mergers as the progenitors of type ia supernovae. *ApJ*, 722:L157–L161, Oct. 2010.
- von Neumann, J. Theory of detonation waves. Prog. Rept. No. 238; O.S.R.D. Rept. No. 549, Ballistic Research Laboratory File No. X-122, Aberdeen Proving Ground, MD, Aberdeen Proving Ground, MD, 1942.
- Wallace, R. K., Woosley, S. E., & Weaver, T. A. The thermonuclear model for x-ray transients. *ApJ*, 258:696–715, July 1982.
- Wang, B., Chen, X., Meng, X., & Han, Z. Evolving to type ia supernovae with short delay times. *The Astrophysical Journal*, 701(2):1540, 2009.
- Wang, B., Podsiadlowski, P., & Han, Z. He-accreting carbon-oxygen white dwarfs and Type Ia supernovae. *MNRAS*, 472(2):1593–1599, Dec. 2017.
- Webbink, R. F. Double white dwarfs as progenitors of R Coronae Borealis stars and Type I supernovae. *ApJ*, 277:355–360, Feb. 1984.
- Wheeler, J. C. & Harkness, R. P. Type I supernovae. *Reports of Progress in Physics*, 53: 1467–1557, 1990.
- Whelan, J. & Iben, I. J. Binaries and supernovae of type I. *ApJ*, 186:1007–1014, Dec. 1973.
- Wilson, J. R. Supernovae and post-collapse behavior. *Numerical astrophysics*, page 422, 1985.
- Wong, T. L. S. & Schwab, J. Evolution of helium star–white dwarf binaries leading up to thermonuclear supernovae. *ApJ*, 878(2):100, 2019.
- Wong, T. L. S., Schwab, J., & Götberg, Y. Pre-explosion properties of helium star donors to thermonuclear supernovae. *The Astrophysical Journal*, 922(2):241, 2021.
- Woosley, S. E., Arnett, W. D., & Clayton, D. D. The explosive burning of oxygen and silicon. *ApJS*, 26:231, Nov. 1973.
- Woosley, S. E., Taam, R. E., & Weaver, T. A. Models for Type I supernova. I – Detonations in white dwarfs. *ApJ*, 301:601–623, Feb. 1986.

- Woosley, S. E., Almgren, A., Bell, J. B., et al. Type Ia supernovae. *Journal of Physics Conference Series*, 78(1):012081, July 2007.
- Woosley, S. E., Kerstein, A. R., Sankaran, V., Aspden, A. J., & Röpke, F. K. Type Ia Supernovae: Calculations of Turbulent Flames Using the Linear Eddy Model. *ApJ*, 704:255–273, Oct. 2009.
- Yamaguchi, H., Badenes, C., Foster, A. R., et al. A chandrasekhar mass progenitor for the type ia supernova remnant 3c 397 from the enhanced abundances of nickel and manganese. *ApJ*, 801(2):L31, 2015.
- Yaron, O., Prialnik, D., Shara, M. M., & Kovetz, A. An Extended Grid of Nova Models. II. The Parameter Space of Nova Outbursts. *ApJ*, 623:398–410, Apr. 2005.
- Yungelson, L., Livio, M., Tutukov, A., & Kenyon, S. J. A model for the galactic population of symbiotic stars with white dwarf accretors. *ApJ*, 447:656, July 1995.
- Zel'dovich, Y. B. On the theory of the propagation of detonations on gaseous system. *Zh. Eksp. Teor. Fiz.*, 10:542–568, 1940. In Russian.
- Zheng, W., Kelly, P. L., & Filippenko, A. V. An Empirical Fitting Method for Type Ia Supernova Light Curves. II. Estimating the First-light Time and Rise Time. *ApJ*, 848(1):66, Oct. 2017.
- Zingale, M., Almgren, A. S., Bell, J. B., Nonaka, A., & Woosley, S. E. Low Mach Number Modeling of Type IA Supernovae. IV. White Dwarf Convection. *ApJ*, 704:196–210, Oct. 2009.
- Zingale, M., Nonaka, A., Almgren, A. S., et al. The Convective Phase Preceding Type Ia Supernovae. *ApJ*, 740:8, Oct. 2011.
- Zingale, M., Nonaka, A., Almgren, A. S., et al. Low mach number modeling of convection in helium shells on sub-chandrasekhar white dwarfs. I. Methodology. *ApJ*, 764:97, Feb. 2013.